

Non-adiabatic Dynamics in Excited Molecular Systems and their Manifestation in X-ray Spectroscopic Observables

Dissertation
zur Erlangung des Doktorgrades
an der Fakultät für Mathematik, Informatik und Naturwissenschaften
Fachbereich Chemie
der Universität Hamburg

vorgelegt von
Antonia Hannah Rebekka Freibert

Hamburg
2024

Gutachter/in der Dissertation:

Prof. Dr. Carmen Herrmann
Prof. Dr. Oriol Vendrell

Zusammensetzung der Prüfungskommission:

Prof. Dr. Carmen Herrmann
Prof. Dr. Gabriel Bester
Prof. Dr. Graham Worth

Vorsitzende der Prüfungskommission:

Prof. Dr. Carmen Herrmann

Datum der Disputation:

07.06.2024

Datum der Druckfreigabe:

07.06.2024

The work underlying this dissertation has been carried out from October 2020 to April 2024 at the University of Hamburg.

List of Publications

1. M. Ochmann, J. Harich, R. Ma, **A. Freibert***, J. H. Lee, D. Nam, S. Kim, I. Eom, M. Kim, Y. Kim, M. Gopannagari, D. H. Hong, B. A. Yorkee, T. K. Kim* and N. Huse*, *UV photochemistry of the L-cystine disulfide bridge in aqueous solution investigated by femtosecond X-ray absorption spectroscopy*, submitted (2024)
2. L. Cruz-Rodriguez[†], D. Dey[†], **A. Freibert[†]** and P. Stammer[†], *Quantum phenomena in attosecond science*, arXiv preprint arXiv:2403.05482 (2024)
3. **A. Freibert***, D. Mendive-Tapia, O. Vendrell* and N. Huse, *A Fully Dynamical Description of Time-Resolved Resonant Inelastic X-ray Scattering of Pyrazine*, arXiv preprint arXiv:2403.11005 (2024)
4. O. Bennett, **A. Freibert**, K. E. Spinlove and G. A. Worth, *Prediction Through Quantum Dynamics Simulations: Photo-excited Cyclobutanone*, *J. Chem. Phys.* **160** (2024), 174305
5. **A. Freibert***, D. Mendive-Tapia, N. Huse and O. Vendrell*, *Time-Dependent Resonant Inelastic X-ray Scattering of Pyrazine at the Nitrogen K-Edge: A Quantum Dynamics Approach*, *J. Chem. Theory Comput.*, **20(5)** (2024), 2167-2180
6. **A. Freibert***, D. Mendive-Tapia, N. Huse and O. Vendrell*, *Femtosecond X-ray Absorption Spectroscopy of Pyrazine at the Nitrogen K-edge: On the Validity of the Lorentzian Limit*, *J. Phys. B: At. Mol. Opt. Phys.* **54** (2022), 244003
7. G. Christopoulou, **A. Freibert** and G. A. Worth, *Improved algorithm for the direct dynamics variational multi-configurational Gaussian method*, *J. Chem. Phys.* **154** (2021), 124127
8. **A. Freibert**, J. M. Dieterich and B. Hartke, *Exploring self-organization of molecular tether molecules on a gold surface by global structure optimization*, *J. Comput. Chem.* **40** (2019), 1978 – 1989

List of Abbreviations

ADC	algebraic-diagrammatic construction
BOA	Born-Oppenheimer approximation
CC	coupled cluster
CCSD	CC singles and doubles
CPP	complex polarisation propagator
CVS	core-valence separation
CW	continuous wave
DFT	density functional theory
DVR	discrete variable representation
EOM	equation of motion
fc	frozen core
FC	Franck-Condon
fs	femtosecond
fwhm	full width at half maximum
KHD	Kramers-Heisenberg-Dirac
MCSCF	multiconfiguration self-consistent field
MCTDH	multiconfiguration time-dependent Hartree
ML-MCTDH	multi-layer MCTDH
MRCI	multireference configuration interaction
PES	potential energy (hyper-)surface
RAS	resonant Auger scattering
RIXS	resonant inelastic X-ray scattering
SPFs	single particle functions
TDSE	time-dependent Schrödinger equation
UV	ultraviolet
XANES	X-ray absorption near-edge structure
XAS	X-ray absorption spectroscopy
XES	X-ray emission spectroscopy
XFEL	X-ray free electron laser

Abstract

Time-resolved experimental techniques have significantly advanced our understanding of fundamental chemical processes. The emergence and ongoing refinement of ultrafast and intense X-ray sources have facilitated the extension of ultrafast pump-probe methods into the X-ray domain. These innovative techniques, combining element-specific core-level probing with femtosecond time-resolution, have become invaluable for studying dynamical processes in transient species in real time.

Given the intricate nature of these processes, advancements in experimental capabilities are generally accompanied by theoretical developments enabling the deciphering of mechanistic information from experimental data and providing support for their analysis. During the past two decades, various electronic structure methods have been devised to simulate advanced X-ray spectroscopy techniques, albeit often overlooking the influence of nuclear motion. While this is justified to some extent by the short lifetimes of core-excited states, nonlinear X-ray spectroscopy may reveal a more significant impact of nuclear dynamics.

This thesis focuses on elucidating the role of nuclear dynamics in nonlinear X-ray spectroscopy at the nitrogen K-edge of pyrazine. Employing a comprehensive time-dependent approach including wavepacket dynamics in both valence- and core-excited state manifolds, we aim to assess the validity of the commonly used short-time approximation and investigate the effects of employing progressively longer pump pulses in transient X-ray absorption spectroscopy. Furthermore, our investigations uncover instances of ultrafast symmetry breaking induced by core-excited state dynamics, leading to spectral features in resonant inelastic X-ray scattering that would remain inaccessible without accounting for nuclear motion. Furthermore, the time-dependent framework enables the exploration of the influence of pulsed incident X-ray radiation on resonant inelastic X-ray scattering spectra, providing a basis for cutting-edge time-resolved experiments with coherent light sources. Such experiments necessitate a time-dependent framework capable of accurately describing non-adiabatic dynamics in both valence- and core-excited states to fully elucidate the underlying mechanisms.

Zusammenfassung

Zeitaufgelöste Spektroskopiemethoden haben unser Verständnis grundlegender chemischer Prozesse geprägt. Die Erweiterung ultraschneller Pump-Probe-Methoden in den Röntgenbereich wurde schließlich durch das Aufkommen ultraschneller und intensiver Röntgenquellen und deren stetiger Weiterentwicklung möglich. Die Kombination aus elementspezifischer Abtastung mit Femtosekunden-Zeitauflösung machen diese Techniken enorm wertvoll um dynamische Prozesse von transienten Spezies in Echtzeit zu untersuchen.

Angesichts der komplexen Natur der zugrundeliegenden Prozesse gehen experimentelle Fortschritte stets mit theoretischen Entwicklungen einher, ohne die eine präzise Datenauswertung kaum möglich wär. In den letzten beiden Jahrzehnten wurden daher verschiedene Elektronenstrukturmethoden entwickelt, wobei der Einfluss der Kernbewegung noch weitestgehend außer Acht gelassen wird. Während dies bis zu einem gewissen Grad durch die kurzen Lebensdauern der kernangeregten Zustände gerechtfertigt werden kann, weisen insbesondere Spektren nichtlinearer Prozesse teils erhebliche Signaturen von Kernbewegung auf.

In dieser Arbeit wird die Rolle der Kerndynamik in nichtlinearer Röntgenspektroskopie an der Stickstoff K-Kante von Pyrazin untersucht. Mit Hilfe eines vollständig zeitabhängigen Ansatzes, der die Wellenpaketdynamik in allen elektronischen Zuständen einschließt, konnte die Gültigkeit der gängigen Kurzzeitnäherung sowie die Auswirkung endlicher Pumpimpulse im Rahmen der transienten Röntgenabsorption untersucht werden. Darüber hinaus konnten wir durch Kernbewegung verursachte Symmetriebrüche beobachten, die zu weiteren, ohne Kerndynamik unzugänglichen spektralen Banden in resonanter inelastischer Röntgenstreuung führte. Zudem wurde der Einfluss einfallender gepulster Röntgenstrahlung auf die Spektren der resonanten inelastischen Röntgenstreuung verdeutlicht. Letzteres liefert die Grundlage für Berechnungen modernster zeitaufgelöster Experimente mit kohärenten Lichtquellen. Insbesondere solche Experimente erfordern einen zeitabhängigen Rahmen, in dem nicht-adiabatische Dynamik im gesamten elektronischen Raum präzise beschrieben werden kann, um die zugrunde liegenden Mechanismen vollständig aufzuklären.

Contents

Abstract	
Zusammenfassung	
1 Introduction	1
2 Theoretical Background	7
2.1 The Molecular Schrödinger Equation	7
2.2 Born-Oppenheimer Approximation	8
2.3 Adiabatic-to-Diabatic Transformation	10
2.4 Time-Dependent Molecular Spectroscopy	13
2.4.1 Light-Matter-Interaction	13
2.4.2 Absorption Spectroscopy	14
2.4.3 Resonance Raman Spectroscopy	20
3 Methodology	26
3.1 Multi-Configuration Time-Dependent Hartree Method	27
3.2 Coupled-Cluster Theory and its Derivatives	30
4 Results	32
4.1 Pyrazine	32
4.2 Construction of Model Hamiltonian	33
4.3 Femtosecond X-ray Absorption Spectroscopy	37
4.4 Resonant Inelastic X-ray Scattering	49
4.5 Femtosecond Resonant Inelastic X-ray Scattering	60
5 Conclusion & Outlook	72
References	75
Appendix	I

Chapter 1

Introduction

Light-induced chemical and physical reactions are ubiquitous in natural (chemical and biological) and technological systems. [1–15] Understanding what happens to a molecule after absorption of a photon and determining methods to influence its behavior have long intrigued researchers, driving advances in both experimental and theoretical techniques.

Upon absorbing a photon, a molecule is, in general, promoted to an excited state, typically leading to a non-equilibrium geometry of the nuclei. Thus, to dissipate the excess of energy, the molecule undergoes various relaxation processes, intramolecular vibrational energy redistribution across different modes and to surrounding baths, as well as electronic relaxation via radiative and non-radiative pathways between distinct electronic states where the latter usually occurs near conical intersections, in which multiple electronic states become degenerate. Alternatively, the molecule may undergo photochemical reactions in its excited electronic state, such as electron- or proton-transfer, dissociation, or isomerisation before returning back to the ground state.

In order to monitor such light-induced molecular phenomena, time-resolved spectroscopy plays a pivotal role, and among this class of spectroscopic methods, pump-probe schemes are those that provide highest time-resolution. In the latter set of techniques an initial pulse, termed pump pulse, triggers a dynamic process through photoexcitation, while the subsequent evolution of the system is monitored using a temporally delayed probe pulse. By varying the time delay between the pulses, sequential spectroscopic measurements capture the molecular behavior over time, akin to a series of frames in a movie. Various pump-probe schemes, including transient absorption, laser-induced fluorescence, or photoelectron spectroscopy, are available where the wavelength of the pulses dictates which transitions can be detected and thus what aspect of the underlying process is monitored.

Spectroscopy in the infrared and optical regime (spanning visible and ultraviolet (UV) ranges), has proven effective in investigating rotational, vibrational, and electronic valence excitations, respectively, with a high sensitivity to the local chemical environment. X-ray spectroscopy, on the other hand, targets transitions involving inner-shell electrons, thereby providing element-specificity. The X-ray spectrum is typically classified into soft (~ 100 - 2000 eV) and hard (~ 2 - 200 keV) X-ray regimes where this thesis mainly focus on *in silico* femtosecond soft X-ray spectroscopy.

The historical narrative of X-ray spectroscopy dates back over a century, commencing with the discovery of hard X-ray radiation in 1895, [16] and their first applications in spectroscopic methodology. [17-20] However, it was the advent of 2nd generation synchrotron radiation facilities dedicated to X-ray spectroscopy during the 1970s that marked a significant milestone. [21,22] This scientific era saw the establishment of X-ray absorption spectroscopy (XAS) and successively X-ray emission spectroscopy (XES) as robust tools for elucidating the structural and electronic configurations of unknown systems propelling X-ray spectroscopy to a routinely employed set of scientific methods. Subsequent experimental advances, including significant enhancements in spectral brightness and intensity of 3rd and 4th-generation synchrotron radiation sources, [23,24] promoted the emergence of numerous powerful spectroscopic techniques, e.g. XAS with 20 nm resolution, XES, resonant inelastic X-ray scattering (RIXS) and resonant Auger scattering (RAS). The versatility of these techniques has been demonstrated in studying properties of isolated molecules, liquids, and solids, further solidifying X-ray spectroscopy's status as an indispensable scientific tool in materials research.

The emergence of X-ray free electron laser (XFEL) facilities [25-30] marked a further significant advancement in X-ray spectroscopy, particularly in exploiting ultrashort X-ray pulses to study ultrafast phenomena in matter. XFELs represent a novel generation of light sources characterised by a substantial increase in spectral brightness and spatial coherence compared to synchrotron radiation sources, and the ability to generate ultrashort X-ray pulses, down to sub-femtosecond duration. This technological innovation, coupled with ongoing advances, finally enabled the extension of ultrafast pump-probe techniques to the X-ray domain. The combination of element-specific core-level probing with femtosecond time-resolution has emerged as an important capability to understanding molecular dynamics on its intrinsic timescale, thereby still paving the way for novel applications across various research areas such as biology, materials science, chemistry, and physics. [31]

Nonetheless, harnessing the full capabilities of modern synchrotron radiation and XFEL sources requires robust theoretical and computational support. Extensive ef-

forts have been dedicated to developing quantum chemical methods for addressing core-excited states and computing X-ray spectra. These encompass wavefunction-based theories such as multiconfiguration self-consistent field (MCSCF), [32–34] multireference configuration interaction (MRCI), [35,36] coupled cluster (CC) [37–41] or algebraic-diagrammatic construction (ADC) [42–46] as well as density functional theory (DFT) based approaches. [47–49] The primary advantage of DFT-based methods is their lower computational cost compared to wavefunction-based methods, enabling simulations of larger molecules comprising several hundred atoms. However, this computational efficiency often comes at the expense of reduced reliability and accuracy of results. [50,51] Conversely, wavefunction-based methods are renowned for providing accurate descriptions of excited states, with established avenues for systematic improvement, albeit their applicability is typically constrained to small- or medium-sized molecules. The capabilities of both frameworks are demonstrated in various applications of linear and non-linear X-ray spectroscopy. [52]

A practical hurdle, common for all electronic structure theories, arises from the nature of core-excited states within the high-energy X-ray region, embedded in a continuum of valence-excited states. Directly tackling the eigenvalue problem by employing numerical iterative eigenvalue solvers, such as the Davidson algorithm, [53] to obtain the lowest energy eigenstates is hence excessively computationally demanding and unfeasible for most X-ray spectroscopic investigations. A widely used approximation circumventing this issue is the core-valence separation (CVS) scheme [54,55] which decouples the core and valence excitation spaces, thereby facilitating direct computation of core-excited states. The CVS approximation has been successfully implemented in various electronic structure methods. [36,37,39,40,43,44,48,56–58] Alternatively, the complex polarisation propagator (CPP) approach [59–61] has demonstrated viability in addressing X-ray spectroscopies, offering a balanced treatment of both core- and valence-excited states. This approach proves particularly advantageous in scenarios necessitating the inclusion of both valence- and core-excited states, as e.g. encountered in RIXS [62]

An important, yet often neglected aspect in X-ray spectroscopy simulations is the influence of nuclear motion. Typically, it is assumed that the evolution of the wavepacket within the short lifetime of core-excited states is negligible. [63,64] Generally, the lifetime of an excited state is inversely proportional to the total sum of radiative and non-radiative decay transitions. For core-excited states of atoms in the first two rows of the periodic table, Auger decay constitutes the dominant de-excitation process and as a good approximation, the mean lifetime can be con-

sidered as an intrinsic property of these atomic species, typically falling within the few-femtosecond (fs) range. [65,66]

While ignoring nuclear motion is partially justified for steady-state linear X-ray spectroscopy techniques such as XAS, it has been demonstrated that steady-state nonlinear X-ray spectroscopy methods, such as RIXS or RAS, are indeed sensitive to ultrafast nuclear dynamics occurring in the intermediate core-excited state manifold. [67] Various strategies have been proposed to incorporate dynamical effects, ranging from frequency-domain approaches which e.g. incorporate interference effects through the consideration of electronic state superpositions, [68] to semiclassical descriptions [69] enabling the treatment of more complex systems, and even (partially) time-dependent representations of RIXS using reduced-dimensional models within [70–72] and beyond [73] the Born-Oppenheimer approximation. However, due to multi-dimensional complex potential energy landscapes and vibrational mode coupling, the X-ray induced nuclear wavepacket dynamics can be very complicated, making the selection of the dominant driving modes not always straightforward.

Beyond the computation of steady-state X-ray spectra, where analytical expressions are principally available in both, the frequency and the time domain, the simulation of nuclear dynamics becomes important when aiming to achieve an accurate description of transient X-ray spectroscopy. In many systems, pump-induced excited state dynamics are governed by the interplay and competition among various dynamical processes involving multiple electronic states. These processes may involve channels with comparable energies, making it challenging to predict the molecule’s dynamics solely from static information obtained by electronic structure calculations. Furthermore, these processes are frequently affected by pronounced quantum effects such as tunneling through potential energy barriers, interference phenomena, and non-radiative decay processes occurring near conical intersections. Consequently, when probing such dynamics using X-ray techniques, a time-dependent quantum mechanical description is necessary to comprehensively understand and unravel the photochemical behavior in both the valence- and core-excited states. To address this demand, this thesis presents fully quantum mechanical time-dependent analyses of three nonlinear X-ray spectroscopic methods.

Within the first project [74], we calculated femtosecond X-ray absorption near-edge structure (XANES) spectra at the nitrogen K-edge of pyrazine. Enabled by the development of XFELs, fs-XANES emerges as a valuable technique to follow photoinduced molecular processes [75–80] by offering element-specific core-level probing with unprecedented time resolution. Numerous theoretical strategies have been developed to aid in experimental data interpretation and prediction. [52] However, the

majority of studies predominantly operates within the frequency domain, thereby neglecting nuclear motion effects. Even in dynamical transient **XAS** simulations, the prevalent approach often entails employing the short-time approximation, wherein transient valence-state dynamics are explicitly simulated followed by static X-ray spectra calculations after a specified time delay. [78, 81–87] In order to delineate the validity range of this approximation, we computed **fs-XANES** spectra with and without this simplification, maintaining otherwise identical setups and Hamiltonian parameters. We were thus able to provide a comparative analysis elucidating the impact of the short-time approximation without any further assumptions. Moreover, the time-dependent framework facilitated an explicit description of the external electric field, allowing to explore the effects of finite pulse durations — an essential factor when seeking an optimal synergy between experiment and theory.

The second project [88] is dedicated to the time-dependent description of **RIXS** of pyrazine. **RIXS** is a coherent Raman scattering process in which the system is resonantly excited into short-lived core-excited states, followed by spontaneous photon emission, returning the system to its electronic ground or energetically lower excited states. [89, 90] This photon-in-photon-out technique enables the population of final excited states that are inaccessible via linear absorption spectroscopy due to symmetry constraints. [68, 91, 92] Furthermore, **RIXS** can probe valence-excited states across a broad spectral range (>20 eV), even in condensed phases, [93] without being limited by phenomenological core-hole lifetime broadening. The versatility of **RIXS** to ground and valence-excited states has already been demonstrated in various applications such as hydrogen-bond interactions, [94–97] photochemistry of transition-metal complexes, [98–104] or proton transfer dynamics. [105–107] Moreover, by adjusting the excitation energy **RIXS** has proven effective in monitoring, controlling or even preventing ultrafast core-excited state dynamics such as dissociation, [108, 109] vibrational collapse, [110, 111] or symmetry distortion. [112–115] In order to explore the N-1s **RIXS** process of pyrazine and accurately capture dynamic phenomena occurring within the ultrashort core-hole lifetime, we employed a quantum dynamics approach leveraging the advantages of time-dependent methods. Additionally, we investigated how an incoming ultrashort X-ray pulse manifests in the resulting spectra.

The time-dependent formulation of **RIXS** becomes particularly important when aiming at describing time-resolved **RIXS** experiments with **XFEL** pulses leading to the third project [116] outlined in this thesis. While **RIXS** was initially enabled by synchrotron radiation X-ray sources with increased spectral brightness, [23] the advances of **XFELs** facilitated the extension of **RIXS** to pump-probe spec-

troscopy [67, 117, 118] where the electronic (Raman) excitation spectrum of excited molecules up to the vacuum UV spectral range is probed rather than a single X-ray resonance (as is done in fs-XANES spectroscopy). The complex nature of the underlying probe processes from valence-excited state demands the utilisation of advanced computational techniques. Prior theoretical investigations of time-resolved RIXS in chemical applications exclusively operated in the frequency domain, treating transient pump-induced states as isolated quasi-static snapshots for which steady-state RIXS spectra were simulated, neglecting any nuclear motion effects and comparing against molecular states or structures that seem chemically possible. [103, 119–121] However, the real-time evolution of the pump-induced wavepacket can substantially influence the overall experimental signal. Within this final project, we present a comprehensive quantum dynamical treatment of fs-RIXS spectroscopy applied to pyrazine. This treatment incorporates dynamics of both valence- and core-excited states, along with an explicit description of the probe pulse emphasising the significance of adopting a full time-domain approach to achieve an accurate description of time-resolved RIXS signals.

In this thesis, the essential theoretical concepts to study multi-dimensional photoexcited non-adiabatic molecular systems along with an intense discussion how to derive spectroscopic observables out of wavepacket dynamics simulations are provided in Chapter 2. The subsequent Chapter 3 provides a succinct introduction to the specific methodologies employed in this thesis while Chapter 4 presents and thoroughly discusses the outcomes of our *in silico* X-ray spectroscopic experiments. Finally, a summary of our findings along with an outlook into future research directions concludes this thesis in Chapter 5.

Chapter 2

Theoretical Background

Throughout this thesis, we use a unit system with $\hbar = 1$ and consider only non-relativistic quantum systems unless otherwise stated. The bold font has been used to signify vectors and matrices while $\hat{}$ indicates operators.

2.1 The Molecular Schrödinger Equation

For a precise depiction of the temporal progression and non-equilibrium properties of photo-induced molecular systems it is necessary to solve the full time-dependent Schrödinger equation (TDSE) [122,123]

$$i\frac{\partial}{\partial t}|\Psi(\mathbf{r}, \mathbf{R}, t)\rangle = \hat{H}(\mathbf{r}, \mathbf{R}, t)|\Psi(\mathbf{r}, \mathbf{R}, t)\rangle \quad (2.1)$$

where the molecular wavefunction $|\Psi\rangle$ depends on the electronic and nuclear coordinates, \mathbf{r} and \mathbf{R} , respectively, as well as on the time, t . The Hermitian operator \hat{H} defines the full Hamiltonian whose eigenvalues with respect to $|\Psi\rangle$ are representing the total energy of the system. In absence of any external field and neglecting relativistic effects, the Hamiltonian of an isolated molecule can be written as the time-independent sum

$$\hat{H}_{\text{mol}}(\mathbf{r}, \mathbf{R}) = \hat{T}_N(\mathbf{R}) + \hat{H}_{\text{el}}(\mathbf{r}, \mathbf{R}) \quad (2.2)$$

where \hat{T}_N is the nuclear kinetic energy operator and \hat{H}_{el} denotes the electronic Hamiltonian containing the electronic kinetic energy operator as well as all Coulomb repulsion and attraction terms. In particular, \hat{H}_{el} does not include any differential operator with respect to the nuclear coordinates and depends only parametrically on \mathbf{R} .

As the molecular Hamiltonian \hat{H}_{mol} is time-independent, the formal solution of the molecular **TDSE** is

$$|\Psi(\mathbf{r}, \mathbf{R}, t)\rangle = \exp\left(-i\hat{H}_{\text{mol}}(\mathbf{r}, \mathbf{R})t\right) |\Psi(\mathbf{r}, \mathbf{R}, 0)\rangle \quad (2.3)$$

i.e. the time-evolution is determined by the initial wavefunction at time $t = 0$.

Furthermore, since a complete basis $\{|\Psi_i\rangle\}_i$ of orthonormal eigenfunctions exists for any Hermitian operator \hat{H} , the initial wavefunction can be written as

$$|\Psi(\mathbf{r}, \mathbf{R}, 0)\rangle = \sum_i c_i |\Psi_i(\mathbf{r}, \mathbf{R})\rangle \quad (2.4)$$

where $c_i \equiv c_i(0)$ are the expansion coefficients and the basis eigenfunctions $|\Psi_i\rangle$ satisfy

$$\hat{H}(\mathbf{r}, \mathbf{R})|\Psi_i(\mathbf{r}, \mathbf{R})\rangle = E_i|\Psi_i(\mathbf{r}, \mathbf{R})\rangle \quad (2.5)$$

with real energy eigenvalues E_i . Inserting the initial wavefunction **(2.4)** into the time-evolution **(2.3)** eventually leads to the following expression of the molecular wavefunction

$$|\Psi(\mathbf{r}, \mathbf{R}, t)\rangle = \sum_i c_i \exp(-iE_i t) |\Psi_i(\mathbf{r}, \mathbf{R})\rangle \quad (2.6)$$

at any time t .

As expectation values of eigenfunctions of time-independent operators are time-independent, the wavefunctions $|\Psi_i\rangle$ are also called stationary states. However, a linear combination of stationary states, as e.g. in **(2.6)**, is, in general, not stationary. A non-stationary wavefunction is called a wavepacket.

2.2 Born-Oppenheimer Approximation

Due to the complexity of molecular systems, exact analytical solutions for the **TDSE** are generally unattainable (with only a few exceptions). Consequently, the quantum mechanical treatment of molecular systems necessitates the implementation of numerous assumptions and approximations. One of the most common approximations in molecular quantum mechanics is the Born-Oppenheimer approximation **(BOA)**. **[124]** Justified by the mass difference between the nuclei and electrons, the **BOA** assumes that the nuclear and electronic motions happen on different timescales and can therefore be decoupled.

For this purpose, a basis of adiabatic electronic eigenfunctions $\{|\Psi_i^a\rangle\}_i$ satisfying

$$\hat{H}_{\text{el}}(\mathbf{r}, \mathbf{R})|\Psi_i^a(\mathbf{r}, \mathbf{R})\rangle = V_i(\mathbf{R})|\Psi_i^a(\mathbf{r}, \mathbf{R})\rangle \quad (2.7)$$

is chosen that allows to consider each electronic state separately. The real eigenvalues V_i generate the corresponding to $|\Psi_i^a\rangle$ adiabatic potential energy (hyper-)surface (**PES**) on which the nuclei are moving around. In particular, the adiabatic **PES** are well-ordered by their energy value, i.e. the first adiabatic state corresponds to the lowest energy values at each geometry \mathbf{R} , while the subsequent adiabatic states follow suit with sequentially higher energy values at each geometry.

The full molecular wavefunction $|\Psi\rangle$ can then be expanded in this basis of electronic eigenfunctions

$$|\Psi(\mathbf{r}, \mathbf{R}, t)\rangle = \sum_i |\Psi_i^{\text{nuc}}(\mathbf{R}, t)\rangle |\Psi_i^a(\mathbf{r}, \mathbf{R})\rangle \quad (2.8)$$

yielding the so-called adiabatic representation **[125]** in which the expansion coefficients are given by the nuclear wavefunctions $|\Psi_i^{\text{nuc}}\rangle$. Inserting this wavefunction *ansatz* into the molecular **TDSE** leads to a set of coupled differential equations **[126-128]**

$$i \frac{\partial}{\partial t} |\Psi^{\text{nuc}}(\mathbf{R}, t)\rangle = \left(\hat{T}_N(\mathbf{R}) \mathbb{1} + \mathbf{V}(\mathbf{R}) - \mathbf{\Lambda}(\mathbf{r}, \mathbf{R}) \right) |\Psi^{\text{nuc}}(\mathbf{R}, t)\rangle \quad (2.9)$$

where the vector $|\Psi^{\text{nuc}}\rangle$ has a component for each state $|\Psi_i^{\text{nuc}}\rangle$, $\mathbb{1}$ denotes the identity matrix, \mathbf{V} is the real diagonal matrix containing all adiabatic potential energies V_i and $\mathbf{\Lambda}$ is the non-adiabatic coupling matrix defined by

$$\mathbf{\Lambda} = \frac{1}{2M} (\mathbf{G} + 2\mathbf{F} \cdot \nabla) \quad (2.10)$$

with the vector differential operator ∇ , the scalar coupling matrix \mathbf{G} and the derivative coupling matrix \mathbf{F} . The matrix elements of \mathbf{G} and \mathbf{F} are given by

$$G_{ij}(\mathbf{r}, \mathbf{R}) = \langle \Psi_j^a(\mathbf{r}, \mathbf{R}) | \nabla^2 \Psi_i^a(\mathbf{r}, \mathbf{R}) \rangle \quad (2.11)$$

$$F_{ij}(\mathbf{r}, \mathbf{R}) = \langle \Psi_j^a(\mathbf{r}, \mathbf{R}) | \nabla \Psi_i^a(\mathbf{r}, \mathbf{R}) \rangle \quad (2.12)$$

respectively. Moreover, using the relation

$$\mathbf{G} = \nabla \cdot \mathbf{F} + \mathbf{F} \cdot \mathbf{F} \quad (2.13)$$

between the scalar and derivative coupling matrix, the Schrödinger equation **[2.9]**

for the nuclei can be written in the following compact form

$$i\frac{\partial}{\partial t}|\Psi^{\text{nuc}}(\mathbf{R}, t)\rangle = \left(-\frac{1}{2M}(\nabla + \mathbf{F}(\mathbf{r}, \mathbf{R}))^2 + \mathbf{V}(\mathbf{R})\right)|\Psi^{\text{nuc}}(\mathbf{R}, t)\rangle \quad (2.14)$$

where the non-adiabaticity is exclusively determined by the derivative coupling terms contained in \mathbf{F} . As the adiabatic electronic states $|\Psi_i^a\rangle$ are orthonormal, the vector elements of the derivative coupling matrix \mathbf{F} are given by

$$F_{ij}(\mathbf{r}, \mathbf{R}) = \frac{\langle \Psi_i^a(\mathbf{r}, \mathbf{R}) | \nabla \hat{H}_{\text{el}}(\mathbf{r}, \mathbf{R}) | \Psi_j^a(\mathbf{r}, \mathbf{R}) \rangle}{V_j(\mathbf{R}) - V_i(\mathbf{R})} \quad (2.15)$$

with a reciprocal proportionality to the energy gap $\Delta V_{ji}(\mathbf{R}) = V_j(\mathbf{R}) - V_i(\mathbf{R})$ between the i^{th} and j^{th} electronic state.

Within the **BOA** all non-adiabatic coupling terms are neglected simplifying the nuclear Schrödinger equation to

$$i\frac{\partial}{\partial t}|\Psi^{\text{nuc}}(\mathbf{R}, t)\rangle = \left(\hat{T}_N(\mathbf{R})\mathbb{1} + \mathbf{V}(\mathbf{R})\right)|\Psi^{\text{nuc}}(\mathbf{R}, t)\rangle \quad (2.16)$$

where no transitions between different adiabatic electronic states can be induced by the nuclear motion. According to (2.15), the **BOA** is valid as long as the electronic states are energetically well separated, a condition typically met in ground state calculations. However, the closer electronic states are in energy, the more significant are the derivative coupling vectors. In particular, if two (or more) states reach energetic degeneracy, such as in conical intersections, the derivative coupling vectors diverge, causing the breakdown of the **BOA** and a manifold of coupled electronic states must be considered.

2.3 Adiabatic-to-Diabatic Transformation

The breakdown of the **BOA** is particularly prevalent in the photochemistry of polyatomic molecules, where numerous energetically close lying electronic states offer ultrafast radiationless relaxation pathways on the femtosecond timescale. [127–131] Consequently, in the treatment of multi-state molecular systems, the derivative coupling vectors are not generally smooth and frequently end up in singularities resulting in unstable numerical algorithms for solving the **TDSE**.

To overcome this issue, it is possible to convert the adiabatic representation (2.14) into what is known as the diabatic representation, wherein the problematic derivative coupling matrix \mathbf{F} formally disappears. This transformation is accomplished by

using a unitary transformation \mathbf{S} on the adiabatic basis $\{|\Psi_i^a\rangle\}_i$ yielding an electronic diabatic basis $\{|\Psi_i^d\rangle\}_i$ at each point \mathbf{R} in configuration space, i.e.

$$|\Psi^d(\mathbf{r}, \mathbf{R})\rangle = \mathbf{S}(\mathbf{R})|\Psi^a(\mathbf{r}, \mathbf{R})\rangle \quad (2.17)$$

where $|\Psi^a\rangle$ and $|\Psi^d\rangle$ denote the vectors containing all adiabatic and diabatic wavefunctions as entries, respectively. Due to the orthonormality of the adiabatic states, the elements of the adiabatic-to-diabatic transformation matrix \mathbf{S} are defined by the overlap of the related adiabatic and diabatic states, i.e.

$$S_{ij}(\mathbf{R}) = \langle \Psi_i^a(\mathbf{r}, \mathbf{R}) | \Psi_j^d(\mathbf{r}, \mathbf{R}) \rangle \quad (2.18)$$

If the adiabatic-to-diabatic transformation matrix \mathbf{S} additionally fulfills [\[132\]](#), [\[133\]](#)

$$\nabla \mathbf{S} = -\mathbf{F} \mathbf{S} \quad (2.19)$$

the adiabatic form of the nuclear Schrödinger equation [\(2.14\)](#) can be transformed into the diabatic form

$$i \frac{\partial}{\partial t} |\Psi^{\text{nuc}}(\mathbf{R}, t)\rangle = \left(\hat{T}_N(\mathbf{R}) \mathbb{1} + \mathbf{W}(\mathbf{R}) \right) |\Psi^{\text{nuc}}(\mathbf{R}, t)\rangle \quad (2.20)$$

where the diabatic potential matrix \mathbf{W} is defined by

$$\mathbf{W} = \mathbf{S} \mathbf{V} \mathbf{S}^\dagger \quad (2.21)$$

$$\text{with } W_{ij}(\mathbf{R}) = \langle \Psi_i^d(\mathbf{r}, \mathbf{R}) | \hat{H}_{\text{el}}(\mathbf{r}, \mathbf{R}) | \Psi_j^d(\mathbf{r}, \mathbf{R}) \rangle \quad (2.22)$$

In order to analyse the diabatic [PES](#) topology, the diabatic potential matrix \mathbf{W} can be polynomially represented using a Taylor expansion around an arbitrary point \mathbf{R}_0 , usually the Franck-Condon [\(FC\)](#) point. Without loss of generality, the diabatic basis can be assumed to be equal to the adiabatic basis at \mathbf{R}_0 because the matrix \mathbf{S} is uniquely defined only up to a constant unitary transformation. Thus, collecting terms of the same order together, \mathbf{W} can be written as

$$\mathbf{W}(\mathbf{R}) = \mathbf{W}^{(0)}(\mathbf{R}) + \mathbf{W}^{(1)}(\mathbf{R}) + \mathbf{W}^{(2)}(\mathbf{R}) + \dots \quad (2.23)$$

where the zero-order matrix $\mathbf{W}^{(0)}$ is a diagonal matrix given by

$$\mathbf{W}^{(0)}(\mathbf{R}) \equiv \mathbf{W}^{(0)}(\mathbf{R}_0) = \mathbf{V}(\mathbf{R}_0) \quad (2.24)$$

and the first order matrix $\mathbf{W}^{(1)}$ is defined by the matrix elements

$$W_{ij}^{(1)}(\mathbf{R}) = \nabla \langle \Psi_i^d(\mathbf{r}, \mathbf{R}) | \hat{H}_{\text{el}}(\mathbf{r}, \mathbf{R}) | \Psi_j^d(\mathbf{r}, \mathbf{R}) \rangle \Big|_{\mathbf{R}=\mathbf{R}_0} (\mathbf{R} - \mathbf{R}_0) \quad (2.25)$$

$$= \langle \Psi_i^a(\mathbf{r}, \mathbf{R}) | \nabla \hat{H}_{\text{el}}(\mathbf{r}, \mathbf{R}) | \Psi_j^a(\mathbf{r}, \mathbf{R}) \rangle \Big|_{\mathbf{R}=\mathbf{R}_0} (\mathbf{R} - \mathbf{R}_0) \quad (2.26)$$

In particular, the off-diagonal expansion coefficients (2.26) are directly related to the derivative coupling matrix elements (2.15).

For a complete (infinite) set of electronic states the necessary condition (2.19) is inherently fulfilled. Nevertheless, managing an infinite set of states in practical computations is obviously unfeasible. Therefore, the electronic basis must be truncated to a subset that satisfies condition (2.19), thereby establishing a consistently defined diabatic basis. [132-134]

Both the adiabatic and diabatic representations exhibit distinct advantages and drawbacks. Unlike the adiabatic representation, the diabatic basis is not composed of electronic eigenfunctions and lacks uniqueness. It thus necessitates the selection of a reference point for its construction. However, within the diabatic representation, the coupling is well behaved, contrasting with adiabatic surfaces where conical intersections lead to singularities. [128,130] Furthermore, the diabatic picture eliminates other artificial phenomena, such as the geometric or Berry phase, [135,136] that only appears in adiabatic calculations involving a conical intersection. Hence, the diabatic representation generally simplifies the treatment of multidimensional molecular systems involving several coupled electronic states and is also used within this thesis to perform nuclear quantum dynamics simulations.

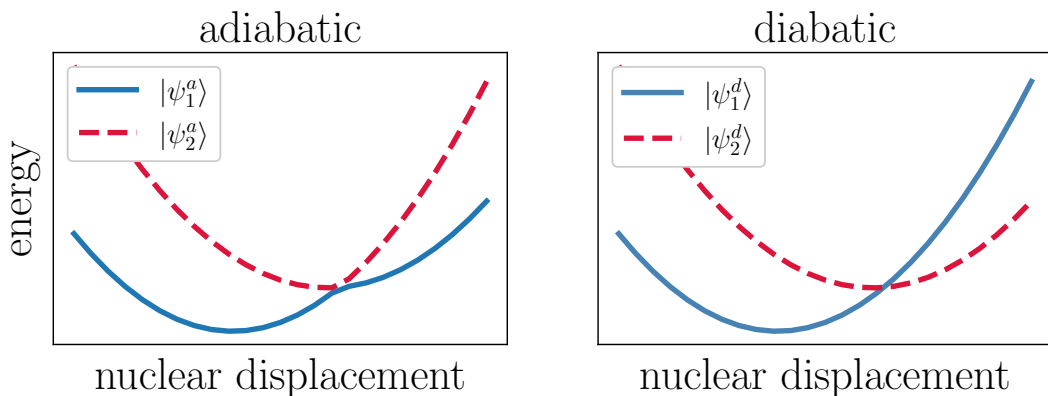


Figure 2.1: Schematic representation of adiabatic (left) and diabatic (right) potential energy curves. Adiabatic states are ordered by their energy value at each geometry in configuration space, whereas diabatic states are allowed to cross maintaining the state symmetry according to the reference point.

2.4 Time-Dependent Molecular Spectroscopy

Generally, the selection of the probing wavelength in spectroscopic experiments governs the detectability of transitions between the initial and final states of a chemical process, thereby influencing which aspects of a reaction are detected. This thesis primarily concentrates on electronic transitions instigated by either optical or X-ray radiation. The subsequent sections introduce fundamental principles for investigating electronic transitions within a time-dependent framework, pertinent to both excitation ranges. Specific concepts related to X-ray spectroscopy are expounded upon in chapter [4](#).

2.4.1 Light-Matter-Interaction

In order to describe the molecular behaviour after light exposure, the full Hamiltonian \hat{H} can be split into the sum

$$\hat{H} = \hat{H}_{\text{mol}} + \hat{H}_{\text{light}} + \hat{H}_{\text{int}} \quad (2.27)$$

with the time-independent molecular Hamiltonian, \hat{H}_{mol} , and the time-dependent operators describing the external electromagnetic field, \hat{H}_{light} , and corresponding light-matter-interaction, \hat{H}_{int} . Using a semi-classical approach and neglecting the effect that the molecule has on the external field, the light-driven Hamiltonian reads

$$\hat{H}(\mathbf{r}, \mathbf{R}, t) = \hat{H}_{\text{mol}}(\mathbf{r}, \mathbf{R}) + \hat{H}_{\text{int}}(\mathbf{R}, t) \quad (2.28)$$

where the molecule is described fully quantum mechanically while the light is treated as a classical electromagnetic field acting as a perturbation on the molecular system. Within the length gauge, electric dipole and Condon approximation [\[137, 138\]](#) the interaction Hamiltonian is given by

$$\hat{H}_{\text{int}}(\mathbf{R}, t) = -\hat{\mu}(\mathbf{R}) \cdot \vec{\mathcal{E}}(t) \approx -\hat{\mu} \cdot \vec{\mathcal{E}}(t) \quad (2.29)$$

where $\hat{\mu}(\mathbf{R}) \approx \hat{\mu}(\mathbf{R}_0) \equiv \hat{\mu}$ is the molecular electric transition dipole moment operator and $\vec{\mathcal{E}}$ is the external electric field at the position of the molecule. Within this work, we assume a single polarisation direction and thus drop the arrows from the vector quantities in the following.

Within the weak-field regime, an useful tool to find an approximate solution of the [TDSE](#) is provided by time-dependent perturbation theory. In this framework,

the evolving wavefunction is expanded in a series of successive approximations

$$|\Psi(t)\rangle = \sum_n |\Psi^{(n)}(t)\rangle \quad (2.30)$$

where $\Psi^{(i)}$ is the i^{th} order correction to the system wavefunction leading to a series of differential equations for each expansion term

$$i \frac{\partial}{\partial t} |\Psi^{(0)}(t)\rangle = \hat{H}_{\text{mol}} |\Psi^{(0)}(t)\rangle \quad (2.31)$$

$$i \frac{\partial}{\partial t} |\Psi^{(1)}(t)\rangle = \hat{H}_{\text{mol}} |\Psi^{(1)}(t)\rangle + \hat{H}_{\text{int}}(t) |\Psi^{(0)}(t)\rangle \quad (2.32)$$

$$i \frac{\partial}{\partial t} |\Psi^{(2)}(t)\rangle = \hat{H}_{\text{mol}} |\Psi^{(2)}(t)\rangle + \hat{H}_{\text{int}}(t) |\Psi^{(1)}(t)\rangle \quad (2.33)$$

and so on. Note, that we only include the time-dependent aspect in this context and drop the coordinate dependencies for simplicity. Assuming that the system initially is in an unperturbed state, i.e. $\Psi(t_0) = \Psi^{(0)}(t_0)$ and thus $\Psi^{(1)}(t_0) = \Psi^{(2)}(t_0) = 0$, leads to the following solutions

$$|\Psi^{(0)}(t)\rangle = e^{-i\hat{H}_{\text{mol}}(t-t_0)} |\Psi(t_0)\rangle \quad (2.34)$$

$$|\Psi^{(1)}(t)\rangle = \frac{1}{i} \int_{t_0}^t dt' e^{-i\hat{H}_{\text{mol}}(t-t')} \hat{H}_{\text{int}}(t') e^{-i\hat{H}_{\text{mol}}(t'-t_0)} |\Psi(t_0)\rangle \quad (2.35)$$

$$|\Psi^{(2)}(t)\rangle = - \int_{t_0}^t dt' \int_{t_0}^{t'} dt'' e^{-i\hat{H}_{\text{mol}}(t-t')} \hat{H}_{\text{int}}(t') e^{-i\hat{H}_{\text{mol}}(t'-t'')} \hat{H}_{\text{int}}(t'') e^{-i\hat{H}_{\text{mol}}(t''-t_0)} |\Psi(t_0)\rangle \quad (2.36)$$

of the first three expansion terms. While zero-order perturbation theory is simply the [TDDSE](#) for the unperturbed, time-independent molecular Hamiltonian \hat{H}_{mol} , higher order corrections are essential for describing linear and non-linear spectroscopic phenomena. [139](#), [140](#)

2.4.2 Absorption Spectroscopy

Linear Absorption Spectroscopy

The molecular absorption spectrum is a measure of the ratio of incident radiation absorbed by the sample over a range of frequencies of electromagnetic radiation.

The absorption spectrum can be generally obtained by [140–142]

$$I_{\text{Abs}}(\omega) \propto -\frac{\text{Im}\left(\tilde{P}(\omega)\tilde{\mathcal{E}}^*(\omega)\right)}{|\tilde{\mathcal{E}}(\omega)|^2} \quad (2.37)$$

where $\tilde{\mathcal{E}}^*$ is the complex conjugated Fourier transform of the time-dependent electric field \mathcal{E} and \tilde{P} denotes the Fourier transform of the time-dependent polarisation

$$P(t) = \langle \Psi(t) | \hat{\mu} | \Psi(t) \rangle \quad (2.38)$$

The non-perturbative approach [2.37] maintains broad validity and particularly remains applicable in scenarios of strong field interactions, where an explicit treatment of coupled dynamics across the electronic state manifold and especially during the excitation phase is required. Nevertheless, within the weak field limit, employing time-dependent perturbation theory is often advantageous for simplifying computational processes. Thus, in the case of weak fields, the polarisation [2.38] can be systematically developed in perturbation orders

$$P(t) = \sum_n P^{(n)}(t) \quad (2.39)$$

where each term $P^{(i)}$ can in turn be identified with one or more terms in the perturbative expansion of the wavefunction [140]

$$P^{(0)}(t) = \langle \Psi^{(0)}(t) | \hat{\mu} | \Psi^{(0)}(t) \rangle \quad (2.40)$$

$$P^{(1)}(t) = \langle \Psi^{(0)}(t) | \hat{\mu} | \Psi^{(1)}(t) \rangle + c.c. \quad (2.41)$$

$$P^{(2)}(t) = \langle \Psi^{(0)}(t) | \hat{\mu} | \Psi^{(2)}(t) \rangle + c.c. + \langle \Psi^{(1)}(t) | \hat{\mu} | \Psi^{(1)}(t) \rangle \quad (2.42)$$

$$P^{(3)}(t) = \langle \Psi^{(0)}(t) | \hat{\mu} | \Psi^{(3)}(t) \rangle + c.c. + \langle \Psi^{(1)}(t) | \hat{\mu} | \Psi^{(2)}(t) \rangle + c.c. \quad (2.43)$$

...

$$P^{(n)}(t) = \sum_{i=0}^n P_{in-i}^{(n)}(t) \quad \text{with} \quad P_{ij}^{(n)}(t) := \langle \Psi^{(i)}(t) | \hat{\mu} | \Psi^{(j)}(t) \rangle \quad (2.44)$$

where c.c. stands for the complex conjugative of the preceding term. While the zero-order polarisation $P^{(0)}$ describes the permanent dipole moment of the molecule and thus vanishes in an isotropic medium, the first-order term $P^{(1)}$ is the central dynamical object in linear absorption spectroscopy. [139, 140] Assuming the system is initially in an stationary eigenstate $|\phi_i\rangle \equiv |\phi_i(-\infty)\rangle = |\Psi^{(0)}(-\infty)\rangle$, the first-order

polarisation term $P_{01}^{(1)}(t)$ can be rewritten as

$$P_{01}^{(1)}(t) = \frac{1}{i} \int_{-\infty}^t dt' \langle \Psi^{(0)}(t) | \hat{\mu} e^{-i\hat{H}_{\text{mol}}(t-t')} (-\hat{\mu} \mathcal{E}(t')) | \Psi^{(0)}(t) \rangle \quad (2.45)$$

$$= i \int_0^{\infty} d\tau \langle \phi_i | \hat{\mu} e^{-i\hat{H}_{\text{mol}}\tau} \hat{\mu} | \phi_i \rangle \mathcal{E}(t - \tau) \quad (2.46)$$

$$= i (S(t) \otimes \mathcal{E}(t)) \quad (2.47)$$

where \otimes denotes the convolution and S is the causal form of the autocorrelation function

$$S(t) = \begin{cases} \langle \phi_i | \hat{\mu} e^{-i\hat{H}_{\text{mol}}t} \hat{\mu} | \phi_i \rangle & \text{for } t \geq 0 \\ 0 & \text{else} \end{cases} \quad (2.48)$$

Inserting (2.47) into (2.37) and exploiting the Fourier transformation properties yields the well-known time-domain formula [143, 144]

$$I_{\text{Abs}}(\omega) \propto -\frac{\text{Im} \left(\tilde{P}_{01}^{(1)}(\omega) \tilde{\mathcal{E}}^*(\omega) \right)}{|\tilde{\mathcal{E}}(\omega)|^2} \propto \int_{-\infty}^{\infty} dt \langle \phi_i | \hat{\mu} e^{-i\hat{H}_{\text{mol}}t} \hat{\mu} | \phi_i \rangle e^{i\omega t} = \int_{-\infty}^{\infty} dt C(t) e^{i\omega t} \quad (2.49)$$

where the linear absorption spectrum is determined by the Fourier transform of the wavepacket autocorrelation function $C(t) = \langle \Phi_i | \Phi_i(t) \rangle$ with $|\Phi_i\rangle \equiv \hat{\mu} |\phi_i\rangle$ and $|\Phi_i(t)\rangle = e^{-i\hat{H}_{\text{mol}}t} |\Phi_i\rangle$.

Alternatively, the expression for the absorption cross-section can be derived by examining the rate of change of the population in the excited state, as this rate is directly related to the quantity of absorbed photons per unit time. For this purpose, the field is taken as a monochromatic continuous wave (CW)

$$\mathcal{E}(t) = -\frac{1}{2} \hat{\mu} \varepsilon_I e^{-i\omega_I t} \quad (2.50)$$

with the incoming photon frequency ω_I and field amplitude ε_I . As the excited state population is determined by

$$\langle \Psi^{(1)}(t) | \Psi^{(1)}(t) \rangle = \frac{\varepsilon_I^2}{4} \int_{-\infty}^t dt' \int_{-\infty}^t dt'' \langle \phi_i | \hat{\mu} e^{-i\hat{H}_{\text{mol}}(t''-t')} \hat{\mu} | \phi_i \rangle e^{i\omega_I(t''-t')} \quad (2.51)$$

where $\tilde{\omega}_I := E_i + \omega_I$ with E_i being the eigenenergy of ϕ_i , the rate of change can be obtained using the chain rule and appropriate variable changes

$$\frac{d}{dt} \langle \Psi^{(1)}(t) | \Psi^{(1)}(t) \rangle = \frac{\varepsilon_I^2}{4} \int_{-\infty}^{\infty} dt \langle \phi_i | \hat{\mu} e^{-i\hat{H}_{\text{mol}}t} \hat{\mu} | \phi_i \rangle e^{i\tilde{\omega}_I t} \quad (2.52)$$

Comparing (2.49) and (2.52) eventually results in the following relation

$$I_{\text{Abs}}(\omega_I) \propto \frac{d}{dt} \langle \Psi^{(1)}(t) | \Psi^{(1)}(t) \rangle \propto \int_{-\infty}^{\infty} dt C(t) e^{i\tilde{\omega}_I t} \quad (2.53)$$

for calculating time-dependent absorption spectra. Performing the time integral in (2.53) and inserting a complete set of excited state eigenstates $\{\phi_n\}_n$ eventually yield the conventional frequency domain formula [145]

$$I_{\text{Abs}}(\omega_I) \propto \sum_j |\langle \phi_j | \hat{\mu} | \phi_i \rangle|^2 \delta(\tilde{\omega}_I - \omega_j) \quad (2.54)$$

commonly known as Fermi's golden rule. In particular, both, the time-dependent (2.53) and time-independent (2.54), approaches for linear absorption spectroscopy are completely equivalent comprising the same weak field assumption. Here, the time-independent approach represents a boundary value problem which, for a single

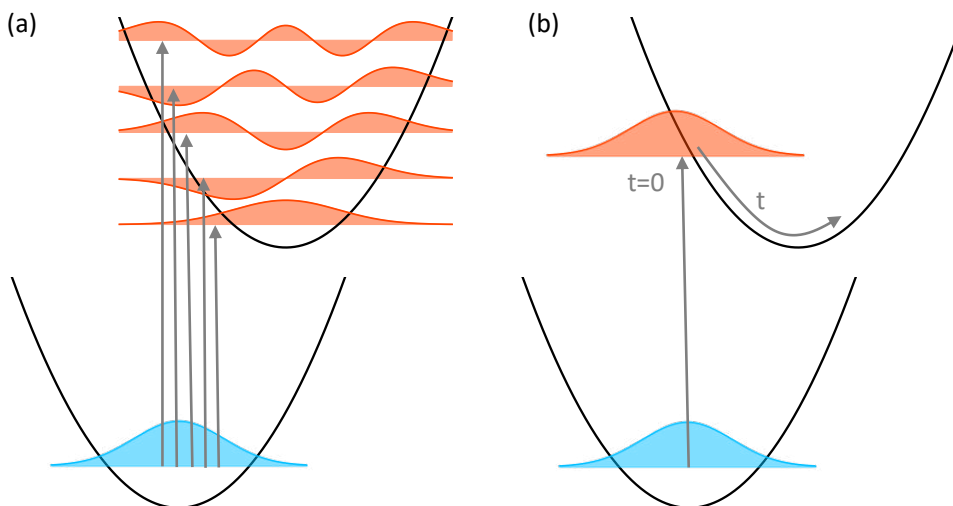


Figure 2.2: Schematic comparison between the time-independent and time-dependent approach to calculate linear absorption spectra. (a) Within the static approach the transition intensities are determined by the Franck-Condon overlaps according to Fermi's golden rule (2.54) while (b) the dynamical approach (2.53) explores the autocorrelation function of the excited wavepacket.

energy, is indeed computationally favourable compared to the time-dependent initial value problem which contains the time as an additional variable. Nevertheless, the time-dependent approach offers the entire absorption spectrum within a single calculation, as the time-dependent wavepacket encompasses all energies by *ansatz*. Thus, the determination of which approach is more advantageous for numerical simulations and final interpretations is highly dependent on the specific characteristics of the system and cannot be conclusively decided in a singular manner. [144]

However, a branch where time-dependent approaches distinctly excel is in time-resolved spectroscopy. In this context, time-dependent methodologies typically offer a seamless transition from the linear to nonlinear regime, whereas time-independent approaches often lack analytical expressions and consequently rely on additional approximations.

Transient Absorption Spectroscopy

In transient absorption spectroscopy, the system is initially excited by a short laser pulse into an excited state. Subsequently, a temporally delayed probe pulse is used to monitor changes in the absorption spectrum of the sample as a function of time. Hence, the total electric field reads

$$\mathcal{E}(t, \tau) = \mathcal{E}_{\text{pu}}(t) + \mathcal{E}_{\text{pr}}(t, \tau) \quad (2.55)$$

where \mathcal{E}_{pu} and \mathcal{E}_{pr} represents the pump and probe pulse, respectively, separated by a time delay τ . By varying the time delay, transient absorption spectroscopy can provide detailed information about the relaxation pathways and dynamics of photoexcited states.

In order to calculate the transient absorption cross section, the general non-perturbative approach [2.37] can be simply extended to [142]

$$I_{\text{TAS}}(\omega, \tau) \propto -\frac{\text{Im}\left(\tilde{P}(\omega)\tilde{\mathcal{E}}^*(\omega, \tau)\right)}{|\tilde{\mathcal{E}}(\omega, \tau)|^2} \quad (2.56)$$

where, analogously to before, $\tilde{\mathcal{E}}$ is the Fourier transform of the full electric field \mathcal{E} , and \tilde{P} represents the dipole spectrum.

Within the perturbative regime, excited state absorption arises from the coherence terms $P_{12}^{(3)}(t) = \langle \Psi^{(1)}(t) | \hat{\mu} | \Psi^{(2)}(t) \rangle$ of the third-order polarisation $P^{(3)}$. [139]

Similar to (2.45)-(2.46), this term can be rewritten as (146)

$$P_{12}^{(3)}(t) = \int_{-\infty}^{\infty} dt' \langle \Psi^{(1)}(\tau) | e^{i\hat{H}_{\text{mol}}(t-\tau)} \hat{\mu} e^{-i\hat{H}_{\text{mol}}(t-\tau)} \hat{\mu} | \Psi^{(1)}(\tau) \rangle \mathcal{E}(t') \quad (2.57)$$

Assuming a short time interaction with the probe pulse (140) and inserting this expression into (2.56) yields the perturbative approach for transient absorption spectroscopy (63)

$$I_{\text{TAS}}(\omega, \tau) \propto \int_{-\infty}^{\infty} dt C(t, \tau) e^{i\omega t - \Gamma t/2} \quad (2.58)$$

where Γ is a damping factor related to the inverse final state lifetime and $C(t, \tau)$ is the dipole-dipole correlation function

$$C(t, \tau) = \langle \Psi^{(1)}(\tau) | e^{i\hat{H}_{\text{mol}}(t-\tau)} \hat{\mu} e^{-i\hat{H}_{\text{mol}}(t-\tau)} \hat{\mu} | \Psi^{(1)}(\tau) \rangle \quad (2.59)$$

In instances where the final excited state decay is fast, such as core-excited states, the commutator $[e^{i\hat{H}_{\text{mol}}t}, \hat{\mu}]$ can be assumed to be negligible, allowing for the reversal of the order of the two operators without significantly affecting the integral in (2.58). Assuming there is no radiationless transition between the electronic manifolds described where $|\Psi^{(1)}\rangle$ and $|\Psi^{(2)}\rangle$ are propagated, the molecular Hamiltonian has the matrix form

$$\mathbf{H}_{\text{mol}} = \begin{pmatrix} \mathbf{H}_1 & 0 \\ 0 & \mathbf{H}_2 \end{pmatrix} \quad (2.60)$$

with the diabatic Hamiltonian $\hat{H}_i = \hat{T}_N + \hat{W}_i$ responsible for the evolution of $|\Psi^{(i)}\rangle$, $i = 1, 2$. If the propagator and dipole moment operator commute, it follows that

$$e^{i\hat{H}_1(t-\tau)} \hat{\mu} e^{-i\hat{H}_2(t-\tau)} \hat{\mu} \approx \hat{\mu} e^{-i(\hat{H}_2 - \hat{H}_1)(t-\tau)} \hat{\mu} = \hat{\mu} e^{-i(\hat{W}_2 - \hat{W}_1)(t-\tau)} \hat{\mu} \quad (2.61)$$

i.e. the propagation of the wavepacket subsequent to the probe pulse is disregarded. This leads to the Lorentzian limit or short-time approximation of the transient absorption signal (63, 64)

$$I_L(\omega, \tau) \propto \text{Re} \int_0^{\infty} dt \langle \Psi^{(1)}(\tau) | \hat{\mu} e^{-i(\hat{W}_2 - \hat{W}_1)(t-\tau)} \hat{\mu} | \Psi^{(1)}(\tau) \rangle e^{i\omega t - \Gamma t/2} \quad (2.62)$$

with the frequency-dependent counterpart

$$I(\omega, \tau)_L \propto \sum_{i,f} \int \cdots \int d\mathbf{R} |\mu_{if}|^2 |\Psi_i(\mathbf{R}, \tau)|^2 \frac{\frac{\Gamma}{2}}{(\frac{\Gamma}{2})^2 + (V_f(\mathbf{R}) - V_i(\mathbf{R}) - \omega)^2} \quad (2.63)$$

where the indices i and f refer to intermediate and final electronic states, respectively, with the corresponding transition dipole moment μ_{ij} and where $\Psi_i(\mathbf{R}, \tau)$ is the nuclear wavepacket in the i -th electronic state at the time τ . This approach is hence equivalent to calculating static absorption spectra at specific points on the manifold of excited states triggered by the pump pulse. While pump-induced dynamical processes can still be monitored using the short-time approximation, the transient absorption spectra might lack spectral features stemming from the dynamics in the final excited states.

Especially in the field of ultrafast X-ray spectroscopy, the short-time approximation is prevalent, due to the short lifetime of core-excited states. However, Section 4.3 extensively deliberates upon the validity of this approximation and provides a meticulous elucidation of its consequences in the assessment of femtosecond X-ray absorption spectroscopy.

2.4.3 Resonance Raman Spectroscopy

In the following, the representation of the underlying theory as well as their further development is strongly aligned to [88] and [116].

Steady-State Resonance Raman Spectroscopy

Resonance Raman scattering is a coherent two-photon process in which the system is resonantly excited into an excited state, followed by spontaneous emission of a photon. [147] As this mechanism involves two photon interactions, the time-dependent approach must be derived by second-order time-dependent perturbation theory for light-matter interaction. [148, 149] In accordance to (2.53), the weak field Raman intensity I_{Ram} can be obtained from the time evolution of the second order correction to the system wavefunction [140, 150]

$$I_{\text{Ram}}(\omega_S; \omega_I) \propto \frac{d}{dt} \langle \Psi^{(2)}(t) | \Psi^{(2)}(t) \rangle. \quad (2.64)$$

where an incident CW excitation, characterised by a single frequency ω_I , is assumed. Starting from an initial eigenstate $|\phi_i\rangle$, the time-dependent second order

perturbation wavefunction is then explicitly given by [\[140, 148\]](#)

$$|\Psi^{(2)}(t)\rangle = -\frac{\varepsilon_S}{2i} \int_{-\infty}^t dt' e^{-i(\hat{H}_{\text{mol}} - i\frac{\Gamma_f}{2})(t-t')} \hat{\mu}_S e^{i\omega_S t'} |\Psi^{(1)}(t')\rangle \quad (2.65)$$

with the scattering field amplitude and frequency, ε_S and ω_S , respectively, and the first-order wavefunction

$$|\Psi^{(1)}(t')\rangle = -\frac{\varepsilon_I}{2i} \int_{-\infty}^{t'} dt'' e^{-i(\hat{H}_{\text{mol}} - i\frac{\Gamma_i}{2})(t'-t'')} \hat{\mu}_I e^{-i\tilde{\omega}_I t''} |\phi_i\rangle \quad (2.66)$$

where Γ_i and Γ_f characterise the inverse lifetime of the intermediate and final states, respectively. By changing the variables $\tau = t' - t''$, the first order wavefunction can be rewritten as

$$|\Psi^{(1)}(t')\rangle = -\frac{\varepsilon_I}{2i} \int_{-\infty}^{t'} dt'' e^{-i(\hat{H}_{\text{mol}} - i\frac{\Gamma_i}{2})(t'-t'')} \hat{\mu}_I e^{-i\tilde{\omega}_I t''} |\phi_i\rangle \quad (2.67)$$

$$= -\frac{\varepsilon_I}{2i} e^{-i\tilde{\omega}_I t'} |\mathcal{R}(\omega_I)\rangle \quad (2.68)$$

where the Raman wavefunction $|\mathcal{R}(\omega_I)\rangle$ is defined by

$$|\mathcal{R}(\omega_I)\rangle := \int_0^{\infty} d\tau e^{-i(\hat{H}_{\text{mol}} - i\frac{\Gamma_i}{2})\tau} \hat{\mu}_I e^{i\tilde{\omega}_I \tau} |\phi_i\rangle. \quad (2.69)$$

In particular, the Raman wavefunction itself is time-independent serving as an intermediate state containing all dynamical information prior to the scattering event and the second-order wavefunction attains the structure of a pseudo-first-order wavefunction

$$|\Psi^{(2)}\rangle = -\frac{\varepsilon_I \varepsilon_S}{4} \int_{-\infty}^t dt' e^{-i\hat{H}_{\text{mol}}(t-t')} \hat{\mu}_S e^{i\tilde{\omega}_S t'} |\mathcal{R}(\omega_I)\rangle \quad (2.70)$$

where $\tilde{\omega}_S := \omega_S - \tilde{\omega}_I$ denotes the energy loss of the system. Thus, the Raman wavefunction plays the role of the initial state in [\(2.70\)](#). Substituting the last expression into [\(2.64\)](#) eventually leads to the time-dependent Raman intensity formula

$$I_{\text{Ram}}(\omega_S; \omega_I) \propto \int_{-\infty}^{\infty} dt e^{-i\tilde{\omega}_S t - \Gamma_f t/2} \langle \tilde{\mathcal{R}}(\omega_I) | \tilde{\mathcal{R}}(\omega_I, t) \rangle \quad (2.71)$$

where $|\tilde{\mathcal{R}}(\omega_I, t)\rangle := e^{-i\hat{H}_{\text{mol}}t}|\tilde{\mathcal{R}}(\omega_I)\rangle$ with $|\tilde{\mathcal{R}}(\omega_I)\rangle = \hat{\mu}_S|\mathcal{R}(\omega_I)\rangle$ is a wavepacket evolving in the final electronic state manifold reached by the scattering event.

As for linear absorption spectroscopy, an equivalent frequency domain approach can be derived for steady-state resonance Raman spectroscopy by performing the time integral in (2.71) and inserting a complete set of eigenstates $\{\phi_j\}_j$. The frequency-dependent Raman intensity is governed by

$$I_{\text{Ram}}(\omega_S; \omega_I) \propto \sum_f |\alpha_{fi}(\omega_I)|^2 \Delta(E_i - E_f + \omega_I - \omega_S, \Gamma_f) \quad (2.72)$$

where the scattering polarisability tensor α_{fi} is defined by the well-known Kramers-Heisenberg-Dirac (KHD) formula [151–153]

$$\alpha_{fi}(\omega_I) = \sum_n \frac{\langle \phi_f | \hat{\mu}_S | \phi_n \rangle \langle \phi_n | \hat{\mu}_I | \phi_i \rangle}{\tilde{\omega}_I - E_n + i\Gamma_i} \quad (2.73)$$

with $|\phi_i\rangle$, $|\phi_n\rangle$ and $|\phi_f\rangle$ being the initial, intermediate and final vibronic eigenstates involved in the resonance Raman process with energies E_i , E_n and E_f , respectively, and with a phenomenological Lorentzian line shape broadening

$$\Delta(\Omega, \Gamma) = \frac{\Gamma}{\pi(\Omega^2 + \Gamma^2)} \quad (2.74)$$

with full width at half maximum (fwhm) Γ . The KHD equation involves a summation over all intermediate vibronic states of the molecule offering a static perspective of the Raman scattering event. Here, the scattering amplitudes rely on the Franck-Condon overlaps of all relevant states, alongside the amount of detuning $\Omega = E_n - \tilde{\omega}_I$ from each intermediate state.

In order to provide a precise description of the Raman spectrum, the time-independent KHD approach requires knowledge of numerous eigenfunctions across multiple PESs. Conversely, the time-dependent approach can exploit the limited probing of only a small region of the PES and thus necessitates propagation over a brief time interval only while providing a high level of accuracy. Moreover, the time-dependent approach inherently establishes a clear connection between the spectroscopic properties and the underlying dynamics.

Both the time-dependent (2.71) and time-independent (2.72) equations for the Raman intensity are formulated under CW conditions, thereby disregarding any influence from the spectral content of the incident radiation. However, this is especially important when utilising resonance Raman spectroscopy in pump-probe

experiments. We thus transcend the CW framework and assume an \mathcal{A} -shaped pulse

$$\mathcal{E}(t) = \mathcal{A}(t)e^{-i\omega_I t} \quad (2.75)$$

with carrier frequency ω_I , centered at $t_0 = 0$, in order to encompass the spectral attributes required for a finite duration of the incident field. While this field is used to prepare the intermediate excited state wavepacket

$$|\Psi^{(1)}(t')\rangle = -\frac{\varepsilon_I}{2i} \int_{-\infty}^{t'} dt'' e^{-i(\hat{H}_{\text{mol}} - i\frac{\Gamma_i}{2})(t'-t'')} \hat{\mu}_I \mathcal{A}(t'') e^{-i\tilde{\omega}_I t''} |\phi_i\rangle, \quad (2.76)$$

the second-order wavefunction describing the spontaneous emission process is still recursively defined by

$$|\Psi^{(2)}(t)\rangle = -\frac{\varepsilon_S}{2i} \int_{-\infty}^t dt' e^{-i(\hat{H}_{\text{mol}} - i\frac{\Gamma_f}{2})(t-t')} \hat{\mu}_S e^{i\omega_S t'} |\Psi^{(1)}(t')\rangle \quad (2.77)$$

Using the Fourier representation of the envelope function

$$\mathcal{A}(t'') = \mathcal{F}^{-1}(\tilde{\mathcal{A}})(t'') = \frac{1}{2\pi} \int_{-\infty}^{\infty} \tilde{\mathcal{A}}(\omega'') e^{i\omega'' t''} d\omega'' \quad (2.78)$$

allows to circumvent the non-linear time-dependence of the incident field envelope function such that the first-order wavefunction can be rewritten as

$$|\Psi^{(1)}(t')\rangle = \frac{-\varepsilon_I}{4i\pi} \int_{-\infty}^{t'} dt'' e^{-i(\hat{H}_{\text{mol}} - i\frac{\Gamma_i}{2})(t'-t'')} \hat{\mu}_I \int_{-\infty}^{\infty} \tilde{\mathcal{A}}(\omega'') e^{i\omega'' t''} d\omega'' e^{-i\tilde{\omega}_I t''} |\phi_i\rangle \quad (2.79)$$

$$= \frac{-\varepsilon_I}{4i\pi} \int_{-\infty}^{\infty} d\omega'' \tilde{\mathcal{A}}(\omega'') e^{-i(\tilde{\omega}_I - \omega'')t'} \int_0^{\infty} d\tau e^{-i(\hat{H}_{\text{mol}} - i\frac{\Gamma_i}{2})\tau} \hat{\mu}_I e^{i(\tilde{\omega}_I - \omega'')\tau} |\phi_i\rangle \quad (2.80)$$

$$= \frac{1}{2\pi} \int_{-\infty}^{\infty} d\omega'' \tilde{\mathcal{A}}(\omega'') |\tilde{\Psi}^{(1)}(t', \tilde{\omega}_I - \omega'')\rangle \quad (2.81)$$

$$= \frac{1}{2\pi} (\tilde{\mathcal{A}} \otimes |\tilde{\Psi}^{(1)}(t', \cdot)\rangle)(\tilde{\omega}_I) \quad (2.82)$$

where $|\tilde{\Psi}^{(1)}\rangle$ is given by

$$|\tilde{\Psi}^{(1)}(t', \tilde{\omega}_I - \omega'')\rangle := \frac{-\varepsilon_I}{2i} e^{-i(\tilde{\omega}_I - \omega'')t'} |\mathcal{R}(\tilde{\omega}_I - \omega'')\rangle \quad (2.83)$$

Analogously to before, the second order term $|\tilde{\Psi}^{(2)}\rangle$ can be recursively defined by

$$|\tilde{\Psi}^{(2)}(t, \tilde{\omega}_I - \omega'')\rangle := -\frac{\varepsilon_S}{2i} \int_{-\infty}^t dt' e^{-i(\hat{H}_{\text{mol}} - i\frac{\Gamma_f}{2})(t-t')} \hat{\mu}_S e^{i\omega_S t'} |\tilde{\Psi}^{(1)}(t', \tilde{\omega}_I - \omega'')\rangle \quad (2.84)$$

leading to the following expression for the second-order scattering wavefunction

$$|\Psi^{(2)}(t)\rangle = \frac{1}{2\pi} (\tilde{\mathcal{A}} \otimes |\tilde{\Psi}^{(2)}(t, \cdot)\rangle) (\tilde{\omega}_I) \quad (2.85)$$

As the spontaneous emission from a wavepacket is incoherent in the sense that every transition from this wavepacket populates a different and hence orthogonal final state of the molecule, [88] it holds

$$\begin{aligned} \langle \Psi^{(2)}(t) | \Psi^{(2)}(t) \rangle &= \frac{1}{4\pi^2} \int_{-\infty}^{\infty} d\omega' \int_{-\infty}^{\infty} d\omega'' \tilde{\mathcal{A}}^*(\omega') \tilde{\mathcal{A}}(\omega'') \langle \tilde{\Psi}^{(2)}(t', \tilde{\omega}_I - \omega') | \tilde{\Psi}^{(2)}(t', \tilde{\omega}_I - \omega'') \rangle \\ &= \frac{1}{4\pi^2} \int_{-\infty}^{\infty} d\omega'' |\tilde{\mathcal{A}}(\omega'')|^2 \langle \tilde{\Psi}^{(2)}(t', \tilde{\omega}_I - \omega'') | \tilde{\Psi}^{(2)}(t', \tilde{\omega}_I - \omega'') \rangle \quad (2.86) \end{aligned}$$

$$= \frac{1}{4\pi^2} \left(|\tilde{\mathcal{A}}|^2 \otimes \langle \tilde{\Psi}^{(2)}(t', \cdot) | \tilde{\Psi}^{(2)}(t', \cdot) \rangle \right) (\tilde{\omega}_I) \quad (2.87)$$

Thus, it finally follows for the Raman intensity induced by a coherent, temporally finite pulse

$$I_{\text{Ram}}(\tilde{\omega}_I) \propto \left(|\tilde{\mathcal{A}}|^2 \otimes \frac{d}{dt} \langle \tilde{\Psi}^{(2)}(t, \cdot) | \tilde{\Psi}^{(2)}(t, \cdot) \rangle \right) (\tilde{\omega}_I) \quad (2.88)$$

$$\propto \left(|\tilde{\mathcal{A}}|^2 \otimes \int_{-\infty}^{\infty} dt \exp(-i\tilde{\omega}_S t) \langle \tilde{\mathcal{R}}(\cdot) | \tilde{\mathcal{R}}(\cdot, t) \rangle \right) (\tilde{\omega}_I) \quad (2.89)$$

since the time derivation is distributive over the convolution. In particular, [2.88] illustrates that the influence of a finite pulse duration manifests not only in a greater number of enclosed resonances due to the wide spectral range but also induces a general broadening of the Raman spectra, as determined by the convolution with the squared absolute value of the Fourier transform of the incident field envelope function. Thus, utilising longitudinally coherent pulses diminishes the spectral sensitivity to detuning effects as well as impacts the finer details of vibronic substructures and peak intensities in the resulting spectra.

Transient Raman Spectroscopy

Steady-state resonant Raman spectroscopy operates by employing narrow-band excitations, where the frequency of photons matches (or is nearly resonant with) the energy of the excited state. This strategy helps minimise uncertainties in the excitation process and prevents broadening effects. To apply resonant Raman spectroscopy effectively in ultrafast spectroscopy, it is hence crucial to balance the narrow-band condition necessary for resonant excitation with the broad-band requirement essential for achieving adequate time resolution in order to track the dynamical processes.

Similar to transient absorption spectroscopy, the total electric field in transient Raman spectroscopy

$$\mathcal{E}(t, \tau) = \mathcal{E}_{\text{pu}}(t) + \mathcal{E}_{\text{pr}}(t, \tau) \quad (2.90)$$

comprises a pump pulse \mathcal{E}_{pu} initiating the excited state dynamics and a probe pulse \mathcal{E}_{pr} examining the induced dynamics by invoking the Raman scattering process after a temporal delay τ . Because the expression for the Raman signal generated by coherent light neither depends on steady-state nor on **CW** conditions, the expression **(2.89)** can be readily expanded to acquire the transient Raman signal

$$I_{\text{TRS}}(\omega_S, \omega_I, \tau) \propto \left(|\tilde{\mathcal{A}}_{\text{pr}}|^2 \otimes \int_{-\infty}^{\infty} dt \exp(-i\tilde{\omega}_S t) \langle \tilde{\mathcal{R}}(\cdot; \tau) | \tilde{\mathcal{R}}(\cdot, t, \tau) \rangle \right) (\tilde{\omega}_I) \quad (2.91)$$

where the evolving wavepacket $|\tilde{\mathcal{R}}(\omega, t, \tau)\rangle = e^{-i\hat{H}_{\text{mol}}t} |\tilde{\mathcal{R}}(\omega, \tau)\rangle$ is defined by the projection $|\tilde{\mathcal{R}}(\omega, \tau)\rangle = \hat{\mu} |\mathcal{R}(\omega, \tau)\rangle$ of the Raman wavefunction

$$|\mathcal{R}(\omega, \tau)\rangle = \int_0^{\infty} dt e^{-i(\hat{H}_{\text{mol}} - i\frac{\Gamma_i}{2})t} \hat{\mu} e^{i(\tilde{\omega}_I - \omega)(t - \tau)} |\Psi^{(1)}(t)\rangle \quad (2.92)$$

assuming without loss of generality that the pump pulse is centered at $t_0 = 0$ whereas the probe pulse is centered at $t = \tau > 0$. In particular, the Raman wavefunction is still a pseudo-time-independent object that only parametrically depends on τ .

Chapter 3

Methodology

Molecular dynamics simulations have become an essential tool to study photoexcited molecular systems. Aiming an accurate description of photochemical or photophysical systems necessitates to solve the full [TDSE](#), a task often simplified by separating the system into a time-independent electronic component and time-dependent nuclear counterpart. In this picture, the molecular system is represented as a set of nuclei moving over [PESs](#), which are governed by the behavior of the electrons. When a single [PES](#) suffices to depict the system under study, classical mechanical techniques usually suffice for conducting molecular dynamics. However, for the description of non-adiabatic systems involving more than one [PES](#), quantum effects come into play, mandating the adoption of a quantum mechanical framework. For this purpose, various semi-classical as well as full quantum mechanical strategies have emerged over the last decades, [\[154–159\]](#) facilitating the simulation of nuclear dynamics across multiple [PESs](#).

As the nuclear dynamics is very sensitive to the surface topology, the success of molecular dynamics calculations hinges significantly on the fidelity of [PES](#) descriptions which are typically obtained from *ab-initio* quantum chemistry calculations. For this purpose, a wide range of electronic structure methods has been developed providing different levels of accuracy where an appropriate method effectively capture the system’s nuances while balancing computational effort.

In this thesis, nuclear quantum dynamics simulations were performed employing the multiconfiguration time-dependent Hartree ([MCTDH](#)) method, [\[160–162\]](#) renowned for its efficacy in solving the [TDSE](#). [\[162–165\]](#) Section [3.1](#) provides a concise overview of this method, with comprehensive details available in relevant literature. [\[160, 162, 163, 165\]](#) The underlying electronic structure calculations were executed using [CC](#) theory [\[166–172\]](#) and its extensions for excited states. [\[172–177\]](#) Section [3.2](#) briefly outlines this approach. For a detailed description of these meth-

ods and their implementations the reader is once more referred to the literature. Moreover, a general overview of common electronic structure methods can be found in various quantum chemistry text books. [178–180]

3.1 Multi-Configuration Time-Dependent Hartree Method

The **MCTDH** method [160–162] is a grid-based, variational approach to solve the **TDSE** allowing to treat multi-dimensional, non-adiabatic systems fully quantum mechanically. In this method, the generally high-dimensional nuclear wavefunction is expanded in direct products of low-dimensional basis functions to which the time evolution can be restricted. The **MCTDH** *ansatz* for the nuclear wavefunction reads [160–162]

$$\Psi^{\text{nuc}}(\mathbf{R}, t) = \sum_J A_J(t) \Phi_J(\mathbf{R}, t) = \sum_{j_1 \dots j_f} A_{j_1 \dots j_f}(t) \prod_{i=1}^f \varphi_{j_i}^{(i)}(R_i, t) \quad (3.1)$$

with time-dependent complex-valued coefficients $A_J = A_{j_1 \dots j_f}$ of the product of low-dimensional basis functions $\varphi_{j_i}^{(i)}$, so-called single particle functions (**SPFs**). Using a linear combinations of time-independent primitive basis functions $\xi_{r_i}^{(i)}$, the time-dependent **SPFs** are themselves represented by

$$\varphi_{j_i}^{(i)}(R_i, t) = \sum_{r_i} c_{r_i j_i}(t) \xi_{r_i}^{(i)}(R_i) \quad (3.2)$$

providing an underlying grid. Commonly, a discrete variable representation (**DVR**) [181] grid is used for all degrees of freedom.

In order to guarantee a variationally optimal evolution of the nuclear wavefunction, the Dirac-Frenkel variational principle [182–184]

$$\langle \delta \Psi^{\text{nuc}} | i\partial/\partial t - \hat{H} | \Psi^{\text{nuc}} \rangle \quad (3.3)$$

is used where the variation of the wavefunction is specified as

$$\delta \Psi^{\text{nuc}} = \sum_J \delta A_J \Phi_J + \sum_i \left(\sum_{l_i} \delta \varphi_{l_i}^{(i)} \psi_{l_i}^{(i)} \right) \quad (3.4)$$

with the single-hole functions $\psi_{l_i}^{(i)}$ defined by all the terms in the wavefunction which

would contain the l_i^{th} function of the i^{th} mode, i.e.

$$\begin{aligned} \psi_{l_i}^{(i)}(R_i, t) = & \sum_{l_1 \dots l_{i-1} l_{i+1} \dots l_f} A_{l_1 \dots l_{i-1} l_{i+1} \dots l_f}(t) \\ & \cdot \varphi_{l_1}^{(1)}(R_1, t) \dots \varphi_{l_{i-1}}^{(i-1)}(R_{i-1}, t) \varphi_{l_{i+1}}^{(i+1)}(R_{i+1}, t) \dots \varphi_{l_f}^{(f)}(R_f, t) \end{aligned} \quad (3.5)$$

In particular, the Dirac-Frenkel variational principle can be applied to both variations δA_J and $\delta \varphi_{l_i}^{(i)}$ independently yielding the following equation of motion (**EOM**)s

$$i \frac{\partial}{\partial t} A_I = \sum_J \langle \Phi_I | \hat{H} | \Phi_J \rangle A_J \quad (3.6)$$

for the expansion coefficients and

$$i \frac{\partial}{\partial t} \varphi^{(i)} = (1 - \hat{P}^{(i)}) (\rho^{(i)})^{-1} \hat{\mathbf{H}}^{(i)} \varphi^{(i)} \quad (3.7)$$

for the **SPFs** where the reduced density matrix $\rho^{(i)}$, the mean-field Hamiltonian matrix $\hat{\mathbf{H}}^{(i)}$ and the subspace projector $\hat{P}^{(i)}$ in the i^{th} subspace are defined by

$$\rho_{jk}^{(i)} = \langle \psi_j^{(i)} | \psi_k^{(i)} \rangle \quad (3.8)$$

$$\hat{H}_{jk}^{(i)} = \langle \psi_j^{(i)} | \hat{H} | \psi_k^{(i)} \rangle \quad (3.9)$$

$$\hat{P}^{(i)}(t) = \sum_j |\varphi_j^{(i)}(t)\rangle \langle \varphi_j^{(i)}(t)| \quad (3.10)$$

respectively.

In order to describe the actual propagation of the nuclear wavepacket, an additional coordinate is included responsible for the electronic states. Within the single-set formalism, there is one set of **SPFs** for all electronic states, i.e.

$$\Psi^{\text{nuc}}(\mathbf{R}, \sigma, t) = \sum_{j_1, \dots, j_f, \sigma} A_{j_1 \dots j_f \sigma}(t) \prod_{i=1}^f \varphi_{j_i}^{(i)}(R_i, t) |\sigma\rangle \quad (3.11)$$

where $\{|\sigma\rangle\}$ denotes the set of electronic states. Contrary, within the multi-set formalism different sets of **SPFs** are used for each state leading to

$$\Psi^{\text{nuc}}(\mathbf{R}, \sigma, t) = \sum_{\sigma} \Psi^{(\sigma)}(\mathbf{R}, t) |\sigma\rangle \quad (3.12)$$

$$\Psi^{(\sigma)}(\mathbf{R}, t) = \sum_{j_1^{\sigma}, \dots, j_f^{\sigma}} A_{j_1^{\sigma} \dots j_f^{\sigma}}^{(\sigma)}(t) \prod_{i=1}^f \varphi_{j_i^{\sigma}}^{(i, \sigma)}(R_i, t) |\sigma\rangle \quad (3.13)$$

requiring a generalisation of the **EOMs**. [163] While both approaches converge to the same result, the single-set formalism is of advantage if the shape of the different electronic states and thus the nuclear dynamics are similar, by contrast, the multi-set formulation is more efficient when the dynamics on the various diabatic states is rather different. Moreover, in order to save computational effort, the **SPFs** can be multi-dimensional accommodating correlations within a combined-mode subspace $R_i = (R_{i_1}, \dots, R_{i_n})$. [162, 185]

An improved, hierarchical variant of **MCTDH** has been developed providing an efficient strategy to treat systems up to several hundred degrees of freedom fully quantum mechanically. Within this **ML-MCTDH** method, [186–189] the multi-dimensional **SPFs** are recursively expanded in the form of (3.1) yielding the following *ansatz*

$$\Psi^{\text{nuc}}(\mathbf{R}, t) = \sum_J A_J^{[1]}(t) \Phi_J^{[1]}(\mathbf{R}, t) = \sum_J A_J^{[1]} \prod_{i_1=1}^{f_1} \varphi_{j_{i_1}}^{[1](i_1)}(R_{i_1}, t) \quad (3.14)$$

for the first layer which is equivalent to (3.1). However, the same type of expansion is also used for the first-layer **SPFs** $\varphi_{j_{i_1}}^{[1](i_1)}(R_{i_1}, t)$ yielding

$$\varphi_j^{[1](i_1)}(R_{i_1}, t) = \sum_J A_{j,J}^{[2](i_1)}(t) \Phi_J^{[2](i_1)}(R_{i_1}, t) = \sum_J A_{j,J}^{[2](i_1)}(t) \prod_{i_2=1}^{f_{i_1}^{[2]}} \varphi_{j_{i_2}}^{[2](i_1, i_2)}(R_{(i_1, i_2)}, t) \quad (3.15)$$

This procedure is repeated until the last layer of time-dependent **SPFs** is represented by the discrete time-independent grid according to (3.2). The **ML-MCTDH**

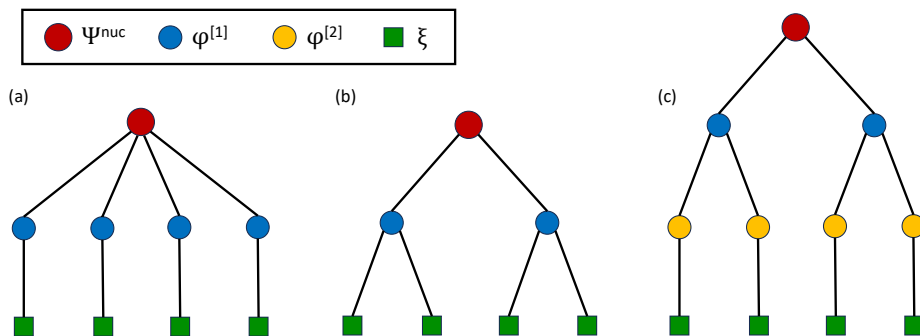


Figure 3.1: Diagrammatic representation of a (a) traditional **MCTDH**, (b) combined mode **MCTDH** and (c) multi-layer **MCTDH** (**ML-MCTDH**) approach for the nuclear wavefunction Ψ^{nuc} of an imaginary system with four degrees of freedom.

EOMs exhibit likewise an hierarchical layer structure **[189]** which can be recursively computed. **[187, 188]**

3.2 Coupled-Cluster Theory and its Derivatives

In this section, we drop all coordinate dependencies for a better readability of the underlying electronic structure methodology used in this thesis. In order to study the electronic structure of atoms and molecules **CC** **[166-172]** theory provides a powerful computational tool. The electronic ground state wavefunction within the **CC** formalism is represented by

$$|\Psi_{\text{CC}}\rangle = e^{\hat{\mathcal{T}}}\Phi_0\rangle \quad (3.16)$$

where $|\Phi_0\rangle$ is the reference wavefunction, typically a Slater determinant constructed from Hartree–Fock molecular orbitals, and $\hat{\mathcal{T}}$ is the so-called cluster operator

$$\hat{\mathcal{T}} = \hat{\mathcal{T}}_1 + \hat{\mathcal{T}}_2 + \dots + \hat{\mathcal{T}}_N \quad (3.17)$$

$$\text{with } \hat{\mathcal{T}}_k|\Phi_0\rangle = \left(\frac{1}{k!}\right)^2 \sum_{ij\dots} \sum_{ab\dots} t_{ij\dots}^{ab\dots} \hat{\tau}_{ij\dots}^{ab\dots}|\Phi_0\rangle = \left(\frac{1}{k!}\right)^2 \sum_{ij\dots} \sum_{ab\dots} t_{ij\dots}^{ab\dots}|\Phi_{ij\dots}^{ab\dots}\rangle \quad (3.18)$$

where N is the number of electrons, t are the amplitudes, $\hat{\tau}$ denote the excitation operators, and the indices $\{i, j, \dots\}$ and $\{a, b, \dots\}$ refer to occupied and virtual orbitals in the reference determinant, respectively. Inserting the **CC** wavefunction *ansatz* **(3.16)** into the electronic Schrödinger equation and multiplying with $e^{-\hat{\mathcal{T}}}$ from left yields the following eigenvalue problem

$$\hat{H}|\Phi_0\rangle = E_{\text{CC}}|\Phi_0\rangle \quad (3.19)$$

with $\hat{H} := e^{-\hat{\mathcal{T}}}\hat{H}^{\text{el}}e^{\hat{\mathcal{T}}}$. In particular, projecting against the reference $\langle\Phi_0|$ and excited determinant $\langle\Phi_{ij\dots}^{ab\dots}|$ lead to the **CC** energy and amplitude equations

$$\langle\Phi_0|\hat{H}|\Phi_0\rangle = E_{\text{CC}} \quad (3.20)$$

$$\langle\Phi_{ij\dots}^{ab\dots}|\hat{H}|\Phi_0\rangle = 0 \quad (3.21)$$

respectively.

While **CC** theory provides accurate descriptions of systems that can be adequately represented by a single Slater determinant, it is inadequate in handling degeneracies or characterising excited states. Nonetheless, various methods and ex-

tensions based on [CC](#) have been developed capable of capturing static correlation or to characterise excited states. The latter can be explored through the [EOM-CC](#) [\[172–177\]](#) approach, wherein a reference state, approximated well by a Slater determinant, is chosen. The [CC](#) equations are then solved for the well-balanced system, followed by the application of an operator to transform it into the target state to be studied.

Within [EOM-CC](#), each excited state is associated with left and right eigenvectors due to the non-Hermiticity of the similarity transformed Hamiltonian \hat{H} , yielding the following parametrisation *ansatz*

$$\langle \Psi_i | = \langle \Phi_0 | \hat{\mathcal{L}}_i \quad (3.22)$$

$$| \Psi_j \rangle = \hat{\mathcal{R}}_j | \Phi_0 \rangle \quad (3.23)$$

with the de-excitation and excitation operators $\hat{\mathcal{L}}_i$ and $\hat{\mathcal{R}}_j$, respectively. This leads in turn to two sets of eigenvalue problems

$$\langle \Phi_0 | \hat{\mathcal{L}}_i \hat{H} = \langle \Phi_0 | \hat{\mathcal{L}}_i E_i \quad (3.24)$$

$$\hat{H} \hat{\mathcal{R}}_j | \Phi_0 \rangle = E_j \hat{\mathcal{R}}_j | \Phi_0 \rangle \quad (3.25)$$

where the eigenvectors of the Hamiltonian form a biorthonormal set, i.e.

$$\langle \Phi_0 | \hat{\mathcal{L}}_i \hat{\mathcal{R}}_j | \Phi_0 \rangle = \delta_{ij} \quad (3.26)$$

In practice, it is impossible to apply the full exponential *ansatz* to the reference determinant and the operators $\hat{\mathcal{T}}$, $\hat{\mathcal{L}}$ and $\hat{\mathcal{R}}$ must be truncated where the most common truncation, also used within this thesis, is after single and double excitations leading to the [\(EOM-\)CC](#) singles and doubles [\(CCSD\)](#) method. The [CCSD](#) wavefunction is thus represented by

$$| \Psi_{\text{CCSD}} \rangle = e^{\hat{\mathcal{T}}_1 + \hat{\mathcal{T}}_2} | \Phi_0 \rangle = \left(1 + \hat{\mathcal{T}}_1 + \hat{\mathcal{T}}_2 + \frac{1}{2} \hat{\mathcal{T}}_1^2 + \hat{\mathcal{T}}_1 \hat{\mathcal{T}}_2 + \frac{1}{2} \hat{\mathcal{T}}_2^2 + \dots \right) | \Phi_0 \rangle \quad (3.27)$$

To compute core-excited states, the [EOM-CC](#) method can be expanded incorporating both the frozen core [\(fc\)](#) and [CVS](#) approach. [\[39\]](#) In this context, the [fc](#) approximation [\[190,191\]](#) entails keeping the orbitals corresponding to the core electrons unchanged throughout the calculation. Meanwhile, the [CVS](#) approximation [\[54,55\]](#) separates valence and core excitations, supported by the energy difference between core and valence orbitals, facilitating direct equation solving for the core electrons.

Chapter 4

Results

In this chapter, the theoretical tools and methodologies previously introduced in Chapter 2 and 3 are applied to simulate non-linear X-ray spectroscopy at the nitrogen K-edge of pyrazine. Our findings have led to three publications [74,88,116] which serve as the basis of this chapter. Given the utilisation of slightly different model Hamiltonians in each project, we commence by presenting the general conceptual framework shared among all three studies in section 4.2. Subsequently, pertinent to each specific project, we furnish the respective section with the specific parameters and computational details. Furthermore, a complete set of parameters in the form of a MCTDH operator file is deposited in the Appendix for each project.

4.1 Pyrazine

The aromatic heterocyclic molecule pyrazine ($C_4H_4N_2$) exhibits interesting photophysical behavior upon UV exposure, attracting significant attention over the past three decades through both experimental [87,192–205] and theoretical [84,85,185,206–242] studies. The low energy regime of the UV absorption spectrum, shown in Figure 4.1, reveals two distinct bands corresponding to transitions to the $B_{3u}(n\pi^*)$ and $B_{2u}(\pi\pi^*)$ states. While the former band displays well-resolved vibrational features, the latter shows a broader profile indicating ultrafast non-radiative decay, which was confirmed by time-resolved photoelectron spectroscopy. [198,199,201,202,204]

To comprehensively understand the ultrafast photophysics of pyrazine, various theoretical frameworks employing non-adiabatic nuclear dynamics simulations have been developed. While earlier studies primarily focused on characterising the conical intersection between the two bright $B_{2u}(\pi\pi^*)$ and $B_{3u}(n\pi^*)$ states, [185,206–208,211,214,215,218,222,226] more recent investigations suggest the potential involve-

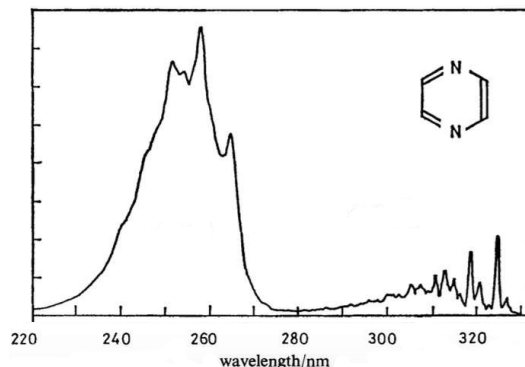


Figure 4.1: Experimental UV absorption spectrum of pyrazine. The absorption band at lower wavelength can be attributed with a $\pi\pi^*$ -transition to the energetically higher B_{2u} electronic state while the band at higher wavelength corresponds to a $n\pi^*$ -transition to the lower B_{3u} state. Used with permission of Royal Society of Chemistry, from [192]; permission conveyed through Copyright Clearance Center, Inc.

ment of an additional dark electronic state influencing the photoinduced dynamics. [224, 227–229, 232] However, deciphering the significance of this dark $A_u(n\pi^*)$ state poses challenges, as theoretical models accommodating or excluding its presence can accurately reproduce the UV spectrum of pyrazine. Moreover, the precise energetic ordering of electronic states heavily relies on the selected level of theory. An experimental validation of the precise mechanism has also proven challenging due to the short timescales involved and signal overlap from different electronic states.

Hence, there is a pressing need for alternative time-resolved experimental techniques capable of tracking the photoinduced dynamics of pyrazine while distinguishing contributions from individual excited states. [87, 236] For this purpose, ultrafast X-ray spectroscopy emerges as a promising avenue, by combining element specific core-level probing with femtosecond time-resolution. [77, 243–246] Consequently, pyrazine serves as an ideal testbed for benchmarking full time-dependent approaches in nonlinear X-ray spectroscopy, thereby facilitating the anticipation of state-of-the-art time-resolved X-ray experiments.

4.2 Construction of Model Hamiltonian

Pyrazine is a planar molecule belonging to the point group D_{2h} at the neutral ground state equilibrium geometry. Its 24 vibrational normal modes are classified by the irreducible representations

$$\Gamma = 5A_g + 1B_{1g} + 2B_{2g} + 4B_{3g} + 2A_u + 4B_{1u} + 4B_{2u} + 2B_{3u} \quad (4.1)$$

The displacement vectors associated with these modes are illustrated in Figure 4.2 while the computed vibrational frequencies, symmetries and experimental data are listed in Table 4.1.

The main objective of this thesis is to devise approaches for the simulation of non-linear X-ray spectroscopy completely in the time domain. To attain the temporal evolution of the system, we perform nuclear quantum dynamics simulation utilising the MCTDH method. For this purpose, a precomputed model Hamiltonian is required capable of accurately describing the nuclear motion on both valence- and core-excited states. To simplify the full molecular Hamiltonian, we completely decouple the valence- and core-excited states concerning non-adiabatic transitions which is substantiated by the large energy difference between them, leading to two isolated subspaces. Within each subspace, we apply the group adiabatic approximation, [128,248] thereby restricting the number of states in the final computations resulting in the following matrix representation of the molecular Hamiltonian

$$\mathbf{H}_{\text{mol}} = \begin{pmatrix} \mathbf{H}_v & 0 \\ 0 & \mathbf{H}_c \end{pmatrix} \quad (4.2)$$

where \mathbf{H}_v and \mathbf{H}_c denote the sub-Hamiltonian acting on the valence- and core-

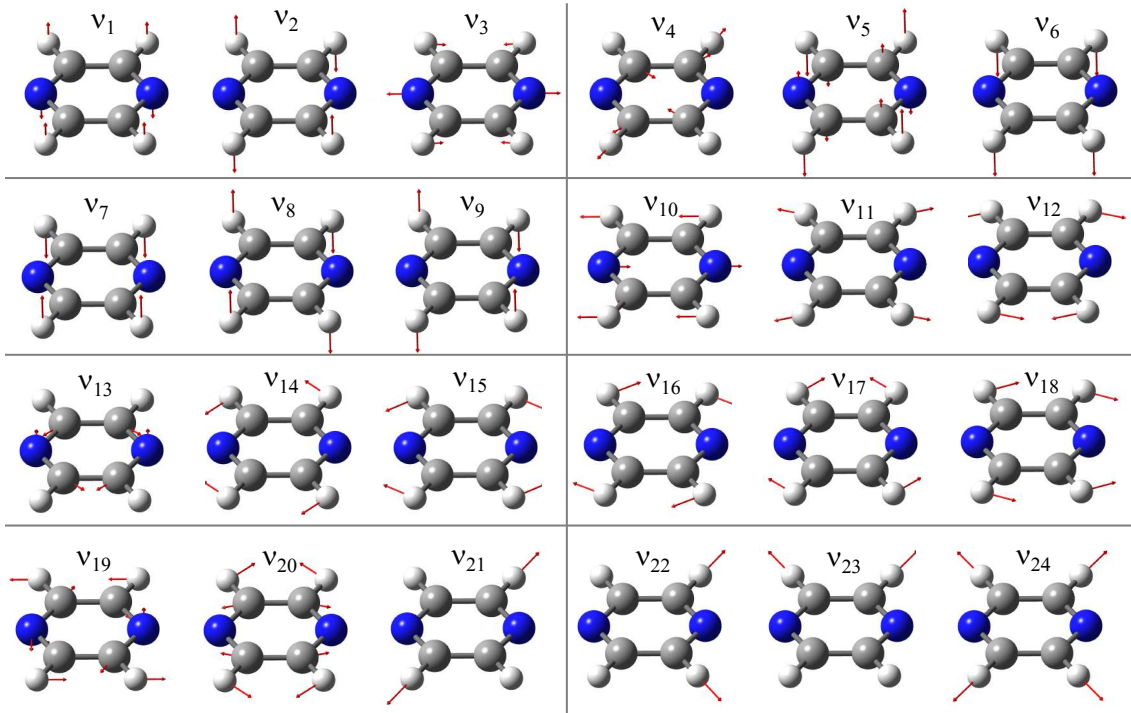


Figure 4.2: Vibrational normal modes of pyrazine obtained from CCSD/aug-cc-pVDZ calculations at the equilibrium ground state structure.

Table 4.1: Harmonic ground-state vibrational frequencies (in cm^{-1}) obtained at the [CCSD](#)/aug-cc-pVDZ level within this thesis along with MP2/aug-cc-pVDZ [\[228\]](#) and experimental [\[195\]](#) data. The modes are labeled by ascending frequency or using Wilson’s notation. [\[247\]](#)

Mode ^{b,c}	Wilson ^a	Symmetry	CCSD ^b	MP2 ^{a,c}	Exp.
ν_1	ν_{16a}	A_u	350	337	341
ν_2	ν_{16b}	B_{3u}	425	417	420
ν_3	ν_{6a}	A_g	604	593	596
ν_4	ν_{6b}	B_{3g}	709	700	704
ν_5	ν_4	B_{2g}	737	734	756
ν_6	ν_{11}	B_{3u}	805	797	785
ν_7	ν_{10a}	B_{1g}	943	936	919
ν_8	ν_5	B_{2g}	950	942	983
ν_9	ν_{17a}	A_u	980	966	960
ν_{10}	ν_{12}	B_{1u}	1033	1022	1021
ν_{11}	ν_1	A_g	1038	1017	1015
ν_{12}	ν_{18b}	B_{2u}	1091	1079	1063
ν_{13}	ν_{14}	B_{2u}	1146	1364	1149
ν_{14}	ν_{18a}	B_{1u}	1162	1148	1136
ν_{15}	ν_{9a}	A_g	1253	1242	1230
ν_{16}	ν_3	B_{3g}	1367	1352	1346
ν_{17}	ν_{19b}	B_{2u}	1441	1440	1416
ν_{18}	ν_{19a}	B_{1u}	1518	1486	1484
ν_{19}	ν_{8b}	B_{3g}	1595	1553	1525
ν_{20}	ν_{8a}	A_g	1650	1605	1582
ν_{21}	ν_{7b}	B_{3g}	3196	3205	3040
ν_{22}	ν_{13}	B_{1u}	3197	3206	3012
ν_{23}	ν_{20b}	B_{2u}	3213	3221	3063
ν_{24}	ν_2	A_g	3218	3226	3055

^a used in section [4.3](#), [\[74\]](#) ^b used in section [4.4](#), [\[88\]](#) ^c used in section [4.5](#), [\[116\]](#)

excited state manifold, respectively. Within this work, both sub-Hamiltonian are represented in a diabatic electronic basis in order to avoid singularities in the non-adiabatic coupling terms. [\[127,128\]](#) Thus, according to [\(2.20\)](#), each sub-Hamiltonian can be written as

$$\mathbf{H}_x = \hat{T}_N \mathbb{1} + \mathbf{W}_x, \quad x \in \{v, c\} \quad (4.3)$$

with the corresponding diabatic potential matrix \mathbf{W}_x . To approximate a diabatic Hamiltonian including multiple coupled electronic states, a simple yet effective method is provided by the vibronic coupling model. [\[127,249,250\]](#) In this approach, the diabatic potential matrix is expanded using a Taylor series around an arbitrary point in configuration space, where in spectroscopic applications the ground

electronic state equilibrium geometry is commonly chosen as the expansion point. Usually, the Taylor expansion is conveniently expressed in terms of dimensionless ground state mass- and frequency-scaled normal coordinates [127], assembled in the vector \mathbf{Q} , yielding

$$\mathbf{H}_x(\mathbf{Q}) = \mathbf{H}^{(0)}(\mathbf{Q}) + \mathbf{W}_x(\mathbf{Q}) \quad (4.4)$$

$$= \mathbf{H}^{(0)}(\mathbf{Q}) + \mathbf{W}_x^{(0)}(\mathbf{Q}) + \mathbf{W}_x^{(1)}(\mathbf{Q}) + \mathbf{W}_x^{(2)}(\mathbf{Q}) + \dots \quad (4.5)$$

for both sub-matrices in (4.2). The zeroth-order Hamiltonian $\mathbf{H}^{(0)}(\mathbf{Q})$ here is the ground state vibrational Hamiltonian in the harmonic approximation

$$\mathbf{H}^{(0)}(\mathbf{Q}) = \sum_i \frac{\omega_i}{2} \left(-\frac{\partial^2}{\partial Q_i^2} + Q_i^2 \right) \mathbb{1} \quad (4.6)$$

where ω_i is the harmonic vibrational frequency of the vibrational mode Q_i . The Taylor expansion of \mathbf{W}_x then covers all changes in the excited state potentials with respect to the ground state yielding up to second order

$$W_{\alpha\alpha}(\mathbf{Q}) = V^{(\alpha)} + \sum_i \kappa_i^{(\alpha)} Q_i + \sum_{i,j} \gamma_{ij}^{(\alpha)} Q_i Q_j \quad (4.7)$$

$$W_{\alpha\beta}(\mathbf{Q}) = \sum_i \lambda_i^{(\alpha\beta)} Q_i + \sum_{i,j} \nu_{ij}^{(\alpha\beta)} Q_i Q_j, \quad \alpha \neq \beta \quad (4.8)$$

where $V^{(\alpha)} \equiv V_\alpha$ denote the vertical adiabatic excitation energies of the α -th electronic state and

$$\kappa_i^{(\alpha)} = \left. \frac{\partial V^{(\alpha)}}{\partial Q_i} \right|_{\mathbf{Q}=\mathbf{Q}_0} \quad (4.9)$$

are the linear intrastate coupling constants related to the gradients of the adiabatic potentials at the Franck-Condon point \mathbf{Q}_0 . Furthermore, the linear interstate coupling constants

$$\lambda_i^{(\alpha\beta)} = \left. \frac{\partial \langle \Psi_\alpha | \hat{H}_{el} | \Psi_\beta \rangle}{\partial Q_i} \right|_{\mathbf{Q}=\mathbf{Q}_0} \quad (4.10)$$

determine the interaction between the α -th and β -th electronic states under displacements of mode Q_i while the bilinear intrastate coupling constants $\gamma_{ij}^{(\alpha)}$ account for the mode-coupling Duschinsky rotation. The bilinear interstate coupling constants $\nu_{ij}^{(\alpha\beta)}$ and higher-order terms are of minor importance in our considerations and can be hence neglected. If the expansion (4.5) is truncated at first order, this

approach is also known as the linear vibronic coupling model.

For symmetric molecules, like pyrazine, group theory can be used to reduce the number of contributing parameters in the vibronic coupling model. The conditions of the three most significant coupling parameters to be non-vanishing can be summarised to

$$\left\{ \kappa_i^{(\alpha)} \mid \Gamma_i \supseteq \Gamma_{A_g} \right\} \quad (4.11)$$

$$\left\{ \gamma_{ij}^{(\alpha)} \mid \Gamma_i \otimes \Gamma_j \supseteq \Gamma_{A_g} \right\} \quad (4.12)$$

$$\left\{ \lambda_i^{(\alpha\beta)} \mid \Gamma_\alpha \otimes \Gamma_i \otimes \Gamma_\beta \supseteq \Gamma_{A_g} \right\} \quad (4.13)$$

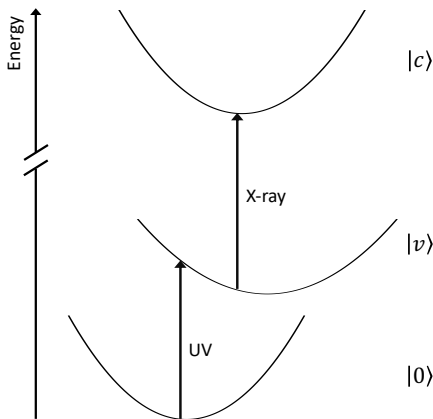
where Γ_{A_g} is the totally symmetric irreducible representation of the symmetry point group of the molecule at the expansion point (here D_{2h}), Γ_i and Γ_j refer to the symmetry of the normal modes Q_i and Q_j , respectively, and Γ_α and Γ_β to the corresponding electronic state symmetries.

For our projects, we have generally constructed a linear vibronic coupling Hamiltonian augmented with diagonal quadratic terms for the non-totally symmetric modes for the most relevant electronic states. The number of electronic states as well as the exact parameter values differ for each project and are thus separately stated in each of the following sections.

4.3 Femtosecond X-ray Absorption Spectroscopy

Due to the short-lived nature of electronic core-excited states reached by X-rays, time-resolved [XAS](#) calculations frequently apply the short time approximation, also known as the Lorentzian limit, as outlined in Section [2.4.2](#). While this approximation proves useful in capturing important aspects of the X-ray response from

Figure 4.3: Schematic representation of the transient photoabsorption process considered within this section. An [UV](#) pump pulse promotes the system from its equilibrium ground state $|0\rangle$ into the valence-excited state manifold $|v\rangle$. The subsequent dynamics is then probed using an X-ray pulse triggering a transition from the valence- to the core-excited states $|c\rangle$.



the underlying valence-excited state dynamics, a comprehensive assessment of its applicability and scope, along with a comparative analysis of time-resolved **XAS** spectra computed with and without this approximation, is missing. This deficiency formed the primary motivation behind our first project [74], upon which this section is founded. Additionally, we delve into the impact of the external electric field, a significant yet often overlooked factor in quantum dynamical investigations.

Computational Details and Model Parametrisation

For this purpose the nuclear **TDSE** was solved employing the **MCTDH** method in its multi-state formalism as implemented in the Heidelberg **MCTDH** package, version 8.4.20. [251] In order to decrease the computational effort, we used a reduced-dimensional model including nine vibrational normal modes capturing the most relevant nuclear dynamics in the valence-excited states. [228] The mode-combination scheme, grid points as well as the number of **SPFs** for the valence-excited states were adopted from [228] without modification. The number of **SPFs** for the core-excited states were incrementally increased until spectra convergence was achieved (visually indistinguishable upon plotting), with specific values detailed in Table 4.2. While the model constructed in [228] served as the basis for parameterising the valence Hamiltonian \mathbf{H}_v , parameter values for the core-excited Hamiltonian \mathbf{H}_c were obtained by fitting diabatic potential terms to adiabatic potential energy surfaces using the VCHam tools, a component of the Heidelberg MCTDH package. Adiabatic core-excited state properties were derived from **fc-CVS-EOM-CCSD** calculations using Pople’s 6-311++G** basis set [252], consistent with the level of theory employed in [39] on the same system. All electronic structure calculations were carried out using the quantum chemistry software package Q-Chem, version 4. [253]

The adapted model for the valence Hamiltonian \mathbf{H}_v includes the ground and the three lowest valence-excited states. The related non-adiabatic coupling param-

Table 4.2: Computational details of MCTDH calculations within this project. The mode-combination and numbers of primitive grid functions were exactly as given in [228] where harmonic oscillator (HO)-type **DVRs** were chosen. The number of state-specific **SPFs** were extended to include the core-excited states.

Combination of modes	Numbers of SPFs	DVR	Numbers of grid points
(ν_{6a}, ν_{10a})	[4, 30, 34, 14, 8, 4, 12]	HO	(32,40)
(ν_1, ν_4)	[4, 12, 15, 8, 8, 4, 12]	HO	(16,20)
$(\nu_{9a}, \nu_3, \nu_{8b})$	[4, 13, 14, 8, 8, 4, 12]	HO	(14,10,14)
(ν_{8a}, ν_5)	[4, 20, 24, 8, 8, 4, 12]	HO	(24,10)

Table 4.3: Transition dipole moments $\mu_{\beta\alpha}$ between two electronic states α and β , where the transition dipole moments to valence-excited states, μ_{01} and μ_{03} , are taken from [228]. The valence-core transition dipole moments are obtained from `fc-CVS-EOM-CCSD` calculations.

State transition	$\mu_{\beta\alpha}$
$S_1 \leftarrow S_0$	0.08
$S_3 \leftarrow S_0$	0.3
$X_2 \leftarrow S_0$	0.10
$X_1 \leftarrow S_1$	0.06
$X_3 \leftarrow S_2$	0.06
$X_3 \leftarrow S_3$	0.03

Table 4.4: Vertical excitation energies $V^{(\alpha)}$ (in eV) and symmetries of all electronic states considered in this project. The ground and valence-excited state data are adopted from [228]. The vertical N-1s excitation energies are obtained from `fc-CVS-EOM-CCSD` calculations at the Franck-Condon point.

State	Symmetry	$V^{(\alpha)}$
S_0	A_g	0.00
S_1	B_{3u}	3.93
S_2	A_u	4.45
S_3	B_{2u}	4.79
X_1	B_{2g}	399.970
X_2	B_{3u}	399.972
X_3	B_{1g}	402.770

eters can be found in [228] or in the corresponding operator file provided in the Appendix. Vibrational normal mode frequencies and symmetries are reported in Table 4.1, where we used Wilson’s notation for this project. In order to determine the relevant core-excited states entering \mathbf{H}_c we computed transition dipole moments and oscillator strength at the `FC` point. Specifically, we considered the three lowest dipole allowed transitions at the nitrogen K-edge starting from the ground and from each of the three valence-excited states. By disregarding transitions where the oscillator strength ratio compared to the strongest valence-core transition fell below 0.01, we identified four dipole-allowed transitions leading to three distinct core-excited states. The corresponding transition dipole moments as well as vertical excitation energies and state symmetries are collected in Table 4.3 and Table 4.4, respectively.

The core Hamiltonian \mathbf{H}_c containing three electronic states was approximated by a linear vibronic coupling model, encompassing the same nine vibrational modes as in \mathbf{H}_v . According to (4.11), the linear intrastate couplings $\kappa_i^{(\alpha)}$ are non-zero for totally symmetric vibrational modes. These couplings play a pivotal role in

Table 4.5: Linear intrastate coupling constant $\kappa_i^{(\alpha)}$ values (in eV) for the core-excited states, X_α , obtained in this work.

State	κ_{6a}	κ_1	κ_{9a}	κ_{8a}
X_1	-0.03144	-0.00106	0.04845	0.09455
X_2	-0.03134	0.00111	0.04848	0.09464
X_3	-0.13498	-0.02848	-0.14471	-0.28893

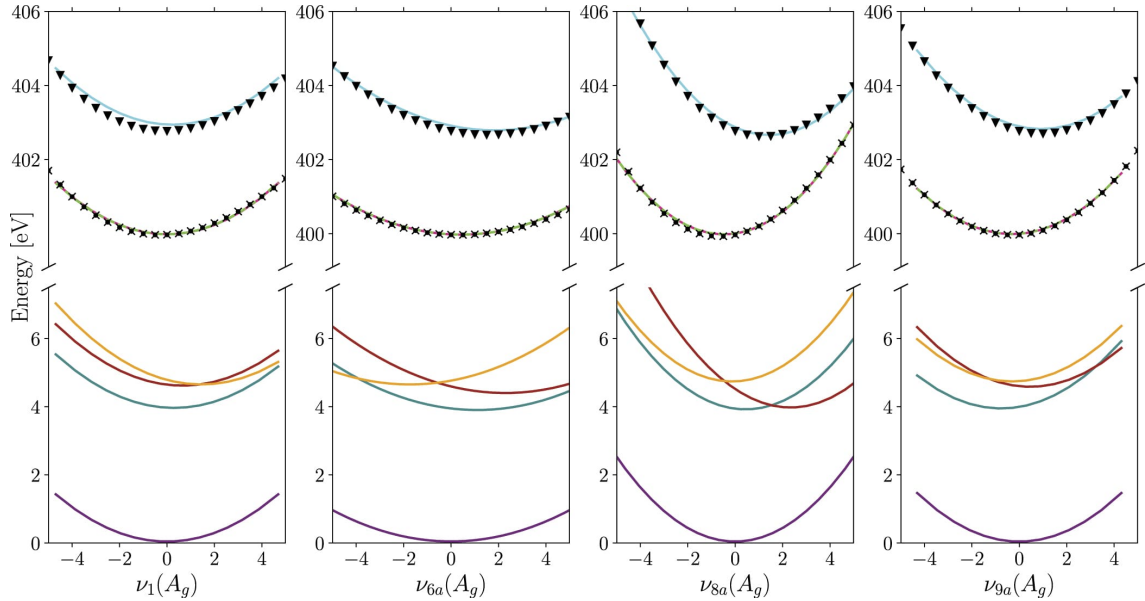


Figure 4.4: Cuts through the diabatic PES along the four totally symmetric normal modes included in this study along with the adiabatic single point energies for the core-excited states X_1 (dots), X_2 (cross) and X_3 (triangle) calculated at the fc-CVS-EOM-CCSD/6-311++G** level of theory. Used with permission of IOP Publishing, Ltd, from [74]; permission conveyed through Copyright Clearance Center, Inc.

governing the short-term dynamics of core-excited wavepackets out of the Franck-Condon region subsequent to interaction with the X-ray probe pulse. Notably, the two lowest N-1s core-excited states exhibit almost degeneracy along the four totally symmetric modes and could be coupled through vibrational modes of symmetry B_{1u} , as per (4.13). However, none of the nine vibrational modes incorporated in this model corresponds to this symmetry representation, and this aspect was not further considered within this project. Consequently, the diabatic core-excited potential matrix is solely characterised by vertical energies $V^{(\alpha)}$ and linear intrastate couplings terms $\kappa_i^{(\alpha)}$. The respective values are listed in Table 4.5. Moreover, the calculated energy points and fitted curves are shown in Fig. 4.4.

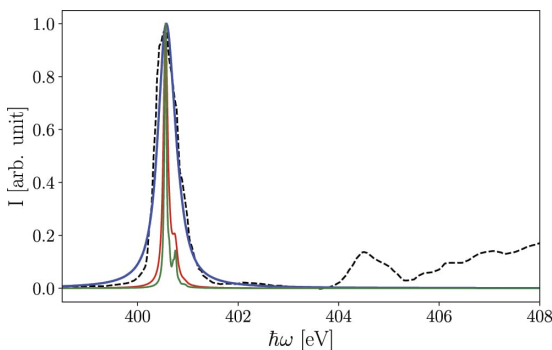


Figure 4.5: Static XANES spectrum of pyrazine. The experimental spectrum (dashed line), redigitised from [254], is shifted by 1.73 eV to match the main peak with the computed spectra (solid lines) for core-hole lifetimes of 3 fs (blue), 8 fs (red) and 15 fs (green). Used with permission of IOP Publishing, Ltd, from [74]; permission conveyed through Copyright Clearance Center, Inc.

The average finite lifetime of N-1s core-excited states is considered as an intrinsic property of the atomic species, [65,66] represented by an imaginary energy term in the core-excited state Hamiltonian \mathbf{H}_c . Accordingly, we adopt a core-hole lifetime of $T = 8$ fs, corresponding to a spectral **fwhm** of 0.11 eV consistent with experimental measurements at the K-edge of molecular nitrogen. [255] However, within this section, we also present comparisons with simulations employing core-hole lifetimes of 15 fs, affording higher spectral resolution. We contrast these outcomes with absorption spectra where the core-hole lifetime is constrained to 3 fs. The latter duration aligns with the lifetime necessary to approximate the Lorentzian contribution of a nitrogen K-edge **XANES** measurement of pyrazine in the ground state, [254] assuming a dominant single transition (see Figure 4.5). Nevertheless, we presume that the width derived from molecular nitrogen measurements more accurately reflects the atomic lifetime, whereas investigations involving more complex species are subject to additional dephasing mechanisms contributing to the observed line widths.

Quantum dynamics propagations were run for various time delays between the pump and probe pulses. The propagation process was terminated once the populations of core-excited states declined to below 5% of their maximum value to save computational effort. Propagation runs evolving in the valence states were set to write output every 0.1 fs, whereas propagations involving simultaneously valence- and core-excited states were set to write output every 0.005 fs, ensuring a sufficient time resolution and frequency span for subsequent Fourier transforms.

On the Validity of the Lorentzian Limit

In order to obtain a direct comparison between **fs-XANES** spectra computed employing the short-time approximation and those derived from exact full dynamical calculations, we adopt δ -like pulses for both the pump and the probe pulse. Thus, the external electric field has the form

$$\mathcal{E}(t) = \delta_{\text{pu}}(t) + \delta_{\text{pr}}(t - \tau) \quad (4.14)$$

where the pump pulse initially promotes the system into the valence-excited state manifold at time $t = 0$ fs, and the probe pulse detects the induced dynamics after a temporal delay $\Delta\tau = \tau$.

The temporal evolution of the pump-induced valence-excited state population dynamics is shown in Figure 4.6. Equivalent to a δ -like pump pulse, the nuclear ground state wavefunction is initially projected into the bright $S_3(B_{2u}(\pi\pi^*))$ state at the **FC** geometry. Subsequently, the population of the S_3 rapidly decays into both

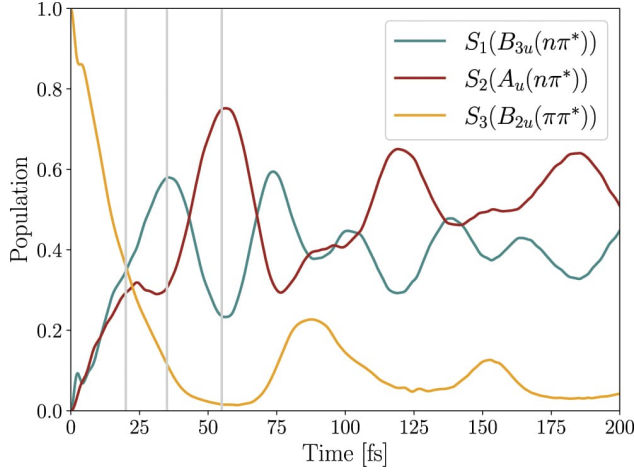


Figure 4.6: Diabatic state population of the three valence-excited states after instantaneous vertical excitation at time $t = 0$ fs. The vertical grey lines indicate the pump-probe delays $\Delta\tau = 0, 20, 35$ and 55 fs used in the following discussion. Used with permission of IOP Publishing, Ltd, from [74]; permission conveyed through Copyright Clearance Center, Inc.

the $S_1(B_{3u}(n\pi^*))$ and $S_2(A_u(n\pi^*))$ states. The competitive population transfer to the S_1 and S_2 states within the first 35 fs can be attributed to low-lying conical intersections between both state pairs, S_3/S_1 and S_3/S_2 . After 55 fs, S_3 is almost fully depopulated with a recurrence seen at about 95 fs. The following state population keeps oscillating with a period of approximately 65 fs, consistent with the frequency of the ν_{6a} normal mode, which predominantly governs the population dynamics.

In order to follow this population dynamics, we simulated **fs-XANES** spectra of pyrazine where we performed two distinct sets of calculations: one utilising the numerically exact dipole-dipole correlation function

$$I_{\text{TRXAS}}(\omega, \tau) \propto \text{Re} \int_0^{\infty} dt \langle \Psi_v(\tau) | e^{i\hat{H}_v(t-\tau)} \hat{\mu} e^{-i\hat{H}_c(t-\tau)} \hat{\mu} | \Psi_v(\tau) \rangle e^{i\omega t - \Gamma_c t/2} \quad (4.15)$$

encompassing nuclear dynamics across both the valence- and core-excited state manifolds, and another employing the Lorentzian limit approach

$$I_L(\omega, \tau) \propto \text{Re} \int_0^{\infty} dt \langle \Psi_v(\tau) | \hat{\mu} e^{-i(\hat{W}_c - \hat{W}_v)(t-\tau)} \hat{\mu} | \Psi_v(\tau) \rangle e^{i\omega t - \Gamma_c t/2} \quad (4.16)$$

where the kinetic energy operator is disregarded after X-ray interaction at time $t = \tau$, thereby excluding the dynamics on the core-excited states. In particular, this facilitates a direct comparison between both approaches, with the only discrepancy between the two sets of results arising from the application of the short-time approximation.

A direct comparison of the **XANES** spectra for time delays $\Delta\tau = 0$ fs, 20 fs, 35 fs and 55 fs are shown in Figure 4.7 where the core-hole decay was set to the intrinsic lifetime $\Gamma_c^{-1} = T = 8$ fs. Within both approaches, the population dynamics

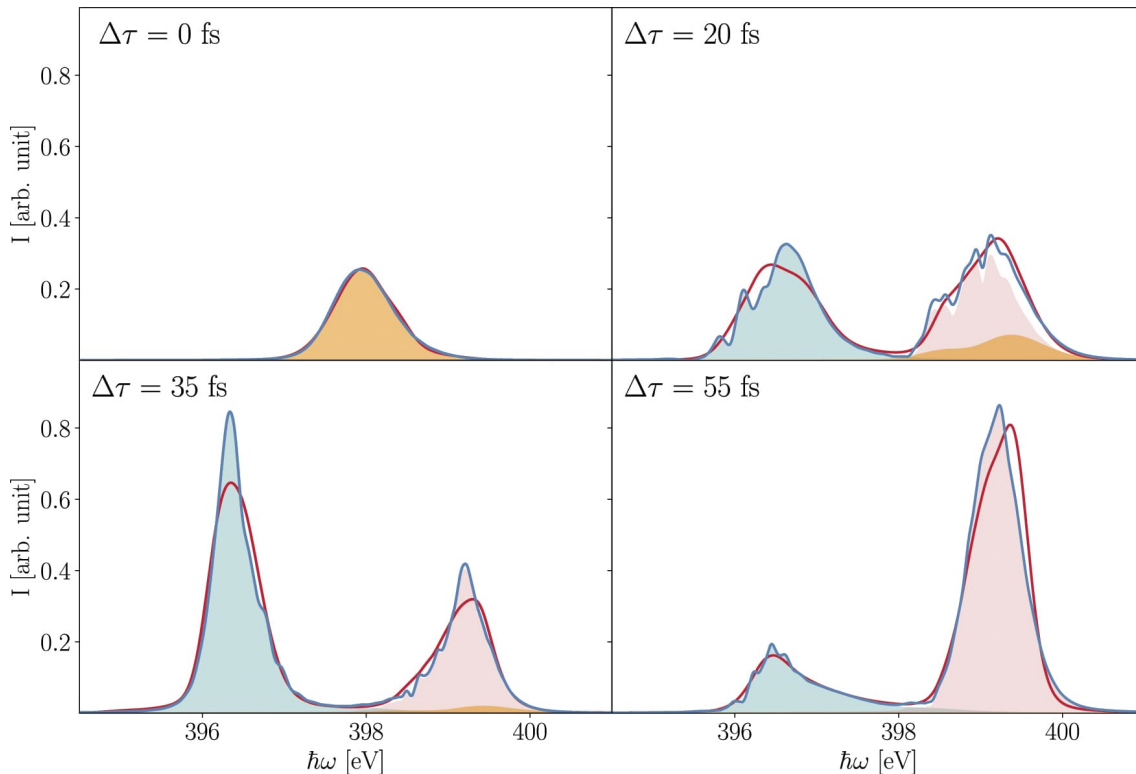


Figure 4.7: Simulated **XANES** spectra of pyrazine at delay times 0 fs, 20 fs, 35 fs and 55 fs with (red solid line) and without (blue solid line) using the short-time approximation. Contributions stemming from transitions from S_1 , S_2 and S_3 to the latter calculation set are highlighted in cyan, red and orange, respectively. Used with permission of IOP Publishing, Ltd, from [74]; permission conveyed through Copyright Clearance Center, Inc.

between the valence-excited states is accurately mapped by the transient absorption spectra. Immediately after the **UV** transition to S_3 , only the $X_3 \leftarrow S_3$ excitation band, located around 398 eV, is visible. After 20 fs, when the population becomes nearly evenly distributed among the three valence-excited states, all three excitation bands in the absorption spectrum appear where the intensities of the $X_1 \leftarrow S_1$ and $X_3 \leftarrow S_2$ bands, centered at approximately 397 eV and 399 eV, respectively, are comparable while the $X_3 \leftarrow S_3$ band intensity is approximately four times lower, consistent with expectations from the transition dipole moments (see Table 4.3). Moreover, the $X_3 \leftarrow S_3$ transition (highlighted in orange) has shifted towards higher frequencies by approximately 1 eV due to vibrational relaxation in the valence-excited state S_3 combined with X-ray transitions to higher vibronic states in X_3 , now overlapping with the $X_3 \leftarrow S_2$ transition (highlighted in red). As predicted from the population dynamics shown in Figure 4.6, the $X_1 \leftarrow S_1$ and $X_3 \leftarrow S_2$ bands reach their maximal intensity at about $\Delta\tau = 35$ fs and $\Delta\tau = 55$ fs, respectively, with only minor contributions of the $X_3 \leftarrow S_3$ transition band.

Generally, the shape of the absorption bands within the Lorentzian approximation (depicted by the red contour in Figure 4.7) closely aligns with the fully time-dependent calculation of the spectrum (depicted by the blue contour in Figure 4.7). Furthermore, the excitation bands exhibit a rather broad and asymmetrical shape in both approaches, which can therefore be attributed to the evolution of nuclear wavepackets on the valence-excited states. However, simulated spectra within the Lorentzian limit miss the finer vibronic structures, as observed, for instance, at delay time 20 fs, where vibrational features are notably absent in both dominant absorption bands, $X_1 \leftarrow S_1$ and $X_3 \leftarrow S_2$. The reason for that is that the Lorentzian limit is only sensitive to the probability distribution of the valence-states wavepacket while the exact polarisability after the probe reflects the coherent wavepacket dynamics in both the valence- and core-excited.

This pronounced loss of dynamical effects is also evident in the $X_3 \leftarrow S_2$ absorption band at $\Delta\tau = 35$ fs and for the $X_1 \leftarrow S_1$ absorption band at 55 fs time delay. Additionally, the primary peak position of the $X_3 \leftarrow S_2$ absorption band exhibits a slight shift at $\Delta\tau = 55$ fs. In contrast, the Lorentzian limit seems to perform optimally for no time delay. This may be attributed to the rapid non-adiabatic dynamics out of the Franck-Condon region in S_3 directly after the optical pump excitation which contribute to a very fast dephasing between the nuclear wavepackets in the valence- and core-excited manifolds. Nonetheless, our simulations suggest that this motion-induced dephasing slows down once the wavepacket in the valence manifold has had time to relax towards the lower energy regions of the corresponding electronic state potentials.

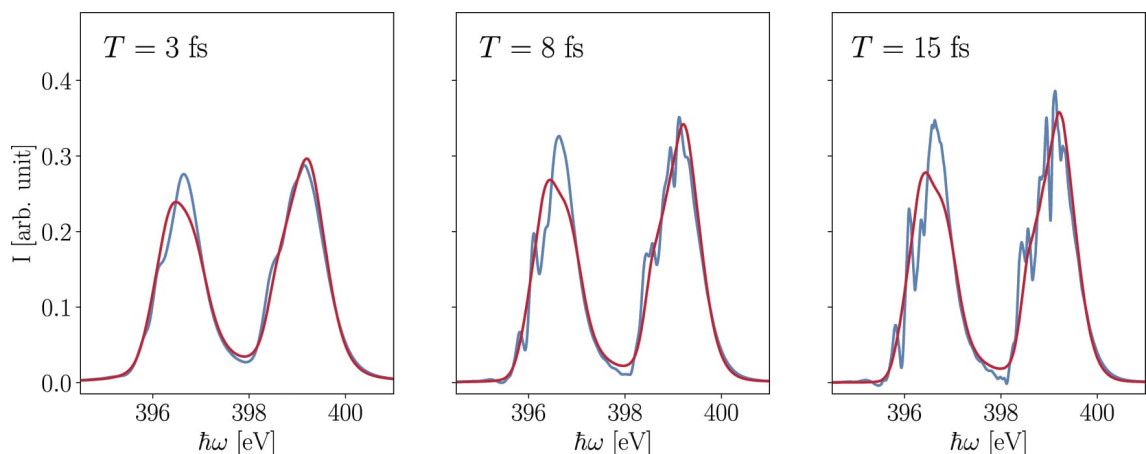


Figure 4.8: XANES spectra of pyrazine at $\Delta\tau = 20$ fs for different mean core-hole lifetimes T , computed within (red solid line) and without (blue solid line) the short-time approximation. Used with permission of IOP Publishing, Ltd, from [74]; permission conveyed through Copyright Clearance Center, Inc.

In particular, the core-hole decay remains the predominant dephasing mechanism dictating the validity of the Lorentzian limit where, as expected, the Lorentzian approximation exhibits enhanced agreement with the exact spectrum for shorter core-hole lifetimes (see Figure 4.8). However, even for 3 fs core-hole lifetime, a slight shift of approximately 0.1 eV is observed in the band around 396 eV between both approaches. Comparing the spectra obtained with core-hole lifetimes of 8 fs and 15 fs reveals a consistent finer vibronic structure, which becomes more significant with increasing core-hole lifetime.

In summary, while the Lorentzian limit effectively captures electronic population dynamics and the broad features of X-ray absorption bands, it proves inadequate for accurately describing the finer vibronic substructure in fs-XANES of pyrazine.

Influence of Finite Pulse Duration

In the subsequent analysis, we include an explicit description of the external electric field and investigate the impact of a finite pump pulse duration on the X-ray probe response beyond the δ -pulse idealisation. For this purpose, the transient absorption spectra are calculated using the non-perturbative approach

$$I_{\text{TRXAS}}(\omega, \tau) \propto -\frac{\text{Im} \left(\tilde{P}(\omega) \tilde{\mathcal{E}}^*(\omega, \tau) \right)}{|\tilde{\mathcal{E}}(\omega, \tau)|^2} \quad (4.17)$$

where \tilde{P} is the Fourier transform of the expectation value of the transition dipole moment and

$$\mathcal{E}(t, \tau) = \mathcal{E}_{\text{pu}}(t) + \mathcal{E}_{\text{pr}}(t, \tau) \quad (4.18)$$

is the electric field, where both components are represented by L^2 -normalised Gaussian envelopes

$$\mathcal{E}_k(t) = \frac{E_k}{\sqrt{N_k}} \exp \left(-\frac{1}{2} \frac{(t - t_{0,k})^2}{\sigma_k^2} \right) \cos(\omega_k(t - t_{0,k})), \quad k = \text{pu, pr} \quad (4.19)$$

with the pulse center of the k -th pulse at $t_{0,k}$, and with carrier frequency ω_k . Further, E_k denotes the maximum amplitude and σ_k the standard deviation linked to the temporal **FWHM** duration by $F_k = 2\sqrt{\ln 2} \sigma_k$. The L^2 -normalisation constant N_k is given by

$$N_k = \frac{\sqrt{\pi}}{2} \sigma_k [1 + \exp(-\sigma_k^2 \omega_k^2)] \quad (4.20)$$

and guarantees isoenergetic pulses when varying the width parameter σ_k , thereby providing the same total amount of population transfer. While keeping the parameters of the X-ray probe pulse fixed, the optical pump duration is varied between 1 fs to about 80 fs. The intensities of both laser pulses are adjusted to ensure one-photon processes in both steps but still being sufficiently high to avoid numerical instabilities caused by insufficient population transfer. All parameters are summarised in Table 4.6.

An overview of the pump pulse effects on the photoexcitation processes is provided by Figure 4.9, where the valence-excited state population, the linear UV absorption spectrum as well as several transient X-ray absorption spectra for different time delays $\Delta\tau$ are shown for different pump pulse durations as given by Table 4.6. The spectral bandwidth of the pump pulse dictates which spectral region of the vibronic valence states forms the initial wavepacket, as the linear absorption spectrum shows in the second column of Figure 4.9. Consequently, due to the reciprocal connection between temporal and spectral width, very short pump pulses illuminate the entire linear absorption spectrum of pyrazine in a single pulse (see (a)), whereas pump pulses with a temporal **fbwm** of 15 fs or longer selectively excite smaller segments of the overall spectrum according to their bandwidth (see (b)-(e)).

From a temporal perspective, the excitation process lasts for the entire pulse duration, leading to blurred excited state dynamics for longer pump pulses. Comparing the state populations obtained via instantaneous vertical excitation, as depicted in Figure 4.6, with the state population in Figure 4.9 reveals that the characteristic oscillation of electronic state populations persists up to a pulse duration of approximately 15 fs, beyond which it becomes rather diffuse. Consequently, the population dynamics are well detected in the transient X-ray spectra (a) and (b), evidenced by the wavering peak intensities of the $X_3 \leftarrow S_2$ and $X_1 \leftarrow S_1$ transition bands. However, longer pump pulses yield spectrally narrower wavepackets, wherein the intrinsic population dynamics are smoothed out during the excitation process (see (c)-(e)). For pump pulses longer than ~ 50 fs, extracting relevant information regarding the underlying dynamical processes becomes exceedingly challenging, as exemplified in panel (e) where the X-ray response is effectively time-independent.

We note that the preceding discussion on the computed transient spectra were restricted to excited state absorption, disregarding transitions originating from the ground electronic state, S_0 . However, in real pump-probe transient absorption experiments, measuring the absorbance solely of the transient species is impossible. Instead, the absorbance of the unexcited sample must be subtracted from the excited absorption spectrum yielding the differential transient X-ray absorption spec-

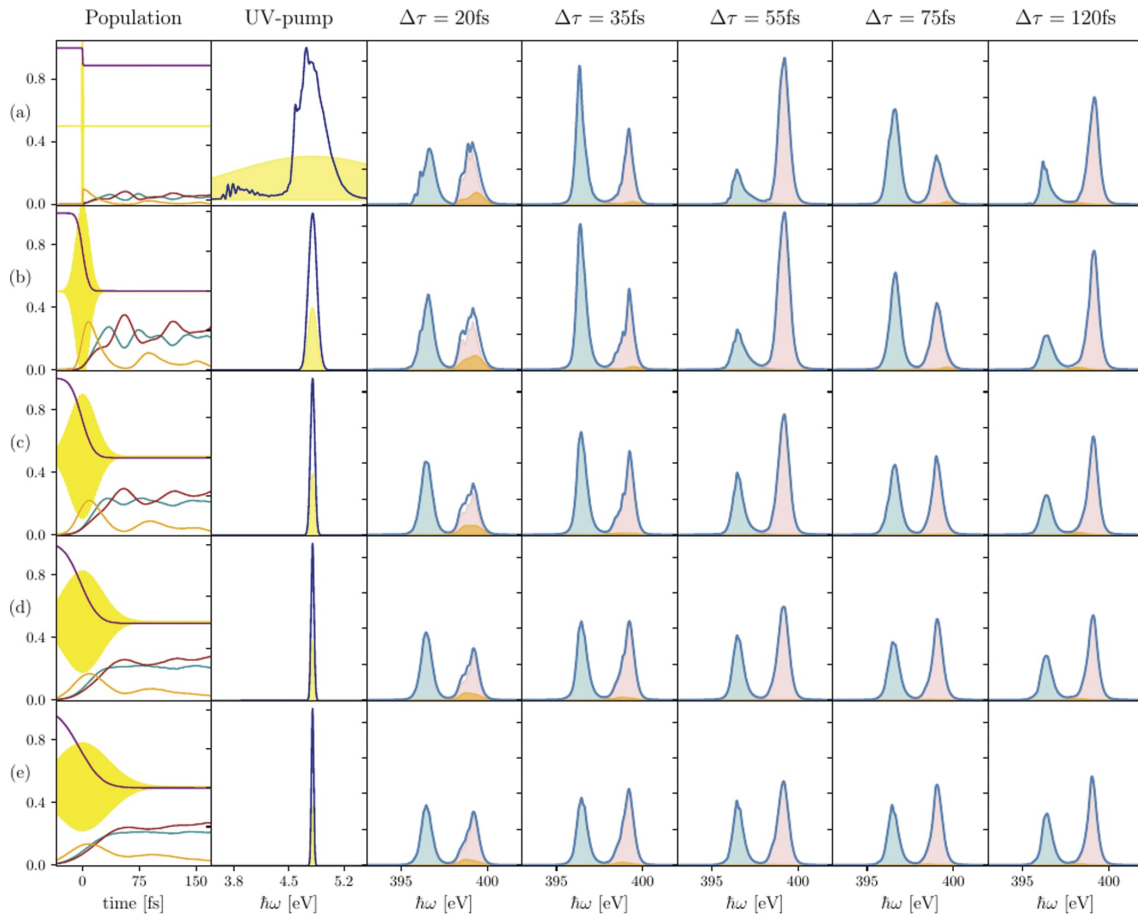


Figure 4.9: Overview of transient X-ray absorption spectra of pyrazine using pump pulses with (a) 1.01 fs, (b) 20.3 fs, (c) 40.5 fs, (d) 60.8 fs and (e) 81.0 fs temporal **fwhm** (see Table **4.6**). Due to the L^2 -normalisation, the electric fields associated with the pump pulses have identical pulsed radiation fluences generally providing the same total amount of population transfer from S_0 (see (b)-(e)). If the temporal pulse lengths become very short, the spectral range of the pulse becomes very broad, covering frequencies beyond the excitation band resulting in less population transfer as seen in (a). For each case the valence-excited state population of S_0 (purple), S_1 (cyan), S_2 (red) and S_3 (orange) as well as the temporal evolution of the pump pulse (yellow) is shown in the first column. For a better visualisation, the pump pulse amplitude was increased by a factor of 50 and the zero-point was shifted along the y-axis by 0.5. The second column displays the linear UV absorption spectrum (dark blue) triggered by the pump pulse. A damping time of 120 fs was used to adjust the S_3 band of the calculated and experimental spectrum (see Fig. **4.1**). The squared absolute value of the pump pulse in the frequency domain is highlighted as yellow area where intensity was increased by a factor of 10. The third to seventh column present the **XANES** spectra for time delays $\Delta\tau = 20$ fs, 35 fs, 55 fs, 75 fs and 120 fs where the $X_2 \leftarrow S_0$ transition was neglected for comparison reasons. The contributions of the $X_1 \leftarrow S_1$, $X_3 \leftarrow S_2$ and $X_3 \leftarrow S_3$ are as before highlighted in cyan, red and orange, respectively. Used with permission of IOP Publishing, Ltd, from **74**; permission conveyed through Copyright Clearance Center, Inc.

Table 4.6: Parameters of the pump and probe pulse used in this project. The intensities E_k are given in a.u., the carrier frequencies ω_k in eV and the temporal **FWHM** F_k in fs. Further, the number of pulse cycles per $2\sigma_k$ unit is given by n_{cyc} .

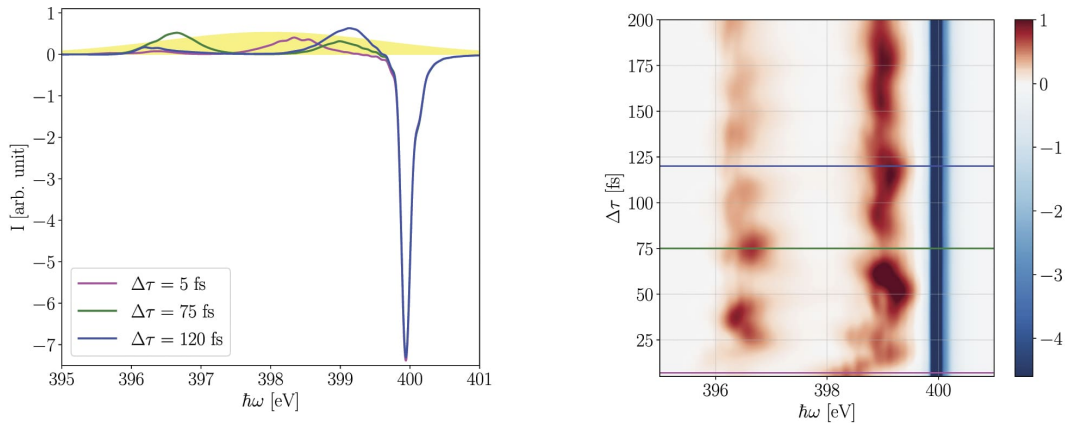
	E_k	ω_k	F_k	σ_k	n_{cyc}
$\mathcal{E}_{pu}^{(a)}(t)$	0.2	4.8	1.01	0.43	1
$\mathcal{E}_{pu}^{(b)}(t)$	0.2	4.8	20.3	8.60	20
$\mathcal{E}_{pu}^{(c)}(t)$	0.2	4.8	40.5	17.2	40
$\mathcal{E}_{pu}^{(d)}(t)$	0.2	4.8	60.8	25.8	60
$\mathcal{E}_{pu}^{(e)}(t)$	0.2	4.8	81.0	34.4	80
$\mathcal{E}_{pr}(t)$	1.0	398	0.50	0.3	60

trum. The resulting difference spectrum then exhibits positive signals stemming from excited state absorption which can be differentiated from the negative signals attributed to the ground state bleaching.

In principle, the time-independent background could obscure some of the relevant time-dependent features due to spectral overlap. We thus additionally compute the differential absorption spectrum of pyrazine, with the respective pump and probe pulse parameters as detailed in Table 4.6(a). Notably, the $X_2 \leftarrow S_0$ transition exhibits considerably higher likelihood compared to X-ray transitions from valence-excited states (see Table 4.3), resulting in a very dominant negative bleach signal at 400 eV (see Figure 4.10). Moreover, as there is no radiationless relaxation mechanism from valence-excited states back to the electronic ground state on the **fs** timescale, the ground state bleach signal remains the same for all time delays considered in this project.

Moreover, two distinct excited state absorption signals are observed: one at 396.5 eV corresponding to the $X_1 \leftarrow S_1$ transition, and another at 399 eV, corresponding to the $X_3 \leftarrow S_3$ and $X_3 \leftarrow S_2$ transitions. Due to the overall slightly higher population of S_2 compared to S_1 , along with the overlap of the $X_3 \leftarrow S_3$ and $X_3 \leftarrow S_2$ bands, the signal around 399 eV exhibits a greater intensity than the signal at 396.5 eV. Furthermore, the intensity of the 396.5 eV peak oscillates with a period of 30 fs, aligning with the population maxima of S_1 , whereas the intensity of the signal around 399 eV remains relatively constant due to the compensatory contribution of the repopulation of S_3 alongside the depopulation of S_2 , as illustrated in Figure 4.6.

Importantly, the simulated differential absorption spectrum within this project suggests that the ground state absorption does not obscure the time-dependent features associated with the excited-state dynamics. However, this may not be



(a) Differential absorption spectra at time delays of 5 fs (magenta), 75 fs (green) and 120 fs (blue). The probe pulse energy is represented by the yellow area, where the amplitude was decreased by a factor of 40 for a better visualisation.

(b) Three-dimensional collection of all computed differential absorption spectra for time delays $\Delta\tau$ between 0 fs and 200 fs with a stepsize of 5 fs. The colored horizontal lines indicate the time delays shown in (a).

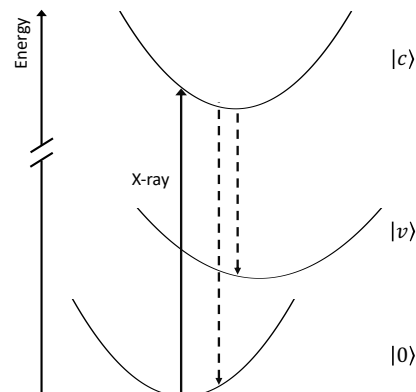
Figure 4.10: Differential X-ray absorption spectra including all dynamical dimensions and an explicit description of both the pump and probe pulse. Used with permission of IOP Publishing, Ltd, from [74]; permission conveyed through Copyright Clearance Center, Inc.

immediately apparent a priori, given the close spectral proximity of the bands at 399 eV and 400 eV, which might overlap, for instance, due to broad vibrational progressions in either the valence- or core-excited states.

4.4 Resonant Inelastic X-ray Scattering

The next X-ray spectroscopy technique investigated in this thesis is **RIXS**, with a particular emphasis on elucidating the manifestation of ultrafast core-excited state dynamics in the resulting spectra. Generally, **RIXS** adheres to electronic dipole se-

Figure 4.11: Schematic representation of the **RIXS** process considered within this section. Incoming X-ray radiation promotes the system into the intermediate core-excited state manifold $|c\rangle$ from where the spontaneous scattering event takes place returning the system into the ground $|0\rangle$ or energetically higher lying valence-excited states $|v\rangle$.



lection rules for both the absorption and emission step, providing valuable insights into the symmetry of occupied and unoccupied molecular orbitals. [68,91,256,257] However, symmetric molecules with equivalent atoms always exhibit core-orbitals that are delocalised over these atoms yielding nearly degenerate core-excited states. [249,258-262] The vibronic coupling between these states can result in ultrafast dynamical symmetry distortion, which in turn enables electronic transitions that would be otherwise dipole-forbidden, thereby significantly impacting the overall RIXS signal. [68,90,91,250,256,263,264] In order to accurately depict the occurring ultrafast dynamical processes as well as their manipulation by detuning, we again apply a full time-dependent framework to study the RIXS process at the nitrogen K-edge of pyrazine. Moreover, we discuss the impact of a coherent pulsed light source providing a foundation for state-of-the-art time-resolved RIXS studies. This section is based on [88].

Computational Details and Model Parameters

The two nitrogen atoms of pyrazine are indistinguishable at the equilibrium ground state structure. Thus, the corresponding molecular N-1s core orbitals shown in Figure 4.12 are, as a linear combination of the two equivalent atomic N-1s orbitals, energetically degenerate leading in turn to degenerate electronic core-excited states which can be vibronically coupled through non-symmetrical normal modes.

In this project, we focus on steady-state resonant Raman scattering via the lowest unoccupied molecular orbital of pyrazine where only the transition involving the antisymmetric $1b_{1u}$ core-orbital is dipole allowed due to symmetry reasons. This electronic transition forms the $X_2(B_{3u})$ core-excited state while the dipole-forbidden transition involving the symmetric $1a_g$ core-orbital yields the dark $X_1(B_{2g})$ state (see Section 4.3). According to (4.13) these states can be vibronically coupled through normal modes of symmetry B_{1u} which was not further considered in the previous

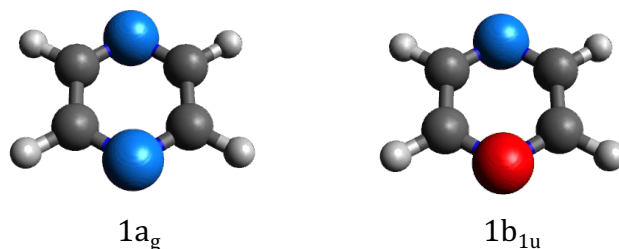


Figure 4.12: Energetically degenerate molecular N-1s core-orbitals of pyrazine delocalised over the two nitrogen atoms.

section as none of the four B_{1u} normal modes were included in the chosen model Hamiltonian. Thus, in order to explicitly include non-adiabatic transitions between these two degenerate core-excited states within this project, we constructed a new full dimensional Hamiltonian including all 24 vibrational normal modes.

Besides the electronic ground and the two lowest core-excited states, we also include 19 valence-excited states in our calculations covering an approximate spectral range of 9 eV. The valence- and core-excited state properties were obtained by (fc-CVS)-EOM-CCSD/aug-cc-pVDZ calculations using Q-Chem, version 5, [265] providing a nearly consistent description of all electronic states. Both, the valence and core Hamiltonian, \mathbf{H}_v and \mathbf{H}_c , respectively, were then approximated by a linear vibronic coupling model. Due to the high density of states in the energy region > 6 eV (see Figure 4.13), the analytical values for the intra- and interstate coupling terms at the FC point were used to parameterise $S_5 - S_{19}$. The rest of the states, i.e. $S_0 - S_4$ and both core-excited states, X_1 and X_2 , were approximated by fitting a series of ab initio single point energy calculations along each normal mode where also on-diagonal bilinear intrastate couplings were included. Moreover, to account

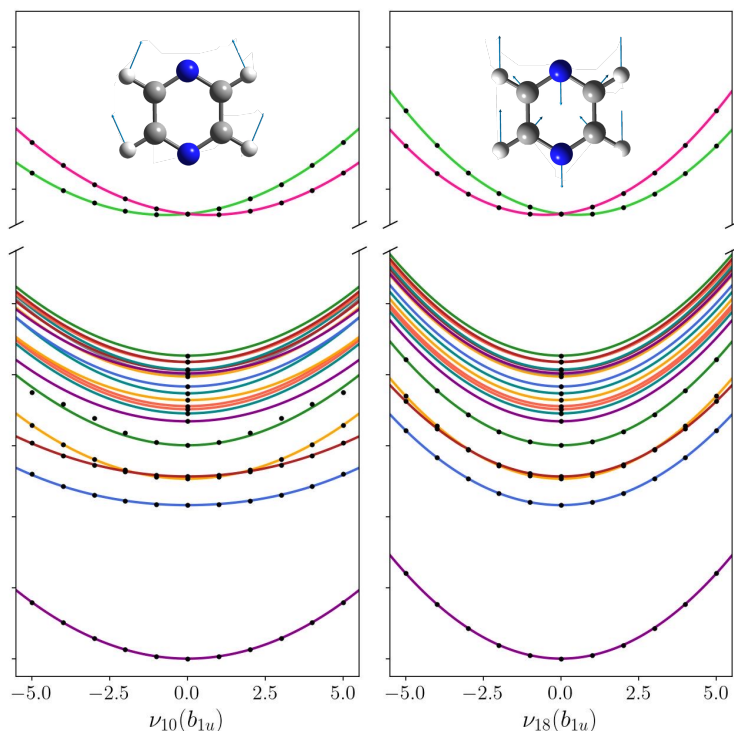


Figure 4.13: Cuts through the diabatic PES along the two vibrational normal modes, ν_{10} and ν_{18} , that mainly drive the symmetry distortion in the core-excited states. The calculated adiabatic energies are represented as black points. Reprinted with permission from [88]. © 2024 by the American Physical Society.

for anharmonicity the highest frequency mode ν_{24} was fitted by Morse potentials

$$W_x^{(\alpha\alpha)}(\mathbf{Q}) = D_0^{(\alpha)} \left\{ 1 - \exp\left(-a_i^{(\alpha)}(Q_i - Q_0)\right) \right\}^2 + E^{(\alpha)} \quad (4.21)$$

where $D_0^{(\alpha)}$ denotes the state-specific dissociation energy, $a_i^{(\alpha)}$ defines the curvature of the potential, and Q_0 is the equilibrium position. As before, the mean lifetime of the core-excited states is assumed to be 8 fs captured by an imaginary energy term in the core Hamiltonian \mathbf{H}_c .

The transition dipole moments were computed at the **FC** point where transition dipole moments below 0.01, accounting for less than 10 % of the strongest core-valence transition, were neglected. The excited state energies, symmetries and transition dipole moments are summarised in Table **4.7**. Notably, due to the different level of theory the order of the close lying states, S_2 and S_3 , is swapped compared to the model used in Section **4.3**. The linear coupling parameters, which mainly drive the core-excited state dynamics at short times, are collected in Table

Table 4.7: Vertical excitation energies $V^{(\alpha)}$ (in eV) and state symmetries along with transition dipole moments $\mu_{\beta\alpha}$ between state α and β obtained from **(fc-CVS)-EOM-CCSD**/aug-cc-pVDZ calculations at the **FC** point.

State	Symmetry	$V^{(\alpha)}$	transition	$\mu_{\beta\alpha}$
S_0	A_g	0.00	$X_2 \leftarrow S_0$	0.10
S_1	B_{3u}	4.32	$X_1 \leftarrow S_1$	0.06
S_2	B_{2u}	5.07		
S_3	A_u	5.13		
S_4	B_{2g}	6.01	$X_2 \leftarrow S_4$	0.06
S_5	A_g	6.68		
S_6	B_{1u}	6.91	$X_1 \leftarrow S_6$	0.02
S_7	B_{1g}	7.02		
S_8	B_{1g}	7.11		
S_9	B_{2u}	7.28		
S_{10}	B_{1u}	7.47		
S_{11}	B_{3u}	7.66		
S_{12}	B_{2u}	7.94		
S_{13}	B_{3g}	8.00		
S_{14}	A_g	8.04		
S_{15}	A_u	8.12		
S_{16}	B_{1u}	8.14	$X_1 \leftarrow S_{16}$	0.04
S_{17}	B_{1g}	8.35		
S_{18}	A_u	8.36	$X_1 \leftarrow S_{18}$	0.04
S_{19}	B_{2g}	8.53		
X_1	B_{2g}	402.30		
X_2	B_{3u}	402.30		

Table 4.8: Linear intra- and interstate coupling constants $\kappa_i^{(\alpha)}$ and $\lambda_i^{(\alpha\beta)}$, respectively, for the core-excited states.

	κ_3	κ_{11}	κ_{15}	κ_{20}
X_1	0.02738	-0.04034	0.05568	0.10433
X_2	0.02627	-0.04050	0.05619	0.10457
	λ_{10}	λ_{14}	λ_{18}	κ_{22}
(X_1, X_2)	0.08680	0.01326	0.09910	0.03014

4.8. A complete list of all parameters can further be found as an operator file in the Appendix.

Nuclear quantum dynamics simulations employing this 22-states-24-modes model Hamiltonian were performed using the ML-MCTDH method (see Section 3.1) within the Heidelberg MCTDH package, version 8.6. 251 The layer structure as well as the DVR, number of grid points and SPFs were adapted from the ML-2 model in 188 without modifications except for the number of electronic states. This multilayer ansatz for a full dimensional wavefunction including all vibrational normal modes was proven to offer a reasonable balance of quality and computational effort. The details are reprinted in Figure 4.14. The data output was written every 0.1 fs guaranteeing a sufficient time resolution and frequency span for subsequent Fourier transforms.

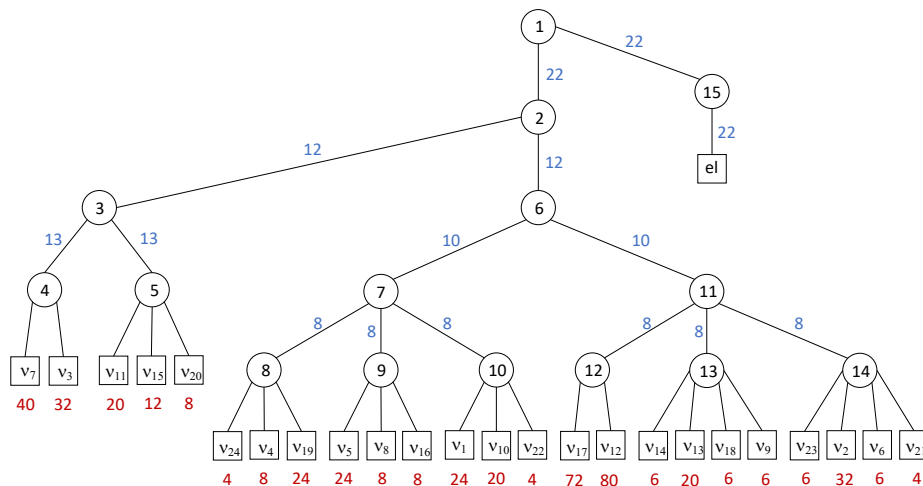


Figure 4.14: ML-MCTDH tree structure where the circles represent the node in the layer structure and the number of SPFs (blue) is given next to the link lines. The last layer contains the vibrational normal modes, where the red number N of primitive functions is used to represent the grid. Reprinted with permission from 88. © 2024 by the American Physical Society.

Symmetry Breaking Caused by Core-Excited State Dynamics

In order to define the resonant energy range for the X-ray radiation in the **RIXS** process, we first calculate the static X-ray absorption spectrum. For this purpose, we assumed a δ -like vertical excitation from the electronic ground state S_0 to the second core-excited state X_2 and compute the X-ray absorption spectrum via the Fourier transform of the autocorrelation function

$$I_{\text{XAS}}(\omega) \propto \text{Re} \int_0^{\infty} dt C(t) e^{i\omega t} \quad (4.22)$$

as outlined in Section **2.4.2**. Here, the autocorrelation function is given by the overlap $C(t) = \langle \Psi_c(0) | \Psi_c(t) \rangle$ of the evolving wavepacket $|\Psi_c(t)\rangle = e^{-i\hat{H}_c t} |\Psi_c(0)\rangle$ in the core-excited states induced by the vertical projection $|\Psi_c(0)\rangle = \mu_{X_2 \leftarrow S_0} |\Psi_0\rangle$ of the initial eigenwavefunction Ψ_0 . The resulting X-ray absorption spectrum is shown in Figure **4.15** along with the corresponding diabatic state population in Figure **4.16**.

As predicted by electronic dipole selection rules, only the bright X_2 state is initially excited. However, X_2 immediately depopulates into the dark X_1 state leading to an almost equally state population distribution within the short core-hole lifetime of 8 fs. This ultrafast population transfer can be attributed to the symmetry-allowed conical intersection existing between X_1 and X_2 , which is formed directly at the **FC** point (see Figure **4.13**). In particular, these dynamics, mainly driven by

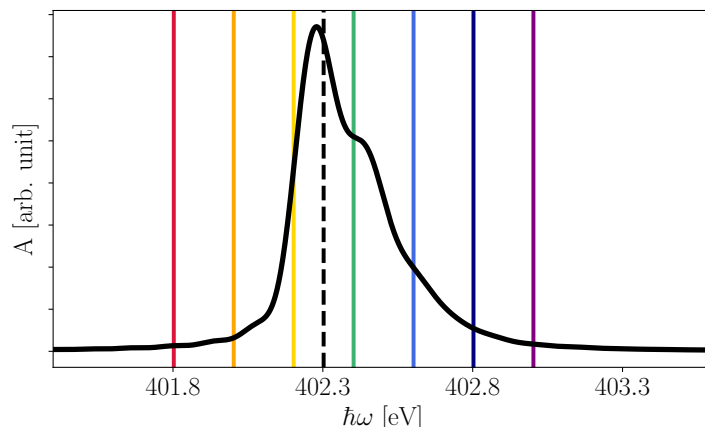


Figure 4.15: Static X-ray absorption spectrum at the nitrogen K-edge of pyrazine. The vertical lines indicate the incoming photon energies used to simulate the **RIXS** spectra where the dashed black line corresponds to the vertical excitation energy of X_2 . Reprinted with permission from **[88]**. © 2024 by the American Physical Society.

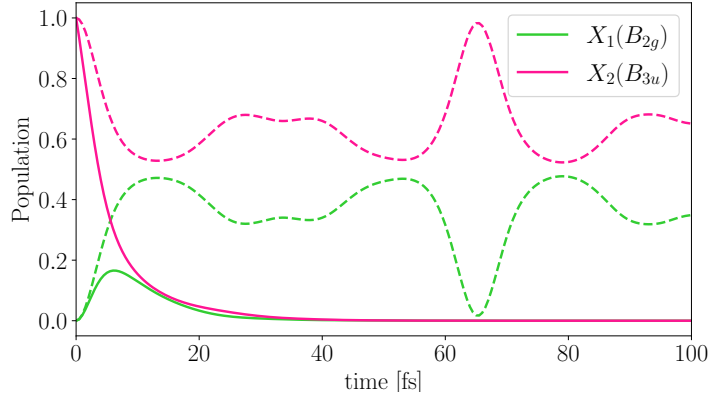


Figure 4.16: Diabatic core-excited state populations after an instantaneous, vertical excitation to X_2 at time $t = 0$ fs. The solid lines represent the total diabatic state population including the core-hole decay while the dashed lines correspond to the normalised state population. Reprinted with permission from [88]. © 2024 by the American Physical Society.

the two asymmetric normal modes ν_{10} and ν_{18} , result in symmetry breaking of the system and thus, in a final localisation of the core-hole, underscoring the potential significance of nuclear core-excited state dynamics even within very short timescales.

In order to understand how this behaviour is reflected in the final **RIXS** signal of pyrazine, we compute various spectra using the full time-dependent approach, introduced in Section 2.4.3. For this purpose, we assume a monochromatic **CW** excitation

$$\mathcal{E}(t) = \varepsilon_I e^{-i\omega_I t} \quad (4.23)$$

characterised by a well-defined incoming photon energy ω_I . The **RIXS** spectrum is then obtained by

$$I_{\text{RIXS}}(\omega_S; \omega_I) \propto \int_{-\infty}^{\infty} dt e^{-i\tilde{\omega}_S t - \Gamma_v t/2} \langle \tilde{\mathcal{R}}(\omega_I) | \tilde{\mathcal{R}}(\omega_I, t) \rangle \quad (4.24)$$

where $|\tilde{\mathcal{R}}(\omega_I)\rangle = \hat{\mu}_S |\mathcal{R}(\omega_I)\rangle$ is the down projection of the Raman wavefunction

$$|\mathcal{R}(\omega_I)\rangle = \int_0^{\infty} d\tau e^{-i(\hat{H}_c - i\frac{\Gamma_c}{2})\tau} \hat{\mu}_I e^{i\tilde{\omega}_I \tau} |\Psi_0\rangle. \quad (4.25)$$

with $\tilde{\omega}_I = \omega_I + \omega_0$ and ω_0 being the eigenenergy of Ψ_0 . In particular, the time interval $[0, T]$ that contributes to the Raman wavefunction, i.e. the actual propagation time

of the system in the intermediate core-excited states and thus the effective scattering duration in **RIXS**, can be controlled by adjusting the the incoming excitation energy ω_I . More precisely, the effective scattering duration is given by

$$T = \frac{1}{\sqrt{\Omega^2 + \Gamma_c^2}} \quad (4.26)$$

where Ω is the amount of detuning. Hence, while the scattering duration T is governed by the core-hole lifetime Γ_c for resonant excitations, the actual time the wavepacket spends in the intermediate core-excited states shortens the further away the excitation energy is from resonance. **[90,150]**

Figure **4.17** displays the **RIXS** spectrum of pyrazine using an incoming photon energy of 402.3 eV which is equal to the vertical excitation energy from the ground state to the excited state X_2 . The spectrum exhibits five prominent bands stemming from six electronic transitions, where the asymmetric shape of the elastic peak already suggests that the system undergoes nuclear displacements on the core-excited state manifold. Moreover, the elastic peak predominates in the spectrum, as expected from the transition dipole moments (see Table **4.7**) but without hiding any contributions from inelastic transition thanks to the large energy difference between

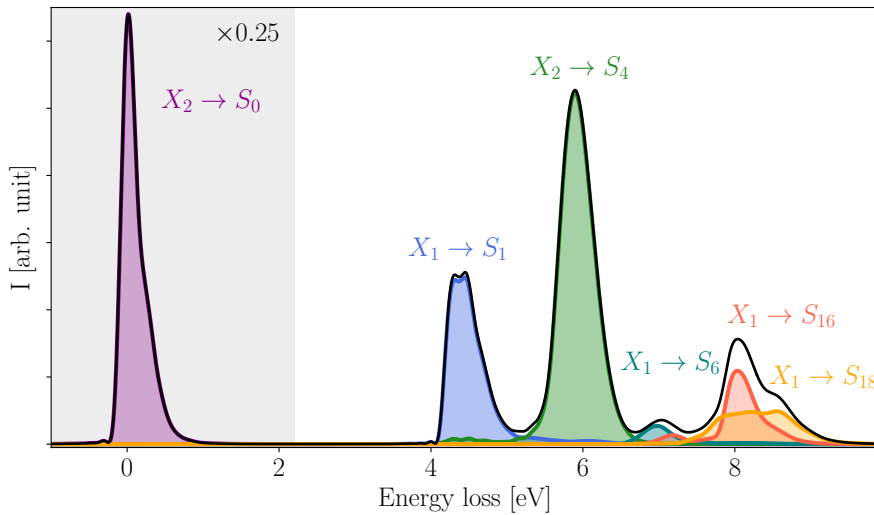


Figure 4.17: Simulated **RIXS** spectrum at the nitrogen K-edge of pyrazine. The contributions of the transitions to S_0 , S_1 , S_4 , S_6 , S_{16} and S_{18} to the total spectrum (solid black line) are highlighted in purple, blue, green, cyan, red and orange, respectively. The elastic peak (purple) is downscaled by 25 % for a better visualisation. Before performing the Fourier transformation in Eq. **(4.24)**, the window function $\cos^2\left(\frac{\pi t}{2T_0}\right)\theta(1 - |t|/T_0)$ was applied reducing Gibbs phenomena. Furthermore, a damping time $T_0 = 30$ fs was assumed to include broadening caused by dephasing mechanisms. Reprinted with permission from **[88]**. © 2024 by the American Physical Society.

the ground and valence-excited states. Beyond the elastic peak, the spectrum reveals five bands of inelastic electronic transitions located at approximately 4.5 eV, 6.0 eV, 7.0 eV, 8.1 eV and 8.6 eV where the latter two exhibit substantial spectral overlap, making them scarcely distinguishable in the overall spectrum. While the emission band located at 6.0 eV arises from the electronic $X_2 \rightarrow S_4$ transition, the remaining four bands originate from population of the optically dark X_1 state which can only be accessed through non-adiabatic population transfer from the bright X_2 state. Consequently, the symmetry breaking caused by ultrafast core-excited state dynamics facilitates four additional electronic transitions within this spectral range that would be otherwise forbidden by strictly adhering to the quadrupole selection rules for [RIXS](#).

The relation [\(4.26\)](#) between the amount of detuning Ω and the scattering duration T along with its influence on the [RIXS](#) signal of pyrazine is demonstrated in [Figure 4.18](#) showing various [RIXS](#) spectra for excitation energies ω_I ranging from 401.8 eV to 403 eV. Especially the four inelastic emission channels originating from

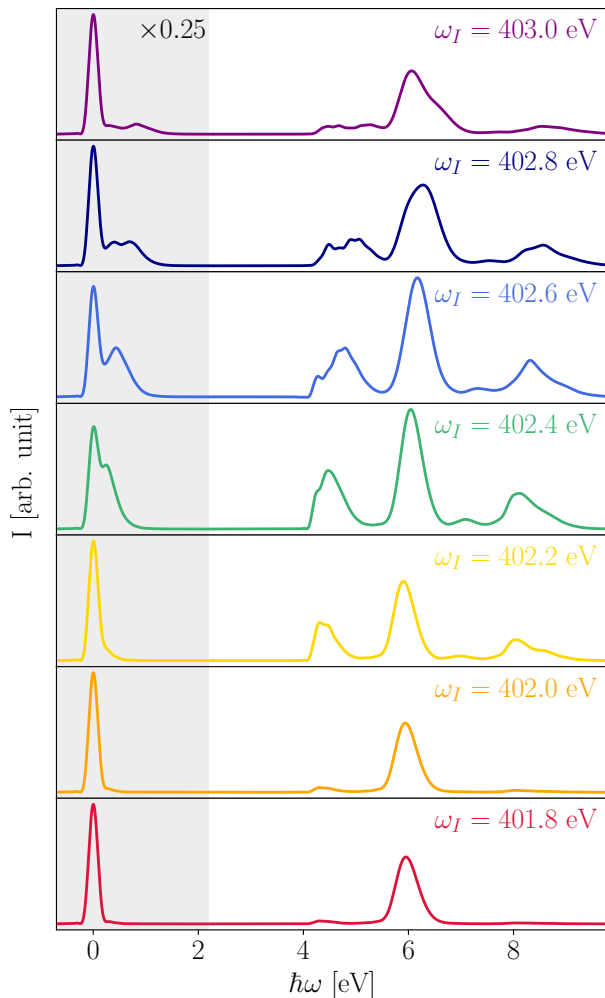


Figure 4.18: Dependence of the [RIXS](#) profile of pyrazine on the incident photon energy ω_I . All spectra are independently normalised to their respective elastic peak before rescaling the signals in the gray spectral region to 25%. The energies of the incident radiation used for these calculation are also highlighted in the static X-ray absorption spectrum shown in [Figure 4.15](#). Reprinted with permission from [\[88\]](#). © 2024 by the American Physical Society.

the dark X_1 state display a pronounced dependence on the incident photon energy. Specifically, when far from resonance, i.e. for incoming photon energies below ~ 402.0 eV, these bands almost disappear. Additionally, in this regime the elastic peak exhibits a distinct symmetric Lorentzian line shape, indicating a single transition. Both observations suggest that for large detuning, the effective scattering duration becomes exceedingly short, rendering negligible dynamical effects as the wavepacket in the core-excited states lacks sufficient time to evolve. Conversely, for excitation energies surpassing 402.0 eV, vibrational progressions become evident on the positive energy side of the elastic peak, and inelastic Raman transitions stemming from both core-excited states, X_1 and X_2 , are prominent. The shapes of these transitions vary with excitation energy, reflecting the nuclear dynamics within the core-excited states. In particular, for excitation energies surpassing the vertical excitation energy, each loss peak exhibits a rather broad and asymmetrical shape.

Spectral Distribution due to Finite Pulse Duration

In order to study the influence of the incident X-ray beam duration on the resolution of the **RIXS** spectra, we go beyond the monochromatic **CW** picture and assume a pulsed radiation field of the form

$$\mathcal{E}(t) = \mathcal{A}(t)e^{-i\omega_I(t-t_0)} \quad (4.27)$$

with a normalised Gaussian shaped pulse envelope function

$$\mathcal{A}(t) = \frac{1}{\sqrt{2\pi\sigma^2}} \exp\left(-\frac{(t-t_0)^2}{2\sigma^2}\right) \quad (4.28)$$

where t_0 denotes the pulse center and the standard deviation σ is linked to the temporal **fwhm** duration F_t through $F_t = 2\sqrt{2\ln 2}\sigma$. According to the derivation in Section **2.4.3**, the **RIXS** spectrum is then given by

$$I_{\text{RIXS}}(\tilde{\omega}_I) \propto \left(|\tilde{\mathcal{A}}|^2 \otimes \int_{-\infty}^{\infty} dt \exp(-i\tilde{\omega}_I t) \langle \tilde{\mathcal{R}}(\cdot) | \tilde{\mathcal{R}}(\cdot, t) \rangle \right) (\tilde{\omega}_I) \quad (4.29)$$

where a spectral broadening is caused by the convolution with the square of the absolute value of the Fourier transform $\tilde{\mathcal{A}}$ of the envelope function

$$|\tilde{\mathcal{A}}(\omega)|^2 = \exp(-\sigma^2\omega^2) \quad (4.30)$$

Moreover, due to the reciprocal connection between the temporal and spectral width, shorter pulses create spectrally broader wavepackets and vice versa, leading to different signatures of the RIXS signal. This is described by the term

$$\int_{-\infty}^{\infty} dt \exp(-i\tilde{\omega}st) \langle \tilde{\mathcal{R}}(\cdot) | \tilde{\mathcal{R}}(\cdot, t) \rangle \quad (4.31)$$

in (4.29) and can be considered independently from the general broadening of the signal described by the convolution with (4.30) although both aspects have the same origin.

Figure 4.19 illustrates both effects on the RIXS spectrum of pyrazine for different incoming X-ray pulses where the temporal duration was varied while keeping the carrier frequency ω_I fixed at 402.3 eV. Here, the signals shown in blue are evaluated according to (4.31) while the orange shadowed areas represent the total spectrum as obtained from (4.29).

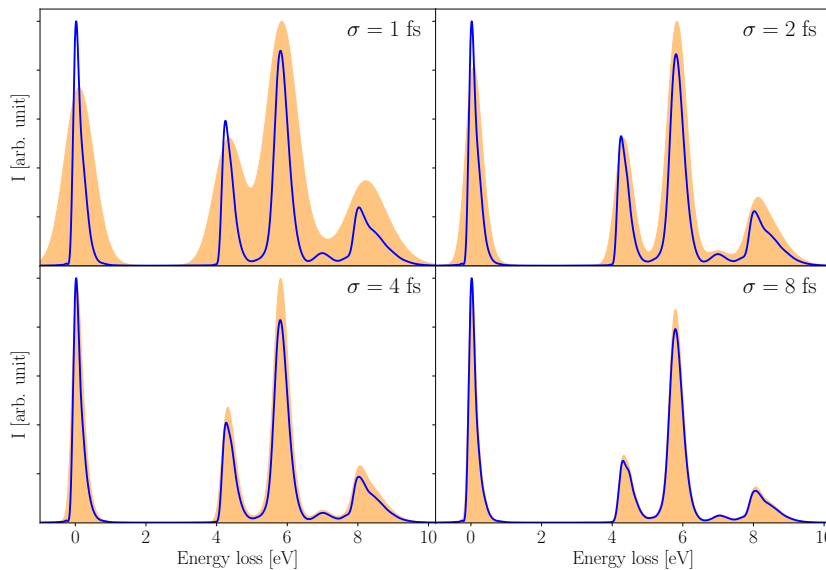


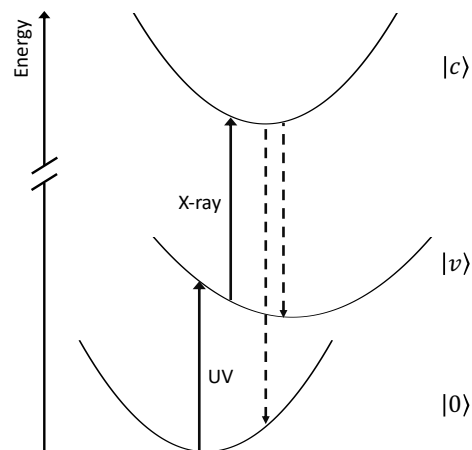
Figure 4.19: Influence of the duration of incident radiation field on the RIXS spectrum of pyrazine. Each panel displays the total spectrum according to (4.29) (orange shadow) and contributions stemming from (4.31). For each case, a Gaussian X-ray pulse with temporal standard deviations varying from 1 fs to 8 fs while keeping the carrier frequency fixed at 402.3 eV. The same window function as in Figure 4.17 was applied before performing the Fourier transformation. Reprinted with permission from [88]. © 2024 by the American Physical Society.

In general, the various **RIXS** spectra are in good agreement. However, the relative intensities are subject to variation based on the duration of the X-ray pulse. Particularly the emission channels originating from the dark X_1 state at approximately 6.0 eV, 7.0 eV, and 8.4 eV tend to be more prominent with shorter pulse durations. Additionally, the spectral line shapes undergo slight alterations depending on the field distribution. This is particularly evident in the $X_1 \rightarrow S_1$ emission band, where distinct progressions become more pronounced with longer pulse durations. While for pulses lasting half the core-hole lifetime or longer, broadening stemming from the spectral field distribution is less significant compared to other dephasing effects, shorter pulses lead to a more pronounced broadening of the signal, as indicated by the orange shadow. Considering this effect is not only important for an optimal spectral and temporal resolution, but also significantly impact the detuning capability. Especially for very short pulses, the finer details of the vibronic structure within the emission bands are nearly entirely suppressed, complicating the analysis of core-excited state dynamics when detuning effectiveness as a control mechanism is also diminished.

4.5 Femtosecond Resonant Inelastic X-ray Scattering

Within the third and final project of this thesis, we extended the full time-dependent description of steady-state **RIXS** to calculate time-resolved **RIXS** spectra at the nitrogen K-edge of pyrazine. This thorough dynamical approach is indispensable for accurately representing the dynamics of valence-excited states induced by **UV** irradiation, subsequently detected via **RIXS** as a probing technique where nuclear motion effects arising from the dynamics of intermediate core-excited states can significantly

Figure 4.20: Schematic representation of the transient **RIXS** process considered within this section. Initially, an **UV** pump pulse promotes the system from the equilibrium ground state $|0\rangle$ into the valence-excited state manifold $|v\rangle$. The induced dynamics is then **RIXS**-probed by further exciting the system into the intermediate core-excited state manifold $|c\rangle$ from where it continuously decays back to the ground $|0\rangle$ or energetically higher lying valence-excited states $|v\rangle$.



influence the resulting spectra as demonstrated in Section 4.4. In particular, our approach transcends the conventional quasi-static approach typically employed when simulating transient RIXS spectra in molecular systems. [103, 119–121] In this framework, pump-induced states are treated as isolated quasi-static snapshots, for which steady-state RIXS spectra are simulated. While this simplified method may aid in discerning contributions from distinct chemical species, it inadequately captures the real-time evolution of the wavepacket, which is heavily reliant on the underlying potential energy surfaces. Particularly in molecular systems like pyrazine, where excited-state dynamics are predominantly governed by physical alterations rather than chemical reactions involving bond dissociation and formation, the approximate quasi-static frequency domain approach is insufficient for accurately simulating transient RIXS spectra.

Computational Details and Model Parameters

In order to perform *in silico* fs-RIXS experiments at the nitrogen K-edge of pyrazine, we used a hybrid model combining elements from both Hamiltonian frameworks introduced in Section 4.3 and Section 4.4. For modeling the dynamics of pump-induced valence-excited states, we opted for the vibronic coupling model outlined in Section 4.3, specifically constructed for simulating UV-induced valence-excited state dynamics. [228] Thus, we used this model to parameterise the ground and four lowest valence-excited states $S_0 - S_4$ with detailed parameters provided in [228] or accessible in the Appendix. In order to parameterise the higher-lying valence-excited states $S_4 - S_{19}$, only reached by the scattering event rather than the initial UV pumping, we employed the RIXS model Hamiltonian detailed in Section 4.4. A global energy shift of -0.6 eV was applied to maintain the energy separation between S_4 and S_5 . Furthermore, we extended the core Hamiltonian \mathbf{H}_c of Section 4.4 by two core-

Table 4.9: Vertical excitation energies $E^{(\alpha)}$ as well as linear intra- and interstate coupling constants $\kappa_i^{(\alpha)}$ and $\lambda_i^{(\alpha\beta)}$, respectively, for the core-excited states contained in \mathbf{H}_{c2} . All values are in eV.

	Symmetry		E	
X_3	B_{1g}		405.05	
X_4	A_u		405.06	
	κ_3	κ_{11}	κ_{15}	κ_{20}
X_3	0.1231	-0.0787	-0.1236	-0.2731
X_4	0.1230	-0.0787	-0.1240	-0.2754
	λ_{10}	λ_{14}	λ_{18}	λ_{22}
(X_3, X_4)	0.0998	0.1087	0.0213	0.0224

Table 4.10: Transition dipole moments $\mu_{\alpha\beta}$ between two states $|\alpha\rangle$ and $|\beta\rangle$. The transition dipole moments to valence- and core-excited states are obtained from EOM-CCSD and fc-CVS-EOM-CCSD calculations, respectively.

State transition	$\mu_{\alpha\beta}$
$S_3 \leftarrow S_0$	0.25
$S_1 \leftarrow S_0$	0.82
$X_2 \leftarrow S_0$	0.10
$X_1 \leftarrow S_1$	0.06
$X_3 \leftarrow S_2$	0.06
$X_3 \leftarrow S_3$	0.03
$X_2 \leftarrow S_4$	0.04
$X_1 \leftarrow S_6$	0.02
$X_4 \leftarrow S_7$	0.04
$X_3 \leftarrow S_{12}$	0.05
$X_1 \leftarrow S_{16}$	0.04
$X_1 \leftarrow S_{18}$	0.04

excited states, X_3 and X_4 . While X_3 is directly accessible via X-ray excitation from S_2 and S_3 (as discussed in Section 4.3), X_4 serves as the energetically degenerate counterpart vibronically coupled through vibrational normal modes of symmetry B_{1u} . Parameters for both, X_3 and X_4 , were derived from ab-initio fc-CVS-EOM-CCSD/aug-cc-pVDZ single point energies, matching the level of theory used for X_1 and X_2 using a linear vibronic coupling approach including quadratic intrastate coupling constants. Similar to X_1 and X_2 , the harmonic expression of the diabatic potentials for ν_{24} were substituted by state-specific Morse potentials. Moreover, ν_1 is described by the quartic expression

$$W^{(\alpha\alpha)}(Q_i) = E^{(\alpha)} + \frac{1}{2} \left(\omega_i + \gamma_i^{(\alpha)} + \varepsilon_i^{(\alpha)} Q_i^2 \right) Q_i^2 \quad (4.32)$$

where $\varepsilon_i^{(\alpha)}$ denotes the quartic expansion coefficient. The linear parameter values for X_3 and X_4 as well as the most significant computed transition dipole moments are reported in Table 4.9 and Table 4.10 while an operator file including all parameters is deposited in the Appendix.

Transient X-ray Absorption

To determine appropriate excitation energies for observing the UV-induced dynamics of pyrazine using RIXS probing, we firstly recalculated the fs-XANES spectra of Section 4.3 utilising the full-dimensional Hamiltonian employed within this project.

Herein, we employed δ -pulses for both the pump and probe steps

$$\mathcal{E}(t) = \delta_{\text{pu}}(t) + \delta_{\text{pr}}(t - \tau) \quad (4.33)$$

computing the transient absorption spectra via the Fourier transform of the dipole-dipole correlation

$$I_{\text{TRXAS}}(\omega, \tau) \propto \text{Re} \int_0^{\infty} dt \langle \Psi_v(\tau) | e^{i\hat{H}_v(t-\tau)} \hat{\mu} e^{-i\hat{H}_c(t-\tau)} \hat{\mu} | \Psi_v(\tau) \rangle e^{i\omega t - \Gamma_c t/2} \quad (4.34)$$

The resulting diabatic state population dynamics, along with a three-dimensional collection of differential absorption spectra, are presented in Figure 4.21. The overall state population demonstrates remarkable consistency with our previous calculations in Section 4.3 showing the rapid population decay from S_3 to both S_2 and S_1 within the first 50 fs followed by the oscillatory population dynamics between S_1 and S_2 .

While the transient X-ray absorption spectra exhibit an overall good alignment with our prior simulations, two notable distinctions arise compared to Figure 4.10. Firstly, an overall energy shift of the absorption bands is observed, attributable to differences in the level of theory employed in the underlying electronic structure calculations utilised in Section 4.3 and the current study. However, this discrepancy

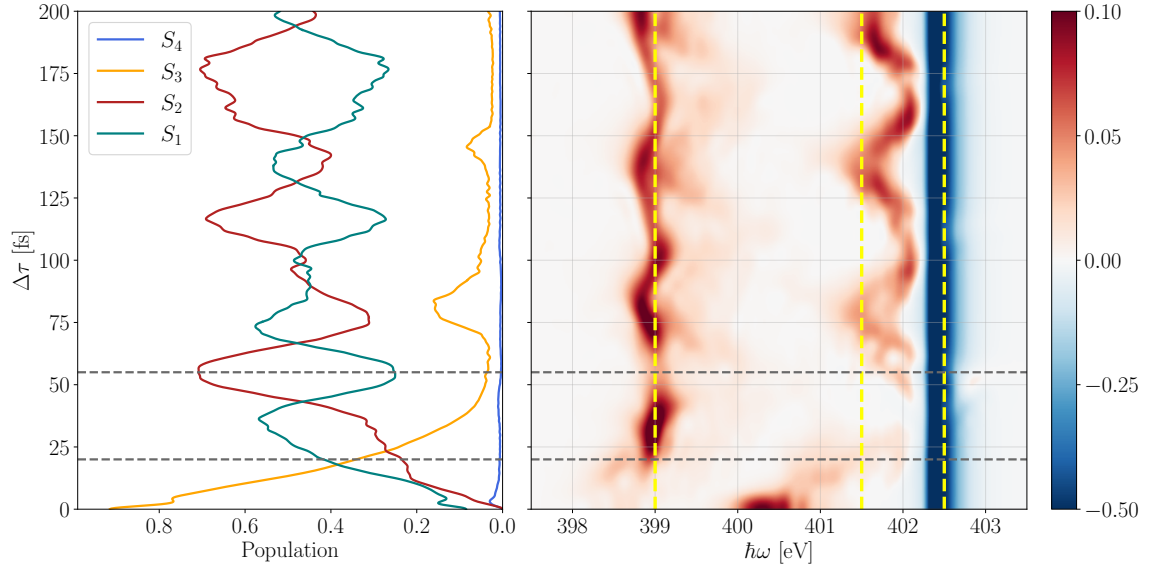


Figure 4.21: Left: diabatic state population after instantaneous, vertical excitation to S_3 and S_1 at time $t = 0$ fs. Right: three-dimensional collection of differential X-ray absorption spectra for time delays between 0 fs and 200 fs with a stepsize of 5 fs. The horizontal (grey) and vertical (yellow) lines indicate the time delays and excitation energies used for subsequent transient RIXS calculations, respectively.

can be easily rectified through a global energy adjustment of all core-excited states. Secondly, a greater modulation of the excited state absorption bands is observed, notably pronounced in the band approximately at 401.8 eV which originates from transitions corresponding to $X_3 \leftarrow S_3$ and $X_3 \leftarrow S_2$. This effect arises due to the contrasting dimensionality of the model Hamiltonian. In our previous computations, we employed a reduced-dimensional model encompassing solely the nine most dominant vibrational normal modes. Conversely, the present study adopts a comprehensive 24-dimensional model, resulting in a more delocalised wavepacket across the valence-excited state manifold. Additionally, due to the reduced dimensionality, non-adiabatic transitions between the core-excited states were omitted as stated in Section 4.3. To ascertain whether the broader, asymmetrical line shapes and increased modulation stem from non-adiabatic coupling in the core-excited states or from wavepacket delocalisation in the valence-excited states, we also calculated transient X-ray absorption spectra using the full dimensional model but without the interstate coupling terms $\lambda_i^{(\alpha\beta)}$. However, a comparison between the fs-XANES spectra with (Figure 4.21) and without (Figure 4.22) interstate non-adiabatic coupling clearly reveals that ultrafast non-adiabatic core-excited state dynamics exert minimal influence on the resulting transient X-ray absorption spectra of pyrazine, contrasting with the significant impact observed on the RIXS spectra in Section 4.4.

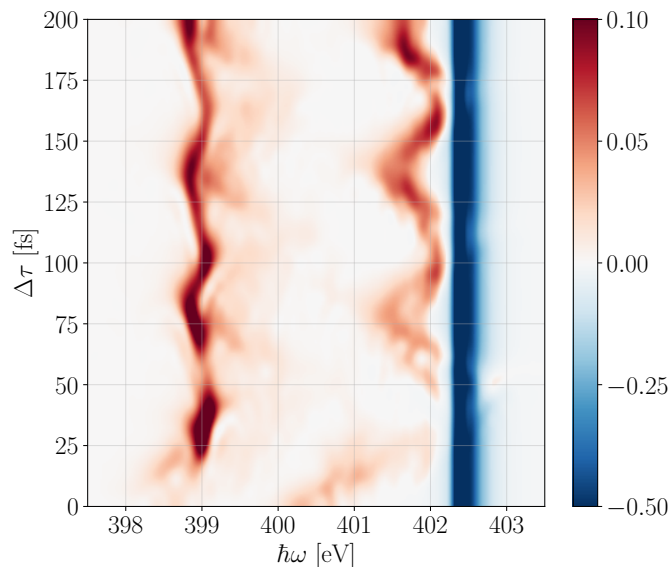


Figure 4.22: Three-dimensional collection of differential absorption spectra for time delays between 0 fs and 200 fs with a stepsize of 5 fs using the full dimensional Hamiltonian but without interstate coupling terms $\lambda_i^{(\alpha\beta)}$.

In particular, the different shape and time evolution of the excited state absorption bands can be hence attributed to the artificial localisation of the wavepacket within the reduced dimensional model, underscoring the critical importance of judiciously selecting the appropriate model Hamiltonian.

Based on the time-dependent differential absorption map depicted in Figure 4.21, excitation energies of 399.0 eV and 401.5 eV have been designated for the subsequent fs-RIXS simulations, facilitating the exploration of the S_1 and S_2/S_3 dynamics, respectively. The latter X-ray excitation energy is selected slightly below the centroid of the fluctuating absorption band, thereby circumventing contributions from ground-state bleaching. Moreover, additional fs-RIXS calculations were conducted for an excitation energy of 402.5 eV to elucidate the behavior in the overlap region between the bleach signal and the closely situated excited state absorption.

Transient Resonant Inelastic X-ray Scattering

In order to simulate the fs-RIXS process of pyrazine, we assume a total electric field

$$\mathcal{E}(t, \tau) = \delta_{\text{pu}}(t) + \mathcal{E}_{\text{pr}}(t, \tau) \quad (4.35)$$

comprising a δ -like pump pulse at time $t = 0$ fs and a Gaussian-shaped X-ray probe pulse

$$\mathcal{E}_{\text{pr}}(t, \tau) = \mathcal{A}(t - \tau) \cos(\omega_I(t - \tau)) \quad (4.36)$$

$$= \frac{1}{\sqrt{2\pi\sigma^2}} \exp\left(-\frac{(t - \tau)^2}{2\sigma^2}\right) \cos(\omega_I(t - \tau)) \quad (4.37)$$

centered at time $t = \tau$. The transient RIXS spectra of pyrazine are then obtained by

$$I_{\text{RIXS}}(\omega_S, \omega_I, \tau) \propto \left(|\tilde{\mathcal{A}}|^2 \otimes \int_{-\infty}^{\infty} dt \exp(-i\tilde{\omega}_S t) \langle \tilde{\mathcal{R}}(\cdot; \tau) | \tilde{\mathcal{R}}(\cdot, t, \tau) \rangle \right) (\tilde{\omega}_I) \quad (4.38)$$

wherein the eventual evolving wavepacket $|\tilde{\mathcal{R}}(\omega, t, \tau)\rangle = e^{-i\hat{H}_v t} |\tilde{\mathcal{R}}(\omega, \tau)\rangle$ is governed by the projected Raman wavefunction generated by the X-ray probe. In particular, the temporal duration of the probe pulse must be carefully balanced; it should be sufficiently prolonged to meet the narrow-band excitation criteria of RIXS, but also short enough to afford adequate time resolution for probing the underlying dynamics. From our previous investigations, we discern that the dynamics initiated by the optical pump pulse is primarily driven by the interstate coupling parameters between

the state pairs S_1/S_3 and S_1/S_2 , each exhibiting oscillation periods of 19 fs and 21 fs, respectively. Consequently, to track this ultrafast dynamics without compromising pertinent information due to spectral broadening induced by broadband excitation pulses, we opt for a Gaussian X-ray probe pulse with a temporal **FWHM** duration of approximately 8 fs.

Figure 4.23 presents **fs-RIXS** spectra for carrier frequencies ω_I of 399.0 eV and 401.5 eV, spanning time-delays $\Delta\tau$ from 5 fs to 200 fs in a three-dimensional collection, along with a single transient **RIXS** spectrum at $\Delta\tau = 105$ fs. Additionally, a two-dimensional representation of the time evolution of the **fs-RIXS** spectrum in 10 fs steps for both excitation energies are shown in Figure 4.24 and Figure 4.25.

At an excitation energy of 399.0 eV, **RIXS** probing only induces $X_1 \leftarrow S_1$ transitions, resulting in turn in four dipole-allowed scattering transitions to the valence-excited states S_1 , S_6 , S_{16} , and S_{18} (see Table 4.10). However, as previously elaborated upon in Section 4.4, the two lowest core-excited states are vibronically coupled by vibrational normal modes of symmetry B_{1u} , leading to ultrafast symmetry breaking within the core-excited states. This, in turn, give rise to two additional

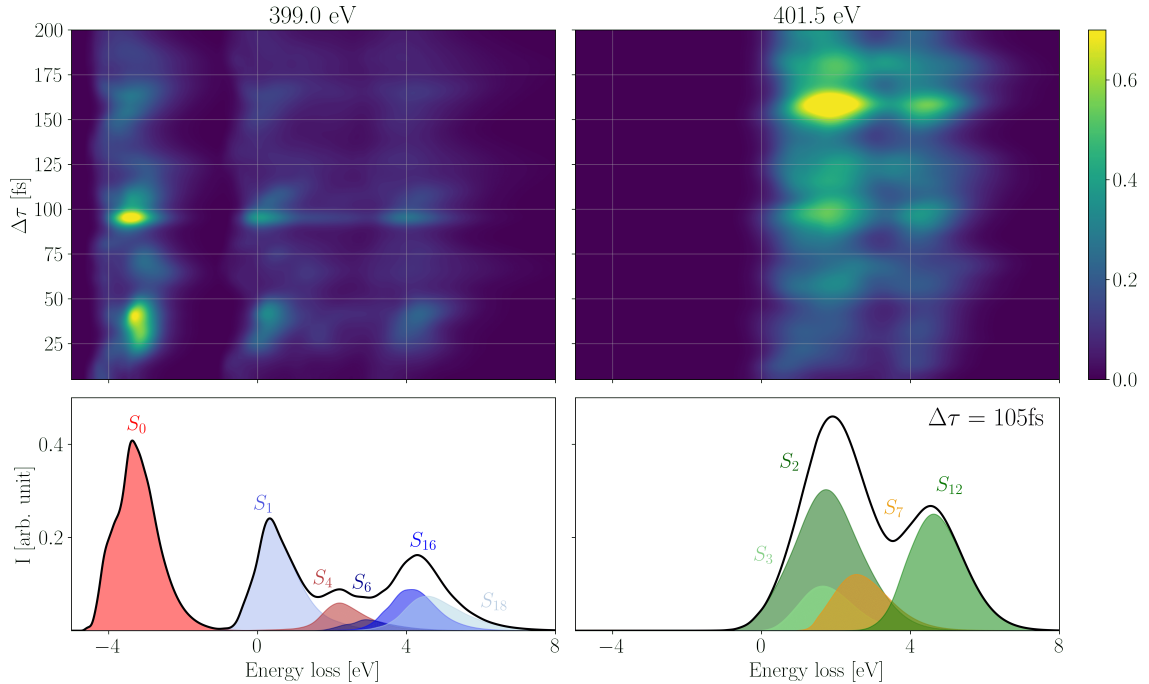


Figure 4.23: Top: collection of simulated **fs-RIXS** spectra for time delays between 5 fs and 200 fs with a stepsize of 5 fs using carrier frequencies of 399.0 eV (left) and 401.5 eV (right). Bottom: transient **RIXS** spectrum at time delay $\Delta\tau = 105$ fs for both excitation energies. Transitions stemming from X_1 , X_2 , X_3 and X_4 are highlighted in blue, red, green and yellow, respectively. The final electronic state for each transition is annotated in the plot.

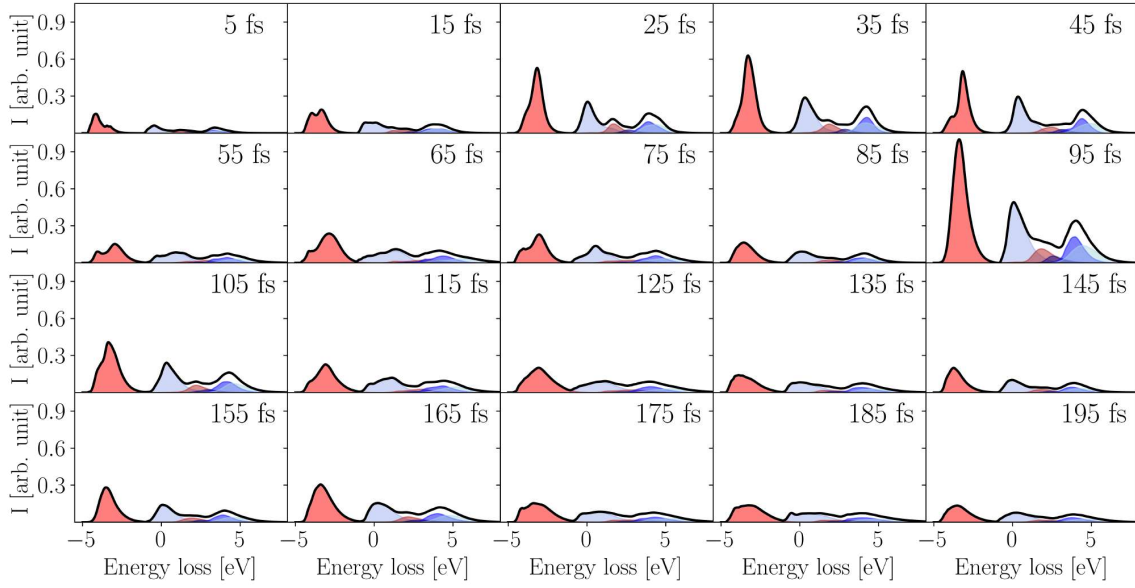


Figure 4.24: Time evolution of the **RIXS** spectrum between 5 fs and 195 fs with a stepsize of 10 fs steps using an excitation energy of $\omega_I = 399.0$ fs. Transitions stemming from X_1 and X_2 are highlighted in blue and red, respectively. The corresponding final states can be derived from the labelling in Figure **4.23**.

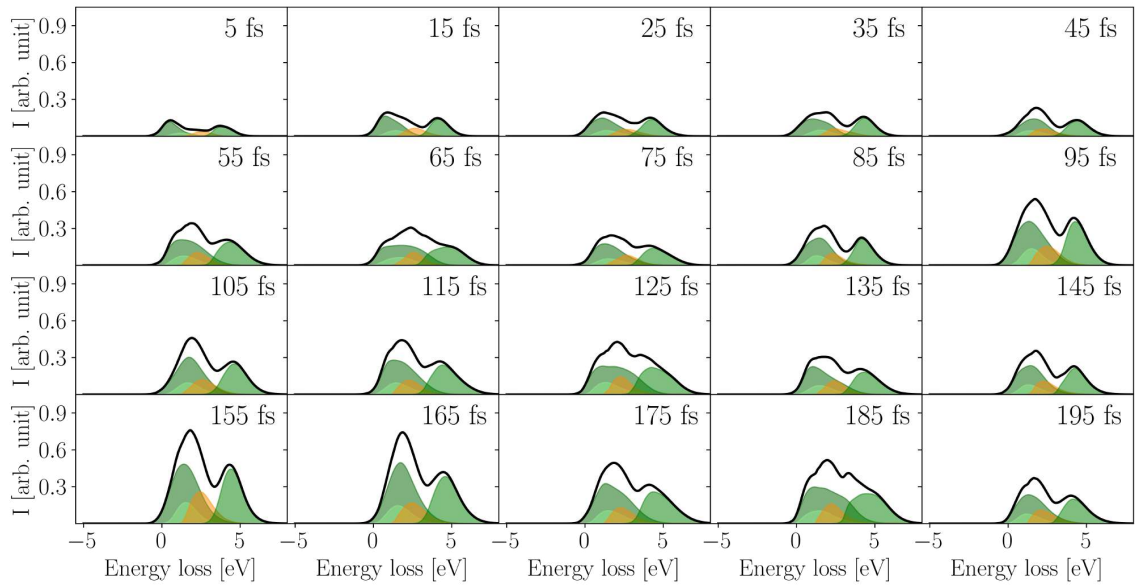


Figure 4.25: Time evolution of the **RIXS** spectrum between 5 fs and 195 fs with a stepsize of 10 fs steps using an excitation energy of $\omega_I = 401.5$ fs. Transitions stemming from X_3 and X_4 are highlighted in green and yellow, respectively. The corresponding final states can be derived from the labelling in Figure **4.23**.

scattering channels originating from X_2 : a pronounced anti-Stokes signal at -3.8 eV and a weaker transition band at 2.0 eV. Furthermore, the variations in the overall peak intensity reflect the diabatic state population of S_1 .

The transient **RIXS** spectra observed at 401.5 eV encompass $X_3 \leftarrow S_2$ as well as $X_3 \leftarrow S_3$ transitions. However, the latter transitions make a substantial contribution only within the initial 20-30 fs due to the rapid depopulation of S_3 . Generally, these spectra reveal two dominant, broad spectral bands located approximately at 2 eV and 5 eV, with the lower band actually originating from three energetically overlapping transitions, as depicted in the bottom right panel of Figure 4.23. Although ultrafast symmetry distortion due to vibronic coupling of X_3 and X_4 is also observed, the related spectroscopic effects cannot be distinctly discerned in the final signal due to the overlapping transition bands. Moreover, the transient **RIXS** spectra at 401.5 eV do not manifest anti-Stokes signals, indicating a different symmetry of the involved core-excited states reached by the 401.5 eV photon energy compared to those at 399.0 eV. Furthermore, an increase in the overall signal strength is noted for time delays $\Delta\tau$ beyond 100 fs, attributable to the considerably lower transition dipole moment $\mu_{X_3 \leftarrow S_3}$ compared to $\mu_{X_3 \leftarrow S_2}$, resulting in less probable transitions at very early times. Additionally, the pronounced modulation of this absorption band yielding a significant detuning effect for time delays ranging between 20 fs and 80 fs.

Figure 4.26 presents a three-dimensional map of transient **RIXS** spectra for an X-ray probing frequency of 402.5 eV, while a two-dimensional representation is depicted in Figure 4.27. Notably, the most prominent overlap between the bleach and excited state **RIXS** signal occurs between 30 fs and 60 fs. Additionally, less significant overlap signals are discernible around 110 fs and 175 fs. However, in each

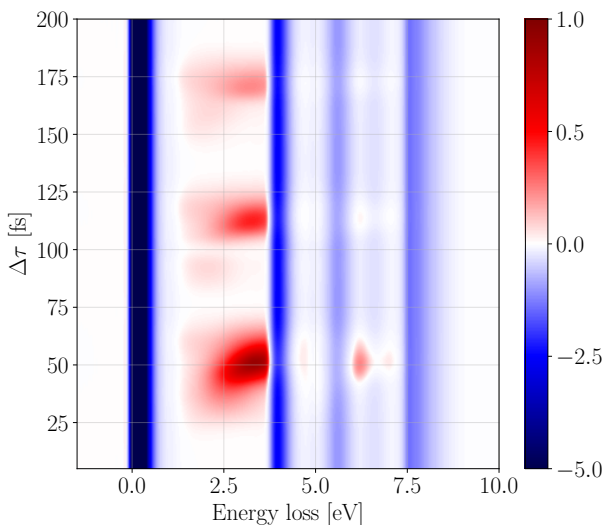


Figure 4.26: Three-dimensional collection of calculated difference **RIXS** spectra for time delays $\Delta\tau$ between 5 fs and 200 fs with a stepsize of 5 fs using an excitation energies ω_I of 402.5 eV. The corresponding two-dimensional representation is shown in Figure 4.27.

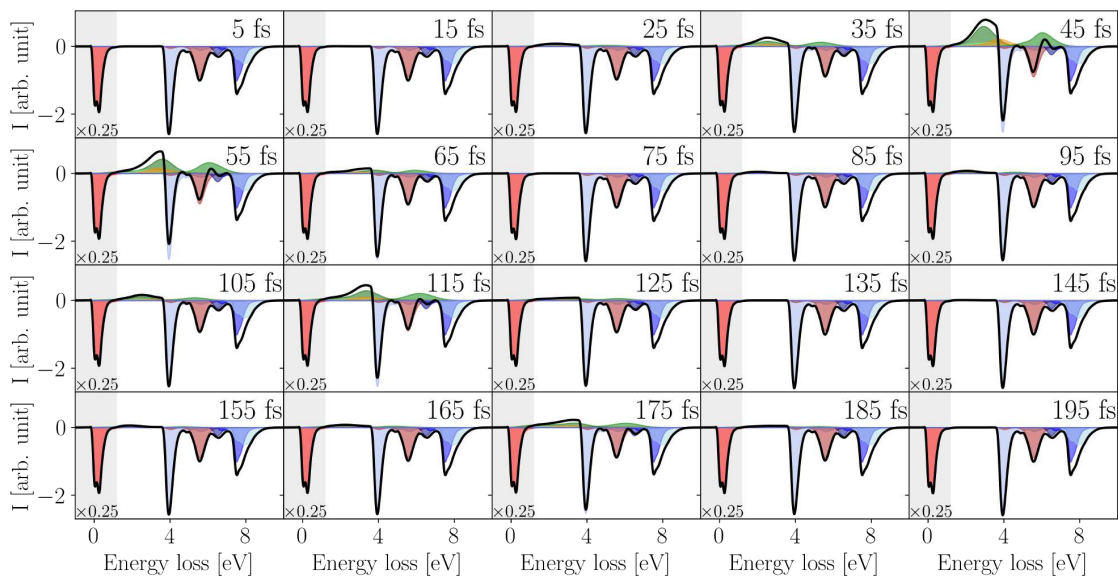


Figure 4.27: Time evolution of the **RIXS** spectrum between 5 fs and 195 fs with a stepsize of 10 fs steps using an excitation energy of $\omega_I = 402.5$ eV. Transitions stemming from X_1 , X_2 , X_3 and X_4 are highlighted in blue, red, green and yellow, respectively. The corresponding final states can be derived from the labelling in Figure 4.23. The strong negative bleach signal stemming from the $X_2 \rightarrow S_0$ transition was rescaled by 25 % for a better visualisation.

instance, the excited state features are notably weaker compared to the bleach signal, rendering the extraction of excited state mechanisms nearly impractical using this excitation energy. Moreover, the ground state bleach signal encompasses five dominant emission bands originating from six X_1/X_2 transitions. The pattern can be analogously explained to the one reached with 399.0 eV probing energy.

So far, we have maintained a fixed X-ray excitation energy to capture a temporal scan of the transient **RIXS** signal. A different view can be obtained by varying the excitation energy ω_I of the X-ray probe pulse and the energy loss $\tilde{\omega}_S$ to the molecule at a fixed time delay. Figure 4.28 illustrates these **RIXS** maps alongside the corresponding differential **XANES** spectra at time delays $\Delta\tau = 20$ fs and $\Delta\tau = 55$ fs. Both the transient absorption and the **RIXS** spectra exhibit positive features stemming from valence-excited state transitions and negative bleach signals related to ground-state transitions of the non-excited system. The bleach signal remains constant for both time delays, as there is no radiationless relaxation mechanism from excited states back to the ground state on the femtosecond timescale. Moreover, as predicted from Table 4.10 X-ray transitions involving the ground state S_0 are considerably more likely compared to valence-excited state transitions, resulting in a dominant

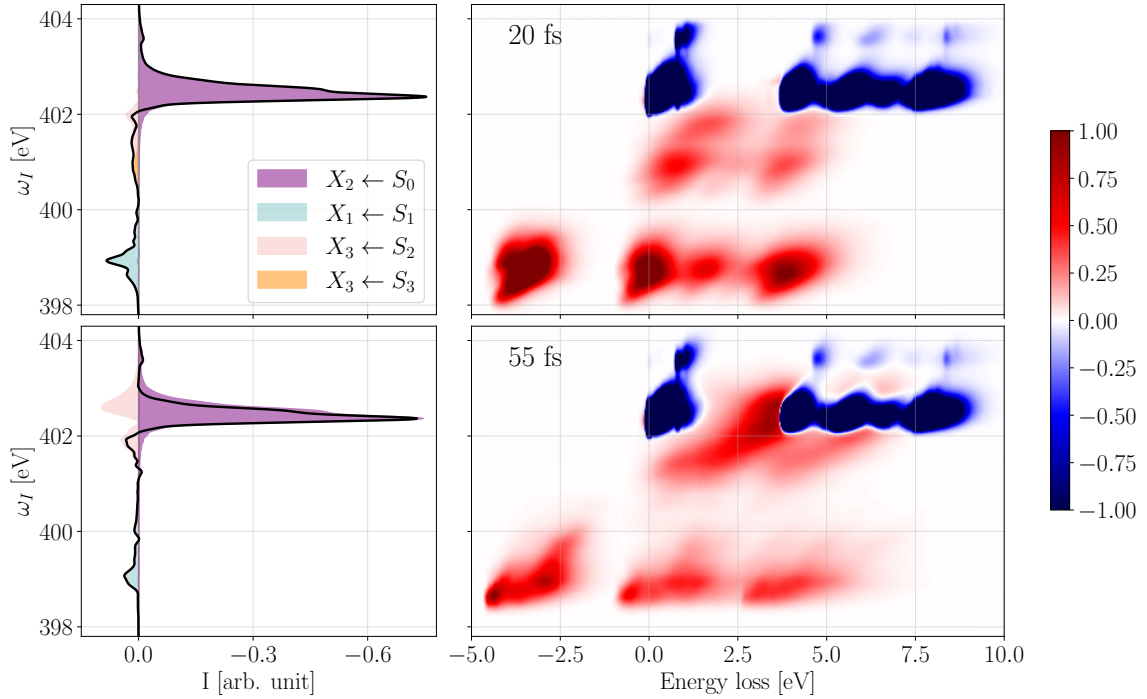


Figure 4.28: Transient **XANES** (left) and corresponding **RIXS** spectra (right) for time delays $\Delta\tau = 20$ fs (top) and $\Delta\tau = 55$ fs (bottom). The transient **RIXS** spectra are calculated for excitation energies ω_I ranging from 397.0 eV to 404.9 eV with a stepsize of 0.1 eV.

bleach signal at approximately 402.5 eV. The overall shape of the excited-state transition bands is broad and asymmetrical for both probing techniques, attributable to the evolution of the nuclear wavepacket of the **UV** pumped system. While the transient X-ray absorption spectra are particularly sensitive to the **UV**-induced dynamics, the **fs-RIXS** maps also contain dynamical features from the intermediate core-excited states as well as from the final ground and valence-excited states.

For both time delays shown in Figure 4.28, the RIXS bleach signal comprises five transition bands (stemming from six core-to-valence state transitions). The higher four bands are energetically separated from the lowest transition band by approximately 3.9 eV, 5.3 eV, 6.5 eV, and 7.5 eV. As the lowest transition band of the bleach signal is located just above 0 eV, it can be unequivocally assigned to the electronic ground state. Moreover, for a 20 fs time delay, the energy-level separation pattern of the bleach signal repeats in the excited-state signals at 399.0 eV, shifted by -3.9 eV, suggesting that the corresponding initial ground and valence-excited states address the same core-excited state pair, eventually leading to similar emission bands. However, the progressive valence-excited state dynamics after 55 fs blur the recurrences, making a direct assignment without additional analysis challenging.

The spectral proximity of the **RIXS** band around 401.5 eV obscures parts of the time-dependent signal. Particularly at 55 fs, the dominant time-independent bleach signal overlaps with the stronger part of the excited-state signal. At 20 fs time delay, the two signals do not appreciably overlap before population transfer to S_2 shifts the resonance - and hence, the **RIXS** signal - to higher energy. As discussed earlier, the absence of energy-gain features at 401.5 eV clearly indicates X-ray transitions to another pair of core-excited states.

In summary, time-resolved **RIXS** emerges as a reliable technique for investigating the rapid photophysical processes of pyrazine. It enhances the capabilities of other ultrafast X-ray spectroscopic methods like **fs-XANES** providing deeper insights into dynamical aspects by revealing symmetry distortions arising from non-adiabatic transitions within core-excited states. Moreover, it offers understanding into higher-energy valence excited states, which may be inaccessible in time-resolved **XAS** due to symmetry limitations or weak transition dipole moments.

Chapter 5

Conclusion & Outlook

Within this thesis, we investigated the manifestations of non-adiabatic nuclear dynamics as well as the bandwidth/duration of pulsed laser sources in [fs-XANES](#), [RIXS](#), and [fs-RIXS](#) spectroscopy at the nitrogen K-edge of pyrazine. For this purpose, we derived the spectral properties from full time-dependent nuclear quantum dynamics simulations within the [MCTDH](#) framework, including all dynamical dimensions.

Our findings indicate that while neglecting core-excited state dynamics still captures the primary features in [fs-XANES](#), it lacks finer vibronic substructure. However, non-adiabatic core-excited state dynamics are indispensable for accurately describing the [RIXS](#) signal, which can be significantly influenced by ultrafast core-excited state dynamics, including symmetry distortion and, associated therewith, alteration of dipole selection rules. Going one step further, a fully time-dependent framework capable of describing non-adiabatic phenomena is essential to accurately capture the interplay between population transfers within the valence-excited state manifold and the symmetry-breaking nuclear motions during X-ray interrogation in the context of [fs-RIXS](#).

Directly comparing these three nonlinear X-ray spectroscopy techniques reveals how different aspects of a molecular system can be elucidated within the same spectral range. We observed a substantial influence of [UV](#)-induced valence-excited state population dynamics on final [fs-XANES](#) spectra, attributable to radiationless transitions through conical intersections, with less impact from dynamical phenomena within the core-excited states. In contrast, a complete description of [RIXS](#) spectra necessitates inclusion of ultrafast non-adiabatic core-excited state dynamics, validated by the detuning dependence of the [RIXS](#) signal which serves as an effective control mechanism for ultrafast dynamical processes in [RIXS](#). Furthermore, [RIXS](#) processes provide access to valence-excited states not directly reachable by dipole

transitions from the ground state using one-photon techniques due to electronic symmetry constraints. Moreover, [fs-RIXS](#) as a combination of both, [fs-XANES](#) and [RIXS](#), offers additional information about the number and symmetry of low-lying core-excited states, as well as access to more valence-excited states. However, as demonstrated in this thesis, the underlying processes can be exceedingly complex, even for small systems like pyrazine, such that computer simulations are absolutely required to unravel the high information content of the spectra.

In addition to the consideration of nuclear quantum dynamics, our time-dependent framework facilitates the explicit inclusion of an external electric field to investigate the influence of bandwidth/time duration of pulsed laser sources and their coherent properties, an aspect often overlooked in quantum dynamics simulations. Within the context of [fs-XANES](#), we illustrated the impact of a finite pump pulse duration, observing that longer temporal [fwhm](#) durations result in increasingly blurred valence-excited state dynamics. Specifically, in the case of pyrazine, pump pulses exceeding approximately 50 fs lead to transient X-ray absorption spectra devoid of time-dependent information.

In contrast to absorption spectroscopy, the [RIXS](#) process heavily depends on [CW](#) conditions, providing a well-defined incoming photon energy. We developed the mathematical foundations to describe [RIXS](#) as a time-dependent process with pulsed coherent sources, thus enabling to study the impact of laser pulses on resonant Raman processes as manifest in [RIXS](#) spectra that come about due to the spectral distribution of temporally short coherent X-ray pulses. Moreover, short pulses suppress the detuning effect, thereby complicating the final analysis of the [RIXS](#) spectra. Nevertheless, employing [RIXS](#) as a probe technique in time-resolved studies necessitates temporally short pulses to investigate pump-induced dynamics. Hence, a carefully evaluation to strike the appropriate balance between time and spectral resolution is imperative in transient [RIXS](#) experiments.

A prospective aim beyond this thesis is to expand the time-domain approaches within the [MCTDH](#) framework to explore additional nonlinear X-ray spectroscopic methods. [\[31,266-268\]](#) For instance, in stimulated X-ray Raman scattering, an X-ray photon is absorbed from the first pulse, inducing a core-electron excitation, followed by a second X-ray pulse that stimulates an emission process. This method can thus be viewed as an extension of [RIXS](#) as the X-ray analogue of femtosecond stimulated Raman scattering, [\[269\]](#) allowing for the investigation of core-excited state dynamics with additional experimental control. Furthermore, the introduction of a third pulse within this scheme allows to extend stimulated X-ray Raman scattering into the attosecond regime enabling the exploration of electronic dynamics

and higher-order correlations by probing core-level transitions in atoms of different chemical elements with a molecule or between two molecules that may be connected by hydrogen bonds, e.g. a protic molecule in aqueous solution. The general non-adiabatic framework presented in this thesis, incorporating an explicit treatment of light-matter interactions, is highly suitable for describing not only these impulsive Raman scattering processes but also other nonlinear X-ray techniques applied to molecular systems with a high degree of accuracy.

Another important aspect of theoretical spectroscopy in general, which demands attention in future developments, is the inclusion of environments, given that a large class of molecular (bio-)chemical reactions occur within an environment, i.e. molecular systems encountered outside the laboratory are predominantly situated in the condensed phase rather than the gas phase. While studies conducted in the gas phase enable the examination of the intrinsic properties of an isolated molecule with finer detail, thereby serving as a crucial foundation for investigating complex systems, the presence of a solvent or a protein micro-environment can induce ultrafast secondary reactions such as recombination on non-diffusive (sub-picosecond) timescales or exhibit local interactions that significantly influence the photoinduced reaction pathways. Thus, it is also imperative to incorporate these environmental effects into the theoretical modeling of (X-ray) spectroscopies via explicit solvent models (or other embedding schemes for more static environments). However, conventional grid-based methods such as **MCTDH** may quickly encounter limitations due to the necessity of precalculated **PESs**. Consequently, direct-dynamics methods, wherein **PESs** are computed on-the-fly, emerge as more suitable alternatives for explicitly incorporating far from equilibrium dynamics in environments, thereby providing essential quantum chemical tools to analyse and understand complex molecular systems that are highly relevant in science, e.g. as laid out in the grand challenges in science.

Bibliography

- [1] Parthenopoulos, D. A. and Rentzepis, P. M. *Three-dimensional optical storage memory*. *Science*, **245**(4920):843–845, (1989).
- [2] Johnston, H. S. *Atmospheric ozone*. *Annu. Rev. Phys. Chem.*, **43**(1):1–31, (1992). PMID: 18338974.
- [3] Yu, G., Gao, J., Hummelen, J. C., et al. *Polymer photovoltaic cells: Enhanced efficiencies via a network of internal donor-acceptor heterojunctions*. *Science*, **270**(5243):1789–1791, (1995).
- [4] Ravishankara, A. R., Hancock, G., Kawasaki, M., and Matsumi, Y. *Photochemistry of ozone: Surprises and recent lessons*. *Science*, **280**(5360):60–61, (1998).
- [5] Sinha, R. P. and Häder, D.-P. *Uv-induced dna damage and repair: a review*. *Photochem. Photobiol. Sci.*, **1**(4):225–236, (2002).
- [6] Green, B. R. and W., P. W. *Light-Harvesting Antennas in Photosynthesis*. Springer Netherlands, (2003).
- [7] Brédas, J.-L., Beljonne, D., Coropceanu, V., and Cornil, J. *Charge-transfer and energy-transfer processes in π -conjugated oligomers and polymers: A molecular picture*. *Chem. Rev.*, **104**(11):4971–5004, (2004).
- [8] Günes, S., Neugebauer, H., and Sariciftci, N. S. *Conjugated polymer-based organic solar cells*. *Chem. Rev.*, **107**(4):1324–1338, (2007).
- [9] Frutos, L. M., Andruniów, T., Santoro, F., et al. *Tracking the excited-state time evolution of the visual pigment with multiconfigurational quantum chemistry*. *Proc. Natl. Acad. Sci. U.S.A.*, **104**(19):7764–7769, (2007).
- [10] Kerwin, B. A. and Remmele, R. L. *Protect from light: Photodegradation and protein biologics*. *J. Pharm. Sci.*, **96**(6):1468–1479, (2007).

- [11] Sanderson, K. *Chemistry: The photon trap*. Nature, **452**(7186):400–402, (2008).
- [12] Cheng, Y.-C. and Fleming, G. R. *Dynamics of light harvesting in photosynthesis*. Annu. Rev. Phys. Chem., **60**(1):241–262, (2009). PMID: 18999996.
- [13] Polli, D., Altoè, P., Weingart, O., et al. *Conical intersection dynamics of the primary photoisomerization event in vision*. Nature, **467**(7314):440–443, (2010).
- [14] Lu, Y., Lan, Z., and Thiel, W. *Hydrogen bonding regulates the monomeric nonradiative decay of adenine in dna strands*. Angew. Chem., Int. Ed., **50**(30):6864–6867, (2011).
- [15] Shuai, Z. and Peng, Q. *Excited states structure and processes: Understanding organic light-emitting diodes at the molecular level*. Phys. Rep., **537**(4):123–156, (2014).
- [16] Röntgen, W. C. *Über Eine Neue Art von Strahlen*. Springer Berlin Heidelberg, (1949).
- [17] de Broglie, M. *Sur une nouveau procédé permettant d’obtenir la photographie des spectres de raies des rayons röntgen*. Comptes Rendus, **157**:924–926, (1913).
- [18] Moseley, H. *Xciii. the high-frequency spectra of the elements*. London Edinburgh Philos. Mag. & J. Sci., **26**(156):1024–1034, (1913).
- [19] Stenström, W. *Experimentelle Untersuchungen der Röntgespektra: 1. Prüfung der Beziehung $[\eta]/[\lambda]$* . C. Bloms boktryckeri, (1919).
- [20] Siegbahn, M. *Röntgenspektroskopische präzisionsmessungen*. Ann. Phys., **364**(9):56–72, (1919).
- [21] Watson, R. E. and Perlman, M. L. *Seeing with a new light: Synchrotron radiation*. Science, **199**(4335):1295–1302, (1978).
- [22] Duke, P. *Synchrotron Radiation*. Oxford Series on Synchrotron Radiation. Oxford University Press, London, England, (2009).
- [23] Willmott, P. *An Introduction to Synchrotron Radiation*. John Wiley & Sons, Ltd, (2019).

-
- [24] Chapman, H. N. *Fourth-generation light sources*. IUCrJ, **10**(Pt 3):246–247, (2023).
- [25] Emma, P., Akre, R., Arthur, J., et al. *First lasing and operation of an ångstrom-wavelength free-electron laser*. Nat. Photonics, **4**(9):641–647, (2010).
- [26] Jamison, S. *X-ray fel shines brightly*. Nat. Photonics, **4**(9):589–591, (2010).
- [27] McNeil, B. W. J. and Thompson, N. R. *X-ray free-electron lasers*. Nat. Photonics, **4**(12):814–821, (2010).
- [28] Seddon, E. A., Clarke, J. A., Dunning, D. J., et al. *Short-wavelength free-electron laser sources and science: a review**. Rep. Prog. Phys., **80**(11):115901, (2017).
- [29] Zhao, Z., Wang, D., Gu, Q., et al. *Status of the sxfel facility*. Appl. Sci., **7**(6), (2017).
- [30] Duris, J., Li, S., Driver, T., et al. *Tunable isolated attosecond x-ray pulses with gigawatt peak power from a free-electron laser*. Nat. Photonics, **14**(1):30–36, (2020).
- [31] Kraus, P. M., Zürich, M., Cushing, S. K., et al. *The ultrafast x-ray spectroscopic revolution in chemical dynamics*. Nat. Rev. Chem., **2**(6):82–94, (2018).
- [32] Pinjari, R. V., Delcey, M. G., Guo, M., et al. *Restricted active space calculations of L-edge X-ray absorption spectra: From molecular orbitals to multiplet states*. J. Chem. Phys., **141**(12):124116, (2014).
- [33] Allehyani, B. H., Hassan, W. I., Aziz, S. G., et al. *Solvation and speciation of cobalt(ii). a theoretical x-ray absorption and rixs study*. Chem. Phys., **532**:110681, (2020).
- [34] Helmich-Paris, B. *Simulating x-ray absorption spectra with complete active space self-consistent field linear response methods*. Int. J. Quantum Chem., **121**(3):e26559, (2021).
- [35] Butscher, W., Buenker, R. J., and Peyerimhoff, S. D. *All-electron ci calculations for core-ionized, core-valence excited and shake-up states of n2*. Chem. Phys. Lett., **52**(3):449–456, (1977).
- [36] Seidu, I., Neville, S. P., Kleinschmidt, M., et al. *The simulation of X-ray absorption spectra from ground and excited electronic states using core-valence separated DFT/MRCI*. J. Chem. Phys., **151**(14):144104, (2019).
-

- [37] Coriani, S. and Koch, H. *Communication: X-ray absorption spectra and core-ionization potentials within a core-valence separated coupled cluster framework*. J. Chem. Phys., **143**(18):181103, (2015).
- [38] Peng, B., Lestrangle, P. J., Goings, J. J., et al. *Energy-specific equation-of-motion coupled-cluster methods for high-energy excited states: Application to k-edge x-ray absorption spectroscopy*. J. Chem. Theory Comput., **11**(9):4146–4153, (2015).
- [39] Vidal, M. L., Feng, X., Epifanovsky, E., et al. *New and efficient equation-of-motion coupled-cluster framework for core-excited and core-ionized states*. J. Chem. Theory Comput., **15**(5):3117–3133, (2019).
- [40] Vidal, M. L., Pokhilko, P., Krylov, A. I., and Coriani, S. *Equation-of-motion coupled-cluster theory to model l-edge x-ray absorption and photoelectron spectra*. J. Phys. Chem. Lett., **11**(19):8314–8321, (2020).
- [41] Vidal, M. L., Krylov, A. I., and Coriani, S. *Dyson orbitals within the fc-cvs-eom-ccsd framework: theory and application to x-ray photoelectron spectroscopy of ground and excited states*. Phys. Chem. Chem. Phys., **22**:2693–2703, (2020).
- [42] Schirmer, J., Trofimov, A. B., Randall, K. J., et al. *K-shell excitation of the water, ammonia, and methane molecules using high-resolution photoabsorption spectroscopy*. Phys. Rev. A, **47**:1136–1147, (1993).
- [43] Trofimov, A. B., Moskovskaya, T. É., Gromov, E. V., et al. *Core-level electronic spectra in adc(2) approximation for polarization propagator: Carbon monoxide and nitrogen molecules*. J. Struct. Chem., **41**(3):483–494, (2000).
- [44] Wenzel, J., Wormit, M., and Dreuw, A. *Calculating core-level excitations and x-ray absorption spectra of medium-sized closed-shell molecules with the algebraic-diagrammatic construction scheme for the polarization propagator*. J. Comput. Chem., **35**(26):1900–1915, (2014).
- [45] Wenzel, J., Wormit, M., and Dreuw, A. *Calculating x-ray absorption spectra of open-shell molecules with the unrestricted algebraic-diagrammatic construction scheme for the polarization propagator*. J. Chem. Theory Comput., **10**(10):4583–4598, (2014).

-
- [46] Rehn, D. R., Dreuw, A., and Norman, P. *Resonant inelastic x-ray scattering amplitudes and cross sections in the algebraic diagrammatic construction/intermediate state representation (adc/isr) approach*. *J. Chem. Theory Comput.*, **13**(11):5552–5559, (2017).
- [47] Besley, N. A. and Asmuruf, F. A. *Time-dependent density functional theory calculations of the spectroscopy of core electrons*. *Phys. Chem. Chem. Phys.*, **12**:12024–12039, (2010).
- [48] Besley, N. A. *Density functional theory based methods for the calculation of x-ray spectroscopy*. *Acc. Chem. Res.*, **53**(7):1306–1315, (2020).
- [49] Besley, N. A. *Modeling of the spectroscopy of core electrons with density functional theory*. *WIREs Comput Mol Sci.*, **11**(6):e1527, (2021).
- [50] Cohen, A. J., Mori-Sánchez, P., and Yang, W. *Challenges for density functional theory*. *Chem. Rev.*, **112**(1):289–320, (2012).
- [51] Verma, P. and Truhlar, D. G. *Status and challenges of density functional theory*. *Trends Chem.*, **2**(4):302–318, (2020). Special Issue - Laying Groundwork for the Future.
- [52] Norman, P. and Dreuw, A. *Simulating x-ray spectroscopies and calculating core-excited states of molecules*. *Chem. Rev.*, **118**(15):7208–7248, (2018).
- [53] Davidson, E. R. *The iterative calculation of a few of the lowest eigenvalues and corresponding eigenvectors of large real-symmetric matrices*. *J. Comput. Phys.*, **17**(1):87–94, (1975).
- [54] Cederbaum, L. S., Domcke, W., and Schirmer, J. *Many-body theory of core holes*. *Phys. Rev. A*, **22**:206–222, (1980).
- [55] Barth, A. and Cederbaum, L. S. *Many-body theory of core-valence excitations*. *Phys. Rev. A*, **23**:1038–1061, (1981).
- [56] Stener, M., Fronzoni, G., and de Simone, M. *Time dependent density functional theory of core electrons excitations*. *Chem. Phys. Lett.*, **373**(1):115–123, (2003).
- [57] Halbert, L., Vidal, M. L., Shee, A., et al. *Relativistic eom-ccsd for core-excited and core-ionized state energies based on the four-component dirac-coulomb(-gaunt) hamiltonian*. *J. Chem. Theory Comput.*, **17**(6):3583–3598, (2021).
-

- [58] Herbst, M. F. and Fransson, T. *Quantifying the error of the core–valence separation approximation*. J. Chem. Phys., **153**(5):054114, (2020).
- [59] Norman, P., Bishop, D. M., Jørgensen, H., and Oddershede, J. *Near-resonant absorption in the time-dependent self-consistent field and multiconfigurational self-consistent field approximations*. J. Chem. Phys., **115**(22):10323–10334, (2001).
- [60] Ekström, U., Norman, P., Carravetta, V., and Ågren, H. *Polarization propagator for x-ray spectra*. Phys. Rev. Lett., **97**:143001, (2006).
- [61] Fahleson, T., Ågren, H., and Norman, P. *A polarization propagator for non-linear x-ray spectroscopies*. J. Phys. Chem. Lett., **7**(11):1991–1995, (2016).
- [62] Vaz da Cruz, V., Ignatova, N., Couto, R. C., et al. *Nuclear dynamics in resonant inelastic X-ray scattering and X-ray absorption of methanol*. J. Chem. Phys., **150**(23):234301, (2019).
- [63] Lee, S.-Y., Pollard, W., and Mathies, R. A. *Quantum theory for transition state absorption*. Chem. Phys. Lett., **160**(5):531–537, (1989).
- [64] Lee, S.-Y., Pollard, W., and Mathies, R. A. *Quasi-classical models of transition state absorption or emission*. Chem. Phys. Lett., **163**(1):11–18, (1989).
- [65] Ohno, M. *Lifetime of core two-hole states in atoms*. J. Electron Spectrosc. Relat. Phenom., **143**(1):13–19, (2005).
- [66] Nicolas, C. and Miron, C. *Lifetime broadening of core-excited and -ionized states*. J. Electron Spectrosc. Relat. Phenom., **185**(8):267–272, (2012).
- [67] Gel'mukhanov, F., Odellius, M., Polyutov, S. P., et al. *Dynamics of resonant x-ray and auger scattering*. Rev. Mod. Phys., **93**:035001, (2021).
- [68] Gel'mukhanov, F. and Ågren, H. *Resonant inelastic x-ray scattering with symmetry-selective excitation*. Phys. Rev. A, **49**:4378–4389, (1994).
- [69] Ljungberg, M. P. *Vibrational effects in x-ray absorption and resonant inelastic x-ray scattering using a semiclassical scheme*. Phys. Rev. B, **96**:214302, (2017).
- [70] Ignatova, N., Cruz, V. V., Couto, R. C., et al. *Gradual collapse of nuclear wave functions regulated by frequency tuned x-ray scattering*. Sci. Rep., **7**(1):43891, (2017).

-
- [71] Couto, R. C., Cruz, V. V., Ertan, E., et al. *Selective gating to vibrational modes through resonant x-ray scattering*. Nat. Commun., **8**(1):14165, (2017).
- [72] Vaz da Cruz, V., Ertan, E., Couto, R. C., et al. *A study of the water molecule using frequency control over nuclear dynamics in resonant x-ray scattering*. Phys. Chem. Chem. Phys., **19**:19573–19589, (2017).
- [73] Couto, R. C., Guarise, M., Nicolaou, A., et al. *Coupled electron-nuclear dynamics in resonant $1\sigma \rightarrow 2\pi$ x-ray raman scattering of co molecules*. Phys. Rev. A, **93**:032510, (2016).
- [74] Freibert, A., Mendive-Tapia, D., Huse, N., and Vendrell, O. *Femtosecond x-ray absorption spectroscopy of pyrazine at the nitrogen k-edge: on the validity of the lorentzian limit*. J. Phys. B, **54**(24):244003, (2022).
- [75] Bressler, C. and Chergui, M. *Molecular struct. dyn. probed by ultrafast x-ray absorption spectroscopy*. Annu. Rev. Phys. Chem., **61**:263–282, (2010).
- [76] Chen, L. X., Zhang, X., and Shelby, M. L. *Recent advances on ultrafast x-ray spectroscopy in the chemical sciences*. Chem. Sci., **5**:4136–4152, (2014).
- [77] Wolf, T. J. A., Myhre, R. H., Cryan, J. P., et al. *Probing ultrafast $\pi\pi^*/n\pi^*$ internal conversion in organic chromophores via k-edge resonant absorption*. Nat. Commun., **8**(1):29, (2017).
- [78] Bhattacharjee, A., Pemmaraju, C. D., Schnorr, K., et al. *Ultrafast intersystem crossing in acetylacetone via femtosecond x-ray transient absorption at the carbon k-edge*. J. Am. Chem. Soc., **139**(46):16576–16583, (2017).
- [79] Kim, Y., Ma, R., Lee, J., et al. *Ligand-field effects in a ruthenium(ii) polypyridyl complex probed by femtosecond x-ray absorption spectroscopy*. J. Phys. Chem. Lett., **12**(51):12165–12172, (2021).
- [80] Jay, R. M., Banerjee, A., Leitner, T., et al. *Tracking c–h activation with orbital resolution*. Science, **380**(6648):955–960, (2023).
- [81] Capano, G., Milne, C. J., Chergui, M., et al. *Probing wavepacket dynamics using ultrafast x-ray spectroscopy*. J. Phys. B, **48**(21):214001, (2015).
- [82] Neville, S. P., Averbukh, V., Patchkovskii, S., et al. *Beyond structure: ultrafast x-ray absorption spectroscopy as a probe of non-adiabatic wavepacket dynamics*. Faraday Discuss., **194**:117–145, (2016).
-

- [83] Penfold, T. J., Pápai, M., Rozgonyi, T., et al. *Probing spin–vibronic dynamics using femtosecond x-ray spectroscopy*. Faraday Discuss., **194**:731–746, (2016).
- [84] Tsuru, S., Vidal, M. L., Pápai, M., et al. *Time-resolved near-edge X-ray absorption fine structure of pyrazine from electronic structure and nuclear wave packet dynamics simulations*. J. Chem. Phys., **151**(12):124114, (2019).
- [85] Northey, T., Norell, J., Fouda, A. E. A., et al. *Ultrafast nonadiabatic dynamics probed by nitrogen k-edge absorption spectroscopy*. Phys. Chem. Chem. Phys., **22**:2667–2676, (2020).
- [86] List, N. H., Dempwolff, A. L., Dreuw, A., et al. *Probing competing relaxation pathways in malonaldehyde with transient x-ray absorption spectroscopy*. Chem. Sci., **11**:4180–4193, (2020).
- [87] Scutelnic, V., Tsuru, S., Pápai, M., et al. *X-ray transient absorption reveals the $1au$ ($n\pi^*$) state of pyrazine in electronic relaxation*. Nat. Commun., **12**(1):5003, (2021).
- [88] Freibert, A., Mendive-Tapia, D., Huse, N., and Vendrell, O. *Time-dependent resonant inelastic x-ray scattering of pyrazine at the nitrogen k-edge: A quantum dynamics approach*. J. Chem. Theory Comput., **20**(5):2167–2180, (2024).
- [89] Ament, L. J. P., van Veenendaal, M., Devereaux, T. P., et al. *Resonant inelastic x-ray scattering studies of elementary excitations*. Rev. Mod. Phys., **83**:705–767, (2011).
- [90] Gel'mukhanov, F. and Ågren, H. *Resonant x-ray raman scattering*. Phys. Rep., **312**(3):87–330, (1999).
- [91] Skytt, P., Guo, J., Wassdahl, N., et al. *Probing symmetry breaking upon core excitation with resonant x-ray fluorescence*. Phys. Rev. A, **52**:3572–3576, (1995).
- [92] Sun, Y.-P., Pietzsch, A., Hennies, F., et al. *Internal symmetry and selection rules in resonant inelastic soft x-ray scattering*. J. Phys. B, **44**(16):161002, (2011).
- [93] Ochmann, M., Vaz da Cruz, V., Eckert, S., et al. *R-group stabilization in methylated formamides observed by resonant inelastic x-ray scattering*. Chem. Commun., **58**:8834–8837, (2022).

-
- [94] Harada, Y., Takeuchi, T., Kino, H., et al. *Electronic structure of dna nucleobases and their dinucleotides explored by soft x-ray spectroscopy*. J. Phys. Chem. A, **110**(49):13227–13231, (2006).
- [95] Weinhardt, L., Ertan, E., Iannuzzi, M., et al. *Probing hydrogen bonding orbitals: resonant inelastic soft x-ray scattering of aqueous nh₃*. Phys. Chem. Chem. Phys., **17**:27145–27153, (2015).
- [96] Hussain, A., Huse, N., and Vendrell, O. *Sensitivity of core-level spectroscopy to electrostatic environments of nitrile groups: An ab initio study*. Struct. Dyn., **4**(5):054102, (2017).
- [97] Vaz da Cruz, V., Gel'mukhanov, F., Eckert, S., et al. *Probing hydrogen bond strength in liquid water by resonant inelastic x-ray scattering*. Nature Communications, **10**(1):1013, (2019).
- [98] van Schooneveld, M. M., Gosselink, R. W., Eggenhuisen, T. M., et al. *A multi-spectroscopic study of 3d orbitals in cobalt carboxylates: The high sensitivity of 2p3d resonant x-ray emission spectroscopy to the ligand field*. Angew. Chem., Int. Ed., **52**(4):1170–1174, (2013).
- [99] Wernet, P., Kunnus, K., Schreck, S., et al. *Dissecting local atomic and intermolecular interactions of transition-metal ions in solution with selective x-ray spectroscopy*. J. Phys. Chem. Lett., **3**(23):3448–3453, (2012).
- [100] Kunnus, K., Zhang, W., Delcey, M. G., et al. *Viewing the valence electronic structure of ferric and ferrous hexacyanide in solution from the fe and cyanide perspectives*. J. Phys. Chem. B, **120**(29):7182–7194, (2016).
- [101] Hahn, A. W., Van Kuiken, B. E., Chilkuri, V. G., et al. *Probing the valence electronic structure of low-spin ferrous and ferric complexes using 2p3d resonant inelastic x-ray scattering (rixs)*. Inorg. Chem., **57**(15):9515–9530, (2018). PMID: 30044087.
- [102] Jay, R. M., Eckert, S., Fondell, M., et al. *The nature of frontier orbitals under systematic ligand exchange in (pseudo-)octahedral fe(ii) complexes*. Phys. Chem. Chem. Phys., **20**:27745–27751, (2018).
- [103] Jay, R. M., Eckert, S., Van Kuiken, B. E., et al. *Following metal-to-ligand charge-transfer dynamics with ligand and spin specificity using femtosecond resonant inelastic x-ray scattering at the nitrogen k-edge*. J. Phys. Chem. Lett., **12**(28):6676–6683, (2021).
-

- [104] Biasin, E., Nascimento, D. R., Poulter, B. I., et al. *Revealing the bonding of solvated ru complexes with valence-to-core resonant inelastic x-ray scattering*. Chem. Sci., **12**:3713–3725, (2021).
- [105] Jeyachandran, Y. L., Meyer, F., Nagarajan, S., et al. *Ion-solvation-induced molecular reorganization in liquid water probed by resonant inelastic soft x-ray scattering*. J. Phys. Chem. Lett., **5**(23):4143–4148, (2014). PMID: 26278946.
- [106] Eckert, S., Norell, J., Miedema, P. S., et al. *Ultrafast independent n-h and n-c bond deformation investigated with resonant inelastic x-ray scattering*. Angew. Chem., Int. Ed., **56**(22):6088–6092, (2017).
- [107] Savchenko, V., Brumboiu, I. E., Kimberg, V., et al. *Vibrational resonant inelastic x-ray scattering in liquid acetic acid: a ruler for molecular chain lengths*. Sci. Rep., **11**(1), (2021).
- [108] Gel'mukhanov, F. and Ågren, H. *X-ray resonant scattering involving dissociative states*. Phys. Rev. A, **54**:379–393, (1996).
- [109] Björneholm, O., Sundin, S., Svensson, S., et al. *Femtosecond dissociation of core-excited hcl monitored by frequency detuning*. Phys. Rev. Lett., **79**:3150–3153, (1997).
- [110] Sundin, S., Kh. Gel'mukhanov, F., Ågren, H., et al. *Collapse of vibrational structure in the auger resonant raman spectrum of co by frequency detuning*. Phys. Rev. Lett., **79**:1451–1454, (1997).
- [111] Gel'mukhanov, F., Privalov, T., and Ågren, H. *Collapse of vibrational structure in spectra of resonant x-ray raman scattering*. Phys. Rev. A, **56**:256–264, (1997).
- [112] Harada, Y., Tokushima, T., Takata, Y., et al. *Dynamical symmetry breaking under core excitation in graphite: Polarization correlation in soft x-ray recombination emission*. Phys. Rev. Lett., **93**:017401, (2004).
- [113] Hennies, F., Polyutov, S., Minkov, I., et al. *Nonadiabatic effects in resonant inelastic x-ray scattering*. Phys. Rev. Lett., **95**:163002, (2005).
- [114] Maganas, D., Kristiansen, P., Duda, L.-C., et al. *Combined experimental and Ab Initio multireference configuration interaction study of the resonant inelastic x-ray scattering spectrum of co₂*. J. Phys. Chem. C, **118**(35):20163–20175, (2014).

- [115] Eckert, S., Vaz da Cruz, V., Ochmann, M., et al. *Breaking the symmetry of pyrimidine: Solvent effects and core-excited state dynamics*. J. Phys. Chem. Lett., **12**(35):8637–8643, (2021).
- [116] Freibert, A., Mendive-Tapia, D., Vendrell, O., and Huse, N. A fully dynamical description of time-resolved resonant inelastic x-ray scattering of pyrazine, (2024).
- [117] Beye, M., Wernet, P., Schüßler-Langeheine, C., and Föhlisch, A. *Time resolved resonant inelastic x-ray scattering: A supreme tool to understand dynamics in solids and molecules*. J. Electron Spectrosc. Relat. Phenom., **188**:172–182, (2013).
- [118] Lu, H., Gauthier, A., Hepting, M., et al. *Time-resolved rixs experiment with pulse-by-pulse parallel readout data collection using x-ray free electron laser*. Sci. Rep., **10**(1):22226, (2020).
- [119] Kunnus, K., Josefsson, I., Rajkovic, I., et al. *Anti-stokes resonant x-ray raman scattering for atom specific and excited state selective dynamics*. New J. Phys., **18**(10):103011, (2016).
- [120] Kunnus, K., Josefsson, I., Rajkovic, I., et al. *Identification of the dominant photochemical pathways and mechanistic insights to the ultrafast ligand exchange of $Fe(CO)_5$ to $Fe(CO)_4EtOH$* . Struct. Dyn., **3**(4):043204, (2016).
- [121] Banerjee, A., Jay, R. M., Leitner, T., et al. *Accessing metal-specific orbital interactions in $c-h$ activation with resonant inelastic x-ray scattering*. Chem. Sci., **15**:2398–2409, (2024).
- [122] Schrödinger, E. *An undulatory theory of the mechanics of atoms and molecules*. Phys. Rev., **28**:1049–1070, (1926).
- [123] Schrödinger, E. *Quantisierung als eigenwertproblem*. Ann. Phys., **384**(6):489–527, (1926).
- [124] Born, M. and Oppenheimer, R. *Zur quantentheorie der molekeln*. Ann. Phys., **389**(20):457–484, (1927).
- [125] Born, M., Huang, K., and Lax, M. *Dynamical theory of crystal lattices*. Am. J. Phys., **23**(7):474–474, (1955).

- [126] W. Domcke, H. K. and Cederbaum, L. *Spectroscopic effects of conical intersections of molecular potential energy surfaces*. Mol. Phys., **43**(4):851–875, (1981).
- [127] Köuppel, H., Domcke, W., and Cederbaum, L. S. *Multimode Molecular Dynamics Beyond the Born-Oppenheimer Approximation*, pages 59–246. John Wiley & Sons, Ltd, (1984).
- [128] Worth, G. A. and Cederbaum, L. S. *Beyond born-oppenheimer: Molecular dynamics through a conical intersection*. Annu. Rev. Phys. Chem., **55**(1):127–158, (2004). PMID: 15117250.
- [129] Yarkony, D. R. *Diabolical conical intersections*. Rev. Mod. Phys., **68**:985–1013, (1996).
- [130] Domcke, W., Yarkony, D., and Köppel, H. *Conical Intersections: Electronic Structure, Dynamics & Spectroscopy*. Advanced series in physical chemistry. World Scientific, (2004).
- [131] Domcke, W. and Yarkony, D. R. *Role of conical intersections in molecular spectroscopy and photoinduced chemical dynamics*. Annu. Rev. Phys. Chem., **63**(1):325–352, (2012). PMID: 22475338.
- [132] Baer, M. *Adiabatic and diabatic representations for atom-molecule collisions: Treatment of the collinear arrangement*. Chem. Phys. Lett., **35**(1):112–118, (1975).
- [133] Baer, M. *Beyond Born–Oppenheimer*. John Wiley & Sons, Ltd, (2006).
- [134] Baer, M., Billing, G., Prigogine, I., and Rice, S. *The Role of Degenerate States in Chemistry, Volume 124*. Advances in Chem. Phys. Wiley, (2003).
- [135] Berry, M. V. *Quantal phase factors accompanying adiabatic changes*. Proc. R. Soc. Lond. A, **392**(1802):45–57, (1984).
- [136] Mead, C. A. *The geometric phase in molecular systems*. Rev. Mod. Phys., **64**:51–85, (1992).
- [137] Franck, J. and Dymond, E. G. *Elementary processes of photochemical reactions*. Trans. Faraday Soc., **21**:536–542, (1926).
- [138] Condon, E. U. *Nuclear motions associated with electron transitions in diatomic molecules*. Phys. Rev., **32**:858–872, (1928).

-
- [139] Mukamel, S. *Principles of Nonlinear Optical Spectroscopy*. Oxford series in optical and imaging sciences. Oxford University Press, (1995).
- [140] Tannor, D. *Introduction to Quantum Mechanics*. University Science Books, (2007).
- [141] Shen, Y. *The Principles of Nonlinear Optics*. Wiley classics library. Wiley, (2003).
- [142] Wu, M., Chen, S., Camp, S., et al. *Theory of strong-field attosecond transient absorption*. J. Phys. B At. Mol. Opt. Phys., **49**(6):062003, (2016).
- [143] Heller, E. J. *Quantum corrections to classical photodissociation models*. J. Chem. Phys., **68**(5):2066–2075, (1978).
- [144] Schinke, R. *Photodissociation Dynamics: Spectroscopy and Fragmentation of Small Polyatomic Molecules*. Cambridge Monographs on Atomic, Molecular and Chem. Phys. Cambridge University Press, (1995).
- [145] Dirac, P. A. M. *The quantum theory of the emission and absorption of radiation*. Proc. R. Soc. Lond. A Math. Phys. Sci., **114**(767):243–265, (1927).
- [146] Pollard, W. T., Lee, S., and Mathies, R. A. *Wave packet theory of dynamic absorption spectra in femtosecond pump–probe experiments*. J. Chem. Phys., **92**(7):4012–4029, (1990).
- [147] Clark, R. and Hester, R. *Advances in Infrared and Raman Spectroscopy*. Number Bd. 9 in Advances in Infrared and Raman Spectroscopy. Heyden, (1982).
- [148] Lee, S. and Heller, E. J. *Time-dependent theory of Raman scattering*. J. Chem. Phys., **71**(12):4777–4788, (1979).
- [149] Williams, S. O. and Imre, D. G. *Raman spectroscopy: time-dependent pictures*. J. Phys. Chem., **92**(12):3363–3374, (1988).
- [150] Heller, E. J., Sundberg, R., and Tannor, D. *Simple aspects of raman scattering*. J. Phys. Chem., **86**(10):1822–1833, (1982).
- [151] Kramers, H. A. and Heisenberg, W. *Über die streuung von strahlung durch atome*. Zeitschrift für Physik, **31**(1):681–708, (1925).
- [152] Dirac, P. and Fowler, R. *The quantum theory of dispersion*. Proc. R. Soc. Lond. A Math. Phys. Sci., **114**(769):710–728, (1927).
-

- [153] Tannor, D. J. and Heller, E. J. *Polyatomic raman scattering for general harmonic potentials*. J. Chem. Phys., **77**(1):202–218, (1982).
- [154] Tully, J. C. *Nonadiabatic Dynamics*, pages 34–72. World Scientific, (1998).
- [155] G.A. Worth, M. R. and Lasorne, B. *Solving the time-dependent schrödinger equation for nuclear motion in one step: direct dynamics of non-adiabatic systems*. Mol. Phys., **106**(16-18):2077–2091, (2008).
- [156] Tully, J. C. *Perspective: Nonadiabatic dynamics theory*. J. Chem. Phys., **137**(22):22A301, (2012).
- [157] Yarkony, D. R. *Nonadiabatic quantum chemistry—past, present, and future*. Chem. Rev., **112**(1):481–498, (2012).
- [158] Curchod, B. F. E. and Martínez, T. J. *Ab initio nonadiabatic quantum molecular dynamics*. Chem. Rev., **118**(7):3305–3336, (2018).
- [159] González, L. and Lindh, R. *Quantum Chemistry and Dynamics of Excited States: Methods and Applications*. Wiley, (2021).
- [160] Meyer, H.-D., Manthe, U., and Cederbaum, L. *The multi-configurational time-dependent hartree approach*. Chem. Phys. Lett., **165**(1):73–78, (1990).
- [161] Manthe, U., Meyer, H., and Cederbaum, L. S. *Wave-packet dynamics within the multiconfiguration Hartree framework: General aspects and application to NOCl*. J. Chem. Phys., **97**(5):3199–3213, (1992).
- [162] Beck, M., Jäckle, A., Worth, G., and Meyer, H.-D. *The multiconfiguration time-dependent hartree (mctdh) method: a highly efficient algorithm for propagating wavepackets*. Phys. Rep., **324**(1):1–105, (2000).
- [163] Meyer, H.-D., Gatti, F., and Worth, G. A. *Multidimensional Quantum Dynamics*. John Wiley & Sons, Ltd, (2009).
- [164] Gatti, F., Lasorne, B., Meyer, H., and Nauts, A. *Applications of Quantum Dynamics in Chemistry*. Lecture Notes in Chemistry. Springer International Publishing, (2017).
- [165] Worth, G. A., Meyer, H.-D., Köppel, H., et al. *Using the mctdh wavepacket propagation method to describe multimode non-adiabatic dynamics*. Int. Rev. Phys. Chem., **27**(3):569–606, (2008).

-
- [166] Coester, F. *Bound states of a many-particle system*. Nucl. Phys., **7**:421–424, (1958).
- [167] Coester, F. and Kümmel, H. *Short-range correlations in nuclear wave functions*. Nucl. Phys., **17**:477–485, (1960).
- [168] Čížek, J. *On the Correlation Problem in Atomic and Molecular Systems. Calculation of Wavefunction Components in Ursell-Type Expansion Using Quantum-Field Theoretical Methods*. J. Chem. Phys., **45**(11):4256–4266, (1966).
- [169] Čížek, J. *On the Use of the Cluster Expansion and the Technique of Diagrams in Calculations of Correlation Effects in Atoms and Molecules*, pages 35–89. John Wiley & Sons, Ltd, (1969).
- [170] Paldus, J., Čížek, J., and Shavitt, I. *Correlation problems in atomic and molecular systems. iv. extended coupled-pair many-electron theory and its application to the bh_3 molecule*. Phys. Rev. A, **5**:50–67, (1972).
- [171] Purvis, I., George D. and Bartlett, R. J. *A full coupled-cluster singles and doubles model: The inclusion of disconnected triples*. J. Chem. Phys., **76**(4):1910–1918, (1982).
- [172] Bartlett, R. J. and Musiał, M. *Coupled-cluster theory in quantum chemistry*. Rev. Mod. Phys., **79**:291–352, (2007).
- [173] Emrich, K. *An extension of the coupled cluster formalism to excited states: (ii). approximations and tests*. Nucl. Phys. A, **351**(3):397–438, (1981).
- [174] Stanton, J. F. and Bartlett, R. J. *The equation of motion coupled-cluster method. A systematic biorthogonal approach to molecular excitation energies, transition probabilities, and excited state properties*. J. Chem. Phys., **98**(9):7029–7039, (1993).
- [175] Geertsen, J., Rittby, M., and Bartlett, R. J. *The equation-of-motion coupled-cluster method: Excitation energies of be and co* . Chem. Phys. Lett., **164**(1):57–62, (1989).
- [176] Bartlett, R. J. *Coupled-cluster theory and its equation-of-motion extensions*. WIREs Comput Mol Sci., **2**(1):126–138, (2012).
- [177] Sneskov, K. and Christiansen, O. *Excited state coupled cluster methods*. WIREs Comput Mol Sci., **2**(4):566–584, (2012).
-

- [178] Szabo, A. and Ostlund, N. *Modern Quantum Chemistry: Introduction to Advanced Electronic Structure Theory*. Dover Books on Chemistry. Dover Publications, (1996).
- [179] Helgaker, T., Jorgensen, P., and Olsen, J. *Molecular Electronic-Structure Theory*. Wiley, (2014).
- [180] Jensen, F. *Introduction to Computational Chemistry*. Wiley, (2017).
- [181] Light, J. C., Hamilton, I. P., and Lill, J. V. *Generalized discrete variable approximation in quantum mechanics*. J. Chem. Phys., **82**(3):1400–1409, (1985).
- [182] Dirac, P. A. M. *Note on exchange phenomena in the thomas atom*. Math. Proc. Camb. Philos. Soc., **26**(3):376–385, (1930).
- [183] Frenkel, J. *Wave Mechanics*. 1. Clarendon Press, (1932).
- [184] Kramer, P. and Saraceno, M. *Geometry of the Time-Dependent Variational Principle in Quantum Mechanics*. Lecture Notes in Physics. Springer Berlin Heidelberg, (1981).
- [185] Worth, G. A., Meyer, H.-D., and Cederbaum, L. S. *Relaxation of a system with a conical intersection coupled to a bath: A benchmark 24-dimensional wave packet study treating the environment explicitly*. J. Chem. Phys., **109**(9):3518–3529, (1998).
- [186] Wang, H. and Thoss, M. *Multilayer formulation of the multiconfiguration time-dependent Hartree theory*. J. Chem. Phys., **119**(3):1289–1299, (2003).
- [187] Manthe, U. *A multilayer multiconfigurational time-dependent Hartree approach for quantum dynamics on general potential energy surfaces*. J. Chem. Phys., **128**(16):164116, (2008).
- [188] Vendrell, O. and Meyer, H.-D. *Multilayer multiconfiguration time-dependent Hartree method: Implementation and applications to a Henon–Heiles Hamiltonian and to pyrazine*. J. Chem. Phys., **134**(4):044135, (2011).
- [189] Wang, H. *Multilayer multiconfiguration time-dependent hartree theory*. J. Phys. Chem. A, **119**(29):7951–7965, (2015).
- [190] Weeks, J. D., Hazi, A., and Rice, S. A. *On the use of pseudopotentials in the quantum theory of atoms and molecules*. Adv. Chem. Phys., pages 283–342, (1969).

-
- [191] Sachs, E. S., Hinze, J., and Sabelli, N. H. *Frozen core approximation, a pseudopotential method tested on six states of NaH*. J. Chem. Phys., **62**(9):3393–3398, (1975).
- [192] Yamazaki, I., Murao, T., Yamanaka, T., and Yoshihara, K. *Intramolecular electronic relaxation and photoisomerization processes in the isolated azabenzene molecules pyridine, pyrazine and pyrimidine*. Faraday Discuss. Chem. Soc., **75**:395–405, (1983).
- [193] Bolovinos, A., Tsekeris, P., Philis, J., et al. *Absolute vacuum ultraviolet absorption spectra of some gaseous azabenzenes*. J. Mol. Spectrosc., **103**(2):240–256, (1984).
- [194] Kommandeur, J., Majewski, W. A., Meerts, W. L., and Pratt, D. W. *Pyrazine: An "exact" solution to the problem of radiationless transitions*. Annu. Rev. Phys. Chem., **38**:433–462, (1987).
- [195] Innes, K., Ross, I., and Moomaw, W. R. *Electronic states of azabenzenes and azanaphthalenes: A revised and extended critical review*. J. Mol. Spectrosc., **132**(2):492–544, (1988).
- [196] Okuzawa, Y., Fujii, M., and Ito, M. *Direct observation of second excited $1,3(n, \pi^*)$ states of pyrazine by uv – ir double resonance dip spectroscopy*. Chem. Phys. Lett., **171**(4):341–346, (1990).
- [197] Walker, I. C. and Palmer, M. H. *The electronic states of the azines. iv. pyrazine, studied by vuv absorption, near-threshold electron energy-loss spectroscopy and *ab initio* multi-reference configuration interaction calculations*. Chem. Phys., **153**(1):169–187, (1991).
- [198] Wang, L., Kohguchi, H., and Suzuki, T. *Femtosecond time-resolved photoelectron imaging*. Faraday Discuss., **113**:37–46, (1999).
- [199] Stert, V., Farmanara, P., and Radloff, W. *Electron configuration changes in excited pyrazine molecules analyzed by femtosecond time-resolved photoelectron spectroscopy*. J. Chem. Phys., **112**(10):4460–4464, (2000).
- [200] Suzuki, T. *Femtosecond time-resolved photoelectron imaging*. Annu. Rev. Phys. Chem., **57**(Volume 57, 2006):555–592, (2006).
- [201] Horio, T., Fuji, T., Suzuki, Y.-I., and Suzuki, T. *Probing ultrafast internal conversion through conical intersection via time-energy map of photoelectron*
-

- angular anisotropy*. Journal of the American Chemical Society, **131**(30):10392–10393, (2009).
- [202] Suzuki, Y.-I., Fuji, T., Horio, T., and Suzuki, T. *Time-resolved photoelectron imaging of ultrafast $S_2 \rightarrow S_1$ internal conversion through conical intersection in pyrazine*. J. Chem. Phys., **132**(17):174302, (2010).
- [203] Stener, M., Decleva, P., Holland, D. M. P., and Shaw, D. A. *A study of the valence shell electronic states of pyrimidine and pyrazine by photoabsorption spectroscopy and time-dependent density functional theory calculations*. J. Phys. B, **44**(7):075203, (2011).
- [204] Horio, T., Spesyvtsev, R., Nagashima, K., et al. *Full observation of ultrafast cascaded radiationless transitions from $S_2(\pi\pi^*)$ state of pyrazine using vacuum ultraviolet photoelectron imaging*. J. Chem. Phys., **145**(4):044306, (2016).
- [205] Chang, Y.-P., Balciunas, T., Yin, Z., et al. *Observation of electronic coherence created at conical intersections and its decoherence in aqueous solution*, (2024).
- [206] Schneider, R. and Domcke, W. *S_1 - s_2 conical intersection and ultrafast $s_2 \rightarrow s_1$ internal conversion in pyrazine*. Chem. Phys. Lett., **150**(3):235–242, (1988).
- [207] Schneider, R. and Domcke, W. *Surface-hopping-induced femtosecond vibrational dephasing in strongly vibronically coupled systems*. Chem. Phys. Lett., **159**(1):61–65, (1989).
- [208] Stock, G., Schneider, R., and Domcke, W. *Theoretical studies on the femtosecond real-time measurement of ultrafast electronic decay in polyatomic molecules*. J. Chem. Phys., **90**(12):7184–7194, (1989).
- [209] Stock, G. and Domcke, W. *Theory of femtosecond pump-probe spectroscopy of ultrafast internal conversion processes in polyatomic molecules*. J. Opt. Soc. Am. B, **7**(9):1970–1980, (1990).
- [210] Stock, G. and Domcke, W. *Theory of resonance Raman scattering and fluorescence from strongly vibronically coupled excited states of polyatomic molecules*. J. Chem. Phys., **93**(8):5496–5509, (1990).
- [211] Manthe, U. and Köppel, H. *Dynamics on potential energy surfaces with a conical intersection: Adiabatic, intermediate, and diabatic behavior*. J. Chem. Phys., **93**(3):1658–1669, (1990).

-
- [212] Seel, M. and Domcke, W. *Femtosecond time-resolved ionization spectroscopy of ultrafast internal-conversion dynamics in polyatomic molecules: Theory and computational studies*. J. Chem. Phys., **95**(11):7806–7822, (1991).
- [213] Stock, G. and Domcke, W. *Detection of ultrafast molecular-excited-state dynamics with time- and frequency-resolved pump-probe spectroscopy*. Phys. Rev. A, **45**:3032–3040, (1992).
- [214] Seidner, L., Stock, G., Sobolewski, A. L., and Domcke, W. *Ab initio characterization of the $S1$ – $S2$ conical intersection in pyrazine and calculation of spectra*. J. Chem. Phys., **96**(7):5298–5309, (1992).
- [215] Seidner, L., Domcke, W., and von Niessen, W. *$X2ag$ – $\tilde{A} 2b1g$ conical intersection in the pyrazine cation and its effect on the photoelectron spectrum*. Chem. Phys. Lett., **205**(1):117–122, (1993).
- [216] Domcke, W., Sobolewski, A., and Woywod, C. *Internal conversion funnel in benzene and pyrazine: adiabatic and diabatic representation*. Chem. Phys. Lett., **203**(2):220–226, (1993).
- [217] Stock, G. and Domcke, W. *Femtosecond spectroscopy of ultrafast nonadiabatic excited-state dynamics on the basis of ab initio potential-energy surfaces: the $s2$ state of pyrazine*. J. Phys. Chem., **97**(48):12466–12472, (1993).
- [218] Woywod, C., Domcke, W., Sobolewski, A. L., and Werner, H. *Characterization of the $S1$ – $S2$ conical intersection in pyrazine using ab initio multiconfiguration self-consistent-field and multireference configuration-interaction methods*. J. Chem. Phys., **100**(2):1400–1413, (1994).
- [219] Stock, G., Woywod, C., Domcke, W., et al. *Resonance Raman spectroscopy of the $S1$ and $S2$ states of pyrazine: Experiment and first principles calculation of spectra*. J. Chem. Phys., **103**(16):6851–6860, (1995).
- [220] Worth, G. A., Meyer, H., and Cederbaum, L. S. *The effect of a model environment on the $S2$ absorption spectrum of pyrazine: A wave packet study treating all 24 vibrational modes*. J. Chem. Phys., **105**(11):4412–4426, (1996).
- [221] Worth, G., Meyer, H.-D., and Cederbaum, L. *State filtering by a bath: up to 24 mode numerically exact wavepacket propagations*. Chem. Phys. Lett., **299**(5):451–456, (1999).
-

- [222] Raab, A., Worth, G. A., Meyer, H.-D., and Cederbaum, L. S. *Molecular dynamics of pyrazine after excitation to the S2 electronic state using a realistic 24-mode model Hamiltonian*. J. Chem. Phys., **110**(2):936–946, (1999).
- [223] Kühnl, A. and Domcke, W. *Multilevel Redfield description of the dissipative dynamics at conical intersections*. J. Chem. Phys., **116**(1):263–274, (2002).
- [224] Werner, U., Mitrić, R., Suzuki, T., and Bonačić-Koutecký, V. *Nonadiabatic dynamics within the time dependent density functional theory: Ultrafast photodynamics in pyrazine*. Chem. Phys., **349**(1):319–324, (2008).
- [225] Burghardt, I., Giri, K., and Worth, G. A. *Multimode quantum dynamics using Gaussian wavepackets: The Gaussian-based multiconfiguration time-dependent Hartree (G-MCTDH) method applied to the absorption spectrum of pyrazine*. J. Chem. Phys., **129**(17):174104, (2008).
- [226] Shalashilin, D. V. *Nonadiabatic dynamics with the help of multiconfigurational Ehrenfest method: Improved theory and fully quantum 24D simulation of pyrazine*. J. Chem. Phys., **132**(24):244111, (2010).
- [227] Tomasello, G., Humeniuk, A., and Mitrić, R. *Exploring ultrafast dynamics of pyrazine by time-resolved photoelectron imaging*. J. Phys. Chem. A, **118**(37):8437–8445, (2014).
- [228] Sala, M., Lasorne, B., Gatti, F., and Guérin, S. *The role of the low-lying dark $n\pi^*$ states in the photophysics of pyrazine: a quantum dynamics study*. Phys. Chem. Chem. Phys., **16**:15957–15967, (2014).
- [229] Sala, M., Guérin, S., and Gatti, F. *Quantum dynamics of the photostability of pyrazine*. Phys. Chem. Chem. Phys., **17**:29518–29530, (2015).
- [230] Kanno, M., Ito, Y., Shimakura, N., et al. *Ab initio quantum dynamical analysis of ultrafast nonradiative transitions via conical intersections in pyrazine*. Phys. Chem. Chem. Phys., **17**:2012–2024, (2015).
- [231] Sala, M. and Egorova, D. *Two-dimensional photon-echo spectroscopy at a conical intersection: A two-mode pyrazine model with dissipation*. Chem. Phys., **481**:206–217, (2016).
- [232] Mignolet, B., Kanno, M., Shimakura, N., et al. *Ultrafast nonradiative transition pathways in photo-excited pyrazine: Ab initio analysis of time-resolved vacuum ultraviolet photoelectron spectrum*. Chem. Phys., **515**:704–709, (2018).

- [233] Penfold, T., Pápai, M., Møller, K., and Worth, G. *Excited state dynamics initiated by an electromagnetic field within the variational multi-configurational gaussian (vmcg) method*. *Comput. Theor. Chem.*, **1160**:24–30, (2019).
- [234] Xie, W., Sapunar, M., Došlić, N., et al. *Assessing the performance of trajectory surface hopping methods: Ultrafast internal conversion in pyrazine*. *J. Chem. Phys.*, **150**(15):154119, (2019).
- [235] Csehi, A., Badankó, P., Halász, G. J., et al. *On the preservation of coherence in the electronic wavepacket of a neutral and rigid polyatomic molecule*. *J. Phys. B*, **53**(18):184005, (2020).
- [236] Sun, K., Xie, W., Chen, L., et al. *Multi-faceted spectroscopic mapping of ultrafast nonadiabatic dynamics near conical intersections: A computational study*. *J. Chem. Phys.*, **153**(17):174111, (2020).
- [237] Gelin, M. F., Huang, X., Xie, W., et al. *Ab initio surface-hopping simulation of femtosecond transient-absorption pump–probe signals of nonadiabatic excited-state dynamics using the doorway–window representation*. *J. Chem. Theory Comput.*, **17**(4):2394–2408, (2021).
- [238] Huang, X., Xie, W., Došlić, N., et al. *Ab initio quasiclassical simulation of femtosecond time-resolved two-dimensional electronic spectra of pyrazine*. *J. Phys. Chem. Lett.*, **12**(48):11736–11744, (2021).
- [239] Piteša, T., Sapunar, M., Ponzi, A., et al. *Combined surface-hopping, dyson orbital, and b-spline approach for the computation of time-resolved photoelectron spectroscopy signals: The internal conversion in pyrazine*. *J. Chem. Theory Comput.*, **17**(8):5098–5109, (2021).
- [240] Kaczun, T., Dempwolff, A. L., Huang, X., et al. *Tuning uv pump x-ray probe spectroscopy on the nitrogen k edge reveals the radiationless relaxation of pyrazine: Ab initio simulations using the quasiclassical doorway–window approximation*. *J. Phys. Chem. Lett.*, **14**(24):5648–5656, (2023).
- [241] Tsuru, S., Sharma, B., Marx, D., and Hättig, C. *Structural sampling and solvation models for the simulation of electronic spectra: Pyrazine as a case study*. *J. Chem. Theory Comput.*, **19**(8):2291–2303, (2023).
- [242] Pios, S. V., Gelin, M. F., Ullah, A., et al. *Artificial-intelligence-enhanced on-the-fly simulation of nonlinear time-resolved spectra*. *J. Phys. Chem. Lett.*, **15**(9):2325–2331, (2024).

- [243] Bressler, C. and Chergui, M. *Ultrafast x-ray absorption spectroscopy*. Chem. Rev., **104**(4):1781–1812, (2004).
- [244] Attar, A. R., Bhattacharjee, A., Pemmaraju, C. D., et al. *Femtosecond x-ray spectroscopy of an electrocyclic ring-opening reaction*. Science, **356**(6333):54–59, (2017).
- [245] Bhattacharjee, A., Schnorr, K., Oesterling, S., et al. *Photoinduced heterocyclic ring opening of furfural: Distinct open-chain product identification by ultrafast x-ray transient absorption spectroscopy*. J. Am. Chem. Soc., **140**(39):12538–12544, (2018).
- [246] Hua, W., Mukamel, S., and Luo, Y. *Transient x-ray absorption spectral fingerprints of the s_1 dark state in uracil*. J. Phys. Chem. Lett., **10**(22):7172–7178, (2019).
- [247] Wilson, E. B. *The normal modes and frequencies of vibration of the regular plane hexagon model of the benzene molecule*. Phys. Rev., **45**:706–714, (1934).
- [248] Pacher, T., Cederbaum, L. S., and Köppel, H. *Adiabatic and Quasidiabatic States in a Gauge Theoretical Framework*, pages 293–391. John Wiley & Sons, Ltd, (1993).
- [249] Cederbaum, L., Domcke, W., Köppel, H., and Von Niessen, W. *Strong vibronic coupling effects in ionization spectra: The “mystery band” of butatriene*. Chem. Phys., **26**(2):169–177, (1977).
- [250] Domcke, W. and Cederbaum, L. *Vibronic coupling and symmetry breaking in core electron ionization*. Chem. Phys., **25**(2):189–196, (1977).
- [251] Worth, G. A., Beck, M. H., Jäckle, A., and Meyer, H.-D. The MCTDH Package, Version 8.2, (2000). H.-D. Meyer, Version 8.3 (2002), Version 8.4 (2007), Version 8.6 (2020). See <http://mctdh.uni-hd.de>.
- [252] Ditchfield, R., Hehre, W. J., and Pople, J. A. *Self-consistent molecular-orbital methods. ix. an extended gaussian-type basis for molecular-orbital studies of organic molecules*. J. Chem. Phys., **54**(2):724–728, (1971).
- [253] Shao, Y., Gan, Z., Epifanovsky, E., et al. *Advances in molecular quantum chemistry contained in the q-chem 4 program package*. Mol. Phys., **113**(2):184–215, (2015).

-
- [254] Vall-Ilosera, G., Gao, B., Kivimäki, A., et al. *The $c\ 1s$ and $n\ 1s$ near edge x-ray absorption fine structure spectra of five azabenzenes in the gas phase.* J. Chem. Phys., **128**(4):044316, (2008).
- [255] Prince, K., Vondráček, M., Karvonen, J., et al. *A critical comparison of selected $1s$ and $2p$ core hole widths.* J. Electron Spectrosc. Relat. Phenom., **101-103**:141–147, (1999).
- [256] Luo, Y., Ågren, H., Gel'mukhanov, F., et al. *Symmetry-selective resonant inelastic x-ray scattering of c_{60} .* Phys. Rev. B, **52**:14479–14496, (1995).
- [257] Glans, P., Gunnelin, K., Skytt, P., et al. *Resonant x-ray emission spectroscopy of molecular oxygen.* Phys. Rev. Lett., **76**:2448–2451, (1996).
- [258] Hergenhahn, U., Kugeler, O., Rüdell, A., et al. *Symmetry-selective observation of the $n\ 1s$ shape resonance in n_2 .* J. Phys. Chem. A, **105**(23):5704–5708, (2001).
- [259] Kosugi, N. *Exchange interaction in core excitation of diatomic systems.* Chem. Phys., **289**(1):117–134, (2003).
- [260] Bagus, P. S. and Schaefer, I., Henry F. *Localized and Delocalized $1s$ Hole States of the $O\ 2 + Molecular\ Ion$.* J. Chem. Phys., **56**(1):224–226, (2003).
- [261] Ehara, M., Nakatsuji, H., Matsumoto, M., et al. *Symmetry-dependent vibrational excitation in $N\ 1s$ photoionization of N_2 : Experiment and theory.* J. Chem. Phys., **124**(12):124311, (2006).
- [262] Xu, Y.-C., Wang, S.-X., Du, X.-J., et al. *Probing the delocalized core-hole via inner-shell excitation in n_2 .* New J. Phys., **24**(5):053036, (2022).
- [263] Ma, Y., Wassdahl, N., Skytt, P., et al. *Soft-x-ray resonant inelastic scattering at the $c\ k$ edge of diamond.* Phys. Rev. Lett., **69**:2598–2601, (1992).
- [264] Cederbaum, L. S. *Symmetry breaking and localization in resonant photon emission.* J. Chem. Phys., **103**(2):562–567, (1995).
- [265] Epifanovsky, E., Gilbert, A. T. B., Feng, X., et al. *Software for the frontiers of quantum chemistry: An overview of developments in the Q-Chem 5 package.* J. Chem. Phys., **155**(8):084801, (2021).
- [266] Mukamel, S., Healion, D., Zhang, Y., and Biggs, J. D. *Multidimensional attosecond resonant x-ray spectroscopy of molecules: Lessons from the optical regime.* Annu. Rev. Phys. Chem., **64**(Volume 64, 2013):101–127, (2013).
-

- [267] Rohringer, N. *X-ray raman scattering: a building block for nonlinear spectroscopy*. *Phil. Trans. R. Soc. A*, **377**(2145):20170471, (2019).
- [268] Kroll, T., Weninger, C., Fuller, F. D., et al. *Observation of seeded $m\pi$ $K\beta$ stimulated x-ray emission using two-color x-ray free-electron laser pulses*. *Phys. Rev. Lett.*, **125**:037404, (2020).
- [269] Kukura, P., McCamant, D. W., and Mathies, R. A. *Femtosecond stimulated raman spectroscopy*. *Annu. Rev. Phys. Chem.*, **58**(Volume 58, 2007):461–488, (2007).

Appendix

List of Hazardous Substances

No hazardous chemicals according to the Globally Harmonized System of Classification and Labelling of Chemicals (GHS) have been used in the course of this work.

Supporting Information

Details on how to read the following operator files can be found in the MCTDH documentation <https://www.pci.uni-heidelberg.de/tc/usr/mctdh/doc/index.html>.

MCTDH operator file for Section 4.3

```
#####  
###          VC model for Pyrazine, 9 modes, 3 valence and 3 core  
###          Operator file for fs-XANES  
#####  
  
OP_DEFINE-SECTION  
title  
Pyrazine 9-mode model  
end-title  
end-op_define-section  
  
PARAMETER-SECTION  
# constants  
sqrt2 = 2.0^0.5  
ln2 = 0.6931471805599453  
  
# frequencies  
w10a = 936      ,cm-1  #B1g  
w6a  = 593      ,cm-1  #Ag  
w1   = 1017     ,cm-1  #Ag  
w9a  = 1242     ,cm-1  #Ag  
w8a  = 1605     ,cm-1  #Ag  
w4   = 734      ,cm-1  #B2g  
w5   = 942      ,cm-1  #B2g  
w3   = 1352     ,cm-1  #B3g  
w8b  = 1553     ,cm-1  #B3g  
  
# energies  
E1   = 0.00      ,ev    #Ag  
E2   = 3.93      ,ev    #B3u  
E3   = 4.45      ,ev    #Au  
E4   = 4.79      ,ev    #B2u  
E5   = 399.9701 ,ev    #B2g  
E6   = 399.9716 ,ev    #B3u  
E7   = 402.7701 ,ev    #B1g
```

APPENDIX

```
# linear, on-diagonal coupling coefficients
# S1(B3u)
kappa1_6a      = -0.081      ,ev
kappa1_1       = -0.038      ,ev
kappa1_9a      =  0.117      ,ev
kappa1_8a      = -0.087      ,ev
# S2(Au)
kappa2_6a      = -0.168      ,ev
kappa2_1       = -0.083      ,ev
kappa2_9a      = -0.071      ,ev
kappa2_8a      = -0.465      ,ev
# S3(B2u)
kappa3_6a      =  0.128      ,ev
kappa3_1       = -0.183      ,ev
kappa3_9a      =  0.045      ,ev
kappa3_8a      =  0.026      ,ev
# X1(B3g)
kappa4_6a      = -0.03144    ,ev
kappa4_1       = -0.00106    ,ev
kappa4_9a      =  0.04845    ,ev
kappa4_8a      =  0.09455    ,ev
# X2(B1u)
kappa5_6a      = -0.03134    ,ev
kappa5_1       =  0.00111    ,ev
kappa5_9a      =  0.04848    ,ev
kappa5_8a      =  0.09464    ,ev
# X3(B2g)
kappa6_6a      = -0.13498    ,ev
kappa6_1       = -0.02848    ,ev
kappa6_9a      = -0.14471    ,ev
kappa6_8a      = -0.28893    ,ev

# linear, off-diagonal coupling coefficients
lambda13_10a   =  0.195      ,ev
lambda12_3     =  0.065      ,ev
lambda12_8b    =  0.219      ,ev
lambda23_4     =  0.060      ,ev
lambda23_5     =  0.053      ,ev

# quadratic, on-diagonal coupling coefficients
#H(2,2)
gamma1_10a     = -0.012      ,ev
gamma1_3       = -0.006      ,ev
gamma1_8b      = -0.012      ,ev
gamma1_4       = -0.030      ,ev
gamma1_5       = -0.014      ,ev
#H(3,3)
gamma2_10a     = -0.048      ,ev
gamma2_3       = -0.006      ,ev
gamma2_8b      = -0.012      ,ev
gamma2_4       = -0.031      ,ev
gamma2_5       = -0.026      ,ev
#H(4,4)
gamma3_10a     = -0.012      ,ev
gamma3_3       =  0.001      ,ev
gamma3_8b      =  0.007      ,ev
gamma3_4       = -0.031      ,ev
gamma3_5       = -0.026      ,ev

# Dipole moment
#pump pulse
d01            = 0.08      # x, sqrt(0.006)
d03            = 0.3       # y, sqrt(0.1)
#probe pulse
#S0
d0x2          = 0.10      # x
#S1
d1x1          = 0.06      # z
#S2
d2x3          = 0.06      # z
#S3
d3x3          = 0.03      # x

# core excited state decay
L_t = 8, fs
L = 2*L_t
```


$L_e = 1/L$

end-parameter-section

HAMILTONIAN-SECTION

```
-----
modes| v6a | v1 | v9a | v8a | v10a | v4 | v5 | v3 | v8b | e1
modes| Time
-----
```

kinetic energy

```
w6a      |1      KE
w1       |2      KE
w9a      |3      KE
w8a      |4      KE
w10a     |5      KE
w4       |6      KE
w5       |7      KE
w3       |8      KE
w8b      |9      KE
-----
```

harmonic potential

```
0.5*w6a  |1      q^2
0.5*w1   |2      q^2
0.5*w9a  |3      q^2
0.5*w8a  |4      q^2
0.5*w10a |5      q^2
0.5*w4   |6      q^2
0.5*w5   |7      q^2
0.5*w3   |8      q^2
0.5*w8b  |9      q^2
-----
```

electronic states

```
E1      |10     S1&1
E2      |10     S2&2
E3      |10     S3&3
E4      |10     S4&4
E5      |10     S5&5
E6      |10     S6&6
E7      |10     S7&7
# finite lifetime of core states
-I*L_e  |10     S5&5
-I*L_e  |10     S6&6
-I*L_e  |10     S7&7
-----
```

linear intrastate coupling

```
lambda13_10a |5      q      |10     S2&4
lambda23_4   |6      q      |10     S3&4
lambda23_5   |7      q      |10     S3&4
lambda12_3   |8      q      |10     S2&3
lambda12_8b  |9      q      |10     S2&3
-----
```

linear interstate coupling

```
kappa1_6a   |1      q      |10     S2&2
kappa1_1    |2      q      |10     S2&2
kappa1_9a   |3      q      |10     S2&2
kappa1_8a   |4      q      |10     S2&2
kappa2_6a   |1      q      |10     S3&3
kappa2_1    |2      q      |10     S3&3
kappa2_9a   |3      q      |10     S3&3
kappa2_8a   |4      q      |10     S3&3
kappa3_6a   |1      q      |10     S4&4
kappa3_1    |2      q      |10     S4&4
kappa3_9a   |3      q      |10     S4&4
kappa3_8a   |4      q      |10     S4&4
kappa4_6a   |1      q      |10     S5&5
kappa4_1    |2      q      |10     S5&5
kappa4_9a   |3      q      |10     S5&5
kappa4_8a   |4      q      |10     S5&5
-----
```

APPENDIX

kappa5_6a	1	q	10	S6&6
kappa5_1	2	q	10	S6&6
kappa5_9a	3	q	10	S6&6
kappa5_8a	4	q	10	S6&6
kappa6_6a	1	q	10	S7&7
kappa6_1	2	q	10	S7&7
kappa6_9a	3	q	10	S7&7
kappa6_8a	4	q	10	S7&7

```
-----
# quadratic coupling
0.5*gamma1_10a |5      q^2    |10    S2&2
0.5*gamma1_4   |6      q^2    |10    S2&2
0.5*gamma1_5   |7      q^2    |10    S2&2
0.5*gamma1_3   |8      q^2    |10    S2&2
0.5*gamma1_8b  |9      q^2    |10    S2&2
0.5*gamma2_10a |5      q^2    |10    S3&3
0.5*gamma2_4   |6      q^2    |10    S3&3
0.5*gamma2_5   |7      q^2    |10    S3&3
0.5*gamma2_3   |8      q^2    |10    S3&3
0.5*gamma2_8b  |9      q^2    |10    S3&3
0.5*gamma3_10a |5      q^2    |10    S4&4
0.5*gamma3_4   |6      q^2    |10    S4&4
0.5*gamma3_5   |7      q^2    |10    S4&4
0.5*gamma3_3   |8      q^2    |10    S4&4
0.5*gamma3_8b  |9      q^2    |10    S4&4
-----
```

```
end-hamiltonian-section
end-operator
```

MCTDH operator file for Section 4.4

```
#####
###          VC model for Pyrazine, 24 modes, 19 valence and 2 core
###          Operator file for RIXS
#####
OP_DEFINE-SECTION
  TITLE
    24D Pyrazine 22States
  END-TITLE
END-OP_DEFINE-SECTION

PARAMETER-SECTION
#dipole
dx2s0  =      0.2
dx2s4  =      0.2
dx1s1  =      0.17
dx1s17 =      0.12
dx1s19 =      0.14

#lifetime
L_t = 8, fs
L = 2*L_t
L_e = 1/L

#frequencies
omega_1 = 0.04345 , ev
omega_2 = 0.05276 , ev
omega_3 = 0.07494 , ev
omega_4 = 0.08789 , ev
omega_5 = 0.09138 , ev
omega_6 = 0.09984 , ev
omega_7 = 0.11696 , ev
omega_8 = 0.11777 , ev
omega_9 = 0.12153 , ev
omega_10 = 0.12804 , ev
omega_11 = 0.12868 , ev
omega_12 = 0.13525 , ev
omega_13 = 0.14203 , ev
omega_14 = 0.14407 , ev
omega_15 = 0.15542 , ev
omega_16 = 0.16945 , ev
```

```
omega_17      = 0.17867 , ev
omega_18      = 0.18815 , ev
omega_19      = 0.19777 , ev
omega_20      = 0.20453 , ev
omega_21      = 0.39627 , ev
omega_22      = 0.39634 , ev
omega_23      = 0.39840 , ev
omega_24      = 0.39899 , ev

#energies
E1            = 0.00000 , ev
E2            = 4.32244 , ev
E3            = 5.06570 , ev
E4            = 5.12950 , ev
E5            = 6.00695 , ev
E6            = 6.68251 , ev
E7            = 6.90526 , ev
E8            = 7.02394 , ev
E9            = 7.10984 , ev
E10           = 7.28000 , ev
E11           = 7.47034 , ev
E12           = 7.66268 , ev
E13           = 7.94469 , ev
E14           = 8.00322 , ev
E15           = 8.03587 , ev
E16           = 8.12045 , ev
E17           = 8.13950 , ev
E18           = 8.35338 , ev
E19           = 8.35554 , ev
E20           = 8.53117 , ev

X1            = 402.30130 , ev
X2            = 402.30260 , ev

#on-diagonal linear coupling constants (kappa)
kappa2_3      = 0.09079 , ev
kappa2_11     = -0.07481 , ev
kappa2_15     = 0.12181 , ev
kappa2_20     = -0.13183 , ev
kappa3_3      = -0.11182 , ev
kappa3_11     = -0.21403 , ev
kappa3_15     = -0.00427 , ev
kappa3_20     = -0.02891 , ev
kappa4_3      = 0.17725 , ev
kappa4_11     = -0.13295 , ev
kappa4_15     = -0.00671 , ev
kappa4_20     = -0.37844 , ev
kappa5_3      = 0.20914 , ev
kappa5_11     = -0.14007 , ev
kappa5_15     = 0.15338 , ev
kappa5_20     = 0.04179 , ev

#analytical EOM-CCSD/aug-cc-pvdz values at FC
kappa6_3      = -0.03881 , ev
kappa6_11     = -0.16883 , ev
kappa6_15     = -0.05117 , ev
kappa6_20     = -0.17885 , ev
kappa6_24     = 0.03733 , ev
kappa7_3      = -0.08009 , ev
kappa7_11     = -0.06635 , ev
kappa7_15     = -0.05980 , ev
kappa7_20     = -0.15619 , ev
kappa7_24     = -0.00580 , ev
kappa8_3      = 0.28951 , ev
kappa8_11     = -0.15753 , ev
kappa8_15     = -0.01717 , ev
kappa8_20     = -0.16253 , ev
kappa8_24     = 0.07464 , ev
kappa9_3      = -0.07984 , ev
kappa9_11     = -0.06642 , ev
kappa9_15     = -0.05977 , ev
kappa9_20     = -0.15632 , ev
kappa9_24     = -0.00584 , ev
kappa10_3     = 0.17197 , ev
kappa10_11    = 0.03820 , ev
```

APPENDIX

```
kappa10_15 = 0.03730 , ev
kappa10_20 = -0.25809 , ev
kappa10_24 = -0.00149 , ev
kappa11_3 = 0.16987 , ev
kappa11_11 = 0.00664 , ev
kappa11_15 = -0.02059 , ev
kappa11_20 = -0.21801 , ev
kappa11_24 = 0.01102 , ev
kappa12_3 = -0.06130 , ev
kappa12_11 = -0.07675 , ev
kappa12_15 = -0.02988 , ev
kappa12_20 = -0.17033 , ev
kappa12_24 = -0.01339 , ev
kappa13_3 = 0.01687 , ev
kappa13_11 = -0.17105 , ev
kappa13_15 = 0.01355 , ev
kappa13_20 = -0.04513 , ev
kappa13_24 = 0.03582 , ev
kappa14_3 = 0.17506 , ev
kappa14_11 = 0.01019 , ev
kappa14_15 = -0.00477 , ev
kappa14_20 = -0.23923 , ev
kappa14_24 = -0.00292 , ev
kappa15_3 = 0.16932 , ev
kappa15_11 = 0.01919 , ev
kappa15_15 = 0.07767 , ev
kappa15_20 = -0.26638 , ev
kappa15_24 = -0.00749 , ev
kappa16_3 = -0.05003 , ev
kappa16_11 = -0.08945 , ev
kappa16_15 = -0.09501 , ev
kappa16_20 = -0.16226 , ev
kappa16_24 = -0.00674 , ev
kappa17_3 = 0.03746 , ev
kappa17_11 = -0.16458 , ev
kappa17_15 = 0.12776 , ev
kappa17_20 = 0.14672 , ev
kappa17_24 = 0.00147 , ev
kappa18_3 = -0.06741 , ev
kappa18_11 = -0.08585 , ev
kappa18_15 = 0.00540 , ev
kappa18_20 = -0.18250 , ev
kappa18_24 = -0.02424 , ev
kappa19_3 = -0.20211 , ev
kappa19_11 = -0.06997 , ev
kappa19_15 = 0.03820 , ev
kappa19_20 = 0.50935 , ev
kappa19_24 = -0.21177 , ev
kappa20_3 = 0.20212 , ev
kappa20_11 = -0.06999 , ev
kappa20_15 = 0.03829 , ev
kappa20_20 = 0.50939 , ev
kappa20_24 = -0.21175 , ev

#fitted kappa core-hole states
kappax1_3 = 0.02738 , ev
kappax1_11 = -0.04034 , ev
kappax1_15 = 0.05568 , ev
kappax1_20 = 0.10433 , ev
kappax1_24 = -0.35890 , ev
kappax2_3 = 0.02627 , ev
kappax2_11 = -0.04050 , ev
kappax2_15 = 0.05619 , ev
kappax2_20 = 0.10457 , ev
kappax2_24 = -0.35890 , ev

#off-diagonal linear coupling constants (lambda)
lambda2_3_7 = 0.17641 , ev
lambda2_4_16 = -0.06628 , ev
lambda2_4_19 = -0.20934 , ev
lambda2_4_21 = 0.01410 , ev
lambda2_5_10 = -0.18110 , ev
lambda2_5_14 = 0.09724 , ev
```

```
lambda2_5_18      =  0.10545 , ev
lambda2_5_22      =  0.00120 , ev
lambda3_4_5       = -0.05970 , ev
lambda3_4_8       =  0.00252 , ev
lambda3_5_9       = -0.04874 , ev
lambda4_5_12      =  0.06181 , ev
lambda4_5_13      = -0.09166 , ev
lambda4_5_17      =  0.07303 , ev

#analytical EOM-CCSD/aug-cc-pvdz NACs at FC
lambda5_6_5       = -0.02769 , ev
lambda5_6_8       = -0.00303 , ev
lambda5_7_2       =  0.08434 , ev
lambda5_7_6       =  0.02085 , ev
lambda5_8_4       = -0.00330 , ev
lambda5_8_16      =  0.05900 , ev
lambda5_8_19      =  0.21789 , ev
lambda5_8_21      =  0.02783 , ev
lambda5_9_4       =  0.00169 , ev
lambda5_9_16      = -0.00148 , ev
lambda5_9_19      = -0.00469 , ev
lambda5_9_21      =  0.00044 , ev
lambda5_10_1      = -0.00189 , ev
lambda5_10_9      = -0.00334 , ev
lambda5_11_2      =  0.00283 , ev
lambda5_11_6      =  0.00601 , ev
lambda5_12_10     =  0.00311 , ev
lambda5_12_14     = -0.00095 , ev
lambda5_12_18     =  0.00038 , ev
lambda5_12_22     = -0.00106 , ev
lambda5_13_1      = -0.05553 , ev
lambda5_13_9      = -0.01327 , ev
lambda5_14_7      = -0.00781 , ev
lambda5_15_5      = -0.02705 , ev
lambda5_15_8      = -0.02254 , ev
lambda5_16_12     = -0.00273 , ev
lambda5_16_13     =  0.00847 , ev
lambda5_16_17     = -0.00431 , ev
lambda5_16_23     =  0.00309 , ev
lambda5_17_2      =  0.26289 , ev
lambda5_17_6      = -0.00542 , ev
lambda5_18_4      =  0.00083 , ev
lambda5_18_16     = -0.00143 , ev
lambda5_18_19     = -0.00292 , ev
lambda5_18_21     =  0.00023 , ev
lambda5_19_12     =  0.02715 , ev
lambda5_19_13     = -0.21619 , ev
lambda5_19_17     =  0.06190 , ev
lambda5_19_23     = -0.07465 , ev
lambda5_20_3      = -0.00037 , ev
lambda5_20_11     =  0.00107 , ev
lambda5_20_15     =  0.00054 , ev
lambda5_20_20     =  0.00057 , ev
lambda5_20_24     =  0.00076 , ev

lambda6_7_10      =  0.01791 , ev
lambda6_7_14      =  0.00458 , ev
lambda6_7_18      =  0.00514 , ev
lambda6_7_22      = -0.00267 , ev
lambda6_8_7       =  0.00820 , ev
lambda6_9_7       =  0.26807 , ev
lambda6_10_12     = -0.00351 , ev
lambda6_10_13     =  0.04370 , ev
lambda6_10_17     =  0.00913 , ev
lambda6_10_23     =  0.01145 , ev
lambda6_11_10     =  0.07891 , ev
lambda6_11_14     = -0.00457 , ev
lambda6_11_18     =  0.00599 , ev
lambda6_11_22     = -0.00161 , ev
lambda6_12_2      =  0.01028 , ev
lambda6_12_6      = -0.00455 , ev
lambda6_13_12     = -0.00227 , ev
lambda6_13_13     =  0.00267 , ev
lambda6_13_17     =  0.00093 , ev
lambda6_13_23     =  0.00854 , ev
lambda6_14_4      =  0.00403 , ev
lambda6_14_16     = -0.00117 , ev
lambda6_14_19     =  0.00919 , ev
lambda6_14_21     = -0.01303 , ev
```

APPENDIX

lambda6_15_3	=	-0.00900	, ev
lambda6_15_11	=	0.00905	, ev
lambda6_15_15	=	-0.00265	, ev
lambda6_15_20	=	0.01136	, ev
lambda6_15_24	=	0.00552	, ev
lambda6_16_1	=	-0.01143	, ev
lambda6_16_9	=	-0.00412	, ev
lambda6_17_10	=	-0.02671	, ev
lambda6_17_14	=	0.00180	, ev
lambda6_17_18	=	-0.00274	, ev
lambda6_17_22	=	0.00137	, ev
lambda6_18_7	=	0.01352	, ev
lambda6_19_1	=	-0.00311	, ev
lambda6_19_9	=	-0.00728	, ev
lambda6_20_5	=	0.12575	, ev
lambda6_20_8	=	-0.01783	, ev
lambda7_8_1	=	-0.06358	, ev
lambda7_8_9	=	-0.00856	, ev
lambda7_9_1	=	-0.08216	, ev
lambda7_9_9	=	0.03833	, ev
lambda7_10_4	=	-0.00547	, ev
lambda7_10_16	=	0.00557	, ev
lambda7_10_19	=	0.01282	, ev
lambda7_10_21	=	0.00568	, ev
lambda7_11_3	=	0.03910	, ev
lambda7_11_11	=	0.03576	, ev
lambda7_11_15	=	0.03244	, ev
lambda7_11_20	=	0.05961	, ev
lambda7_11_24	=	-0.00620	, ev
lambda7_12_5	=	0.01707	, ev
lambda7_12_8	=	-0.01678	, ev
lambda7_13_4	=	0.04642	, ev
lambda7_13_16	=	0.04537	, ev
lambda7_13_19	=	0.19671	, ev
lambda7_13_21	=	0.00557	, ev
lambda7_14_12	=	0.00999	, ev
lambda7_14_13	=	0.00048	, ev
lambda7_14_17	=	-0.01120	, ev
lambda7_14_23	=	0.00300	, ev
lambda7_15_10	=	0.00999	, ev
lambda7_15_14	=	-0.00161	, ev
lambda7_15_18	=	0.00337	, ev
lambda7_15_22	=	-0.00118	, ev
lambda7_16_7	=	-0.03726	, ev
lambda7_17_3	=	0.01057	, ev
lambda7_17_11	=	0.00903	, ev
lambda7_17_15	=	0.11446	, ev
lambda7_17_20	=	0.23332	, ev
lambda7_17_24	=	-0.00416	, ev
lambda7_18_1	=	-0.16561	, ev
lambda7_18_9	=	0.07083	, ev
lambda7_19_7	=	0.01285	, ev
lambda7_20_2	=	-0.01542	, ev
lambda7_20_6	=	-0.01165	, ev
lambda8_9_3	=	-0.00993	, ev
lambda8_9_11	=	0.00255	, ev
lambda8_9_15	=	-0.00097	, ev
lambda8_9_20	=	0.00156	, ev
lambda8_9_24	=	-0.00053	, ev
lambda8_10_2	=	0.00158	, ev
lambda8_10_6	=	-0.00311	, ev
lambda8_11_1	=	0.03954	, ev
lambda8_11_9	=	-0.00680	, ev
lambda8_12_12	=	0.00046	, ev
lambda8_12_13	=	-0.00109	, ev
lambda8_12_17	=	0.00039	, ev
lambda8_12_23	=	-0.00247	, ev
lambda8_13_2	=	0.18572	, ev
lambda8_13_6	=	0.04772	, ev
lambda8_14_5	=	0.00036	, ev
lambda8_14_8	=	-0.00215	, ev
lambda8_15_7	=	-0.00886	, ev
lambda8_16_10	=	-0.00111	, ev
lambda8_16_14	=	0.00038	, ev
lambda8_16_18	=	-0.00003	, ev
lambda8_16_22	=	-0.00343	, ev
lambda8_17_1	=	-0.08957	, ev

lambda8_17_9	=	-0.03919	, ev
lambda8_18_3	=	-0.01044	, ev
lambda8_18_11	=	0.00160	, ev
lambda8_18_15	=	0.00045	, ev
lambda8_18_20	=	-0.00003	, ev
lambda8_18_24	=	-0.00396	, ev
lambda8_19_10	=	0.00770	, ev
lambda8_19_14	=	-0.00598	, ev
lambda8_19_18	=	-0.01030	, ev
lambda8_19_22	=	0.00654	, ev
lambda8_20_4	=	0.00120	, ev
lambda8_20_16	=	0.00046	, ev
lambda8_20_19	=	-0.00165	, ev
lambda8_20_21	=	0.00413	, ev
lambda9_10_2	=	0.00918	, ev
lambda9_10_6	=	-0.00609	, ev
lambda9_11_1	=	0.04217	, ev
lambda9_11_9	=	-0.00244	, ev
lambda9_12_12	=	-0.00621	, ev
lambda9_12_13	=	-0.04028	, ev
lambda9_12_16	=	0.01675	, ev
lambda9_12_23	=	0.00694	, ev
lambda9_13_2	=	0.02905	, ev
lambda9_13_6	=	-0.00057	, ev
lambda9_14_5	=	0.01387	, ev
lambda9_14_8	=	-0.00780	, ev
lambda9_15_7	=	-0.00231	, ev
lambda9_16_10	=	-0.00334	, ev
lambda9_16_14	=	0.00640	, ev
lambda9_16_18	=	-0.01897	, ev
lambda9_16_22	=	-0.00208	, ev
lambda9_17_1	=	0.03365	, ev
lambda9_17_9	=	-0.02079	, ev
lambda9_18_3	=	-0.01112	, ev
lambda9_18_11	=	0.01167	, ev
lambda9_18_15	=	-0.01324	, ev
lambda9_18_20	=	0.01188	, ev
lambda9_18_24	=	0.01369	, ev
lambda9_19_10	=	0.00270	, ev
lambda9_19_14	=	0.00021	, ev
lambda9_19_18	=	-0.00018	, ev
lambda9_19_22	=	-0.00667	, ev
lambda9_20_4	=	-0.00119	, ev
lambda9_20_16	=	0.02113	, ev
lambda9_20_19	=	0.01637	, ev
lambda9_20_21	=	0.01937	, ev
lambda10_11_4	=	0.01113	, ev
lambda10_11_16	=	0.00083	, ev
lambda10_11_19	=	0.00554	, ev
lambda10_11_21	=	0.01978	, ev
lambda10_12_7	=	0.26330	, ev
lambda10_13_3	=	0.00288	, ev
lambda10_13_11	=	-0.00184	, ev
lambda10_13_15	=	0.00320	, ev
lambda10_13_20	=	0.00256	, ev
lambda10_13_24	=	-0.00844	, ev
lambda10_14_10	=	0.07071	, ev
lambda10_14_14	=	-0.06674	, ev
lambda10_14_18	=	0.01218	, ev
lambda10_14_22	=	-0.02982	, ev
lambda10_15_12	=	0.00128	, ev
lambda10_15_13	=	-0.04956	, ev
lambda10_15_17	=	-0.02883	, ev
lambda10_15_23	=	-0.02254	, ev
lambda10_16_5	=	0.00049	, ev
lambda10_16_8	=	0.00441	, ev
lambda10_17_4	=	-0.02291	, ev
lambda10_17_16	=	0.01410	, ev
lambda10_17_17	=	-0.00385	, ev
lambda10_17_21	=	-0.02066	, ev
lambda10_18_2	=	-0.00655	, ev
lambda10_18_6	=	0.00088	, ev
lambda10_19_5	=	0.00052	, ev
lambda10_19_8	=	-0.00018	, ev
lambda10_20_1	=	-0.01219	, ev
lambda10_20_9	=	-0.00545	, ev

APPENDIX

lambda11_12_5	=	0.00531	, ev
lambda11_12_8	=	0.00133	, ev
lambda11_13_4	=	-0.00841	, ev
lambda11_13_16	=	0.00250	, ev
lambda11_13_19	=	0.00864	, ev
lambda11_13_21	=	0.00904	, ev
lambda11_14_12	=	0.06123	, ev
lambda11_14_13	=	0.04514	, ev
lambda11_14_17	=	-0.00681	, ev
lambda11_14_23	=	0.01442	, ev
lambda11_15_10	=	0.01818	, ev
lambda11_15_14	=	-0.01690	, ev
lambda11_15_18	=	0.01985	, ev
lambda11_15_22	=	0.00864	, ev
lambda11_16_7	=	-0.27856	, ev
lambda11_17_3	=	-0.04791	, ev
lambda11_17_11	=	-0.04251	, ev
lambda11_17_15	=	0.03049	, ev
lambda11_17_20	=	0.05795	, ev
lambda11_17_24	=	0.01486	, ev
lambda11_18_1	=	0.05233	, ev
lambda11_18_9	=	-0.01557	, ev
lambda11_19_7	=	0.00152	, ev
lambda11_20_2	=	-0.01336	, ev
lambda11_20_6	=	0.00766	, ev
lambda12_13_7	=	0.01050	, ev
lambda12_14_1	=	0.01284	, ev
lambda12_14_9	=	0.00580	, ev
lambda12_15_2	=	-0.00773	, ev
lambda12_15_6	=	0.00224	, ev
lambda12_16_4	=	-0.02628	, ev
lambda12_16_16	=	0.02792	, ev
lambda12_16_19	=	0.01837	, ev
lambda12_16_21	=	-0.02587	, ev
lambda12_17_5	=	-0.00726	, ev
lambda12_17_8	=	0.01230	, ev
lambda12_18_12	=	0.00451	, ev
lambda12_18_13	=	0.00867	, ev
lambda12_18_17	=	-0.03727	, ev
lambda12_18_23	=	-0.02668	, ev
lambda12_19_4	=	-0.00343	, ev
lambda12_19_16	=	0.00082	, ev
lambda12_19_19	=	-0.00157	, ev
lambda12_19_21	=	0.00589	, ev
lambda12_20_10	=	-0.02221	, ev
lambda12_20_14	=	0.08441	, ev
lambda12_20_18	=	-0.01223	, ev
lambda12_20_22	=	0.03253	, ev
lambda13_14_10	=	-0.00384	, ev
lambda13_14_14	=	0.00320	, ev
lambda13_14_18	=	0.00317	, ev
lambda13_14_22	=	-0.00557	, ev
lambda13_15_12	=	0.00579	, ev
lambda13_15_13	=	-0.02074	, ev
lambda13_15_17	=	-0.00413	, ev
lambda13_15_23	=	-0.01118	, ev
lambda13_16_5	=	-0.01208	, ev
lambda13_16_8	=	0.03224	, ev
lambda13_17_4	=	-0.01407	, ev
lambda13_17_16	=	0.03959	, ev
lambda13_17_19	=	0.12534	, ev
lambda13_17_21	=	0.01891	, ev
lambda13_18_2	=	0.02712	, ev
lambda13_18_6	=	0.01345	, ev
lambda13_19_5	=	-0.06891	, ev
lambda13_19_8	=	0.05862	, ev
lambda13_20_1	=	-0.11025	, ev
lambda13_20_9	=	-0.04001	, ev
lambda14_15_4	=	0.00281	, ev
lambda14_15_16	=	0.00630	, ev
lambda14_15_19	=	0.00596	, ev
lambda14_15_21	=	-0.03506	, ev
lambda14_16_2	=	-0.00882	, ev
lambda14_16_6	=	0.00525	, ev
lambda14_17_12	=	0.00091	, ev
lambda14_17_13	=	-0.00598	, ev

```
lambda14_17_17      =  0.00754 , ev
lambda14_17_23      = -0.01842 , ev
lambda14_18_5       = -0.00386 , ev
lambda14_18_8       = -0.00001 , ev
lambda14_19_2       = -0.00105 , ev
lambda14_19_6       = -0.00019 , ev
lambda14_20_7       = -0.26988 , ev

lambda15_16_1       = -0.00466 , ev
lambda15_16_9       =  0.00060 , ev
lambda15_17_10      =  0.03312 , ev
lambda15_17_14      = -0.01250 , ev
lambda15_17_18      =  0.01773 , ev
lambda15_17_22      = -0.01891 , ev
lambda15_18_7       =  0.25171 , ev
lambda15_19_1       =  0.01676 , ev
lambda15_19_9       =  0.01311 , ev
lambda15_20_5       = -0.00020 , ev
lambda15_20_8       = -0.00157 , ev

lambda16_17_7       =  0.03172 , ev
lambda16_18_10      =  0.00054 , ev
lambda16_18_14      =  0.00310 , ev
lambda16_18_18      = -0.00248 , ev
lambda16_18_22      = -0.02806 , ev
lambda16_19_3       =  0.00798 , ev
lambda16_19_11      = -0.00099 , ev
lambda16_19_15      = -0.00830 , ev
lambda16_19_20      = -0.04292 , ev
lambda16_19_24      =  0.01901 , ev
lambda16_20_12      =  0.05986 , ev
lambda16_20_13      = -0.02096 , ev
lambda16_20_17      =  0.00174 , ev
lambda16_20_23      =  0.01210 , ev

lambda17_18_1       =  0.09621 , ev
lambda17_18_9       = -0.01870 , ev
lambda17_19_7       =  0.13390 , ev
lambda17_20_2       =  0.04830 , ev
lambda17_20_6       =  0.00848 , ev

lambda18_19_10      =  0.00742 , ev
lambda18_19_14      =  0.00300 , ev
lambda18_19_17      =  0.00882 , ev
lambda18_19_22      =  0.00955 , ev
lambda18_20_4       =  0.00767 , ev
lambda18_20_16      = -0.01765 , ev
lambda18_20_19      = -0.01057 , ev
lambda18_20_21      =  0.04863 , ev

lambda19_20_12      =  0.00056 , ev
lambda19_20_13      = -0.00345 , ev
lambda19_20_17      =  0.00137 , ev
lambda19_20_23      = -0.00927 , ev

#fitted NACs for core-hole states
lambdax1_x2_10     =  0.08680 , ev
lambdax1_x2_14     =  0.01326 , ev
lambdax1_x2_18     =  0.09910 , ev
lambdax1_x2_22     =  0.03014 , ev

#on-diagonal bilinear coupling constants (gamma)
gamma2_1_1         =  0.03452 , ev
gamma2_2_2         = -0.01893 , ev
gamma2_3_3         =  0.00267 , ev
gamma2_4_4         = -0.01476 , ev
gamma2_5_5         = -0.04539 , ev
gamma2_6_6         =  0.02674 , ev
gamma2_7_7         =  0.00120 , ev
gamma2_8_8         =  0.00443 , ev
gamma2_9_9         = -0.00679 , ev
gamma2_10_10       = -0.02824 , ev
gamma2_11_11       =  0.00242 , ev
gamma2_12_12       =  0.00471 , ev
gamma2_13_13       =  0.07069 , ev
gamma2_14_14       = -0.00749 , ev
gamma2_15_15       = -0.00230 , ev
gamma2_16_16       = -0.00628 , ev
gamma2_17_17       = -0.01667 , ev
```

APPENDIX

gamma2_18_18	=	-0.00781	, ev
gamma2_19_19	=	-0.02333	, ev
gamma2_20_20	=	0.00228	, ev
gamma2_21_21	=	0.05903	, ev
gamma2_22_22	=	0.06024	, ev
gamma2_23_23	=	0.06098	, ev
gamma3_1_1	=	-0.02903	, ev
gamma3_2_2	=	-0.05323	, ev
gamma3_3_3	=	-0.01714	, ev
gamma3_4_4	=	-0.00921	, ev
gamma3_5_5	=	-0.05246	, ev
gamma3_6_6	=	0.01932	, ev
gamma3_7_7	=	0.00131	, ev
gamma3_8_8	=	-0.00758	, ev
gamma3_9_9	=	0.00639	, ev
gamma3_10_10	=	-0.00701	, ev
gamma3_11_11	=	0.00674	, ev
gamma3_12_12	=	0.01054	, ev
gamma3_13_13	=	0.10222	, ev
gamma3_14_14	=	-0.00693	, ev
gamma3_15_15	=	-0.01910	, ev
gamma3_16_16	=	0.00516	, ev
gamma3_17_17	=	0.00347	, ev
gamma3_18_18	=	-0.00182	, ev
gamma3_19_19	=	0.00395	, ev
gamma3_20_20	=	0.01406	, ev
gamma3_21_21	=	0.06107	, ev
gamma3_22_22	=	0.06123	, ev
gamma3_23_23	=	0.06017	, ev
gamma4_1_1	=	-0.02195	, ev
gamma4_2_2	=	0.02623	, ev
gamma4_3_3	=	0.01929	, ev
gamma4_4_4	=	-0.03102	, ev
gamma4_5_5	=	-0.05246	, ev
gamma4_6_6	=	0.00409	, ev
gamma4_7_7	=	-0.05024	, ev
gamma4_8_8	=	-0.02844	, ev
gamma4_9_9	=	-0.04634	, ev
gamma4_10_10	=	-0.05358	, ev
gamma4_11_11	=	0.00583	, ev
gamma4_12_12	=	0.00436	, ev
gamma4_13_13	=	0.08289	, ev
gamma4_14_14	=	-0.01173	, ev
gamma4_15_15	=	0.02741	, ev
gamma4_16_16	=	-0.00631	, ev
gamma4_17_17	=	-0.00963	, ev
gamma4_18_18	=	-0.01854	, ev
gamma4_19_19	=	-0.01122	, ev
gamma4_20_20	=	-0.05377	, ev
gamma4_21_21	=	0.05924	, ev
gamma4_22_22	=	0.05933	, ev
gamma4_23_23	=	0.05943	, ev
gamma5_1_1	=	0.01000	, ev
gamma5_2_2	=	-0.04084	, ev
gamma5_3_3	=	-0.02338	, ev
gamma5_4_4	=	-0.01014	, ev
gamma5_5_5	=	-0.03933	, ev
gamma5_6_6	=	0.03290	, ev
gamma5_7_7	=	0.00421	, ev
gamma5_8_8	=	0.01512	, ev
gamma5_9_9	=	-0.00175	, ev
gamma5_10_10	=	-0.02822	, ev
gamma5_11_11	=	0.00125	, ev
gamma5_12_12	=	0.00434	, ev
gamma5_13_13	=	0.08288	, ev
gamma5_14_14	=	-0.00739	, ev
gamma5_15_15	=	-0.00388	, ev
gamma5_16_16	=	-0.00091	, ev
gamma5_17_17	=	-0.00974	, ev
gamma5_18_18	=	-0.00707	, ev
gamma5_19_19	=	-0.04786	, ev

```
gamma5_20_20 = -0.08293 , ev
gamma5_21_21 = 0.05903 , ev
gamma5_22_22 = 0.06151 , ev
gamma5_23_23 = 0.05831 , ev

gammamax1_1_1 = 0.03194 , ev
gammamax1_2_2 = -0.02329 , ev
gammamax1_3_3 = -0.00909 , ev
gammamax1_4_4 = 0.00585 , ev
gammamax1_5_5 = -0.02108 , ev
gammamax1_6_6 = 0.03672 , ev
gammamax1_7_7 = 0.00984 , ev
gammamax1_8_8 = 0.01658 , ev
gammamax1_9_9 = 0.00564 , ev
gammamax1_10_10 = -0.00098 , ev
gammamax1_11_11 = 0.00226 , ev
gammamax1_12_12 = -0.00190 , ev
gammamax1_13_13 = 0.06899 , ev
gammamax1_14_14 = 0.00160 , ev
gammamax1_15_15 = 0.00589 , ev
gammamax1_16_16 = 0.00717 , ev
gammamax1_17_17 = 0.00294 , ev
gammamax1_18_18 = 0.00427 , ev
gammamax1_19_19 = -0.01735 , ev
gammamax1_20_20 = 0.00373 , ev
gammamax1_21_21 = 0.06303 , ev
gammamax1_22_22 = 0.06235 , ev
gammamax1_23_23 = 0.06198 , ev
gammamax2_1_1 = 0.03257 , ev
gammamax2_2_2 = -0.02343 , ev
gammamax2_3_3 = -0.00902 , ev
gammamax2_4_4 = 0.00565 , ev
gammamax2_5_5 = -0.02204 , ev
gammamax2_6_6 = 0.03623 , ev
gammamax2_7_7 = 0.00971 , ev
gammamax2_8_8 = 0.01697 , ev
gammamax2_9_9 = 0.00594 , ev
gammamax2_10_10 = -0.00098 , ev
gammamax2_11_11 = 0.00195 , ev
gammamax2_12_12 = -0.00191 , ev
gammamax2_13_13 = 0.06899 , ev
gammamax2_14_14 = 0.00659 , ev
gammamax2_15_15 = 0.00630 , ev
gammamax2_16_16 = 0.00704 , ev
gammamax2_17_17 = 0.00199 , ev
gammamax2_18_18 = 0.00427 , ev
gammamax2_19_19 = -0.01742 , ev
gammamax2_20_20 = 0.00361 , ev
gammamax2_21_21 = 0.06252 , ev
gammamax2_22_22 = 0.06479 , ev
gammamax2_23_23 = 0.06137 , ev

# Diabatic curves with parameters
1D_24 = 18.843946229 , ev
1A_24 = 0.103785958
1X_24 = -0.017811471
1E_24 = -0.000064276 , ev
2D_24 = 16.605034747 , ev
2A_24 = 0.113697024
2X_24 = -0.071525788
2E_24 = -0.001089266 , ev
3D_24 = 24.183166560 , ev
3A_24 = 0.092830894
3X_24 = -0.173402626
3E_24 = -0.006166348 , ev
4D_24 = 18.704082166 , ev
4A_24 = 0.103455582
4X_24 = -0.054194716
4E_24 = -0.000584688 , ev
5D_24 = 19.274934324 , ev
5A_24 = 0.103723493
5X_24 = -0.097783763
5E_24 = -0.001962816 , ev

x1D_24 = 15.688146043 , ev
x1A_24 = 0.115075181
```

APPENDIX

```
x1X_24 = -0.180268278
x1E_24 = -0.006612717 , ev
x2D_24 = 15.679824447 , ev
x2A_24 = 0.115111540
x2X_24 = -0.182448296
x2E_24 = -0.006772570 , ev

end-parameter-section

LABELS-SECTION

# Diabatic function labels
v1m24=morse1[1D_24,1A_24,1X_24,1E_24]
v2m24=morse1[2D_24,2A_24,2X_24,2E_24]
v3m24=morse1[3D_24,3A_24,3X_24,3E_24]
v4m24=morse1[4D_24,4A_24,4X_24,4E_24]
v5m24=morse1[5D_24,5A_24,5X_24,5E_24]

vx1m24=morse1[x1D_24,x1A_24,x1X_24,x1E_24]
vx2m24=morse1[x2D_24,x2A_24,x2X_24,x2E_24]

end-labels-section

HAMILTONIAN-SECTION
-----
modes| v1 | v2 | v3 | v4 | v5 | v6 | v7 | v8 | v9 | v10 |
modes| v11 | v12 | v13 | v14 | v15 | v16 | v17 | v18 | v19 | v20 |
modes| v21 | v22 | v23 | v24 | e1
-----

# Kinetic Energy
omega_1 |1 KE
omega_2 |2 KE
omega_3 |3 KE
omega_4 |4 KE
omega_5 |5 KE
omega_6 |6 KE
omega_7 |7 KE
omega_8 |8 KE
omega_9 |9 KE
omega_10 |10 KE
omega_11 |11 KE
omega_12 |12 KE
omega_13 |13 KE
omega_14 |14 KE
omega_15 |15 KE
omega_16 |16 KE
omega_17 |17 KE
omega_18 |18 KE
omega_19 |19 KE
omega_20 |20 KE
omega_21 |21 KE
omega_22 |22 KE
omega_23 |23 KE
omega_24 |24 KE

# Potential for Harmonic oscillator
0.5*omega_1 |1 q^2
0.5*omega_2 |2 q^2
0.5*omega_3 |3 q^2
0.5*omega_4 |4 q^2
0.5*omega_5 |5 q^2
0.5*omega_6 |6 q^2
0.5*omega_7 |7 q^2
0.5*omega_8 |8 q^2
0.5*omega_9 |9 q^2
0.5*omega_10 |10 q^2
0.5*omega_11 |11 q^2
0.5*omega_12 |12 q^2
0.5*omega_13 |13 q^2
0.5*omega_14 |14 q^2
0.5*omega_15 |15 q^2
0.5*omega_16 |16 q^2
0.5*omega_17 |17 q^2
```

0.5*omega_18	18	q ²	
0.5*omega_19	19	q ²	
0.5*omega_20	20	q ²	
0.5*omega_21	21	q ²	
0.5*omega_22	22	q ²	
0.5*omega_23	23	q ²	
# Electronic States			
E1	25	S1&1	
E2	25	S2&2	
E3	25	S3&3	
E4	25	S4&4	
E5	25	S5&5	
E6	25	S6&6	
E7	25	S7&7	
E8	25	S8&8	
E9	25	S9&9	
E10	25	S10&10	
E11	25	S11&11	
E12	25	S12&12	
E13	25	S13&13	
E14	25	S14&14	
E15	25	S15&15	
E16	25	S16&16	
E17	25	S17&17	
E18	25	S18&18	
E19	25	S19&19	
E20	25	S20&20	
X1	25	S21&21	
X2	25	S22&22	
-I*L_e	25	S21&21	
-I*L_e	25	S22&22	
# Lambda			
lambda3_4_5	5	q	25 S3&4
lambda2_3_7	7	q	25 S2&3
lambda3_4_8	8	q	25 S3&4
lambda3_5_9	9	q	25 S3&5
lambda2_5_10	10	q	25 S2&5
lambda4_5_12	12	q	25 S4&5
lambda4_5_13	13	q	25 S4&5
lambda2_5_14	14	q	25 S2&5
lambda2_4_16	16	q	25 S2&4
lambda4_5_17	17	q	25 S4&5
lambda2_5_18	18	q	25 S2&5
lambda2_4_19	19	q	25 S2&4
lambda2_4_21	21	q	25 S2&4
lambda2_5_22	22	q	25 S2&5
lambda6_7_10	10	q	25 S6&7
lambda6_7_14	14	q	25 S6&7
lambda6_7_18	18	q	25 S6&7
lambda6_7_22	22	q	25 S6&7
lambda6_8_7	7	q	25 S6&8
lambda6_9_7	7	q	25 S6&9
lambda6_10_12	12	q	25 S6&10
lambda6_10_13	13	q	25 S6&10
lambda6_10_17	17	q	25 S6&10
lambda6_10_23	23	q	25 S6&10
lambda6_11_10	10	q	25 S6&11
lambda6_11_14	14	q	25 S6&11
lambda6_11_18	18	q	25 S6&11
lambda6_11_22	22	q	25 S6&11
lambda6_12_2	2	q	25 S6&12
lambda6_12_6	6	q	25 S6&12
lambda6_13_12	12	q	25 S6&13
lambda6_13_13	13	q	25 S6&13
lambda6_13_17	17	q	25 S6&13
lambda6_13_23	23	q	25 S6&13
lambda6_14_4	4	q	25 S6&14
lambda6_14_16	16	q	25 S6&14
lambda6_14_19	19	q	25 S6&14

APPENDIX

lambda6_14_21	21	q	25	S6&14
lambda6_15_3	3	q	25	S6&15
lambda6_15_11	11	q	25	S6&15
lambda6_15_15	15	q	25	S6&15
lambda6_15_20	20	q	25	S6&15
lambda6_15_24	24	q	25	S6&15
lambda6_16_1	1	q	25	S6&16
lambda6_16_9	9	q	25	S6&16
lambda6_17_10	10	q	25	S6&17
lambda6_17_14	14	q	25	S6&17
lambda6_17_18	18	q	25	S6&17
lambda6_17_22	22	q	25	S6&17
lambda6_18_7	7	q	25	S6&18
lambda6_19_1	1	q	25	S6&19
lambda6_19_9	9	q	25	S6&19
lambda6_20_5	5	q	25	S6&20
lambda6_20_8	8	q	25	S6&20
lambda7_8_1	1	q	25	S7&8
lambda7_8_9	9	q	25	S7&8
lambda7_9_1	1	q	25	S7&9
lambda7_9_9	9	q	25	S7&9
lambda7_10_4	4	q	25	S7&10
lambda7_10_16	16	q	25	S7&10
lambda7_10_19	19	q	25	S7&10
lambda7_10_21	21	q	25	S7&10
lambda7_11_3	3	q	25	S7&11
lambda7_11_11	11	q	25	S7&11
lambda7_11_15	15	q	25	S7&11
lambda7_11_20	20	q	25	S7&11
lambda7_11_24	24	q	25	S7&11
lambda7_12_5	5	q	25	S7&12
lambda7_12_8	8	q	25	S7&12
lambda7_13_4	4	q	25	S7&13
lambda7_13_16	16	q	25	S7&13
lambda7_13_19	19	q	25	S7&13
lambda7_13_21	21	q	25	S7&13
lambda7_14_12	12	q	25	S7&14
lambda7_14_13	13	q	25	S7&14
lambda7_14_17	17	q	25	S7&14
lambda7_14_23	23	q	25	S7&14
lambda7_15_10	10	q	25	S7&15
lambda7_15_14	14	q	25	S7&15
lambda7_15_18	18	q	25	S7&15
lambda7_15_22	22	q	25	S7&15
lambda7_16_7	7	q	25	S7&16
lambda7_17_3	3	q	25	S7&17
lambda7_17_11	11	q	25	S7&17
lambda7_17_15	15	q	25	S7&17
lambda7_17_20	20	q	25	S7&17
lambda7_17_24	24	q	25	S7&17
lambda7_18_1	1	q	25	S7&18
lambda7_18_9	9	q	25	S7&18
lambda7_19_7	7	q	25	S7&19
lambda7_20_2	2	q	25	S7&20
lambda7_20_6	6	q	25	S7&20
lambda8_9_3	3	q	25	S8&9
lambda8_9_11	11	q	25	S8&9
lambda8_9_15	15	q	25	S8&9
lambda8_9_20	20	q	25	S8&9
lambda8_9_24	24	q	25	S8&9
lambda8_10_2	2	q	25	S8&10
lambda8_10_6	6	q	25	S8&10
lambda8_11_1	1	q	25	S8&11
lambda8_11_9	9	q	25	S8&11
lambda8_12_12	12	q	25	S8&12

lambda8_12_13	13	q	25	S8&12
lambda8_12_17	17	q	25	S8&12
lambda8_12_23	23	q	25	S8&12
lambda8_13_2	2	q	25	S8&13
lambda8_13_6	6	q	25	S8&13
lambda8_14_5	5	q	25	S8&14
lambda8_14_8	8	q	25	S8&14
lambda8_15_7	7	q	25	S8&15
lambda8_16_10	10	q	25	S8&16
lambda8_16_14	14	q	25	S8&16
lambda8_16_18	18	q	25	S8&16
lambda8_16_22	22	q	25	S8&16
lambda8_17_1	1	q	25	S8&17
lambda8_17_9	9	q	25	S8&17
lambda8_18_3	3	q	25	S8&18
lambda8_18_11	11	q	25	S8&18
lambda8_18_15	15	q	25	S8&18
lambda8_18_20	20	q	25	S8&18
lambda8_18_24	24	q	25	S8&18
lambda8_19_10	10	q	25	S8&19
lambda8_19_14	14	q	25	S8&19
lambda8_19_18	18	q	25	S8&19
lambda8_19_22	22	q	25	S8&19
lambda8_20_4	4	q	25	S8&20
lambda8_20_16	16	q	25	S8&20
lambda8_20_19	19	q	25	S8&20
lambda8_20_21	21	q	25	S8&20
lambda9_10_2	2	q	25	S9&10
lambda9_10_6	6	q	25	S9&10
lambda9_11_1	1	q	25	S9&11
lambda9_11_9	9	q	25	S9&11
lambda9_12_12	12	q	25	S9&12
lambda9_12_13	13	q	25	S9&12
lambda9_12_16	16	q	25	S9&12
lambda9_12_23	23	q	25	S9&12
lambda9_13_2	2	q	25	S9&13
lambda9_13_6	6	q	25	S9&13
lambda9_14_5	5	q	25	S9&14
lambda9_14_8	8	q	25	S9&14
lambda9_15_7	7	q	25	S9&15
lambda9_16_10	10	q	25	S9&16
lambda9_16_14	14	q	25	S9&16
lambda9_16_18	18	q	25	S9&16
lambda9_16_22	22	q	25	S9&16
lambda9_17_1	1	q	25	S9&17
lambda9_17_9	9	q	25	S9&17
lambda9_18_3	3	q	25	S9&18
lambda9_18_11	11	q	25	S9&18
lambda9_18_15	15	q	25	S9&18
lambda9_18_20	20	q	25	S9&18
lambda9_18_24	24	q	25	S9&18
lambda9_19_10	10	q	25	S9&19
lambda9_19_14	14	q	25	S9&19
lambda9_19_18	18	q	25	S9&19
lambda9_19_22	22	q	25	S9&19
lambda9_20_4	4	q	25	S9&20
lambda9_20_16	16	q	25	S9&20
lambda9_20_19	19	q	25	S9&20
lambda9_20_21	21	q	25	S9&20
lambda10_11_4	4	q	25	S10&11
lambda10_11_16	16	q	25	S10&11
lambda10_11_19	19	q	25	S10&11
lambda10_11_21	21	q	25	S10&11
lambda10_12_7	7	q	25	S10&12
lambda10_13_3	3	q	25	S10&13

APPENDIX

lambda10_13_11	11	q	25	S10&13
lambda10_13_15	15	q	25	S10&13
lambda10_13_20	20	q	25	S10&13
lambda10_13_24	24	q	25	S10&13
lambda10_14_10	10	q	25	S10&14
lambda10_14_14	14	q	25	S10&14
lambda10_14_18	18	q	25	S10&14
lambda10_14_22	22	q	25	S10&14
lambda10_15_12	12	q	25	S10&15
lambda10_15_13	13	q	25	S10&15
lambda10_15_17	17	q	25	S10&15
lambda10_15_23	23	q	25	S10&15
lambda10_16_5	5	q	25	S10&16
lambda10_16_8	8	q	25	S10&16
lambda10_17_4	4	q	25	S10&17
lambda10_17_16	16	q	25	S10&17
lambda10_17_17	17	q	25	S10&17
lambda10_17_21	21	q	25	S10&17
lambda10_18_2	2	q	25	S10&18
lambda10_18_6	6	q	25	S10&18
lambda10_19_5	5	q	25	S10&19
lambda10_19_8	8	q	25	S10&19
lambda10_20_1	1	q	25	S10&20
lambda10_20_9	9	q	25	S10&20
lambda11_12_5	5	q	25	S11&12
lambda11_12_8	8	q	25	S11&12
lambda11_13_4	4	q	25	S11&13
lambda11_13_16	16	q	25	S11&13
lambda11_13_19	19	q	25	S11&13
lambda11_13_21	21	q	25	S11&13
lambda11_14_12	12	q	25	S11&14
lambda11_14_13	13	q	25	S11&14
lambda11_14_17	17	q	25	S11&14
lambda11_14_23	23	q	25	S11&14
lambda11_15_10	10	q	25	S11&15
lambda11_15_14	14	q	25	S11&15
lambda11_15_18	18	q	25	S11&15
lambda11_15_22	22	q	25	S11&15
lambda11_16_7	7	q	25	S11&16
lambda11_17_3	3	q	25	S11&17
lambda11_17_11	11	q	25	S11&17
lambda11_17_15	15	q	25	S11&17
lambda11_17_20	20	q	25	S11&17
lambda11_17_24	24	q	25	S11&17
lambda11_18_1	1	q	25	S11&18
lambda11_18_9	9	q	25	S11&18
lambda11_19_7	7	q	25	S11&19
lambda11_20_2	2	q	25	S11&20
lambda11_20_6	6	q	25	S11&20
lambda12_13_7	7	q	25	S12&13
lambda12_14_1	1	q	25	S12&14
lambda12_14_9	9	q	25	S12&14
lambda12_15_2	2	q	25	S12&15
lambda12_15_6	6	q	25	S12&15
lambda12_16_4	4	q	25	S12&16
lambda12_16_16	16	q	25	S12&16
lambda12_16_19	19	q	25	S12&16
lambda12_16_21	21	q	25	S12&16
lambda12_17_5	5	q	25	S12&17
lambda12_17_8	8	q	25	S12&17
lambda12_18_12	12	q	25	S12&18
lambda12_18_13	13	q	25	S12&18
lambda12_18_17	17	q	25	S12&18
lambda12_18_23	23	q	25	S12&18

lambda12_19_4	4	q	25	S12&19
lambda12_19_16	16	q	25	S12&19
lambda12_19_19	19	q	25	S12&19
lambda12_19_21	21	q	25	S12&19
lambda12_20_10	10	q	25	S12&20
lambda12_20_14	14	q	25	S12&20
lambda12_20_18	18	q	25	S12&20
lambda12_20_22	22	q	25	S12&20
lambda13_14_10	10	q	25	S13&14
lambda13_14_14	14	q	25	S13&14
lambda13_14_18	18	q	25	S13&14
lambda13_14_22	22	q	25	S13&14
lambda13_15_12	12	q	25	S13&15
lambda13_15_13	13	q	25	S13&15
lambda13_15_17	17	q	25	S13&15
lambda13_15_23	23	q	25	S13&15
lambda13_16_5	5	q	25	S13&16
lambda13_16_8	8	q	25	S13&16
lambda13_17_4	4	q	25	S13&17
lambda13_17_16	16	q	25	S13&17
lambda13_17_19	19	q	25	S13&17
lambda13_17_21	21	q	25	S13&17
lambda13_18_2	2	q	25	S13&18
lambda13_18_6	6	q	25	S13&18
lambda13_19_5	5	q	25	S13&19
lambda13_19_8	8	q	25	S13&19
lambda13_20_1	1	q	25	S13&20
lambda13_20_9	9	q	25	S13&20
lambda14_15_4	4	q	25	S14&15
lambda14_15_16	16	q	25	S14&15
lambda14_15_19	19	q	25	S14&15
lambda14_15_21	21	q	25	S14&15
lambda14_16_2	2	q	25	S14&16
lambda14_16_6	6	q	25	S14&16
lambda14_17_12	12	q	25	S14&17
lambda14_17_13	13	q	25	S14&17
lambda14_17_17	17	q	25	S14&17
lambda14_17_23	23	q	25	S14&17
lambda14_18_5	5	q	25	S14&18
lambda14_18_8	8	q	25	S14&18
lambda14_19_2	2	q	25	S14&19
lambda14_19_6	6	q	25	S14&19
lambda14_20_7	7	q	25	S14&20
lambda15_16_1	1	q	25	S15&16
lambda15_16_9	9	q	25	S15&16
lambda15_17_10	10	q	25	S15&17
lambda15_17_14	14	q	25	S15&17
lambda15_17_18	18	q	25	S15&17
lambda15_17_22	22	q	25	S15&17
lambda15_18_7	7	q	25	S15&18
lambda15_19_1	1	q	25	S15&19
lambda15_19_9	9	q	25	S15&19
lambda15_20_5	5	q	25	S15&20
lambda15_20_8	8	q	25	S15&20
lambda16_17_7	7	q	25	S16&17
lambda16_18_10	10	q	25	S16&18
lambda16_18_14	14	q	25	S16&18
lambda16_18_18	18	q	25	S16&18
lambda16_18_22	22	q	25	S16&18
lambda16_19_3	3	q	25	S16&19
lambda16_19_11	11	q	25	S16&19
lambda16_19_15	15	q	25	S16&19
lambda16_19_20	20	q	25	S16&19
lambda16_19_24	24	q	25	S16&19

APPENDIX

lambda16_20_12	12	q	25	S16&20
lambda16_20_13	13	q	25	S16&20
lambda16_20_17	17	q	25	S16&20
lambda16_20_23	23	q	25	S16&20
lambda17_18_1	1	q	25	S17&18
lambda17_18_9	9	q	25	S17&18
lambda17_19_7	7	q	25	S17&19
lambda17_20_2	2	q	25	S17&20
lambda17_20_6	6	q	25	S17&20
lambda18_19_10	10	q	25	S18&19
lambda18_19_14	14	q	25	S18&19
lambda18_19_17	17	q	25	S18&19
lambda18_19_22	22	q	25	S18&19
lambda18_20_4	4	q	25	S18&20
lambda18_20_16	16	q	25	S18&20
lambda18_20_19	19	q	25	S18&20
lambda18_20_21	21	q	25	S18&20
lambda19_20_12	12	q	25	S19&20
lambda19_20_13	13	q	25	S19&20
lambda19_20_17	17	q	25	S19&20
lambda19_20_23	23	q	25	S19&20
lambdax1_x2_10	10	q	25	S21&22
lambdax1_x2_14	14	q	25	S21&22
lambdax1_x2_18	18	q	25	S21&22
lambdax1_x2_22	22	q	25	S21&22
# Kappa				
kappa2_3	3	q	25	S2&2
kappa3_3	3	q	25	S3&3
kappa4_3	3	q	25	S4&4
kappa5_3	3	q	25	S5&5
kappa2_11	11	q	25	S2&2
kappa3_11	11	q	25	S3&3
kappa4_11	11	q	25	S4&4
kappa5_11	11	q	25	S5&5
kappa2_15	15	q	25	S2&2
kappa3_15	15	q	25	S3&3
kappa4_15	15	q	25	S4&4
kappa5_15	15	q	25	S5&5
kappa2_20	20	q	25	S2&2
kappa3_20	20	q	25	S3&3
kappa4_20	20	q	25	S4&4
kappa5_20	20	q	25	S5&5
kappa6_3	3	q	25	S6&6
kappa6_11	11	q	25	S6&6
kappa6_15	15	q	25	S6&6
kappa6_20	20	q	25	S6&6
kappa6_24	24	q	25	S6&6
kappa7_3	3	q	25	S7&7
kappa7_11	11	q	25	S7&7
kappa7_15	15	q	25	S7&7
kappa7_20	20	q	25	S7&7
kappa7_24	24	q	25	S7&7
kappa8_3	3	q	25	S8&8
kappa8_11	11	q	25	S8&8
kappa8_15	15	q	25	S8&8
kappa8_20	20	q	25	S8&8
kappa8_24	24	q	25	S8&8
kappa9_3	3	q	25	S9&9
kappa9_11	11	q	25	S9&9
kappa9_15	15	q	25	S9&9
kappa9_20	20	q	25	S9&9
kappa9_24	24	q	25	S9&9
kappa10_3	3	q	25	S10&10

kappa10_11	11	q	25	S10&10
kappa10_15	15	q	25	S10&10
kappa10_20	20	q	25	S10&10
kappa10_24	24	q	25	S10&10
kappa11_3	3	q	25	S11&11
kappa11_11	11	q	25	S11&11
kappa11_15	15	q	25	S11&11
kappa11_20	20	q	25	S11&11
kappa11_24	24	q	25	S11&11
kappa12_3	3	q	25	S12&12
kappa12_11	11	q	25	S12&12
kappa12_15	15	q	25	S12&12
kappa12_20	20	q	25	S12&12
kappa12_24	24	q	25	S12&12
kappa13_3	3	q	25	S13&13
kappa13_11	11	q	25	S13&13
kappa13_15	15	q	25	S13&13
kappa13_20	20	q	25	S13&13
kappa13_24	24	q	25	S13&13
kappa14_3	3	q	25	S14&14
kappa14_11	11	q	25	S14&14
kappa14_15	15	q	25	S14&14
kappa14_20	20	q	25	S14&14
kappa14_24	24	q	25	S14&14
kappa15_3	3	q	25	S15&15
kappa15_11	11	q	25	S15&15
kappa15_15	15	q	25	S15&15
kappa15_20	20	q	25	S15&15
kappa15_24	24	q	25	S15&15
kappa16_3	3	q	25	S16&16
kappa16_11	11	q	25	S16&16
kappa16_15	15	q	25	S16&16
kappa16_20	20	q	25	S16&16
kappa16_24	24	q	25	S16&16
kappa17_3	3	q	25	S17&17
kappa17_11	11	q	25	S17&17
kappa17_15	15	q	25	S17&17
kappa17_20	20	q	25	S17&17
kappa17_24	24	q	25	S17&17
kappa18_3	3	q	25	S18&18
kappa18_11	11	q	25	S18&18
kappa18_15	15	q	25	S18&18
kappa18_20	20	q	25	S18&18
kappa18_24	24	q	25	S18&18
kappa19_3	3	q	25	S19&19
kappa19_11	11	q	25	S19&19
kappa19_15	15	q	25	S19&19
kappa19_20	20	q	25	S19&19
kappa19_24	24	q	25	S19&19
kappa20_3	3	q	25	S20&20
kappa20_11	11	q	25	S20&20
kappa20_15	15	q	25	S20&20
kappa20_20	20	q	25	S20&20
kappa20_24	24	q	25	S20&20
kappax1_3	3	q	25	S21&21
kappax1_11	11	q	25	S21&21
kappax1_15	15	q	25	S21&21
kappax1_20	20	q	25	S21&21
kappax2_3	3	q	25	S22&22
kappax2_11	11	q	25	S22&22
kappax2_15	15	q	25	S22&22
kappax2_20	20	q	25	S22&22
# On Diagonal Gamma Constants				
0.5*gamma2_1_1	1	q ²	25	S2&2
0.5*gamma3_1_1	1	q ²	25	S3&3

APPENDIX

0.5*gamma4_1_1	1	q ²	25	S4&4
0.5*gamma5_1_1	1	q ²	25	S5&5
0.5*gamma2_2_2	2	q ²	25	S2&2
0.5*gamma3_2_2	2	q ²	25	S3&3
0.5*gamma4_2_2	2	q ²	25	S4&4
0.5*gamma5_2_2	2	q ²	25	S5&5
0.5*gamma2_3_3	3	q ²	25	S2&2
0.5*gamma3_3_3	3	q ²	25	S3&3
0.5*gamma4_3_3	3	q ²	25	S4&4
0.5*gamma5_3_3	3	q ²	25	S5&5
0.5*gamma2_4_4	4	q ²	25	S2&2
0.5*gamma3_4_4	4	q ²	25	S3&3
0.5*gamma4_4_4	4	q ²	25	S4&4
0.5*gamma5_4_4	4	q ²	25	S5&5
0.5*gamma2_5_5	5	q ²	25	S2&2
0.5*gamma3_5_5	5	q ²	25	S3&3
0.5*gamma4_5_5	5	q ²	25	S4&4
0.5*gamma5_5_5	5	q ²	25	S5&5
0.5*gamma2_6_6	6	q ²	25	S2&2
0.5*gamma3_6_6	6	q ²	25	S3&3
0.5*gamma4_6_6	6	q ²	25	S4&4
0.5*gamma5_6_6	6	q ²	25	S5&5
0.5*gamma2_7_7	7	q ²	25	S2&2
0.5*gamma3_7_7	7	q ²	25	S3&3
0.5*gamma4_7_7	7	q ²	25	S4&4
0.5*gamma5_7_7	7	q ²	25	S5&5
0.5*gamma2_8_8	8	q ²	25	S2&2
0.5*gamma3_8_8	8	q ²	25	S3&3
0.5*gamma4_8_8	8	q ²	25	S4&4
0.5*gamma5_8_8	8	q ²	25	S5&5
0.5*gamma2_9_9	9	q ²	25	S2&2
0.5*gamma3_9_9	9	q ²	25	S3&3
0.5*gamma4_9_9	9	q ²	25	S4&4
0.5*gamma5_9_9	9	q ²	25	S5&5
0.5*gamma2_10_10	10	q ²	25	S2&2
0.5*gamma3_10_10	10	q ²	25	S3&3
0.5*gamma4_10_10	10	q ²	25	S4&4
0.5*gamma5_10_10	10	q ²	25	S5&5
0.5*gamma2_11_11	11	q ²	25	S2&2
0.5*gamma3_11_11	11	q ²	25	S3&3
0.5*gamma4_11_11	11	q ²	25	S4&4
0.5*gamma5_11_11	11	q ²	25	S5&5
0.5*gamma2_12_12	12	q ²	25	S2&2
0.5*gamma3_12_12	12	q ²	25	S3&3
0.5*gamma4_12_12	12	q ²	25	S4&4
0.5*gamma5_12_12	12	q ²	25	S5&5
0.5*gamma2_13_13	13	q ²	25	S2&2
0.5*gamma3_13_13	13	q ²	25	S3&3
0.5*gamma4_13_13	13	q ²	25	S4&4
0.5*gamma5_13_13	13	q ²	25	S5&5
0.5*gamma2_14_14	14	q ²	25	S2&2
0.5*gamma3_14_14	14	q ²	25	S3&3
0.5*gamma4_14_14	14	q ²	25	S4&4
0.5*gamma5_14_14	14	q ²	25	S5&5
0.5*gamma2_15_15	15	q ²	25	S2&2
0.5*gamma3_15_15	15	q ²	25	S3&3
0.5*gamma4_15_15	15	q ²	25	S4&4
0.5*gamma5_15_15	15	q ²	25	S5&5
0.5*gamma2_16_16	16	q ²	25	S2&2
0.5*gamma3_16_16	16	q ²	25	S3&3
0.5*gamma4_16_16	16	q ²	25	S4&4
0.5*gamma5_16_16	16	q ²	25	S5&5
0.5*gamma2_17_17	17	q ²	25	S2&2
0.5*gamma3_17_17	17	q ²	25	S3&3
0.5*gamma4_17_17	17	q ²	25	S4&4
0.5*gamma5_17_17	17	q ²	25	S5&5

0.5*gamma2_18_18	18	q ⁻²	25	S2&2
0.5*gamma3_18_18	18	q ⁻²	25	S3&3
0.5*gamma4_18_18	18	q ⁻²	25	S4&4
0.5*gamma5_18_18	18	q ⁻²	25	S5&5
0.5*gamma2_19_19	19	q ⁻²	25	S2&2
0.5*gamma3_19_19	19	q ⁻²	25	S3&3
0.5*gamma4_19_19	19	q ⁻²	25	S4&4
0.5*gamma5_19_19	19	q ⁻²	25	S5&5
0.5*gamma2_20_20	20	q ⁻²	25	S2&2
0.5*gamma3_20_20	20	q ⁻²	25	S3&3
0.5*gamma4_20_20	20	q ⁻²	25	S4&4
0.5*gamma5_20_20	20	q ⁻²	25	S5&5
0.5*gamma2_21_21	21	q ⁻²	25	S2&2
0.5*gamma3_21_21	21	q ⁻²	25	S3&3
0.5*gamma4_21_21	21	q ⁻²	25	S4&4
0.5*gamma5_21_21	21	q ⁻²	25	S5&5
0.5*gamma2_22_22	22	q ⁻²	25	S2&2
0.5*gamma3_22_22	22	q ⁻²	25	S3&3
0.5*gamma4_22_22	22	q ⁻²	25	S4&4
0.5*gamma5_22_22	22	q ⁻²	25	S5&5
0.5*gamma2_23_23	23	q ⁻²	25	S2&2
0.5*gamma3_23_23	23	q ⁻²	25	S3&3
0.5*gamma4_23_23	23	q ⁻²	25	S4&4
0.5*gamma5_23_23	23	q ⁻²	25	S5&5
0.5*gammax1_1_1	1	q ⁻²	25	S21&21
0.5*gammax1_2_2	2	q ⁻²	25	S21&21
0.5*gammax1_3_3	3	q ⁻²	25	S21&21
0.5*gammax1_4_4	4	q ⁻²	25	S21&21
0.5*gammax1_5_5	5	q ⁻²	25	S21&21
0.5*gammax1_6_6	6	q ⁻²	25	S21&21
0.5*gammax1_7_7	7	q ⁻²	25	S21&21
0.5*gammax1_8_8	8	q ⁻²	25	S21&21
0.5*gammax1_9_9	9	q ⁻²	25	S21&21
0.5*gammax1_10_10	10	q ⁻²	25	S21&21
0.5*gammax1_11_11	11	q ⁻²	25	S21&21
0.5*gammax1_12_12	12	q ⁻²	25	S21&21
0.5*gammax1_13_13	13	q ⁻²	25	S21&21
0.5*gammax1_14_14	14	q ⁻²	25	S21&21
0.5*gammax1_15_15	15	q ⁻²	25	S21&21
0.5*gammax1_16_16	16	q ⁻²	25	S21&21
0.5*gammax1_17_17	17	q ⁻²	25	S21&21
0.5*gammax1_18_18	18	q ⁻²	25	S21&21
0.5*gammax1_19_19	19	q ⁻²	25	S21&21
0.5*gammax1_20_20	20	q ⁻²	25	S21&21
0.5*gammax1_21_21	21	q ⁻²	25	S21&21
0.5*gammax1_22_22	22	q ⁻²	25	S21&21
0.5*gammax1_23_23	23	q ⁻²	25	S21&21
0.5*gammax2_1_1	1	q ⁻²	25	S22&22
0.5*gammax2_2_2	2	q ⁻²	25	S22&22
0.5*gammax2_3_3	3	q ⁻²	25	S22&22
0.5*gammax2_4_4	4	q ⁻²	25	S22&22
0.5*gammax2_5_5	5	q ⁻²	25	S22&22
0.5*gammax2_6_6	6	q ⁻²	25	S22&22
0.5*gammax2_7_7	7	q ⁻²	25	S22&22
0.5*gammax2_8_8	8	q ⁻²	25	S22&22
0.5*gammax2_9_9	9	q ⁻²	25	S22&22
0.5*gammax2_10_10	10	q ⁻²	25	S22&22
0.5*gammax2_11_11	11	q ⁻²	25	S22&22
0.5*gammax2_12_12	12	q ⁻²	25	S22&22
0.5*gammax2_13_13	13	q ⁻²	25	S22&22
0.5*gammax2_14_14	14	q ⁻²	25	S22&22
0.5*gammax2_15_15	15	q ⁻²	25	S22&22
0.5*gammax2_16_16	16	q ⁻²	25	S22&22
0.5*gammax2_17_17	17	q ⁻²	25	S22&22
0.5*gammax2_18_18	18	q ⁻²	25	S22&22

```
0.5*gammax2_19_19 |19 q^2 |25 S22&22
0.5*gammax2_20_20 |20 q^2 |25 S22&22
0.5*gammax2_21_21 |21 q^2 |25 S22&22
0.5*gammax2_22_22 |22 q^2 |25 S22&22
0.5*gammax2_23_23 |23 q^2 |25 S22&22
```

```
# Morse/Anti-Morse potential
1.0 |24 v1m24 |25 S1&1
1.0 |24 v2m24 |25 S2&2
1.0 |24 v3m24 |25 S3&3
1.0 |24 v4m24 |25 S4&4
1.0 |24 v5m24 |25 S5&5

1.0 |24 vx1m24 |25 S21&21
1.0 |24 vx2m24 |25 S22&22
```

```
END-HAMILTONIAN-SECTION
END-OPERATOR
```

MCTDH operator file for Section 4.4

```
#####
### VC model for Pyrazine, 24 modes, 19 valence and 4 core
### Operator file for fs-RIXS
#####
OP_DEFINE-SECTION
  TITLE
    24D Pyrazine 24States
  END-TITLE
END-OP_DEFINE-SECTION

PARAMETER-SECTION
#Dipole moment
#optical excitation
d01 = 0.25
d03 = 0.82
#Xray excitation
#S0(Ag)
d0x2 = 0.10
#S1(B1u)
d1x1 = 0.06 # z
#S2(Au)
d2x3 = 0.06 # x
#S3(B3u)
d3x3 = 0.03 # z
#S4(B3g)
d4x2 = 0.04 # z
#S6(B2u)
d6x1 = 0.02
#S7(B2g)
d7x4 = 0.04
#S12(B3u)
d12x3 = 0.05
#S16(B2u)
d16x1 = 0.04
#S18(Au)
d18x1 = 0.04

# lifetime
L_t = 8, fs
L = 2*L_t
L_e = 1/L

#frequencies
omega_1 = 0.04345 , ev
omega_2 = 0.05276 , ev
omega_3 = 0.07494 , ev
omega_4 = 0.08789 , ev
omega_5 = 0.09138 , ev
omega_6 = 0.09984 , ev
omega_7 = 0.11696 , ev
omega_8 = 0.11777 , ev
omega_9 = 0.12153 , ev
omega_10 = 0.12804 , ev
omega_11 = 0.12868 , ev
omega_12 = 0.13525 , ev
omega_13 = 0.14203 , ev
```

```
omega_14      = 0.14407 , ev
omega_15      = 0.15542 , ev
omega_16      = 0.16945 , ev
omega_17      = 0.17867 , ev
omega_18      = 0.18815 , ev
omega_19      = 0.19777 , ev
omega_20      = 0.20453 , ev
omega_21      = 0.39627 , ev
omega_22      = 0.39634 , ev
omega_23      = 0.39840 , ev
omega_24      = 0.39899 , ev

#energies
E1            = 0.00000 , ev
E2            = 3.93000 , ev
E3            = 4.45000 , ev
E4            = 4.79000 , ev
E5            = 5.38000 , ev
#shifted by -0.6mev to maintain distance between S4 and S5
E6            = 6.08251 , ev
E7            = 6.30526 , ev
E8            = 6.42394 , ev
E9            = 6.50984 , ev
E10           = 6.78000 , ev
E11           = 6.87034 , ev
E12           = 7.06268 , ev
E13           = 7.34469 , ev
E14           = 7.40322 , ev
E15           = 7.43587 , ev
E16           = 7.52045 , ev
E17           = 7.53950 , ev
E18           = 7.75338 , ev
E19           = 7.75554 , ev
E20           = 7.93117 , ev

X1            = 402.30130 , ev
X2            = 402.30260 , ev
X3            = 405.05490 , ev
X4            = 405.05550 , ev

#on-diagonal linear coupling constants (kappa)
kappa2_3      = -0.08100 , ev
kappa2_11     = -0.03800 , ev
kappa2_15     = 0.11700 , ev
kappa2_20     = -0.08700 , ev
kappa2_24     = 0.02200 , ev
kappa3_3      = -0.16800 , ev
kappa3_11     = -0.08300 , ev
kappa3_15     = -0.07100 , ev
kappa3_20     = -0.46500 , ev
kappa3_24     = 0.06000 , ev
kappa4_3      = 0.12800 , ev
kappa4_11     = -0.18300 , ev
kappa4_15     = 0.04500 , ev
kappa4_20     = 0.02600 , ev
kappa4_24     = 0.01800 , ev
kappa5_3      = -0.18400 , ev
kappa5_11     = -0.11700 , ev
kappa5_15     = 0.16500 , ev
kappa5_20     = 0.17200 , ev
kappa5_24     = 0.03000 , ev

#analytical EOM-CCSD/aug-cc-pvdz values at FC
kappa6_3      = -0.03881 , ev
kappa6_11     = -0.16883 , ev
kappa6_15     = -0.05117 , ev
kappa6_20     = -0.17885 , ev
kappa6_24     = 0.03733 , ev
kappa7_3      = -0.08009 , ev
kappa7_11     = -0.06635 , ev
kappa7_15     = -0.05980 , ev
kappa7_20     = -0.15619 , ev
kappa7_24     = -0.00580 , ev
kappa8_3      = 0.28951 , ev
kappa8_11     = -0.15753 , ev
```

APPENDIX

```
kappa8_15 = -0.01717 , ev
kappa8_20 = -0.16253 , ev
kappa8_24 = 0.07464 , ev
kappa9_3 = -0.07984 , ev
kappa9_11 = -0.06642 , ev
kappa9_15 = -0.05977 , ev
kappa9_20 = -0.15632 , ev
kappa9_24 = -0.00584 , ev
kappa10_3 = 0.17197 , ev
kappa10_11 = 0.03820 , ev
kappa10_15 = 0.03730 , ev
kappa10_20 = -0.25809 , ev
kappa10_24 = -0.00149 , ev
kappa11_3 = 0.16987 , ev
kappa11_11 = 0.00664 , ev
kappa11_15 = -0.02059 , ev
kappa11_20 = -0.21801 , ev
kappa11_24 = 0.01102 , ev
kappa12_3 = -0.06130 , ev
kappa12_11 = -0.07675 , ev
kappa12_15 = -0.02988 , ev
kappa12_20 = -0.17033 , ev
kappa12_24 = -0.01339 , ev
kappa13_3 = 0.01687 , ev
kappa13_11 = -0.17105 , ev
kappa13_15 = 0.01355 , ev
kappa13_20 = -0.04513 , ev
kappa13_24 = 0.03582 , ev
kappa14_3 = 0.17506 , ev
kappa14_11 = 0.01019 , ev
kappa14_15 = -0.00477 , ev
kappa14_20 = -0.23923 , ev
kappa14_24 = -0.00292 , ev
kappa15_3 = 0.16932 , ev
kappa15_11 = 0.01919 , ev
kappa15_15 = 0.07767 , ev
kappa15_20 = -0.26638 , ev
kappa15_24 = -0.00749 , ev
kappa16_3 = -0.05003 , ev
kappa16_11 = -0.08945 , ev
kappa16_15 = -0.09501 , ev
kappa16_20 = -0.16226 , ev
kappa16_24 = -0.00674 , ev
kappa17_3 = 0.03746 , ev
kappa17_11 = -0.16458 , ev
kappa17_15 = 0.12776 , ev
kappa17_20 = 0.14672 , ev
kappa17_24 = 0.00147 , ev
kappa18_3 = -0.06741 , ev
kappa18_11 = -0.08585 , ev
kappa18_15 = 0.00540 , ev
kappa18_20 = -0.18250 , ev
kappa18_24 = -0.02424 , ev
kappa19_3 = -0.20211 , ev
kappa19_11 = -0.06997 , ev
kappa19_15 = 0.03820 , ev
kappa19_20 = 0.50935 , ev
kappa19_24 = -0.21177 , ev
kappa20_3 = 0.20212 , ev
kappa20_11 = -0.06999 , ev
kappa20_15 = 0.03829 , ev
kappa20_20 = 0.50939 , ev
kappa20_24 = -0.21175 , ev

#fitted kappa core-hole states
kappax1_3 = 0.02738 , ev
kappax1_11 = -0.04034 , ev
kappax1_15 = 0.05568 , ev
kappax1_20 = 0.10433 , ev
kappax2_3 = 0.02627 , ev
kappax2_11 = -0.04050 , ev
kappax2_15 = 0.05619 , ev
```



```
kappax2_20      =  0.10457 , ev
kappax3_3       =  0.12310 , ev
kappax3_11      = -0.07870 , ev
kappax3_15      = -0.12360 , ev
kappax3_20      = -0.27310 , ev
kappax4_3       =  0.12300 , ev
kappax4_11      = -0.07870 , ev
kappax4_15      = -0.12400 , ev
kappax4_20      = -0.27540 , ev
```

```
#off-diagonal linear coupling constants (lambda)
lambda2_3_16    =  0.06500 , ev
lambda2_3_19    =  0.21900 , ev
lambda2_3_21    =  0.02000 , ev
lambda2_4_7     =  0.19500 , ev
lambda2_5_10    =  0.20700 , ev
lambda2_5_14    =  0.09000 , ev
lambda2_5_18    =  0.09400 , ev
lambda3_4_5     =  0.06000 , ev
lambda3_4_8     =  0.05300 , ev
lambda3_5_1     =  0.11200 , ev
lambda3_5_9     =  0.01800 , ev
lambda4_5_12    =  0.04400 , ev
lambda4_5_13    =  0.04400 , ev
lambda4_5_17    =  0.07200 , ev
```

```
#analytical EOM-CCSD/aug-cc-pvdz NACs at FC
```

```
lambda6_7_10    =  0.01791 , ev
lambda6_7_14    =  0.00458 , ev
lambda6_7_18    =  0.00514 , ev
lambda6_7_22    = -0.00267 , ev
lambda6_8_7     =  0.00820 , ev
lambda6_9_7     =  0.26807 , ev
lambda6_10_12   = -0.00351 , ev
lambda6_10_13   =  0.04370 , ev
lambda6_10_17   =  0.00913 , ev
lambda6_10_23   =  0.01145 , ev
lambda6_11_10   =  0.07891 , ev
lambda6_11_14   = -0.00457 , ev
lambda6_11_18   =  0.00599 , ev
lambda6_11_22   = -0.00161 , ev
lambda6_12_2    =  0.01028 , ev
lambda6_12_6    = -0.00455 , ev
lambda6_13_12   = -0.00227 , ev
lambda6_13_13   =  0.00267 , ev
lambda6_13_17   =  0.00093 , ev
lambda6_13_23   =  0.00854 , ev
lambda6_14_4    =  0.00403 , ev
lambda6_14_16   = -0.00117 , ev
lambda6_14_19   =  0.00919 , ev
lambda6_14_21   = -0.01303 , ev
lambda6_15_3    = -0.00900 , ev
lambda6_15_11   =  0.00905 , ev
lambda6_15_15   = -0.00265 , ev
lambda6_15_20   =  0.01136 , ev
lambda6_15_24   =  0.00552 , ev
lambda6_16_1    = -0.01143 , ev
lambda6_16_9    = -0.00412 , ev
lambda6_17_10   = -0.02671 , ev
lambda6_17_14   =  0.00180 , ev
lambda6_17_18   = -0.00274 , ev
lambda6_17_22   =  0.00137 , ev
lambda6_18_7    =  0.01352 , ev
lambda6_19_1    = -0.00311 , ev
lambda6_19_9    = -0.00728 , ev
lambda6_20_5    =  0.12575 , ev
lambda6_20_8    = -0.01783 , ev

lambda7_8_1     = -0.06358 , ev
lambda7_8_9     = -0.00856 , ev
lambda7_9_1     = -0.08216 , ev
lambda7_9_9     =  0.03833 , ev
lambda7_10_4    = -0.00547 , ev
lambda7_10_16   =  0.00557 , ev
lambda7_10_19   =  0.01282 , ev
lambda7_10_21   =  0.00568 , ev
lambda7_11_3    =  0.03910 , ev
lambda7_11_11   =  0.03576 , ev
```

APPENDIX

lambda7_11_15	=	0.03244	, ev
lambda7_11_20	=	0.05961	, ev
lambda7_11_24	=	-0.00620	, ev
lambda7_12_5	=	0.01707	, ev
lambda7_12_8	=	-0.01678	, ev
lambda7_13_4	=	0.04642	, ev
lambda7_13_16	=	0.04537	, ev
lambda7_13_19	=	0.19671	, ev
lambda7_13_21	=	0.00557	, ev
lambda7_14_12	=	0.00999	, ev
lambda7_14_13	=	0.00048	, ev
lambda7_14_17	=	-0.01120	, ev
lambda7_14_23	=	0.00300	, ev
lambda7_15_10	=	0.00999	, ev
lambda7_15_14	=	-0.00161	, ev
lambda7_15_18	=	0.00337	, ev
lambda7_15_22	=	-0.00118	, ev
lambda7_16_7	=	-0.03726	, ev
lambda7_17_3	=	0.01057	, ev
lambda7_17_11	=	0.00903	, ev
lambda7_17_15	=	0.11446	, ev
lambda7_17_20	=	0.23332	, ev
lambda7_17_24	=	-0.00416	, ev
lambda7_18_1	=	-0.16561	, ev
lambda7_18_9	=	0.07083	, ev
lambda7_19_7	=	0.01285	, ev
lambda7_20_2	=	-0.01542	, ev
lambda7_20_6	=	-0.01165	, ev
lambda8_9_3	=	-0.00993	, ev
lambda8_9_11	=	0.00255	, ev
lambda8_9_15	=	-0.00097	, ev
lambda8_9_20	=	0.00156	, ev
lambda8_9_24	=	-0.00053	, ev
lambda8_10_2	=	0.00158	, ev
lambda8_10_6	=	-0.00311	, ev
lambda8_11_1	=	0.03954	, ev
lambda8_11_9	=	-0.00680	, ev
lambda8_12_12	=	0.00046	, ev
lambda8_12_13	=	-0.00109	, ev
lambda8_12_17	=	0.00039	, ev
lambda8_12_23	=	-0.00247	, ev
lambda8_13_2	=	0.18572	, ev
lambda8_13_6	=	0.04772	, ev
lambda8_14_5	=	0.00036	, ev
lambda8_14_8	=	-0.00215	, ev
lambda8_15_7	=	-0.00886	, ev
lambda8_16_10	=	-0.00111	, ev
lambda8_16_14	=	0.00038	, ev
lambda8_16_18	=	-0.00003	, ev
lambda8_16_22	=	-0.00343	, ev
lambda8_17_1	=	-0.08957	, ev
lambda8_17_9	=	-0.03919	, ev
lambda8_18_3	=	-0.01044	, ev
lambda8_18_11	=	0.00160	, ev
lambda8_18_15	=	0.00045	, ev
lambda8_18_20	=	-0.00003	, ev
lambda8_18_24	=	-0.00396	, ev
lambda8_19_10	=	0.00770	, ev
lambda8_19_14	=	-0.00598	, ev
lambda8_19_18	=	-0.01030	, ev
lambda8_19_22	=	0.00654	, ev
lambda8_20_4	=	0.00120	, ev
lambda8_20_16	=	0.00046	, ev
lambda8_20_19	=	-0.00165	, ev
lambda8_20_21	=	0.00413	, ev
lambda9_10_2	=	0.00918	, ev
lambda9_10_6	=	-0.00609	, ev
lambda9_11_1	=	0.04217	, ev
lambda9_11_9	=	-0.00244	, ev
lambda9_12_12	=	-0.00621	, ev
lambda9_12_13	=	-0.04028	, ev
lambda9_12_16	=	0.01675	, ev
lambda9_12_23	=	0.00694	, ev
lambda9_13_2	=	0.02905	, ev
lambda9_13_6	=	-0.00057	, ev
lambda9_14_5	=	0.01387	, ev
lambda9_14_8	=	-0.00780	, ev

lambda9_15_7	=	-0.00231	, ev
lambda9_16_10	=	-0.00334	, ev
lambda9_16_14	=	0.00640	, ev
lambda9_16_18	=	-0.01897	, ev
lambda9_16_22	=	-0.00208	, ev
lambda9_17_1	=	0.03365	, ev
lambda9_17_9	=	-0.02079	, ev
lambda9_18_3	=	-0.01112	, ev
lambda9_18_11	=	0.01167	, ev
lambda9_18_15	=	-0.01324	, ev
lambda9_18_20	=	0.01188	, ev
lambda9_18_24	=	0.01369	, ev
lambda9_19_10	=	0.00270	, ev
lambda9_19_14	=	0.00021	, ev
lambda9_19_18	=	-0.00018	, ev
lambda9_19_22	=	-0.00667	, ev
lambda9_20_4	=	-0.00119	, ev
lambda9_20_16	=	0.02113	, ev
lambda9_20_19	=	0.01637	, ev
lambda9_20_21	=	0.01937	, ev
lambda10_11_4	=	0.01113	, ev
lambda10_11_16	=	0.00083	, ev
lambda10_11_19	=	0.00554	, ev
lambda10_11_21	=	0.01978	, ev
lambda10_12_7	=	0.26330	, ev
lambda10_13_3	=	0.00288	, ev
lambda10_13_11	=	-0.00184	, ev
lambda10_13_15	=	0.00320	, ev
lambda10_13_20	=	0.00256	, ev
lambda10_13_24	=	-0.00844	, ev
lambda10_14_10	=	0.07071	, ev
lambda10_14_14	=	-0.06674	, ev
lambda10_14_18	=	0.01218	, ev
lambda10_14_22	=	-0.02982	, ev
lambda10_15_12	=	0.00128	, ev
lambda10_15_13	=	-0.04956	, ev
lambda10_15_17	=	-0.02883	, ev
lambda10_15_23	=	-0.02254	, ev
lambda10_16_5	=	0.00049	, ev
lambda10_16_8	=	0.00441	, ev
lambda10_17_4	=	-0.02291	, ev
lambda10_17_16	=	0.01410	, ev
lambda10_17_17	=	-0.00385	, ev
lambda10_17_21	=	-0.02066	, ev
lambda10_18_2	=	-0.00655	, ev
lambda10_18_6	=	0.00088	, ev
lambda10_19_5	=	0.00052	, ev
lambda10_19_8	=	-0.00018	, ev
lambda10_20_1	=	-0.01219	, ev
lambda10_20_9	=	-0.00545	, ev
lambda11_12_5	=	0.00531	, ev
lambda11_12_8	=	0.00133	, ev
lambda11_13_4	=	-0.00841	, ev
lambda11_13_16	=	0.00250	, ev
lambda11_13_19	=	0.00864	, ev
lambda11_13_21	=	0.00904	, ev
lambda11_14_12	=	0.06123	, ev
lambda11_14_13	=	0.04514	, ev
lambda11_14_17	=	-0.00681	, ev
lambda11_14_23	=	0.01442	, ev
lambda11_15_10	=	0.01818	, ev
lambda11_15_14	=	-0.01690	, ev
lambda11_15_18	=	0.01985	, ev
lambda11_15_22	=	0.00864	, ev
lambda11_16_7	=	-0.27856	, ev
lambda11_17_3	=	-0.04791	, ev
lambda11_17_11	=	-0.04251	, ev
lambda11_17_15	=	0.03049	, ev
lambda11_17_20	=	0.05795	, ev
lambda11_17_24	=	0.01486	, ev
lambda11_18_1	=	0.05233	, ev
lambda11_18_9	=	-0.01557	, ev
lambda11_19_7	=	0.00152	, ev
lambda11_20_2	=	-0.01336	, ev
lambda11_20_6	=	0.00766	, ev
lambda12_13_7	=	0.01050	, ev

APPENDIX

lambda12_14_1	=	0.01284	, ev
lambda12_14_9	=	0.00580	, ev
lambda12_15_2	=	-0.00773	, ev
lambda12_15_6	=	0.00224	, ev
lambda12_16_4	=	-0.02628	, ev
lambda12_16_16	=	0.02792	, ev
lambda12_16_19	=	0.01837	, ev
lambda12_16_21	=	-0.02587	, ev
lambda12_17_5	=	-0.00726	, ev
lambda12_17_8	=	0.01230	, ev
lambda12_18_12	=	0.00451	, ev
lambda12_18_13	=	0.00867	, ev
lambda12_18_17	=	-0.03727	, ev
lambda12_18_23	=	-0.02668	, ev
lambda12_19_4	=	-0.00343	, ev
lambda12_19_16	=	0.00082	, ev
lambda12_19_19	=	-0.00157	, ev
lambda12_19_21	=	0.00589	, ev
lambda12_20_10	=	-0.02221	, ev
lambda12_20_14	=	0.08441	, ev
lambda12_20_18	=	-0.01223	, ev
lambda12_20_22	=	0.03253	, ev
lambda13_14_10	=	-0.00384	, ev
lambda13_14_14	=	0.00320	, ev
lambda13_14_18	=	0.00317	, ev
lambda13_14_22	=	-0.00557	, ev
lambda13_15_12	=	0.00579	, ev
lambda13_15_13	=	-0.02074	, ev
lambda13_15_17	=	-0.00413	, ev
lambda13_15_23	=	-0.01118	, ev
lambda13_16_5	=	-0.01208	, ev
lambda13_16_8	=	0.03224	, ev
lambda13_17_4	=	-0.01407	, ev
lambda13_17_16	=	0.03959	, ev
lambda13_17_19	=	0.12534	, ev
lambda13_17_21	=	0.01891	, ev
lambda13_18_2	=	0.02712	, ev
lambda13_18_6	=	0.01345	, ev
lambda13_19_5	=	-0.06891	, ev
lambda13_19_8	=	0.05862	, ev
lambda13_20_1	=	-0.11025	, ev
lambda13_20_9	=	-0.04001	, ev
lambda14_15_4	=	0.00281	, ev
lambda14_15_16	=	0.00630	, ev
lambda14_15_19	=	0.00596	, ev
lambda14_15_21	=	-0.03506	, ev
lambda14_16_2	=	-0.00882	, ev
lambda14_16_6	=	0.00525	, ev
lambda14_17_12	=	0.00091	, ev
lambda14_17_13	=	-0.00598	, ev
lambda14_17_17	=	0.00754	, ev
lambda14_17_23	=	-0.01842	, ev
lambda14_18_5	=	-0.00386	, ev
lambda14_18_8	=	-0.00001	, ev
lambda14_19_2	=	-0.00105	, ev
lambda14_19_6	=	-0.00019	, ev
lambda14_20_7	=	-0.26988	, ev
lambda15_16_1	=	-0.00466	, ev
lambda15_16_9	=	0.00060	, ev
lambda15_17_10	=	0.03312	, ev
lambda15_17_14	=	-0.01250	, ev
lambda15_17_18	=	0.01773	, ev
lambda15_17_22	=	-0.01891	, ev
lambda15_18_7	=	0.25171	, ev
lambda15_19_1	=	0.01676	, ev
lambda15_19_9	=	0.01311	, ev
lambda15_20_5	=	-0.00020	, ev
lambda15_20_8	=	-0.00157	, ev
lambda16_17_7	=	0.03172	, ev
lambda16_18_10	=	0.00054	, ev
lambda16_18_14	=	0.00310	, ev
lambda16_18_18	=	-0.00248	, ev
lambda16_18_22	=	-0.02806	, ev
lambda16_19_3	=	0.00798	, ev
lambda16_19_11	=	-0.00099	, ev
lambda16_19_15	=	-0.00830	, ev

```
lambda16_19_20      = -0.04292 , ev
lambda16_19_24      =  0.01901 , ev
lambda16_20_12      =  0.05986 , ev
lambda16_20_13      = -0.02096 , ev
lambda16_20_17      =  0.00174 , ev
lambda16_20_23      =  0.01210 , ev

lambda17_18_1       =  0.09621 , ev
lambda17_18_9       = -0.01870 , ev
lambda17_19_7       =  0.13390 , ev
lambda17_20_2       =  0.04830 , ev
lambda17_20_6       =  0.00848 , ev

lambda18_19_10      =  0.00742 , ev
lambda18_19_14      =  0.00300 , ev
lambda18_19_17      =  0.00882 , ev
lambda18_19_22      =  0.00955 , ev
lambda18_20_4       =  0.00767 , ev
lambda18_20_16      = -0.01765 , ev
lambda18_20_19      = -0.01057 , ev
lambda18_20_21      =  0.04863 , ev

lambda19_20_12      =  0.00056 , ev
lambda19_20_13      = -0.00345 , ev
lambda19_20_17      =  0.00137 , ev
lambda19_20_23      = -0.00927 , ev

#fitted NACs for core-hole states
lambdax1_x2_10     =  0.08680 , ev
lambdax1_x2_14     =  0.01326 , ev
lambdax1_x2_18     =  0.09910 , ev
lambdax1_x2_22     =  0.03014 , ev
lambdax3_x4_10     =  0.09980 , ev
lambdax3_x4_14     =  0.10870 , ev
lambdax3_x4_18     =  0.02130 , ev
lambdax3_x4_22     =  0.02240 , ev

#on-diagonal bilinear coupling constants (gamma)
gamma2_1_1         =  0.01300 , ev
gamma2_2_2         = -0.00000 , ev
gamma2_4_4         = -0.01300 , ev
gamma2_5_5         = -0.03000 , ev
gamma2_6_6         =  0.00000 , ev
gamma2_7_7         = -0.01200 , ev
gamma2_8_8         =  0.01400 , ev
gamma2_9_9         = -0.01600 , ev
gamma2_10_10       = -0.00600 , ev
gamma2_12_12       = -0.00100 , ev
gamma2_13_13       = -0.01900 , ev
gamma2_14_14       = -0.00600 , ev
gamma2_16_16       = -0.00600 , ev
gamma2_17_17       = -0.01300 , ev
gamma2_18_18       = -0.00600 , ev
gamma2_19_19       = -0.01200 , ev
gamma2_21_21       =  0.00300 , ev
gamma2_22_22       =  0.00400 , ev
gamma2_23_23       =  0.00500 , ev
gamma3_1_1         = -0.01300 , ev
gamma3_2_2         = -0.00000 , ev
gamma3_4_4         = -0.01300 , ev
gamma3_5_5         = -0.03100 , ev
gamma3_6_6         =  0.00000 , ev
gamma3_7_7         = -0.04800 , ev
gamma3_8_8         = -0.02600 , ev
gamma3_9_9         = -0.04100 , ev
gamma3_10_10       = -0.02200 , ev
gamma3_12_12       = -0.00300 , ev
gamma3_13_13       = -0.02100 , ev
gamma3_14_14       = -0.00200 , ev
gamma3_16_16       = -0.00600 , ev
gamma3_17_17       = -0.00600 , ev
gamma3_18_18       = -0.01000 , ev
gamma3_19_19       = -0.01200 , ev
gamma3_21_21       =  0.00300 , ev
gamma3_22_22       =  0.00400 , ev
gamma3_23_23       =  0.00300 , ev
```

APPENDIX

gamma4_1_1	=	-0.00800	, ev
gamma4_2_2	=	0.00000	, ev
gamma4_4_4	=	-0.00500	, ev
gamma4_5_5	=	-0.03100	, ev
gamma4_6_6	=	0.00000	, ev
gamma4_7_7	=	-0.01200	, ev
gamma4_8_8	=	-0.02600	, ev
gamma4_9_9	=	-0.01200	, ev
gamma4_10_10	=	-0.00600	, ev
gamma4_12_12	=	-0.00200	, ev
gamma4_13_13	=	-0.02000	, ev
gamma4_14_14	=	-0.00500	, ev
gamma4_16_16	=	0.00100	, ev
gamma4_17_17	=	0.01500	, ev
gamma4_18_18	=	-0.00200	, ev
gamma4_19_19	=	0.00700	, ev
gamma4_21_21	=	0.00400	, ev
gamma4_22_22	=	0.00400	, ev
gamma4_23_23	=	0.00400	, ev
gamma5_1_1	=	-0.00800	, ev
gamma5_2_2	=	-0.00000	, ev
gamma5_4_4	=	-0.00600	, ev
gamma5_5_5	=	-0.02700	, ev
gamma5_6_6	=	0.00000	, ev
gamma5_7_7	=	-0.01300	, ev
gamma5_8_8	=	0.00900	, ev
gamma5_9_9	=	-0.01200	, ev
gamma5_10_10	=	-0.00600	, ev
gamma5_12_12	=	-0.00300	, ev
gamma5_13_13	=	-0.02100	, ev
gamma5_14_14	=	-0.00600	, ev
gamma5_16_16	=	-0.00400	, ev
gamma5_17_17	=	-0.00600	, ev
gamma5_18_18	=	-0.00600	, ev
gamma5_19_19	=	-0.04300	, ev
gamma5_21_21	=	0.00300	, ev
gamma5_22_22	=	0.00300	, ev
gamma5_23_23	=	0.00300	, ev
gammax1_1_1	=	0.03194	, ev
gammax1_2_2	=	-0.02329	, ev
gammax1_3_3	=	-0.00909	, ev
gammax1_4_4	=	0.00585	, ev
gammax1_5_5	=	-0.02108	, ev
gammax1_6_6	=	0.03672	, ev
gammax1_7_7	=	0.00984	, ev
gammax1_8_8	=	0.01658	, ev
gammax1_9_9	=	0.00564	, ev
gammax1_10_10	=	-0.00098	, ev
gammax1_11_11	=	0.00226	, ev
gammax1_12_12	=	-0.00190	, ev
gammax1_13_13	=	0.06899	, ev
gammax1_14_14	=	0.00160	, ev
gammax1_15_15	=	0.00589	, ev
gammax1_16_16	=	0.00717	, ev
gammax1_17_17	=	0.00294	, ev
gammax1_18_18	=	0.00427	, ev
gammax1_19_19	=	-0.01735	, ev
gammax1_20_20	=	0.00373	, ev
gammax1_21_21	=	0.06303	, ev
gammax1_22_22	=	0.06235	, ev
gammax1_23_23	=	0.06198	, ev
gammax2_1_1	=	0.03257	, ev
gammax2_2_2	=	-0.02343	, ev
gammax2_3_3	=	-0.00902	, ev
gammax2_4_4	=	0.00565	, ev
gammax2_5_5	=	-0.02204	, ev
gammax2_6_6	=	0.03623	, ev
gammax2_7_7	=	0.00971	, ev
gammax2_8_8	=	0.01697	, ev
gammax2_9_9	=	0.00594	, ev
gammax2_10_10	=	-0.00098	, ev

```
gammax2_11_11      =  0.00195 , ev
gammax2_12_12      = -0.00191 , ev
gammax2_13_13      =  0.06899 , ev
gammax2_14_14      =  0.00659 , ev
gammax2_15_15      =  0.00630 , ev
gammax2_16_16      =  0.00704 , ev
gammax2_17_17      =  0.00199 , ev
gammax2_18_18      =  0.00427 , ev
gammax2_19_19      = -0.01742 , ev
gammax2_20_20      =  0.00361 , ev
gammax2_21_21      =  0.06252 , ev
gammax2_22_22      =  0.06479 , ev
gammax2_23_23      =  0.06137 , ev
gammax3_1_1        = -0.04150 , ev
gammax3_2_2        =  0.02930 , ev
gammax3_3_3        =  0.00780 , ev
gammax3_4_4        = -0.01010 , ev
gammax3_5_5        = -0.02030 , ev
gammax3_6_6        =  0.01440 , ev
gammax3_7_7        = -0.01700 , ev
gammax3_8_8        = -0.01150 , ev
gammax3_9_9        = -0.03490 , ev
gammax3_10_10      =  0.00320 , ev
gammax3_11_11     =  0.00590 , ev
gammax3_12_12     =  0.01430 , ev
gammax3_13_13     =  0.08140 , ev
gammax3_14_14     = -0.00590 , ev
gammax3_15_15     =  0.00860 , ev
gammax3_16_16     =  0.01400 , ev
gammax3_17_17     =  0.01040 , ev
gammax3_18_18     =  0.00020 , ev
gammax3_19_19     =  0.02330 , ev
gammax3_20_20     =  0.01750 , ev
gammax3_21_21     =  0.06330 , ev
gammax3_22_22     =  0.06340 , ev
gammax3_23_23     =  0.06270 , ev
gammax3_24_24     = -0.00240 , ev
gammax4_1_1       = -0.04150 , ev
gammax4_2_2       =  0.02910 , ev
gammax4_3_3       =  0.00760 , ev
gammax4_4_4       = -0.01030 , ev
gammax4_5_5       = -0.01990 , ev
gammax4_6_6       =  0.01380 , ev
gammax4_7_7       = -0.01740 , ev
gammax4_8_8       = -0.01190 , ev
gammax4_9_9       = -0.03480 , ev
gammax4_10_10     =  0.00680 , ev
gammax4_11_11     =  0.00600 , ev
gammax4_12_12     =  0.01400 , ev
gammax4_13_13     =  0.09020 , ev
gammax4_14_14     =  0.00600 , ev
gammax4_15_15     =  0.00900 , ev
gammax4_16_16     =  0.01410 , ev
gammax4_17_17     =  0.01000 , ev
gammax4_18_18     =  0.00040 , ev
gammax4_19_19     =  0.02350 , ev
gammax4_20_20     =  0.01650 , ev
gammax4_21_21     =  0.06290 , ev
gammax4_22_22     =  0.06340 , ev
gammax4_23_23     =  0.06000 , ev
gammax4_24_24     = -0.00260 , ev
```

```
# Diabatic curves with parameters
```

```
1D_24 = 18.843946229 , ev
1A_24 =  0.103785958
1X_24 = -0.017811471
1E_24 = -0.000064276 , ev
2D_24 = 16.605034747 , ev
2A_24 =  0.113697024
2X_24 = -0.071525788
2E_24 = -0.001089266 , ev
3D_24 = 24.183166560 , ev
3A_24 =  0.092830894
3X_24 = -0.173402626
```

APPENDIX

```

3E_24 = -0.006166348 , ev
4D_24 = 18.704082166 , ev
4A_24 = 0.103455582
4X_24 = -0.054194716
4E_24 = -0.000584688 , ev
5D_24 = 19.274934324 , ev
5A_24 = 0.103723493
5X_24 = -0.097783763
5E_24 = -0.001962816 , ev

x3EPm1 = 0.016861000 , ev
x3GAm1 = -0.070785000 , ev
x4EPm1 = 0.017082000 , ev
x4GAm1 = -0.070897000 , ev

x1D_24 = 15.688146043 , ev
x1A_24 = 0.115075181
x1X_24 = -0.180268278
x1E_24 = -0.006612717 , ev
x2D_24 = 15.679824447 , ev
x2A_24 = 0.115111540
x2X_24 = -0.182448296
x2E_24 = -0.006772570 , ev
x3D_24 = 12.463000000 , ev
x3A_24 = 0.131675207
x3X_24 = -0.415140000
x3E_24 = -0.035268566 , ev
x4D_24 = 12.459000000 , ev
x4A_24 = 0.131764432
x4X_24 = -0.415090000
x4E_24 = -0.035295475 , ev

end-parameter-section

LABELS-SECTION
# Diabatic function labels
v1m24=morse1[1D_24,1A_24,1X_24,1E_24]
v2m24=morse1[2D_24,2A_24,2X_24,2E_24]
v3m24=morse1[3D_24,3A_24,3X_24,3E_24]
v4m24=morse1[4D_24,4A_24,4X_24,4E_24]
v5m24=morse1[5D_24,5A_24,5X_24,5E_24]

vx1m24=morse1[x1D_24,x1A_24,x1X_24,x1E_24]
vx2m24=morse1[x2D_24,x2A_24,x2X_24,x2E_24]
vx3m24=morse1[x3D_24,x3A_24,x3X_24,x3E_24]
vx4m24=morse1[x4D_24,x4A_24,x4X_24,x4E_24]

end-labels-section

HAMILTONIAN-SECTION
-----
modes| v1 | v2 | v3 | v4 | v5 | v6 | v7 | v8 | v9 | v10 |
modes| v11 | v12 | v13 | v14 | v15 | v16 | v17 | v18 | v19 | v20 |
modes| v21 | v22 | v23 | v24 | e1
modes| Time
-----

# Kinetic Energy
omega_1 |1 KE
omega_2 |2 KE
omega_3 |3 KE
omega_4 |4 KE
omega_5 |5 KE
omega_6 |6 KE
omega_7 |7 KE
omega_8 |8 KE
omega_9 |9 KE
omega_10 |10 KE
omega_11 |11 KE
omega_12 |12 KE
omega_13 |13 KE
omega_14 |14 KE
omega_15 |15 KE
omega_16 |16 KE
omega_17 |17 KE
omega_18 |18 KE
omega_19 |19 KE
omega_20 |20 KE
omega_21 |21 KE

```

```

omega_22      |22    KE
omega_23      |23    KE
omega_24      |24    KE
# Potential for Harmonic oscillator
0.5*omega_1   |1     q^-2
0.5*omega_2   |2     q^-2
0.5*omega_3   |3     q^-2
0.5*omega_4   |4     q^-2
0.5*omega_5   |5     q^-2
0.5*omega_6   |6     q^-2
0.5*omega_7   |7     q^-2
0.5*omega_8   |8     q^-2
0.5*omega_9   |9     q^-2
0.5*omega_10  |10    q^-2
0.5*omega_11  |11    q^-2
0.5*omega_12  |12    q^-2
0.5*omega_13  |13    q^-2
0.5*omega_14  |14    q^-2
0.5*omega_15  |15    q^-2
0.5*omega_16  |16    q^-2
0.5*omega_17  |17    q^-2
0.5*omega_18  |18    q^-2
0.5*omega_19  |19    q^-2
0.5*omega_20  |20    q^-2
0.5*omega_21  |21    q^-2
0.5*omega_22  |22    q^-2
0.5*omega_23  |23    q^-2
0.5*omega_24  |24    q^-2
# Electronic States
E1            |25    S1&1
E2            |25    S2&2
E3            |25    S3&3
E4            |25    S4&4
E5            |25    S5&5
E6            |25    S6&6
E7            |25    S7&7
E8            |25    S8&8
E9            |25    S9&9
E10           |25    S10&10
E11           |25    S11&11
E12           |25    S12&12
E13           |25    S13&13
E14           |25    S14&14
E15           |25    S15&15
E16           |25    S16&16
E17           |25    S17&17
E18           |25    S18&18
E19           |25    S19&19
E20           |25    S20&20
X1            |25    S21&21
X2            |25    S22&22
X3            |25    S23&23
X4            |25    S24&24
-I*L_e        |25    S21&21
-I*L_e        |25    S22&22
-I*L_e        |25    S23&23
-I*L_e        |25    S24&24
# Lambda
lambda2_3_16  |16    q    |25    S2&3
lambda2_3_19  |19    q    |25    S2&3
lambda2_3_21  |21    q    |25    S2&3
lambda2_4_7   |7     q    |25    S2&4
lambda2_5_10  |10    q    |25    S2&5
lambda2_5_14  |14    q    |25    S2&5
lambda2_5_18  |18    q    |25    S2&5
lambda3_4_5   |5     q    |25    S3&4
lambda3_4_8   |8     q    |25    S3&4
lambda3_5_1   |1     q    |25    S3&5

```

APPENDIX

lambda3_5_9	9	q	25	S3&5
lambda4_5_12	12	q	25	S4&5
lambda4_5_13	13	q	25	S4&5
lambda4_5_17	17	q	25	S4&5
lambda6_7_10	10	q	25	S6&7
lambda6_7_14	14	q	25	S6&7
lambda6_7_18	18	q	25	S6&7
lambda6_7_22	22	q	25	S6&7
lambda6_8_7	7	q	25	S6&8
lambda6_9_7	7	q	25	S6&9
lambda6_10_12	12	q	25	S6&10
lambda6_10_13	13	q	25	S6&10
lambda6_10_17	17	q	25	S6&10
lambda6_10_23	23	q	25	S6&10
lambda6_11_10	10	q	25	S6&11
lambda6_11_14	14	q	25	S6&11
lambda6_11_18	18	q	25	S6&11
lambda6_11_22	22	q	25	S6&11
lambda6_12_2	2	q	25	S6&12
lambda6_12_6	6	q	25	S6&12
lambda6_13_12	12	q	25	S6&13
lambda6_13_13	13	q	25	S6&13
lambda6_13_17	17	q	25	S6&13
lambda6_13_23	23	q	25	S6&13
lambda6_14_4	4	q	25	S6&14
lambda6_14_16	16	q	25	S6&14
lambda6_14_19	19	q	25	S6&14
lambda6_14_21	21	q	25	S6&14
lambda6_15_3	3	q	25	S6&15
lambda6_15_11	11	q	25	S6&15
lambda6_15_15	15	q	25	S6&15
lambda6_15_20	20	q	25	S6&15
lambda6_15_24	24	q	25	S6&15
lambda6_16_1	1	q	25	S6&16
lambda6_16_9	9	q	25	S6&16
lambda6_17_10	10	q	25	S6&17
lambda6_17_14	14	q	25	S6&17
lambda6_17_18	18	q	25	S6&17
lambda6_17_22	22	q	25	S6&17
lambda6_18_7	7	q	25	S6&18
lambda6_19_1	1	q	25	S6&19
lambda6_19_9	9	q	25	S6&19
lambda6_20_5	5	q	25	S6&20
lambda6_20_8	8	q	25	S6&20
lambda7_8_1	1	q	25	S7&8
lambda7_8_9	9	q	25	S7&8
lambda7_9_1	1	q	25	S7&9
lambda7_9_9	9	q	25	S7&9
lambda7_10_4	4	q	25	S7&10
lambda7_10_16	16	q	25	S7&10
lambda7_10_19	19	q	25	S7&10
lambda7_10_21	21	q	25	S7&10
lambda7_11_3	3	q	25	S7&11
lambda7_11_11	11	q	25	S7&11
lambda7_11_15	15	q	25	S7&11
lambda7_11_20	20	q	25	S7&11
lambda7_11_24	24	q	25	S7&11
lambda7_12_5	5	q	25	S7&12
lambda7_12_8	8	q	25	S7&12
lambda7_13_4	4	q	25	S7&13
lambda7_13_16	16	q	25	S7&13
lambda7_13_19	19	q	25	S7&13
lambda7_13_21	21	q	25	S7&13
lambda7_14_12	12	q	25	S7&14
lambda7_14_13	13	q	25	S7&14

lambda7_14_17	17	q	25	S7&14
lambda7_14_23	23	q	25	S7&14
lambda7_15_10	10	q	25	S7&15
lambda7_15_14	14	q	25	S7&15
lambda7_15_18	18	q	25	S7&15
lambda7_15_22	22	q	25	S7&15
lambda7_16_7	7	q	25	S7&16
lambda7_17_3	3	q	25	S7&17
lambda7_17_11	11	q	25	S7&17
lambda7_17_15	15	q	25	S7&17
lambda7_17_20	20	q	25	S7&17
lambda7_17_24	24	q	25	S7&17
lambda7_18_1	1	q	25	S7&18
lambda7_18_9	9	q	25	S7&18
lambda7_19_7	7	q	25	S7&19
lambda7_20_2	2	q	25	S7&20
lambda7_20_6	6	q	25	S7&20
lambda8_9_3	3	q	25	S8&9
lambda8_9_11	11	q	25	S8&9
lambda8_9_15	15	q	25	S8&9
lambda8_9_20	20	q	25	S8&9
lambda8_9_24	24	q	25	S8&9
lambda8_10_2	2	q	25	S8&10
lambda8_10_6	6	q	25	S8&10
lambda8_11_1	1	q	25	S8&11
lambda8_11_9	9	q	25	S8&11
lambda8_12_12	12	q	25	S8&12
lambda8_12_13	13	q	25	S8&12
lambda8_12_17	17	q	25	S8&12
lambda8_12_23	23	q	25	S8&12
lambda8_13_2	2	q	25	S8&13
lambda8_13_6	6	q	25	S8&13
lambda8_14_5	5	q	25	S8&14
lambda8_14_8	8	q	25	S8&14
lambda8_15_7	7	q	25	S8&15
lambda8_16_10	10	q	25	S8&16
lambda8_16_14	14	q	25	S8&16
lambda8_16_18	18	q	25	S8&16
lambda8_16_22	22	q	25	S8&16
lambda8_17_1	1	q	25	S8&17
lambda8_17_9	9	q	25	S8&17
lambda8_18_3	3	q	25	S8&18
lambda8_18_11	11	q	25	S8&18
lambda8_18_15	15	q	25	S8&18
lambda8_18_20	20	q	25	S8&18
lambda8_18_24	24	q	25	S8&18
lambda8_19_10	10	q	25	S8&19
lambda8_19_14	14	q	25	S8&19
lambda8_19_18	18	q	25	S8&19
lambda8_19_22	22	q	25	S8&19
lambda8_20_4	4	q	25	S8&20
lambda8_20_16	16	q	25	S8&20
lambda8_20_19	19	q	25	S8&20
lambda8_20_21	21	q	25	S8&20
lambda9_10_2	2	q	25	S9&10
lambda9_10_6	6	q	25	S9&10
lambda9_11_1	1	q	25	S9&11
lambda9_11_9	9	q	25	S9&11
lambda9_12_12	12	q	25	S9&12
lambda9_12_13	13	q	25	S9&12
lambda9_12_16	16	q	25	S9&12
lambda9_12_23	23	q	25	S9&12
lambda9_13_2	2	q	25	S9&13
lambda9_13_6	6	q	25	S9&13
lambda9_14_5	5	q	25	S9&14

APPENDIX

lambda9_14_8	8	q	25	S9&14
lambda9_15_7	7	q	25	S9&15
lambda9_16_10	10	q	25	S9&16
lambda9_16_14	14	q	25	S9&16
lambda9_16_18	18	q	25	S9&16
lambda9_16_22	22	q	25	S9&16
lambda9_17_1	1	q	25	S9&17
lambda9_17_9	9	q	25	S9&17
lambda9_18_3	3	q	25	S9&18
lambda9_18_11	11	q	25	S9&18
lambda9_18_15	15	q	25	S9&18
lambda9_18_20	20	q	25	S9&18
lambda9_18_24	24	q	25	S9&18
lambda9_19_10	10	q	25	S9&19
lambda9_19_14	14	q	25	S9&19
lambda9_19_18	18	q	25	S9&19
lambda9_19_22	22	q	25	S9&19
lambda9_20_4	4	q	25	S9&20
lambda9_20_16	16	q	25	S9&20
lambda9_20_19	19	q	25	S9&20
lambda9_20_21	21	q	25	S9&20
lambda10_11_4	4	q	25	S10&11
lambda10_11_16	16	q	25	S10&11
lambda10_11_19	19	q	25	S10&11
lambda10_11_21	21	q	25	S10&11
lambda10_12_7	7	q	25	S10&12
lambda10_13_3	3	q	25	S10&13
lambda10_13_11	11	q	25	S10&13
lambda10_13_15	15	q	25	S10&13
lambda10_13_20	20	q	25	S10&13
lambda10_13_24	24	q	25	S10&13
lambda10_14_10	10	q	25	S10&14
lambda10_14_14	14	q	25	S10&14
lambda10_14_18	18	q	25	S10&14
lambda10_14_22	22	q	25	S10&14
lambda10_15_12	12	q	25	S10&15
lambda10_15_13	13	q	25	S10&15
lambda10_15_17	17	q	25	S10&15
lambda10_15_23	23	q	25	S10&15
lambda10_16_5	5	q	25	S10&16
lambda10_16_8	8	q	25	S10&16
lambda10_17_4	4	q	25	S10&17
lambda10_17_16	16	q	25	S10&17
lambda10_17_17	17	q	25	S10&17
lambda10_17_21	21	q	25	S10&17
lambda10_18_2	2	q	25	S10&18
lambda10_18_6	6	q	25	S10&18
lambda10_19_5	5	q	25	S10&19
lambda10_19_8	8	q	25	S10&19
lambda10_20_1	1	q	25	S10&20
lambda10_20_9	9	q	25	S10&20
lambda11_12_5	5	q	25	S11&12
lambda11_12_8	8	q	25	S11&12
lambda11_13_4	4	q	25	S11&13
lambda11_13_16	16	q	25	S11&13
lambda11_13_19	19	q	25	S11&13
lambda11_13_21	21	q	25	S11&13
lambda11_14_12	12	q	25	S11&14
lambda11_14_13	13	q	25	S11&14
lambda11_14_17	17	q	25	S11&14
lambda11_14_23	23	q	25	S11&14
lambda11_15_10	10	q	25	S11&15
lambda11_15_14	14	q	25	S11&15
lambda11_15_18	18	q	25	S11&15
lambda11_15_22	22	q	25	S11&15

lambda11_16_7	7	q	25	S11&16
lambda11_17_3	3	q	25	S11&17
lambda11_17_11	11	q	25	S11&17
lambda11_17_15	15	q	25	S11&17
lambda11_17_20	20	q	25	S11&17
lambda11_17_24	24	q	25	S11&17
lambda11_18_1	1	q	25	S11&18
lambda11_18_9	9	q	25	S11&18
lambda11_19_7	7	q	25	S11&19
lambda11_20_2	2	q	25	S11&20
lambda11_20_6	6	q	25	S11&20
lambda12_13_7	7	q	25	S12&13
lambda12_14_1	1	q	25	S12&14
lambda12_14_9	9	q	25	S12&14
lambda12_15_2	2	q	25	S12&15
lambda12_15_6	6	q	25	S12&15
lambda12_16_4	4	q	25	S12&16
lambda12_16_16	16	q	25	S12&16
lambda12_16_19	19	q	25	S12&16
lambda12_16_21	21	q	25	S12&16
lambda12_17_5	5	q	25	S12&17
lambda12_17_8	8	q	25	S12&17
lambda12_18_12	12	q	25	S12&18
lambda12_18_13	13	q	25	S12&18
lambda12_18_17	17	q	25	S12&18
lambda12_18_23	23	q	25	S12&18
lambda12_19_4	4	q	25	S12&19
lambda12_19_16	16	q	25	S12&19
lambda12_19_19	19	q	25	S12&19
lambda12_19_21	21	q	25	S12&19
lambda12_20_10	10	q	25	S12&20
lambda12_20_14	14	q	25	S12&20
lambda12_20_18	18	q	25	S12&20
lambda12_20_22	22	q	25	S12&20
lambda13_14_10	10	q	25	S13&14
lambda13_14_14	14	q	25	S13&14
lambda13_14_18	18	q	25	S13&14
lambda13_14_22	22	q	25	S13&14
lambda13_15_12	12	q	25	S13&15
lambda13_15_13	13	q	25	S13&15
lambda13_15_17	17	q	25	S13&15
lambda13_15_23	23	q	25	S13&15
lambda13_16_5	5	q	25	S13&16
lambda13_16_8	8	q	25	S13&16
lambda13_17_4	4	q	25	S13&17
lambda13_17_16	16	q	25	S13&17
lambda13_17_19	19	q	25	S13&17
lambda13_17_21	21	q	25	S13&17
lambda13_18_2	2	q	25	S13&18
lambda13_18_6	6	q	25	S13&18
lambda13_19_5	5	q	25	S13&19
lambda13_19_8	8	q	25	S13&19
lambda13_20_1	1	q	25	S13&20
lambda13_20_9	9	q	25	S13&20
lambda14_15_4	4	q	25	S14&15
lambda14_15_16	16	q	25	S14&15
lambda14_15_19	19	q	25	S14&15
lambda14_15_21	21	q	25	S14&15
lambda14_16_2	2	q	25	S14&16
lambda14_16_6	6	q	25	S14&16
lambda14_17_12	12	q	25	S14&17
lambda14_17_13	13	q	25	S14&17
lambda14_17_17	17	q	25	S14&17
lambda14_17_23	23	q	25	S14&17

APPENDIX

lambda14_18_5	5	q	25	S14&18
lambda14_18_8	8	q	25	S14&18
lambda14_19_2	2	q	25	S14&19
lambda14_19_6	6	q	25	S14&19
lambda14_20_7	7	q	25	S14&20
lambda15_16_1	1	q	25	S15&16
lambda15_16_9	9	q	25	S15&16
lambda15_17_10	10	q	25	S15&17
lambda15_17_14	14	q	25	S15&17
lambda15_17_18	18	q	25	S15&17
lambda15_17_22	22	q	25	S15&17
lambda15_18_7	7	q	25	S15&18
lambda15_19_1	1	q	25	S15&19
lambda15_19_9	9	q	25	S15&19
lambda15_20_5	5	q	25	S15&20
lambda15_20_8	8	q	25	S15&20
lambda16_17_7	7	q	25	S16&17
lambda16_18_10	10	q	25	S16&18
lambda16_18_14	14	q	25	S16&18
lambda16_18_18	18	q	25	S16&18
lambda16_18_22	22	q	25	S16&18
lambda16_19_3	3	q	25	S16&19
lambda16_19_11	11	q	25	S16&19
lambda16_19_15	15	q	25	S16&19
lambda16_19_20	20	q	25	S16&19
lambda16_19_24	24	q	25	S16&19
lambda16_20_12	12	q	25	S16&20
lambda16_20_13	13	q	25	S16&20
lambda16_20_17	17	q	25	S16&20
lambda16_20_23	23	q	25	S16&20
lambda17_18_1	1	q	25	S17&18
lambda17_18_9	9	q	25	S17&18
lambda17_19_7	7	q	25	S17&19
lambda17_20_2	2	q	25	S17&20
lambda17_20_6	6	q	25	S17&20
lambda18_19_10	10	q	25	S18&19
lambda18_19_14	14	q	25	S18&19
lambda18_19_17	17	q	25	S18&19
lambda18_19_22	22	q	25	S18&19
lambda18_20_4	4	q	25	S18&20
lambda18_20_16	16	q	25	S18&20
lambda18_20_19	19	q	25	S18&20
lambda18_20_21	21	q	25	S18&20
lambda19_20_12	12	q	25	S19&20
lambda19_20_13	13	q	25	S19&20
lambda19_20_17	17	q	25	S19&20
lambda19_20_23	23	q	25	S19&20
lambdax1_x2_10	10	q	25	S21&22
lambdax1_x2_14	14	q	25	S21&22
lambdax1_x2_18	18	q	25	S21&22
lambdax1_x2_22	22	q	25	S21&22
lambdax3_x4_10	10	q	25	S23&24
lambdax3_x4_14	14	q	25	S23&24
lambdax3_x4_18	18	q	25	S23&24
lambdax3_x4_22	22	q	25	S23&24
# Kappa				
kappa2_3	3	q	25	S2&2
kappa3_3	3	q	25	S3&3
kappa4_3	3	q	25	S4&4
kappa5_3	3	q	25	S5&5
kappa2_11	11	q	25	S2&2
kappa3_11	11	q	25	S3&3

kappa4_11	11	q	25	S4&4
kappa5_11	11	q	25	S5&5
kappa2_15	15	q	25	S2&2
kappa3_15	15	q	25	S3&3
kappa4_15	15	q	25	S4&4
kappa5_15	15	q	25	S5&5
kappa2_20	20	q	25	S2&2
kappa3_20	20	q	25	S3&3
kappa4_20	20	q	25	S4&4
kappa5_20	20	q	25	S5&5
kappa2_24	24	q	25	S2&2
kappa3_24	24	q	25	S3&3
kappa4_24	24	q	25	S4&4
kappa5_24	24	q	25	S5&5
kappa6_3	3	q	25	S6&6
kappa6_11	11	q	25	S6&6
kappa6_15	15	q	25	S6&6
kappa6_20	20	q	25	S6&6
kappa6_24	24	q	25	S6&6
kappa7_3	3	q	25	S7&7
kappa7_11	11	q	25	S7&7
kappa7_15	15	q	25	S7&7
kappa7_20	20	q	25	S7&7
kappa7_24	24	q	25	S7&7
kappa8_3	3	q	25	S8&8
kappa8_11	11	q	25	S8&8
kappa8_15	15	q	25	S8&8
kappa8_20	20	q	25	S8&8
kappa8_24	24	q	25	S8&8
kappa9_3	3	q	25	S9&9
kappa9_11	11	q	25	S9&9
kappa9_15	15	q	25	S9&9
kappa9_20	20	q	25	S9&9
kappa9_24	24	q	25	S9&9
kappa10_3	3	q	25	S10&10
kappa10_11	11	q	25	S10&10
kappa10_15	15	q	25	S10&10
kappa10_20	20	q	25	S10&10
kappa10_24	24	q	25	S10&10
kappa11_3	3	q	25	S11&11
kappa11_11	11	q	25	S11&11
kappa11_15	15	q	25	S11&11
kappa11_20	20	q	25	S11&11
kappa11_24	24	q	25	S11&11
kappa12_3	3	q	25	S12&12
kappa12_11	11	q	25	S12&12
kappa12_15	15	q	25	S12&12
kappa12_20	20	q	25	S12&12
kappa12_24	24	q	25	S12&12
kappa13_3	3	q	25	S13&13
kappa13_11	11	q	25	S13&13
kappa13_15	15	q	25	S13&13
kappa13_20	20	q	25	S13&13
kappa13_24	24	q	25	S13&13
kappa14_3	3	q	25	S14&14
kappa14_11	11	q	25	S14&14
kappa14_15	15	q	25	S14&14
kappa14_20	20	q	25	S14&14
kappa14_24	24	q	25	S14&14
kappa15_3	3	q	25	S15&15
kappa15_11	11	q	25	S15&15
kappa15_15	15	q	25	S15&15
kappa15_20	20	q	25	S15&15
kappa15_24	24	q	25	S15&15
kappa16_3	3	q	25	S16&16

APPENDIX

kappa16_11	11	q	25	S16&16
kappa16_15	15	q	25	S16&16
kappa16_20	20	q	25	S16&16
kappa16_24	24	q	25	S16&16
kappa17_3	3	q	25	S17&17
kappa17_11	11	q	25	S17&17
kappa17_15	15	q	25	S17&17
kappa17_20	20	q	25	S17&17
kappa17_24	24	q	25	S17&17
kappa18_3	3	q	25	S18&18
kappa18_11	11	q	25	S18&18
kappa18_15	15	q	25	S18&18
kappa18_20	20	q	25	S18&18
kappa18_24	24	q	25	S18&18
kappa19_3	3	q	25	S19&19
kappa19_11	11	q	25	S19&19
kappa19_15	15	q	25	S19&19
kappa19_20	20	q	25	S19&19
kappa19_24	24	q	25	S19&19
kappa20_3	3	q	25	S20&20
kappa20_11	11	q	25	S20&20
kappa20_15	15	q	25	S20&20
kappa20_20	20	q	25	S20&20
kappa20_24	24	q	25	S20&20
kappax1_3	3	q	25	S21&21
kappax1_11	11	q	25	S21&21
kappax1_15	15	q	25	S21&21
kappax1_20	20	q	25	S21&21
kappax2_3	3	q	25	S22&22
kappax2_11	11	q	25	S22&22
kappax2_15	15	q	25	S22&22
kappax2_20	20	q	25	S22&22
kappax3_3	3	q	25	S23&23
kappax3_11	11	q	25	S23&23
kappax3_15	15	q	25	S23&23
kappax3_20	20	q	25	S23&23
kappax4_3	3	q	25	S24&24
kappax4_11	11	q	25	S24&24
kappax4_15	15	q	25	S24&24
kappax4_20	20	q	25	S24&24
# On Diagonal Gamma Constants				
0.5*gamma2_1_1	1	q ²	25	S2&2
0.5*gamma3_1_1	1	q ²	25	S3&3
0.5*gamma4_1_1	1	q ²	25	S4&4
0.5*gamma5_1_1	1	q ²	25	S5&5
0.5*gamma2_2_2	2	q ²	25	S2&2
0.5*gamma3_2_2	2	q ²	25	S3&3
0.5*gamma4_2_2	2	q ²	25	S4&4
0.5*gamma5_2_2	2	q ²	25	S5&5
0.5*gamma2_4_4	4	q ²	25	S2&2
0.5*gamma3_4_4	4	q ²	25	S3&3
0.5*gamma4_4_4	4	q ²	25	S4&4
0.5*gamma5_4_4	4	q ²	25	S5&5
0.5*gamma2_5_5	5	q ²	25	S2&2
0.5*gamma3_5_5	5	q ²	25	S3&3
0.5*gamma4_5_5	5	q ²	25	S4&4
0.5*gamma5_5_5	5	q ²	25	S5&5
0.5*gamma2_6_6	6	q ²	25	S2&2
0.5*gamma3_6_6	6	q ²	25	S3&3
0.5*gamma4_6_6	6	q ²	25	S4&4
0.5*gamma5_6_6	6	q ²	25	S5&5
0.5*gamma2_7_7	7	q ²	25	S2&2
0.5*gamma3_7_7	7	q ²	25	S3&3
0.5*gamma4_7_7	7	q ²	25	S4&4
0.5*gamma5_7_7	7	q ²	25	S5&5

0.5*gamma2_8_8	8	q ⁻²	25	S2&2
0.5*gamma3_8_8	8	q ⁻²	25	S3&3
0.5*gamma4_8_8	8	q ⁻²	25	S4&4
0.5*gamma5_8_8	8	q ⁻²	25	S5&5
0.5*gamma2_9_9	9	q ⁻²	25	S2&2
0.5*gamma3_9_9	9	q ⁻²	25	S3&3
0.5*gamma4_9_9	9	q ⁻²	25	S4&4
0.5*gamma5_9_9	9	q ⁻²	25	S5&5
0.5*gamma2_10_10	10	q ⁻²	25	S2&2
0.5*gamma3_10_10	10	q ⁻²	25	S3&3
0.5*gamma4_10_10	10	q ⁻²	25	S4&4
0.5*gamma5_10_10	10	q ⁻²	25	S5&5
0.5*gamma2_12_12	12	q ⁻²	25	S2&2
0.5*gamma3_12_12	12	q ⁻²	25	S3&3
0.5*gamma4_12_12	12	q ⁻²	25	S4&4
0.5*gamma5_12_12	12	q ⁻²	25	S5&5
0.5*gamma2_13_13	13	q ⁻²	25	S2&2
0.5*gamma3_13_13	13	q ⁻²	25	S3&3
0.5*gamma4_13_13	13	q ⁻²	25	S4&4
0.5*gamma5_13_13	13	q ⁻²	25	S5&5
0.5*gamma2_14_14	14	q ⁻²	25	S2&2
0.5*gamma3_14_14	14	q ⁻²	25	S3&3
0.5*gamma4_14_14	14	q ⁻²	25	S4&4
0.5*gamma5_14_14	14	q ⁻²	25	S5&5
0.5*gamma2_16_16	16	q ⁻²	25	S2&2
0.5*gamma3_16_16	16	q ⁻²	25	S3&3
0.5*gamma4_16_16	16	q ⁻²	25	S4&4
0.5*gamma5_16_16	16	q ⁻²	25	S5&5
0.5*gamma2_17_17	17	q ⁻²	25	S2&2
0.5*gamma3_17_17	17	q ⁻²	25	S3&3
0.5*gamma4_17_17	17	q ⁻²	25	S4&4
0.5*gamma5_17_17	17	q ⁻²	25	S5&5
0.5*gamma2_18_18	18	q ⁻²	25	S2&2
0.5*gamma3_18_18	18	q ⁻²	25	S3&3
0.5*gamma4_18_18	18	q ⁻²	25	S4&4
0.5*gamma5_18_18	18	q ⁻²	25	S5&5
0.5*gamma2_19_19	19	q ⁻²	25	S2&2
0.5*gamma3_19_19	19	q ⁻²	25	S3&3
0.5*gamma4_19_19	19	q ⁻²	25	S4&4
0.5*gamma5_19_19	19	q ⁻²	25	S5&5
0.5*gamma2_21_21	21	q ⁻²	25	S2&2
0.5*gamma3_21_21	21	q ⁻²	25	S3&3
0.5*gamma4_21_21	21	q ⁻²	25	S4&4
0.5*gamma5_21_21	21	q ⁻²	25	S5&5
0.5*gamma2_22_22	22	q ⁻²	25	S2&2
0.5*gamma3_22_22	22	q ⁻²	25	S3&3
0.5*gamma4_22_22	22	q ⁻²	25	S4&4
0.5*gamma5_22_22	22	q ⁻²	25	S5&5
0.5*gamma2_23_23	23	q ⁻²	25	S2&2
0.5*gamma3_23_23	23	q ⁻²	25	S3&3
0.5*gamma4_23_23	23	q ⁻²	25	S4&4
0.5*gamma5_23_23	23	q ⁻²	25	S5&5
0.5*gammax1_1_1	1	q ⁻²	25	S21&21
0.5*gammax1_2_2	2	q ⁻²	25	S21&21
0.5*gammax1_3_3	3	q ⁻²	25	S21&21
0.5*gammax1_4_4	4	q ⁻²	25	S21&21
0.5*gammax1_5_5	5	q ⁻²	25	S21&21
0.5*gammax1_6_6	6	q ⁻²	25	S21&21
0.5*gammax1_7_7	7	q ⁻²	25	S21&21
0.5*gammax1_8_8	8	q ⁻²	25	S21&21
0.5*gammax1_9_9	9	q ⁻²	25	S21&21
0.5*gammax1_10_10	10	q ⁻²	25	S21&21
0.5*gammax1_11_11	11	q ⁻²	25	S21&21
0.5*gammax1_12_12	12	q ⁻²	25	S21&21
0.5*gammax1_13_13	13	q ⁻²	25	S21&21

APPENDIX

0.5*gammax1_14_14	14	q ²	25	S21&21
0.5*gammax1_15_15	15	q ²	25	S21&21
0.5*gammax1_16_16	16	q ²	25	S21&21
0.5*gammax1_17_17	17	q ²	25	S21&21
0.5*gammax1_18_18	18	q ²	25	S21&21
0.5*gammax1_19_19	19	q ²	25	S21&21
0.5*gammax1_20_20	20	q ²	25	S21&21
0.5*gammax1_21_21	21	q ²	25	S21&21
0.5*gammax1_22_22	22	q ²	25	S21&21
0.5*gammax1_23_23	23	q ²	25	S21&21
0.5*gammax2_1_1	1	q ²	25	S22&22
0.5*gammax2_2_2	2	q ²	25	S22&22
0.5*gammax2_3_3	3	q ²	25	S22&22
0.5*gammax2_4_4	4	q ²	25	S22&22
0.5*gammax2_5_5	5	q ²	25	S22&22
0.5*gammax2_6_6	6	q ²	25	S22&22
0.5*gammax2_7_7	7	q ²	25	S22&22
0.5*gammax2_8_8	8	q ²	25	S22&22
0.5*gammax2_9_9	9	q ²	25	S22&22
0.5*gammax2_10_10	10	q ²	25	S22&22
0.5*gammax2_11_11	11	q ²	25	S22&22
0.5*gammax2_12_12	12	q ²	25	S22&22
0.5*gammax2_13_13	13	q ²	25	S22&22
0.5*gammax2_14_14	14	q ²	25	S22&22
0.5*gammax2_15_15	15	q ²	25	S22&22
0.5*gammax2_16_16	16	q ²	25	S22&22
0.5*gammax2_17_17	17	q ²	25	S22&22
0.5*gammax2_18_18	18	q ²	25	S22&22
0.5*gammax2_19_19	19	q ²	25	S22&22
0.5*gammax2_20_20	20	q ²	25	S22&22
0.5*gammax2_21_21	21	q ²	25	S22&22
0.5*gammax2_22_22	22	q ²	25	S22&22
0.5*gammax2_23_23	23	q ²	25	S22&22
0.5*gammax3_1_1	1	q ²	25	S23&23
0.5*gammax3_2_2	2	q ²	25	S23&23
0.5*gammax3_3_3	3	q ²	25	S23&23
0.5*gammax3_4_4	4	q ²	25	S23&23
0.5*gammax3_5_5	5	q ²	25	S23&23
0.5*gammax3_6_6	6	q ²	25	S23&23
0.5*gammax3_7_7	7	q ²	25	S23&23
0.5*gammax3_8_8	8	q ²	25	S23&23
0.5*gammax3_9_9	9	q ²	25	S23&23
0.5*gammax3_10_10	10	q ²	25	S23&23
0.5*gammax3_11_11	11	q ²	25	S23&23
0.5*gammax3_12_12	12	q ²	25	S23&23
0.5*gammax3_13_13	13	q ²	25	S23&23
0.5*gammax3_14_14	14	q ²	25	S23&23
0.5*gammax3_15_15	15	q ²	25	S23&23
0.5*gammax3_16_16	16	q ²	25	S23&23
0.5*gammax3_17_17	17	q ²	25	S23&23
0.5*gammax3_18_18	18	q ²	25	S23&23
0.5*gammax3_19_19	19	q ²	25	S23&23
0.5*gammax3_20_20	20	q ²	25	S23&23
0.5*gammax3_21_21	21	q ²	25	S23&23
0.5*gammax3_22_22	22	q ²	25	S23&23
0.5*gammax3_23_23	23	q ²	25	S23&23
0.5*gammax4_1_1	1	q ²	25	S24&24
0.5*gammax4_2_2	2	q ²	25	S24&24
0.5*gammax4_3_3	3	q ²	25	S24&24
0.5*gammax4_4_4	4	q ²	25	S24&24
0.5*gammax4_5_5	5	q ²	25	S24&24
0.5*gammax4_6_6	6	q ²	25	S24&24
0.5*gammax4_7_7	7	q ²	25	S24&24
0.5*gammax4_8_8	8	q ²	25	S24&24
0.5*gammax4_9_9	9	q ²	25	S24&24
0.5*gammax4_10_10	10	q ²	25	S24&24

0.5*gammax4_11_11	11	q ²	25	S24&24
0.5*gammax4_12_12	12	q ²	25	S24&24
0.5*gammax4_13_13	13	q ²	25	S24&24
0.5*gammax4_14_14	14	q ²	25	S24&24
0.5*gammax4_15_15	15	q ²	25	S24&24
0.5*gammax4_16_16	16	q ²	25	S24&24
0.5*gammax4_17_17	17	q ²	25	S24&24
0.5*gammax4_18_18	18	q ²	25	S24&24
0.5*gammax4_19_19	19	q ²	25	S24&24
0.5*gammax4_20_20	20	q ²	25	S24&24
0.5*gammax4_21_21	21	q ²	25	S24&24
0.5*gammax4_22_22	22	q ²	25	S24&24
0.5*gammax4_23_23	23	q ²	25	S24&24

Morse/Anti-Morse potential

1.0	24	vx1m24	25	S21&21
1.0	24	vx2m24	25	S22&22
1.0	24	vx3m24	25	S23&23
1.0	24	vx4m24	25	S24&24

Quartic potential

0.041667*x3EPm1	1	q ⁴	25	S23&23
0.50000*x3GAm1	1	q ²	25	S23&23
0.041667*x4EPm1	1	q ⁴	25	S24&24
0.50000*x4GAm1	1	q ²	25	S24&24

END-HAMILTONIAN-SECTION
END-OPERATOR

Acknowledgements

First and foremost, I would like to deeply thank my supervisor, Nils Huse. Thank you for being brave enough to bring on a theoretician you hadn't previously known, for involving me in the development of my own projects and for seamlessly integrating me into ongoing projects. Thank you for all the things you have taught me and for being patient in answering even my most silly questions. I am grateful for your unwavering support not only in matters pertaining to this thesis but also in my broader professional pursuits, all while allowing me the flexibility to balance family and academic life. The list could be endless but most importantly, I appreciate your respectful demeanor, always meeting me on equal footing, valuing my input, and fostering an environment where mistakes are viewed as opportunities for growth rather than setbacks. Lastly, I am thankful for the enjoyable conversations and shared laughter beyond science and for chocolate during more arduous writing moments.

I also wish to express my sincere gratitude to my co-supervisor, Oriol Vendrell. Thank you for our numerous Zoom meetings making the start of my PhD as good as it can be during a pandemic situation. I am thankful for your repeated invitations to Heidelberg and the warm hospitality extended during my visits. I also want to thank you for your continuous support for my career aspirations, coupled with your guidance and patience. I appreciate the freedom you afforded me to explore and cultivate my own ideas. It has truly been a pleasure collaborating with both of you, and I sincerely hope for the opportunity to work together again in the future.

Next, I extend my thanks to David Mendive-Tapia for his invaluable assistance with technical challenges, his willingness to address numerous queries, for proof-reading this thesis and for the enjoyable reminiscences of our (independent) London times. I am appreciative of his collaboration on all thesis-related projects.

I would like to thank Carmen Herrmann, Gabriel Bester, and Graham Worth for their dedication and sacrifice of their time as members of my committee. Special thanks to Graham for initially introducing me to the fascinating world of time-dependent quantum mechanics during my Masters. I'm looking forward to more

math-oriented chemistry.

I extend my thanks to all past and present members of the Huse group for fostering a friendly and supportive working environment. In particular, I am grateful to Jessi for being the best office mate and travel companion, for our fruitful scientific collaborations, and for her ever-optimistic outlook. Thank you for repeating ‘Alles wird gut!’ as often as I needed it.

I would also like to express my gratitude to Todd Martinez and his group at Stanford University for their warm welcome during my research stay, and to the German Academic Exchange Service (DAAD) for facilitating this opportunity.

I further thank the Christiane Nüsslein-Volhard Foundation, International Max Planck Research School for Ultrafast Imaging & Structural Dynamics, cluster of excellence CUI: Advanced Imaging of Matter and University of Hamburg for financial and scientific support. I thank the dynaMENT program for mentoring during the final year of my PhD.

I am also greatly indebted to my parents for countless reasons. To my mother, I extend heartfelt thanks for her unwavering support, boundless encouragement, and the love she has always shown me. To my father, I express gratitude for his genuine interest in me and my endeavors, for his effort trying to understand what I’m doing, for holding everything together for a long time and supporting me in any decision I made during my life. Although we are not together to celebrate this achievement, I know how proud you would be (perhaps to a point of embarrassment).

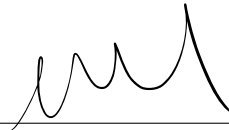
Lastly, I wish to acknowledge my husband, Marco, whose endless support has been a cornerstone throughout my PhD journey. I want to thank you for proof-reading everything despite the challenge of an unfamiliar topic and for assuming any family responsibility without complaint or reproach during the final stretch. Above all, I am grateful for your and our son’s unconditional love, your unwavering presence even during my most trying moments, and for teaching me to set the right priorities in life. Everything I achieved during the last years would not have been possible without the joy you bring to my life.

Eidesstattliche Versicherung

Hiermit versichere ich an Eides statt, die vorliegende Dissertationsschrift selbst verfasst und keine anderen als die angegebenen Quellen und Hilfsmittel benutzt zu haben. Sofern im Zuge der Erstellung der vorliegenden Dissertationsschrift generative Künstliche Intelligenz (gKI) basierte elektronische Hilfsmittel verwendet wurden, versichere ich, dass meine eigene Leistung im Vordergrund stand und dass eine vollständige Dokumentation aller verwendeten Hilfsmittel gemäß der Guten wissenschaftlichen Praxis vorliegt. Ich trage die Verantwortung für eventuell durch die gKI generierte fehlerhafte oder verzerrte Inhalte, fehlerhafte Referenzen, Verstöße gegen das Datenschutz- und Urheberrecht oder Plagiate.

Hamburg, 04.04.2024

Ort, Datum



Unterschrift